Advanced Modeling of Biomass Pyrolysis and Combustion

Gu, Tianbao

DOI (link to publication from Publisher):
10.54337/aau488129355

Publication date:
2022

Document Version
Publisher's PDF, also known as Version of record

ADVANCED MODELING OF BIOMASS PYROLYSIS AND COMBUSTION

BY
TIANBAO GU

DISSERTATION SUBMITTED 2022

AALBORG UNIVERSITY
DENMARK

Advanced Modeling of Biomass Pyrolysis and Combustion

Ph.D. Dissertation

by

Tianbao Gu

AAU Energy, Aalborg University
Pontoppidanstræde 111, 9220 Aalborg Øst, Danmark
E-mail: tig@energy.aau.dk

AALBORG UNIVERSITY
DENMARK

Dissertation submitted June, 2022

Dissertation submitted: June 9th, 2022

PhD supervisor: Chungen Yin, Associate Professor
Aalborg University

Ph.D. co-supervisor: Torsten Berning, Associate Professor
Aalborg University

PhD committee: Associate Professor Matthias Mandø (chair)
Aalborg University, Denmark

Professor Peter Glarborg
Technical University of Denmark, Denmark

Senior Research Scientist Nils Erland L. Haugen
SINTEF Energy Research, Norway

PhD Series: Faculty of Engineering and Science, Aalborg University

Department: AAU Energy

ISSN (online): 2446-1636
ISBN (online): 978-87-7573-884-7

Published by:
Aalborg University Press
Kroghstræde 3
DK – 9220 Aalborg Ø
Phone: +45 99407140
aauf@forlag.aau.dk
forlag.aau.dk

Printed in Denmark by Stibo Complete, 2022

Abstract

As an abundant carbon-neutral resource, biomass has great potential to yield renewable energy and valuable chemicals. The utilization of biomass is significant for achieving carbon neutrality. Thermochemical conversion technologies such as pyrolysis, gasification, and combustion, play a vital role in converting biomass to bioenergy or other by-products. Among them, pyrolysis that can produce high-value bioproducts from the decomposition of solids in the absence of oxygen, is recognized as a promising technology for biomass efficient utilization. Combustion technology, oxidizing fuel into gaseous products with sufficient oxygen and producing heat, is widely applied to various types of biomass for recycling energy. In addition, pyrolysis is an inseparable sub-process of combustion and gasification, i.e., devolatilization of the volatiles. Bearing this in mind, this Ph.D. project aims to investigate pyrolysis and combustion technologies to promote the efficient and clean utilization of biomass.

For biomass pyrolysis, kinetic modeling, which connects the academic research and engineering applications of solid fuel conversion, is of great significance in exploring the underlying mechanism and optimizing the reaction process. Whereas, the complexity of existing kinetic models and the diversity of the evaluated kinetics in previous biomass pyrolysis studies largely compromise the effectiveness of kinetic modeling. In this thesis, a universal description of solid fuel decomposition is derived for all common reaction mechanisms, which shows statistical characteristics. For example, the expression for first-order reactions is consistent with the standardised general extreme value distribution. Accordingly, four applications are demonstrated: conversion peak identification, reaction mechanism determination, conversion rate prediction, and kinetics evaluation. Moreover, a simplified kinetic model with only one kinetic parameter is developed to predict the conversion rate and validated using experimental data. The model has been employed to analyze poplar wood pyrolysis, which exhibited superior performance in terms of accuracy, stability, and simplicity compared to the conventional Arrhenius-type model.

For biomass combustion, municipal solid waste (MSW), as one of the dominant biomass resources, is selected as the incinerating feedstock in this project, for which grate-firing technology is widely employed. Due to the

limitations and difficulties of experimental study, simulation investigation is regarded as powerful and cost-efficient for understanding and optimizing large-scale MSW combustion. In this thesis, a moving-grate boiler incinerating 750 tons of MSW per day was simulated based on Computational Fluid Dynamics (CFD). The coupling strategy: model the fuel bed and freeboard separately and then couple them together, is implemented. An in-house bed model including NO_x formation is developed to describe the solid conversion processes (i.e., drying, pyrolysis, combustion, and gasification) on the moving grate. The freeboard simulation is performed in ANSYS Fluent to solve the turbulent reacting flow, containing the bed model results, namely, profiles of temperature, velocity, and gas species. The simulation results are verified by comparing with the operation data inside the boiler. Subsequently, two simulation-based investigations on this boiler are conducted: the impacts of feedstock change caused by waste classification and co-combustion of MSW and sewage sludge. The former research reveals the potential issues for incinerating the new MSW, e.g., ineffective oxygen utilization, low mixing, and non-uniform temperature in the freeboard, when maintaining the current operating conditions. Subsequently, adjustments in the air supply and thermal input are proposed and probed in the simulation, which addresses these potential issues and shows improvements in operation stability and energy recovery. The latter investigation numerically tests the feasibility of MSW co-firing with sewage sludge and industrial solid waste in the existing boiler, in which the industrial waste serves as the supporting fuel. It explores suitable blends and operation guidelines that promote the combustion stability and NO_x reduction up to 11.54%.

In summary, the contributions of this Ph.D. project are twofold: kinetic modeling of biomass pyrolysis and CFD simulation of MSW combustion, developing two original models for each part. Applications and investigations based on the two models are conducted, resulting in valuable findings and demonstrating their potential for biomass utilization via thermochemical conversion technologies.

Resumé

Biomasse som er en rigelig kulstofneutral ressource har et stort potentiale til at fremstille vedvarende energi og værdifulde produkter, og dens udnyttelse er vigtig for at opnå kulstofneutralitet. Termokemiske omdannelsesteknologier som f.eks. pyrolyse, forgasning og forbrænding spiller en afgørende rolle i omdannelsen af biomasse til bioenergi eller andre biprodukter. Pyrolyse er en lovende teknologi til effektiv udnyttelse af biomasse, som kan producere bio-produkter af høj værdi ved at nedbryde fast brændsel i fravær af ilt. Forbrændingsteknologi anvendes mest til at generere energi fra forskellige typer biomasse, her brændstof oxideres til en røggas og varmeproduktion. Denne proces kræver ilt. Derudover er pyrolyse en uadskillelig delproces af forbrænding og forgasning. Med dette i mente sigter dette Ph.D. projekt efter at undersøge pyrolyse- og forbrændingsteknologier for at fremme effektive og bæredygtige udnyttelser af biomasse.

Kinetisk modellering som forbinder videnskabelig forskning og ingeniørmæssige udnyttelser af biomassepyrolyse er vigtige for at udforske den underliggende mekanisme og optimere reaktionsprocessen. Kompleksiteten af eksisterende kinetiske modeller og mangfoldigheden af den evaluerede kinetik komplicerer væsentligt effektiviteten af kinetiske modelleringsstudier. I denne afhandling er der udledt en universel beskrivelse af brændstofnedbrydning for alle almindelige reaktionsmekanismer, som viser deres statistiske karakteristika. For eksempel er udtrykket for førsteordens reaktioner samme med den standardiserede generelle ekstremværdifordeling. Derfor demonstreres fire applikationer: identifikation af konverteringstop, bestemmelse af reaktionsmekanisme, forudsigelse af konverteringshastighed og kinetisk evaluering. De nyudviklede metoder blev valideret af de eksperimentelle data og sammenlignet med de konventionelle metoder. En forenklet kinetisk model med kun én kinetisk parameter blev udviklet til at forudsige konverteringsraten. Modellen anvendes til at analysere poppeltræ pyrolyse og udviser overlegen ydeevne med hensyn til nøjagtighed, stabilitet og enkelhed i sammenligning med den typiske Arrhenius-type model.

Husholdnings affald blev brugt til biomasseforbrænding i Ph.D. projektet. Ristfyring som er en af de primære forbrændingsteknologier er almindeligt brugt i affaldsforbrænding og simuleringsstudier er både nødvendigt og

omkostningseffektivt for at forstå og optimere forbrændingsprocessen. I denne afhandling blev en kedel med vandrerist, som forbrænder 750 tons affald om dagen, simuleret med Computational Fluid Dynamics (CFD). En koblingsstrategi hvor brændstoflejet og fribordet modelleres separat og derefter kobler dem sammen blev implementeret. En ristmodel til at inkludere NO_x-dannelse blev udviklet til at beskrive faststofkonverteringsprocessen (dvs. tørring, pyrolyse, forbrænding og forgasning) på den bevægelige rist. Fribordssimulering blev udført i ANSYS Fluent for at løse det turbulente reagerende flow, som kombineres med ristmodel resultaterne: profiler af temperatur, hastighed og massefraktioner af arter. Simuleringsresultaterne blev verificeret ved at sammenligne med driftsdataene inde i kedlen. Efterfølgende blev der udført to simulationsbaserede undersøgelser af denne kedel: virkningerne af råmaterialeændringer forårsaget af affaldsklassificering og samforbrænding af affald og spildevandsslam. Tidligere forskning har afsløret de potentielle problemer for den nye affaldsforbrænding, for eksempel ineffektiv fordeling og udnyttelse af ilt, dårlig blanding og uensartet temperatur i fribordet, når de nuværende driftsbetingelser opretholdes. Efterfølgende foreslås justeringer i lufttilførslen og termisk input, som adresserer disse potentielle problemer og viser forbedringer i driftsstabilitet og energigenvinding udefra simuleringsresultaterne. De sidstnævnte studier omfattet CFD baseret simuleringer af forbrænding af en blanding af affald, spildevandsslam og industrielt fast affald i den eksisterende kedel hvori industriaffaldet tjener som hjælpebrændsel. Undersøgelsen udforsker passende blandinger og driftsretningslinjer, der fremmer forbrændingsstabiliteten og medfører NO_x-reduktion op til 11,54 %.

Sammenfattende kan det siges, at bidragene fra dette Ph.D. projekt er todelt: kinetisk modellering af biomassepyrolyse og affaldsforbrændingssimulering, hvor to originale modeller blev udviklet for hver del. Analyser og undersøgelser baseret på de to modeller blev udført, der medfører værdifulde resultater og demonstrerer modellernes potentiale for biomasseudnyttelse via termokemiske konverteringsteknologier.

Contents

Nomenclature

Symbols

a	oxygen reaction order (-)	P	gas pressure (Pa)
A	pre-exponent factor (s^{-1})	$\bar{p}$	mean NO pressure (atm)
A_{BET}	BET surface area (m^2/kg)	$\bar{p}_{NO}$	mean NO partial pressure (atm)
b	temperature order (-)	$p(u)$	temperature integral (-)
C_{CH_4}	CH_4 concentration (kg/m^3)	R	universal gases constant (J/(mol K))
C_{CO}	CO concentration (kg/m^3)	r	reaction rate ($kg/(m^3\ s)$)
C_{H_2}	H_2 concentration (kg/m^3)	R_c	char burning rate ($kg/(m^3\ s)$)
C_{H_2S}	H_2S concentration (kg/m^3)	r_{CO}	CO rection rate ($kg/(m^3\ s)$)
C_{NH_3}	NH_3 concentration (kg/m^3)	R_{vol}	devolatilization rate ($kg/(m^3\ s)$)
C_{NO}	NO concentration (kg/m^3)	S_g	solid conversion rate ($kg/(m^3\ s)$)
C_{pg}	gas specific heat capacity (J/(kg K))	S_T	energy source term ($J/(m^3\ s)$)
C_{ps}	solid specific heat capacity (J/(kg K))	t	time (s)
D_g	effective gas diffusivity (m^2/s)	T	temperature (K)
d_p	solid particle diameter (m)	T_{in}	initial temperature (K)
E_a	activation energy (J/kmol)	T_{rad}	radiation temperature (K)
$f(\alpha)$	reaction model (-)	T_∞	the freeboard temperature (K)
$g(\alpha)$	conversion integral (-)	u	dimensionless variable $u = E_a/(RT)$
h_f	standard formation enthalpy (J/mol)	$\boldsymbol{u}$	superficial velocity in fuel bed (m/s)
h_M	mass transfer coefficient (m/s)	u_{avg}	averaged velocity magnitude (m/s)
h_T	heat transfer coefficient ($W/(m^2\ K)$)	u_j	velocity magnitude of cell j (m/s)
K	bed permeability	$\overline{u_i'}$	fluctuating velocity components (m/s)
k_{eff}	thermal conductivity (W/(m K))	V_j	volume of cell j in the zone (m^3)
k_g	gas thermal conductivity (W/(m K))	V_{tot}	total volume of the zone (m^3)
k_s	solid thermal conductivity (W/(m K))	X_{O_2}	molar fractions of O_2 (-)
$k(T)$	kinetic constant (s^{-1})	Y_{ig}	mass fraction of gas species (-)
m	solid mass (kg)	$Y_{ig,in}$	initial mass fraction of gas species (-)
m_0	initial solid mass (kg)	$Y_{ig,s}$	gas mass fraction (-)
m_∞	final solid mass (kg)	$Y_{ig,\infty}$	mass fraction of air (-)
M_w	molar weight (kg/kmol)	Y_{is}	solid mass fraction (-)

Greek letters

α	conversion (-)	σ	Boltzmann constant (W/(m^2 K^4))
α_p	peak conversion (-)	τ_{jj}	viscous stress in j dimension (Pa)
β	heating rate (K/min)	ρ_g	gas density (kg/m^3)
θ	reaction progress indicator (-)	ρ_s	solid bulk density (kg/m^3)
θ_p	peak of the progress indicator (-)	ρ_{is}	bulk density of solid component (kg/m^3)
ε	system emissivity (-)	ϕ	bed porosity (-)
μ	mixed gas dynamic viscosity (Pa s)		

Abbreviations

BASIC	Bulk Accumulated Solids Incineration Code	MSW	Municipal solid wastes
CDF	Cumulative distribution function	PA	Primary air
CFD	Computational fluid dynamics	PDF	Probablility density function
DAEM	Distributed activation energy model	SIMPLE	Semi-Implicit Method for Pressure-Linked Equations
DEM	Discrete element model	TGA	Thermogravimetric analysis
DTG	Difference thermogravimetry	TKE	Turbulent kinetic energy
FLIC	Fluid Dynamic Incineration Code	UIV	Uniformity index for velocity
FWO	Flynn-Wall-Ozawa	UDF	User-defined function
GEV	Generalized extreme value	WD	Westbrook and Dryer
LHV	Lower heating value	WtE	Waste to energy
KAS	Kissinger-Akahira-Sunose	WSGGM	Weighted sum of gray gases model

Preface

This dissertation is submitted according to the requirements for the Doctor of Philosophy at Faculty of Engineering and Science, Aalborg University (AAU). The work has been carried out at AAU Energy from October 2018 to June 2022. This Ph.D. project is mainly funded by China Scholarship Council, and partially supported by AAU Energy, AAU's Doctoral School of Engineering and Science and Otto Mønsted.

I sincerely appreciate my supervisors, Associate Professor Chungen Yin and Associate Professor Torsten Berning, not only for their brilliant supervision and treasured comments on my project, but also for showing me the appropriate way of doing academic research. Additionally, I would like to express great gratitude to Professor Ronnie Andersson from Chalmers University of Technology, who provided me tremendous supports during my four-month study abroad.

I also would like to acknowledge all the co-authors and reviewers related to my papers. The efforts and help provided by those people made my research to be publishable. Meanwhile, I thank all the colleagues I have met in the last four years, the kindness and help from them mean a lot to me.

In the end, I would like to hand out my special gratefulness to my family and friends. Their unconditional love and company are the most powerful source, constantly delivering strength to me during my entire Ph.D. journey.

Tianbao Gu

Summer 2022, Aalborg

Chapter 1. Introduction

The intention of this Ph.D. project is to promote efficient and clean utilization of biomass via thermochemical conversion technologies, namely, pyrolysis and combustion. Chapter 1 presents the background and state-of-the-art of each are reviewed along with the research challenges. The primary objectives and framework of this Ph.D. thesis are outlined.

1.1. Background

As the fourth largest primary energy resource, biomass, which is recognised as a carbon-neutral fuel, plays a significant role in energy transitions and carbon neutrality [1]. The dominant biomass feedstocks for energy production are wood wastes, municipal solid waste (MSW), agricultural waste and landfill gases with the amount of 64%, 24%, 5% and 5%, respectively [2]. It predicts that the demand for primary energy supply from biomass will increase from 54 EJ in 2018 to over 150 EJ by 2050, representing one-fourth of the global primary energy supply, according to the International Energy Agency [3]. Efficient and clean utilization of biomass is significant to meet this demand, drawing constant attention over the past few decades [4, 5]. Thermochemical conversion technologies including pyrolysis, combustion, and gasification, are promising for biomass utilization [6]. Among them, pyrolysis, which can produce high value-added products in the absence of oxygen, is recognised as an efficient technology for biomass utilization [7, 8]. Attempts to apply biomass pyrolysis have been increasingly carrying out, such as woody biomass pyrolysis for producing bio-oil [9, 10]. In addition, pyrolysis is an inseparable sub-process of other subsequent thermochemical technologies such as combustion and gasification, which would benefit from pyrolysis studies [11]. Meanwhile, combustion, which converts fuel into gaseous oxide with heat production under sufficient oxygen and high temperature, is very popular in recycling energy from various biomass. MSW as the dominant low-quality biomass, was selected as the feedstock for combustion in study [12]. Moreover, the combustion of MSW draws attention not only because of the sustainable energy generation but also because of the environmental issues [13]. Many waste-to-energy (WtE) plants have been built or are under construction globally to incinerate various solid wastes [14, 15]. From the efficient utilization and environmental perspectives, investigation on biomass pyrolysis and combustion is of great significance.

For biomass pyrolysis, the solid conversion rate and products yield are the primary concerns. Accurate prediction of the conversion rate and production is vital for reactor and system design of units using biomass pyrolysis technology [12, 13]. Kinetic modeling, which is capable of computing the solid conversion rate and predicting the products combined with the reaction scheme, is essential to elucidate the underlying mechanism and connect the scientific research and practical applications of biomass pyrolysis [14]. Therefore, developing a reliable kinetic model for the description of biomass pyrolysis was selected as one of the primary objectives of this Ph.D. thesis, which will be discussed in Chapter 2.

For biomass combustion, efficiency, stability, and clean emissions are the most significant concerns, particularly for incinerating solid wastes [15]. On the one hand, practical experimental studies are very limited for the comprehensive investigation of large-scale solid waste incinerators owing to safety and high-cost issues [16]. On the other hand, computational fluid dynamics (CFD) simulation studies, which can predict the combustion process, flow mixing, emissions, etc., are powerful tools for investigating solid fuel combustion from fundamentals to industrial applications [17, 18]. It is also recognised as cost-efficient for the design and optimization of large-scale MSW incinerators, such as boiler retrofitting and manipulation [19]. Thus, developing an advanced CFD simulation for MSW combustion is another primary objective of this Ph.D. thesis, which will be conducted in Chapter 3.

1.2. Review of biomass pyrolysis kinetic modeling

Numerous kinetic studies on biomass pyrolysis have been conducted over the last few decades, which can be roughly divided into two categories: evaluation of kinetic parameters and determination of the reaction mechanism [4, 20]. In the conventional Arrhenius-type kinetic modeling [21], the solid conversion rate is governed by the kinetic constant $k(T)$ and reaction model $f(\alpha)$, as described in Eq. (1.1).

$$\frac{d\alpha}{dt} = k(T)f(\alpha) = A\exp\left(-\frac{E_a}{RT}\right)f(\alpha) \tag{1.1}$$

where the kinetic constant is typically determined by the kinetic parameters or kinetics: pre-exponential factor A and activation energy E_a [9]. The reaction model, a function of conversion α, represents the mechanism of the pyrolysis process [22]. For non-isothermal pyrolysis under a constant heating rate,

$dT/dt \equiv \beta$, the conversion rate in terms of temperature can be derived, as shown in Eq. (1.2) [23].

$$\frac{d\alpha}{dT} = \frac{d\alpha}{dt} \times \frac{dt}{dT} = \frac{A}{\beta} exp(-\frac{E_a}{RT}) f(\alpha) \tag{1.2}$$

Studies on evaluating the kinetic parameters usually assume the reaction model in advance, for example, the first-order reaction model, and then evaluate the kinetics [24]. The evaluated kinetics tend to correspond to the assumed reaction model. In addition, the reasonable determination of the reaction model for solid fuel pyrolysis has also been investigated, not only to reasonably describe the pyrolysis process but also to make the evaluated kinetics more reliable. The state of the art of the two branches is reviewed below.

1.2.1. Evaluation of kinetics

Based on previous publications, the number of studies on the evaluation of kinetics (A, E_a) is higher than that on the determination of the reaction mechanism. The methods used for kinetics evaluation can be identified as two fundamental types: model-fitting and model-free methods [25]. The thermogravimetric analysis (TGA) data are always required for both methods [26]. The fundamentals and characteristics of the well-known model fitting and model-free methods are briefly reviewed in this section.

1.2.1.1 Model-fitting methods

In evaluation of kinetics, the integral conversion $g(\alpha)$ is always used to avoid using differential thermogravimetry (DTG) data, is given in Eq. (1.3) [27].

$$g(\alpha) = \int_0^{\alpha} \frac{d\alpha}{f(\alpha)} = \int_0^{t} k(T)\, dt = \frac{AE_a}{\beta R} \int_0^{u} u^{-2} e^{-u} du = \frac{AE_a}{\beta R} p(u), \tag{1.3}$$

where $u = E_a/RT$, the temperature integration $p(u)$ has no analytical solution. Different approximation equations of $p(u)$ were applied to simplify Eq. (1.3), resulting in various methods.

In model-fitting methods, the reaction model is assumed in advance, and then the kinetics can be obtained using different data fitting approaches based on TGA experiments [28]. For instance, the representative linear model-fitting method: Coats-Redfern method [29], evaluates kinetics using Eq. (1.4).

$$\ln\left(\frac{g(\alpha)}{T^2}\right) = \ln\left[\frac{AR}{\beta E_a}\left(1-\frac{2RT}{E_a}\right)\right] - \frac{E_a}{RT} \tag{1.4}$$

However, at the temperature typically used in biomass pyrolysis, $\frac{2RT}{E_a} \ll 1$, Eq. (1.4) can be simplified to Eq. (1.5) [30].

$$\ln\left(\frac{g(\alpha)}{T^2}\right) = \ln\left(\frac{AR}{\beta E_a}\right) - \frac{E_a}{RT} \tag{1.5}$$

Thus, by plotting $\ln\left(\frac{g(\alpha)}{T^2}\right)$ vs. $1/T$, the activation energy E_a at each heating rate can be obtained from the slope of the linear fitting line, and the pre-exponential factor A can then be calculated using the intercept $\ln\left(\frac{AR}{\beta E_a}\right)$.

For the nonlinear model-fitting method, the kinetics at each heating rate are always estimated by minimizing the difference between the experimental data and the prediction, for example, Min: $\sum |\left(\frac{d\alpha}{dT}\right)_{exp} - \left(\frac{d\alpha}{dT}\right)_{pred}|^2$. Generally, optimization algorithms, such as genetic algorithms and differential evolution algorithms, are employed in the method set [31].

The model-fitting method is extensively applied to estimate the global kinetics for the overall pyrolysis process, which is more convenient for usage in engineering and CFD simulations. Besides, this method only requires TGA data with one heating rate, and the obtained kinetics tend to be dependent on the heating rate [32].

1.2.1.2 Model-free methods

The model-free method, also called the iso-conversional method, does not assume the reaction model in the evaluation of the activation energy, E_a. The method assumes that E_a during pyrolysis varies with the conversion, while also assuming E_a is independent of the heating rate [33]. Accordingly, the model-free method requires a set of TGA data under at least three different heating rates. For example, in the KAS method [34], in which the approximation equation $p(u) = u^{-2}e^{-u}$ is used, the activation energies at different conversion degrees can be evaluated using Eq. (1.6).

$$\ln\left(\frac{\beta}{T^2}\right) = \ln\left(\frac{AR}{E_a g(\alpha)}\right) - \frac{E_a}{RT} \tag{1.6}$$

The E_a at a certain conversion degree can be obtained by plotting $\ln\left(\frac{\beta}{T^2}\right)$ vs. $1/T$. This method does not require a reaction model for evaluating E_a, so it is called the model-free method. However, the calculation of A, derived from the intercept of the linear fitting line, requires the assumption of a reaction model.

Table 1.1 Summary of the typical methods for evaluation of kinetics.

Methods		Plotting equation	Characteristics
Model-fitting	Coats-Redfern	$\ln\left(\frac{g(\alpha)}{T^2}\right) = \ln\left(\frac{AR}{\beta E_a}\right) - \frac{E_a}{RT}$	• Approximation equation $p(u) = u^{-2}e^{-u}$ is used. • The reaction model needs to be assumed to evaluate E_a and A. • Need TGA data under one heating rate. • Kinetics are independent of α, but dependent on β. • The obtained global kinetics is easy to use, but the accuracy is low.
	Doyle	$\ln(g(\alpha)) = \ln\left(\frac{AR}{\beta E_a}\right) - 5.331 - 1.052\frac{E_a}{RT}$	• Approximation equation $\ln p(u) = -5.331 - 1.052u$ used [28]. • Others are the same as Coats-Redfern.
	Non-linear	$Min: \sum \left\| \left(\frac{d\alpha}{dT}\right)_{exp} - \left(\frac{d\alpha}{dT}\right)_{pred} \right\|^2$	• No approximation equation. • DTG data is used, which may magnify the experimental data error. • The obtained kinetics are always with high accuracy but low applicability. • Others are the same as Coats-Redfern.
Model-free	KAS	$\ln\left(\frac{\beta}{T^2}\right) = \ln\left(\frac{AR}{E_a g(\alpha)}\right) - \frac{E_a}{RT}$	• Approximation equation $p(u) = u^{-2}e^{-u}$ is used [35]. • The reaction model is not needed for evaluating E_a, but it is needed for evaluating A. • Need TGA data at least under three different heating rates. • Distributed kinetics are dependent on α, but independent of β. • The obtained distributed kinetics is considered with high accuracy.
	FWO	$\ln(\beta) = \ln\left(\frac{AR}{E_a g(\alpha)}\right) - 5.331 - 1.052\frac{E_a}{RT}$	• Approximation equation $\ln p(u) = -5.331 - 1.052u$ is used. • Others are the same as KAS.
	Friedman	$\ln\left(\beta\frac{d\alpha}{dT}\right) = \ln[Af(\alpha)] - \frac{E_a}{RT}$	• No approximation equation. • DTG data is used, which may magnify the experimental data error [36]. • Others are the same as KAS.

The kinetics evaluated by model-free methods vary with the conversion but are independent of the heating rate. Generally, the accuracy of kinetics from model-free methods is higher than that from model-fitting methods because the kinetics are obtained by data fitting in a small conversion step. The kinetic study committee recommends using a conversion step no bigger than 0.05 to

achieve sufficiently accurate kinetics for describing solid decomposition [41]. The utilization and characteristics of the commonly used model fitting and model-free methods are compared in Table 1.1.

It is worth mentioning that the methods reviewed in this section are fundamental models for kinetics evaluation of solid fuel pyrolysis. Comprehensive models based on these fundamental methods, such as the independent parallel reactions model and distributed activation energy model (DAEM) [37], are not considered in this study.

1.2.2. Determination of the reaction mechanism

According to Eq. (1.2), the reaction model $f(\alpha)$ is the other dominant factor for calculating the conversion rate, besides the kinetic constant. A reaction model that properly describes the pyrolysis mechanism is crucial as a reliable kinetic parameter for pyrolysis kinetic studies. Moreover, the evaluated kinetics usually rely on the reaction model used. Hence, determining the reaction mechanism by selecting a proper reaction model is crucial in kinetic modeling investigations. Several reaction models have been proposed to elucidate the mechanism of solid-fuel pyrolysis progress. The commonly used reaction models can be sorted into four types: reaction order, nucleation, contracting geometry, and diffusion, as summarized in Table 1.2 [38].

1.2.2.1 Master plot

Among these reaction models, selection of a reasonable model to describe the reaction mechanism is crucial. In addition to empirical or experience-based methods, Criado proposed a theoretical method to determine the solid fuel pyrolysis mechanism called the 'master plot' [39]. The idea behind this is to compare the standard master plot $y(\alpha)$ based on the common reaction models and the DTG data carried out experimentally, according to Eq. (1.7). The smaller the difference, the closer the pyrolysis mechanism is to the compared reaction model. The implementation of this method is described in [40], followed by several applications in solid-fuel kinetic studies [21, 41]. The method has been successfully used to determine the reaction mechanism for solid fuel pyrolysis, and is recognised as a reasonable and theoretical way to determine the reaction mechanism.

$$y(\alpha) = \frac{f(\alpha)g(\alpha)}{f(0.5)g(0.5)} = \left(\frac{T}{T_{0.5}}\right)^2 \frac{d\alpha/dt}{(d\alpha/dt)_{0.5}} \tag{1.7}$$

Table 1.2 Summary of the commonly used reaction models for solid fuel pyrolysis [38].

Reaction mechanisms		Differential form $f(\alpha)$	Integral form $g(\alpha)$
Reaction order	First-order (F1)	$1-\alpha$	$-\ln(1-\alpha)$
	Second-order (F2)	$(1-\alpha)^2$	$\frac{\alpha}{1-\alpha}$
	Third-order (F3)	$(1-\alpha)^3$	$[(1-\alpha)^{-2}-1]/2$
	n^{th}-order (Fn)	$(1-\alpha)^n$	$[(1-\alpha)^{-(n-1)}-1]/(n-1)$
Mampel power law	P(2/3)	$2/3\alpha^{-1/2}$	$\alpha^{3/2}$
	P2	$2\alpha^{1/2}$	$\alpha^{1/2}$
	P3	$3\alpha^{2/3}$	$\alpha^{1/3}$
	P4	$4\alpha^{3/4}$	$\alpha^{1/4}$
Nucleation	A1.5	$1.5(1-\alpha)[-\ln(1-\alpha)]^{1/3}$	$[-\ln(1-\alpha)]^{2/3}$
	A2	$2(1-\alpha)[-\ln(1-\alpha)]^{1/2}$	$[-\ln(1-\alpha)]^{1/2}$
	A3	$3(1-\alpha)[-\ln(1-\alpha)]^{2/3}$	$[-\ln(1-\alpha)]^{1/3}$
	A4	$4(1-\alpha)[-\ln(1-\alpha)]^{3/4}$	$[-\ln(1-\alpha)]^{1/4}$
Contracting geometry	Contracting cylinder (R2)	$2(1-\alpha)^{1/2}$	$1-(1-\alpha)^{1/2}$
	Contracting sphere (R3)	$3(1-\alpha)^{2/3}$	$1-(1-\alpha)^{1/3}$
Diffusion	One-dimensional diffusion (D1)	$1/(2\alpha)$	α^2
	One-dimensional diffusion (D2)	$[-\ln(1-\alpha)]^{-1}$	$(1-\alpha)\ln(1-\alpha)+\alpha$
	One-dimensional diffusion (D3)	$3/2(1-\alpha)^{2/3}[1-(1-\alpha)^{1/3}]^{-1}$	$[1-(1-\alpha)^{1/3}]^2$
	One-dimensional diffusion (D4)	$3/2[1-(1-\alpha)^{1/3}]^{-1}$	$1-(2/3)\alpha-(1-\alpha)^{2/3}$

1.2.2.2 Statistical distribution-based model

Statistical distribution-based model is a new series of describing the mechanism or progress of solid-fuel pyrolysis [42]. It differs from the conventional Arrhenius-type models, which assumes that the pyrolysis progress follows one of the statistical distribution functions, such as the Weibull and Gaussian distributions [43]. The reaction model and kinetic constant used in the typical Arrhenius models were replaced by the probability density function (PDF) of the assumed statistical distribution. Likewise, the kinetic parameters are replaced by the statistical parameters, which need to be estimated by fitting the experimental data. For example,

Bojan developed a Weibull mixture model for biomass pyrolysis, in which the conversion rate of each pseudo-component was calculated using the PDF of the Weibull distribution [44]. The overall conversion rate of the biomass was then computed using the weighted sum conversion rates of all pseudo components.

Furthermore, Li *et al.* developed a universal model for describing biomass pyrolysis based on the generalized extreme value (GEV) distribution [45]. This reveals that all first-order pyrolysis can be universally described by a GEV distribution, regardless of the kinetics. The distinct characteristics of the novel model were demonstrated and successfully used to analyze biomass pyrolysis. This is a significant step toward connecting the reaction mechanism and statistical distributions and offers a unique perspective for comprehending solid pyrolysis. However, the reason behind this connection is not clearly explained, and the relevant theoretical derivation is incomplete. Moreover, the generalized model is limited to first-order reactions, which inspired the author to further explore in this way.

1.3. Review of MSW combustion simulation

For MSW combustion, grate-firing, one of the major combustion technologies, has been widely applied in WtE plants for incinerating solid waste with high moisture and low heating value [46, 47], and is the focus in this Ph.D. thesis. CFD simulation studies of MSW incineration have been successfully employed to investigate large-scale grate boilers [46], which usually comprise two parts: fuel bed modeling and freeboard simulation [5]. The bed model, which provides the inlet conditions for freeboard simulation, is the basis for achieving reliable simulation results for the boiler. It usually can not be performed in commercial CFD software directly. The freeboard simulation, carrying the fuel bed modeling results, predicts the detailed combustion metrics inside the boiler, such as temperature and gas species distributions, mixing, and pollutant emissions. The two parts are highly coupled with each other. The state-of-the-art review of the simulation of MSW grate boilers is structured in the following two parts.

1.3.1. Bed modeling of MSW combustion

Modeling the fuel bed of grate boilers is complex, as it includes heat and mass transfer in both the solid and gas phases, homogenous and heterogeneous reactions, fluid flow in the porous zone, particle shrinking, radiation, etc., [47].

Thus, empirical models that roughly divide the fuel bed into several segments (e.g., drying, pyrolysis, char oxidation, and cooling) to ensure the overall mass and heat balance are commonly used early. For instance, Rajh *et al*. developed a 1D empirical model to facilitate CFD simulation of a 13 MW_{th} biomass grate boiler [48]. The simulation results are consistent with the measurement data within an acceptable error range. It is reasonable to perform CFD simulations for grate boilers, but it is not sufficiently accurate. As an assistant tool, the empirical bed model does not contribute to the investigation of the combustion of solids inside the fuel bed.

Furthermore, a better solution for modeling the fuel bed was proposed, that is, developing a stand-alone bed model to comprehensively describe the solid conversion process, considering the heat and mass transfer phenomena in the fuel bed. Bed models can provide accurate profiles of combustion metrics, for example, temperature, velocity, density, and mass fractions of species, along with incineration time or grate length [49]. While the temperature gradient inside solid particles is usually can not be predicted, since the thermally thin particles are assumed to ease computational burden, especially for large-scale boilers [47]. The comprehensive bed model is conducive to investigating fuel bed combustion and largely promotes CFD simulation of the freeboard. Based on the modeling methods, the previous bed models can be divided into Euler-Lagrange and Euler-Euler models.

The Euler-Lagrange model, also called the discrete element model (DEM), treats the gas phase as a continuum and the solid phase as a discrete phase [50]. The model solves the motion and conversion of solid particles individually under the Lagrange framework, and couples the variables of the particles with the continuum gas phase [51]. In physics, the Euler-Lagrange model is more suitable for describing solid particle combustion in a dense fuel bed [52]. However, the computational cost is excessively high for tracking individual particles, particularly for large-scale incinerators with nonuniform solid particles. Currently, it does not seem to be a feasible option for modeling large-scale MSW moving grate boilers [53].

However, the Euler-Euler model, also called the continuum model, treats both the gas and solid phases as a continuous phase in the porous fuel bed [54]. The governing equations for both the solid and gas phases are numerically solved using the Euler framework, with a description of the thermal conversion processes: drying, devolatilization, volatile incineration, and char burning. The well-known stand-alone continuum bed model is called FLIC

(Fluid Dynamic Incineration Code), which was developed at the Sheffield University Waste Incineration Centre approximately two decades ago [49, 55]. The model has been validated by experimental data and successfully applied in studying the fuel bed and facilitating the freeboard simulation, and it is continues to be in use [56]. Whereas, several shortcomings also need to be addressed, such as the simplified boundary conditions, incomplete homogenous reactions, and empirical assumption for volatiles. Several bed models, such as Zhou's model [46] and Ismail's model [57], have the shortcomings mentioned above to some extent. More expertise on the bed model applied in the simulation of large-scale grate boilers was summarized in [47].

Finally, an in-house continuum model for MSW combustion in a fixed bed was developed by the Ph.D. student as part of his master's study and was published in [58]. The developed bed model addresses the shortcomings mentioned above and has been validated by experimental data and cross-validated by other bed models. The new bed model exhibits advances in reliability and flexibility for describing various feedstock combustions. However, it has not been applied to large-scale boilers to model the fuel bed on a moving grate, and either coupled with the freeboard simulation.

1.3.2. Freeboard simulation of MSW grate boiler

The over-bed freeboard CFD simulation, predicting the turbulent reacting gas flow, can be performed using commercial software, such as ANSYS Fluent [59]. Reliable CFD simulation is a powerful tool for designing and optimizing boilers in different aspects, for example, improving combustion efficiency, stability, and clean emissions [60]. Several numerical studies for grate-firing boilers, under the concept of a bed model coupled with freeboard simulation, have been conducted for specific purposes. For instance, the incineration of waste wood in a 13 MW_{th} grate boiler with recycled flue gas was virtually tested by a freeboard simulation coupled with a 1D empirical bed model in [61]. Moreover, the impacts of the gaseous radiative properties and buoyancy effects on the simulation results were revealed. The FLIC model has also been applied in industrial-scale boiler simulations coupled with CFD simulations using ANSYS Fluent to solve the turbulent reaction flow in the freeboard. The FLIC/Fluent combined simulation was used to investigate a Martin-type moving grate boiler incinerating 12 tons of MSW per hour [62]. The combustion metrics in the fuel bed are characterised, indicating the impact of freeboard radiation on bed ignition. The analysis concludes by highlighting

the necessity of enhancing the secondary air (SA) supply in freeboard simulations. Hu *et al.* numerically investigated the NO_x emissions of an MSW incinerator using the FLIC-coupled Fluent mode. They proposed the best combination of SA and overfire air (OFA) for NO_x reduction [63].

Although many numerical studies have been conducted for MSW grate boilers, it is still necessary for different incinerators to meet various demands from an application perspective. From the modeling perspective, more reliable and reasonable boiler simulations, such as coupling an advanced bed model and integrating a proper radiation model, should be pursued.

1.4. Research challenges

Based on the literature review for kinetic modeling of biomass pyrolysis and MSW combustion simulation, the research challenges that attracted the Ph.D. student's attention are summarized below.

Kinetic modeling of biomass pyrolysis:

- The conventional methods for evaluating kinetics are over-reliant on experimental data and the assumed reaction model, and the obtained kinetics cannot be generally applied in biomass pyrolysis.
- Studies on the determination of reaction mechanism for biomass pyrolysis need to be enhanced, and investigations on connecting the reaction mechanism and kinetic evaluation are required.
- Further theoretical work for universal modeling of the pyrolysis process is desired. Applications other than the first-order reactions of biomass pyrolysis also need to be explored.

MSW combustion simulation:

- An advanced bed model for moving-grate fuel beds must be developed to investigate the combustion characteristics in the fuel bed and facilitate the overall boiler simulation.
- A reliable freeboard simulation coupled with an advanced bed model is required as a powerful tool to investigate large-scale MSW grate boilers.
- Simulation-based studies or virtual tests on boiler adjustments are required to satisfy the practical demands of WtE plants.

1.5. Objectives of this study

Considering the above, the main objectives of this Ph.D. thesis are as follows.

Chapter 2: Kinetic modeling of biomass pyrolysis:

- To develop a universal model for description of the pyrolysis process and employ it in the kinetic analysis of biomass pyrolysis with different reaction mechanisms.
- To demonstrate the applicability of the developed model and reveal the kinetic characteristics of woody biomass pyrolysis.

Chapter 3: Advanced simulation MSW combustion:

- To develop a comprehensive bed model for describing the solid fuel conversion on moving grates.
- To accomplish the CFD simulation of the entire grate boiler by coupling the bed model and freeboard simulation.
- To deploy the CFD simulation in guiding the boiler adjustments for specific purposes, that is, feedstock change due to waste classification and co-combustion of MSW and sewage sludge.

1.6. Thesis outline

This paper-based Ph.D. dissertation consists of four chapters and collects four papers, including two main scientific work packages: kinetic modeling of biomass pyrolysis (Chapter 2) and CFD simulation of MSW combustion (Chapter 3). The outline of each chapter is as follows.

Chapter 1 introduces the research background, motivation, and state-of-the-art of the two scientific work packages, as well as the main objectives of this Ph.D. thesis.

Chapter 2 presents a universal description of solid fuel decomposition with its applications in analysing biomass pyrolysis and collects two papers, Papers A and B. The theoretical derivation, validation, and utilization are presented in Paper A, and two supplementary applications are demonstrated in Paper B. The main consequences and conclusions from the two papers are emphasized.

Chapter 3 elaborates the simulation methodology using an in-house bed model for a grate-firing boiler and collects two papers, Papers C and D. A simulation-based investigation, targeting feedstock change due to waste classification, is presented in Paper C. The investigation of MSW co-firing in sewage sludge in an existing boiler is numerically explored in Paper D, extending the simulation to include NO_x formation and emissions. The main consequences and conclusions from the two papers are emphasized.

Chapter 4 summarizes the primary contributions of this Ph.D. project. Several future perspectives on this project are outlined, with the aim of further improvements and extensions.

1.7. List of papers

The major scientific contributions of this Ph.D. project have been disseminated in journal publications. Four papers published or submitted in scientific journals are selected in this Ph.D. dissertation as follows.

- **Paper A:** Gu T, Fu Z, Berning T, Li X, Yin C. A simplified kinetic model based on a universal description for solid fuels pyrolysis: Theoretical derivation, experimental validation, and application demonstration. *Energy*. 2021;225:120133.
- **Paper B:** Gu T, Berning T, Yin C. Application of a New Statistical Model for the Description of Solid Fuel Decomposition in the Analysis of Artemisia apiacea Pyrolysis. *Energies*. 2021;14(18):5789.
- **Paper C:** Gu T, Ma W, Berning T, Guo Z, Andersson B, Yin C. Advanced simulation of a 750 t/d municipal solid waste grate boiler to better accommodate feedstock changes due to waste classification. *Energy*. 2022;254:124338.
- **Paper D:** Gu T, Ma W, Guo Z, Berning T, Yin C. Stable and clean co-combustion of municipal sewage sludge with municipal and industrial solid wastes in a grate boiler: A modeling-based feasibility study. *Fuel* (Under review after a round of major revision).

Other papers published during this Ph.D. study, which are not selected for this dissertation, are listed below.

- Gu T, Yin C, Ma W, Chen G. Municipal solid waste incineration in a packed bed: A comprehensive modeling study with experimental validation. *Applied Energy*. 2019;247:127-139.

- Gu T, Yin C. A parallel reaction kinetic model based on Weibull distribution for biomass pyrolysis. Proceedings of 11th International Conference on Applied Energy, ICAE 2019.
- Han Z, Li J, Gu T, Yan B, Chen G. The synergistic effects of polyvinyl chloride and biomass during combustible solid waste pyrolysis: Experimental investigation and modeling. *Energy Conversion and Management*. 2020;222:113237.
- Gu T, Ma W, Berning T, Guo Z, Andersson R, Yin C. Simulation of municipal solid waste incineration in an industrial grate boiler coupled with an in-house bed model and analysis for the feedstock flexibility. Proceedings of the 16th Conference on Sustainable Development of Energy, Water, and Environment Systems, SDEWES 2021.

Chapter 2. Kinetic Modeling of Biomass Pyrolysis

Chapter 2 derives a universal description associated statistical characteristics for all the commonly used reaction models of solid fuel pyrolysis and demonstrates several applications in kinetic studies of biomass pyrolysis, resulting in two papers, Papers A and B. In Paper A, the derivation process, prediction of the conversion rate, and kinetic analysis of woody biomass pyrolysis were performed. In Paper B, two additional applications based on the developed model were conducted, that is, identifying the conversion peak and determining the reaction mechanism. The theoretical derivation, methodology illustration, experimental description, significant results, and conclusions are presented in this chapter. For more details, refer to Papers A and B.

2.1. Universal description for solid fuel pyrolysis

As mentioned in Section 1.2, the conversion rate for solid fuel pyrolysis is usually governed by the kinetic constant $k(T)$ and the reaction model $f(\alpha)$, as shown in Eq. (1.1). The former is recognised as a function of the temperature T, and the latter is considered a function of the conversion degree α, as defined in Eq. (2.1) [64].

$$\alpha = \frac{m_0 - m}{m_0 - m_\infty} \tag{2.1}$$

where m represents the solid mass and subscripts 0 and ∞ denote the initial and final times of the pyrolysis process, respectively. In kinetic studies, the reaction constant $k(T)$ and reaction model $f(\alpha)$ are assumed to be independent of each other [36].

Setting $\theta \equiv g(\alpha)$, and then taking the logarithm of Eq. (1.3) simplifies the integral form of the conversion rate $g(\alpha)$, which indicates the reaction progress of pyrolysis. One can obtain the expression for θ, namely, the reaction progress indicator, in Eq. (2.2).

$$\theta = \ln g(\alpha) = \ln \int_0^\alpha \frac{d\alpha}{f(\alpha)} = \ln \int_0^t k(T)\, dt \tag{2.2}$$

The differential form of Eq. (2.2) is derived, as shown in Eq. (2.3).

$$\mathrm{d}\theta = \frac{k(T)dt}{\int_0^t k(T)\,dt} = \frac{k(T)}{g(\alpha)}dt \tag{2.3}$$

Accordingly, the general conversion rate in terms of the reaction progress indicator θ is derived, as shown in Eq. (2.4),

$$\frac{d\alpha}{d\theta} = \frac{d\alpha}{dt}\cdot\frac{dt}{d\theta} = k(T)f(\alpha)\cdot\frac{g(\alpha)}{k(T)} = f(\alpha)\cdot g(\alpha) = f(\alpha)\cdot\int_0^{\alpha}\frac{d\alpha}{f(\alpha)} \tag{2.4}$$

in which, the θ-based conversion rate is only contingent on the reaction model.

2.1.1. Derivation of the universal description for first-order reaction model

For first-order reactions, namely the reaction model $f(\alpha) = 1-\alpha$ [10], the reaction progress indicator θ and the corresponding conversion rate $d\alpha/d\theta$ can be expressed in a more simplified manner, as expressed in Eq. (2.5) and (2.6), respectively.

$$\theta = \ln g(\alpha) = \ln\int_0^{\alpha}\frac{d\alpha}{1-\alpha} = \ln(-\ln(1-\alpha)) \tag{2.5}$$

$$\frac{d\alpha}{d\theta} = (1-\alpha)\cdot\int_0^{\alpha}\frac{d\alpha}{(1-\alpha)} = -(1-\alpha)\ln(1-\alpha) \tag{2.6}$$

Reforming Eq. (2.5) and (2.6), by setting θ as the self-variable, we can finally derive the explicit expression of the universal description for first-order reactions in terms of the new dimensionless variable θ, as shown in Eq. (2.7) and (2.8), respectively.

$$\alpha = 1-\exp(-\exp(\theta)) \tag{2.7}$$

$$\frac{d\alpha}{d\theta} = \exp(\theta)\cdot\exp(-\exp(\theta)) \tag{2.8}$$

It is noteworthy that the expressions in Eq. (2.7) and (2.8) are consistent with the cumulative distribution function (CDF) and PDF of the standardised GEV distribution, respectively, as plotted in Fig. 2.1. This explains why GEV distributions, such as the Weibull distribution, can be used to describe the solid fuel pyrolysis process [65].

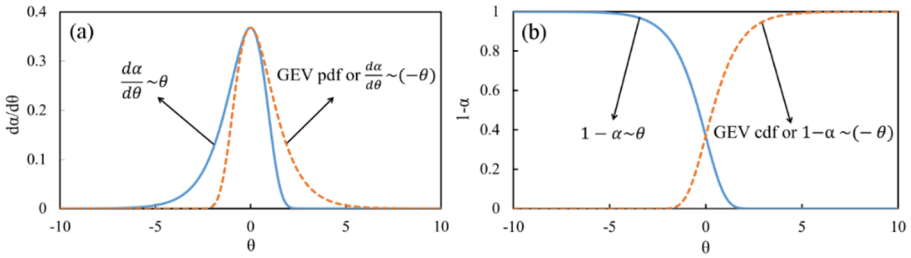

Fig. 2.1. Comparison of the universal description for the first-order reaction model to the standardised GEV distribution [66].

Owing to its consistency with the GEV distribution function, the universal description of first-order reactions carries its distinct statistical characteristics. For example, the conversion rate peak always occurs at $\theta = 0$, with peak conversion $\alpha_p = 1 - 1/e$ and peak rate $(d\alpha/d\theta)_p = 1/e$ for first-order reactions. These statistical characteristics are helpful for the analysis of the solid fuel pyrolysis process.

2.1.2. The universal description for other common reaction models

For other commonly used reaction models of solid fuel pyrolysis, the derivation process of the universal description is the same as that of the first-order reaction model, which is not repeated here. The expressions and characteristics of the common reaction models are summarized in Table 2.1. For each reaction model, the universal description can be recognised as a statistical distribution with distinct characteristics, as shown in Fig. 2.2.

The universal model derived in this section describes the solid pyrolysis process in a statistical physics manner, in which the CDF governs the conversion and the conversion rate is governed by the PDF of a statistical distribution [67]. This provides a fresh perspective for understanding the mechanism of solid fuel pyrolysis and characterising the pyrolysis process. Several applications for analyzing biomass pyrolysis based on a universal model are presented in the next section.

Table 2.1 Summary of the universal description for the commonly used reaction mechanisms of solid fuel pyrolysis [66].

Mechanisms	$f(\alpha)$	$g(\alpha) \equiv e^{\theta}$	$\alpha \sim \theta$	$d\alpha/d\theta$	θ_p	α_p	$(d\alpha/d\theta)_p$
Reaction order: First-order (F1), Second-order (F2), Third-order (F3), nth-order (Fn)							
F1	$1-\alpha$	$-\ln(1-\alpha)$	$1-e^{(-e^{\theta})}$	$e^{\theta}\cdot e^{(-e^{\theta})}$	0	$1-1/e$	$1/e$
F2	$(1-\alpha)^2$	$\alpha/1-\alpha$	$1-1/e^{\theta}+1$	$e^{\theta}/(e^{\theta}+1)^2$	0	0.5	0.25
F3	$(1-\alpha)^3$	$[(1-\alpha)^{-2}-1]/2$	$1-1/(2e^{\theta}+1)^{1/2}$	$e^{\theta}/(2e^{\theta}+1)^{3/2}$	0	$1-1/\sqrt{3}$	$\sqrt{3}/9$
Fn	$(1-\alpha)^n$	$\frac{(1-\alpha)^{1-n}-1}{n-1}$	$1-1/[(n-1)e^{\theta}+1]^{1/(n-1)}$	$\frac{e^{\theta}}{[(n-1)e^{\theta}+1]^{n/(n-1)}}$	0	$1-(\frac{1}{n})^{\frac{1}{n-1}}$	$(\frac{1}{n})^{\frac{n}{n-1}}$
Mampel Power Law							
P(2/3)	$2/3\alpha^{-1/2}$	$\alpha^{3/2}$	$e^{2/3\theta}$	$2/3e^{2/3\theta}$	0	1	2/3
P2	$2\alpha^{1/2}$	$\alpha^{1/2}$	$e^{2\theta}$	$2e^{2\theta}$	0	1	2
P3	$3\alpha^{2/3}$	$\alpha^{1/3}$	$e^{3\theta}$	$3e^{3\theta}$	0	1	3
P4	$4\alpha^{3/4}$	$\alpha^{1/4}$	$e^{4\theta}$	$4e^{4\theta}$	0	1	4
Nucleation							
A1.5	$1.5(1-\alpha)[-\ln(1-\alpha)]^{1/3}$	$[-\ln(1-\alpha)]^{2/3}$	$1-e^{(-e^{(3/2)\theta})}$	$3/2e^{(3/2)\theta}\cdot e^{(-e^{(3/2)\theta})}$	0	$1-1/e$	$3/(2e)$
A2	$2(1-\alpha)[-\ln(1-\alpha)]^{1/2}$	$[-\ln(1-\alpha)]^{1/2}$	$1-e^{(-e^{2\theta})}$	$2e^{2\theta}\cdot e^{(-e^{2\theta})}$	0	$1-1/e$	$2/e$
A3	$3(1-\alpha)[-\ln(1-\alpha)]^{2/3}$	$[-\ln(1-\alpha)]^{1/3}$	$1-e^{(-e^{3\theta})}$	$3e^{3\theta}\cdot e^{(-e^{3\theta})}$	0	$1-1/e$	$3/e$
A4	$4(1-\alpha)[-\ln(1-\alpha)]^{3/4}$	$[-\ln(1-\alpha)]^{1/4}$	$1-e^{(-e^{4\theta})}$	$4e^{4\theta}\cdot e^{(-e^{4\theta})}$	0	$1-1/e$	$4/e$
Contracting geometry: Contracting cylinder (R2), Contracting sphere (R3)							
R2	$2(1-\alpha)^{1/2}$	$1-(1-\alpha)^{1/2}$	$e^{\theta}\cdot(2-e^{\theta})$	$2e^{\theta}\cdot(1-e^{\theta})$	$\ln 1/2$	0.75	0.5
R3	$3(1-\alpha)^{2/3}$	$1-(1-\alpha)^{1/3}$	$1-(1-e^{\theta})^3$	$3e^{\theta}\cdot(1-e^{\theta})^2$	$\ln 1/3$	19/27	4/9
Diffusion: One-dimensional diffusion (D1), Three-dimensional diffusion (Jander, D3)							
D1	$1/(2\,\alpha)$	α^2	$e^{\theta/2}$	$1/2e^{\theta/2}$	0	1	0.5
D3	$3/2(1-\alpha)^{2/3}[1-(1-\alpha)^{1/3}]^{-1}$	$[1-(1-\alpha)^{1/3}]^2$	$1-(1-e^{\theta/2})^3$	$3/2e^{\theta/2}\cdot(1-e^{\theta/2})^2$	$2\ln 1/3$	19/27	2/9

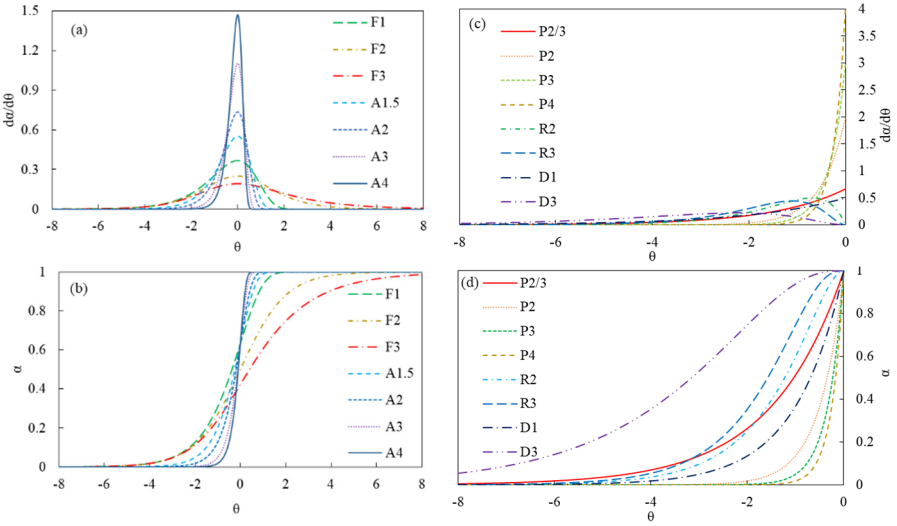

Fig. 2.2. Plots of the universal description for the common reaction mechanisms: θ-based conversion rate (a,c) and conversion (b,d) [66].

2.2. Applications of the universal description

Based on the exclusive characteristics of the universal model, four applications were implemented to investigate biomass pyrolysis: i.e., identification of the conversion peak, determination of the reaction mechanism, prediction of the conversion rate, and evaluation of the kinetics. Accordingly, a simplified kinetic model with only one kinetic parameter was derived in the third application. Relevant experiments for the validation and implementation of the applications were also conducted.

2.2.1. Thermogravimetric experiments

To implement and validate the proposed methods, a series of TGA experiments were designed and performed. Cellulose, one of the major pseudo-components of woody biomass, was selected to undergo pyrolysis for validating the simplified kinetic model [68]. Meanwhile, the real woody biomass, i.e., poplar wood, was also selected as the other experiment material, to test the applicability of the new model. Samples (10 mg) of the two experimental materials were analyzed using a Netzsch STA409PC thermal analyzer with a pure nitrogen flow of 20 ml/min. Different samples were heated at different rates, that is, 10 °C/min, 15 °C/min, and 25 °C/min, from 25 to 1000 °C. Once the maximum temperature was reached, the sample for each

run remained in the furnace for an additional 15 min to minimize experimental error. In addition, the TGA data of Artemisia apiacea, one of the herbal biomass, were used as supplementary material in this study. The data were obtained in [30] by a Netzsch STA449F3 thermal analyzer under five different heating rates:10 °C/min, 20 °C/min, 30 °C/min, 40 °C/min, and 50 °C/min. More details can be found in [30].

2.2.2. Identification of the conversion peak

Based on Table 2.1, the peak conversion rate always occurs at a fixed value of θ for a certain reaction model. For example, $\theta_p \equiv 0$ for the reaction order, Mampel power law, nucleation, and D1 models; $\theta_p \equiv 2\ln 1/3$ for the D3 reaction model, when the conversion rate reaches its peak. Hence, upon determining the reaction model, the peak position of the pyrolysis process can be easily identified by plotting $\theta \sim T$ and $\theta \equiv \theta_p$. The intersection of the two plots corresponds to the position of the conversion-rate peak. An example is illustrated in Fig. 2.3 for the identification of the conversion peak of Artemisia pyrolysis under five different heating rates with different reaction model assumptions. The predicted results showed negligible errors compared with the experimental data. More detailed results and discussion are provided in Paper B.

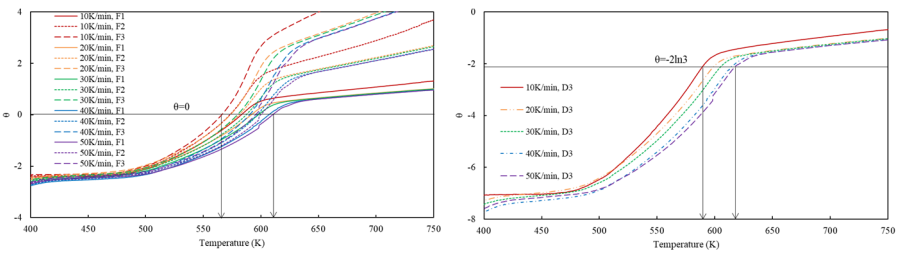

(a) (b)

Fig. 2.3. Conversion peak identification for the Artemisia pyrolysis under multiple heating rates [69].

2.2.3. Determination of the reaction mechanism

Based on the above derivation and discussion, it can be concluded that the reaction mechanisms and the expression of the universal model in Table 2.1 correspond one-to-one. It can be used to determine the reaction mechanism by comparing the real θ-based conversion rate to the universal plots in Fig. 2.2. The methodology for this application is as follows.

For constant-heating-mode pyrolysis, integrating Eq. (1.2) and Eq. (1.3) into the θ-based conversion rate in Eq. (2.4), we can obtain the mathematical relationship between the T-based and θ-based conversion rates, as expressed in Eq. (2.9).

$$\frac{d\alpha}{d\theta} = \frac{\frac{d\alpha}{dt}}{A} e^{u} \cdot \frac{AE_a}{\beta R} p(u) = \frac{d\alpha}{dT} \frac{E_a}{R} e^{u} p(u) \tag{2.9}$$

To increase the applicability of Eq. (2.9), an approximation equation for the temperature integral used in the KAS method, that is, $p(u) \approx e^{-u}/u^2$, is implemented in Eq. (2.9) and conducting a simplified equation, as expressed in Eq. (2.10a).

$$\frac{d\alpha}{d\theta} = \frac{d\alpha}{dT} \frac{RT^2}{E_a} \tag{2.10a}$$

Evidently, the θ-based conversion rate for a practical pyrolysis process can be calculated by the T-based conversion rate and its activation energy. The former can be obtained in DTG data and the latter can be evaluated by model-free methods. Upon calculating the practical $d\alpha/d\theta$, the comparison with the standard θ-based conversion rate for each reaction mechanism in Table 2.1 can be quantified by Eq. (2.11). Here, the $Error^2$ indicates the proximity between the real reaction mechanism to the selected reaction model, $Error^2$=0 implies the pyrolysis process agrees precisely with the selected reaction model.

$$Error^2 = \left[\left(\frac{d\alpha}{d\theta} \right)_{std} - \frac{d\alpha}{dT} \frac{RT^2}{E_a} \right]^2 \tag{2.11}$$

Fig. 2.4 demonstrates this application in determining the reaction mechanism for Artemisia pyrolysis, in which the TGA data and activation energy are achieved in [30]. Seven reaction mechanisms, namely, F1, F2, F3, D1, D3, R2, and R3, were selected for their small values of $Error^2$ and are zoomed in, as displayed in Fig. 2.4b. To determine the best reaction model fitting the pyrolysis among the seven, the relative errors (%), which is the $Error^2$ normalized by the sum of the $Error^2$ of the seven reaction models, are presented in Fig. 2.5. The results demonstrate that the third-order reaction model (F3) best fits the Artemisia pyrolysis, followed by F2, D3, F1, D1, R3, and R2. This conclusion is consistent with previous findings in [30]. This application presents a novel method for theoretically defining the reaction mechanism other than 'master plot'. The usage of the distributed activation

energies in this new method is considered more reasonable than 'master plot', which assumes that kinetics are global throughout the pyrolysis process [40].

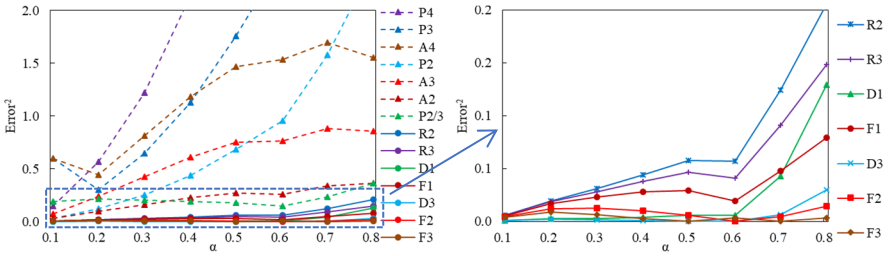

(a) (b)

Fig. 2.4. Comparison of the θ-based conversion rate for Artemisia pyrolysis to the universal description in Table 2.1 [69].

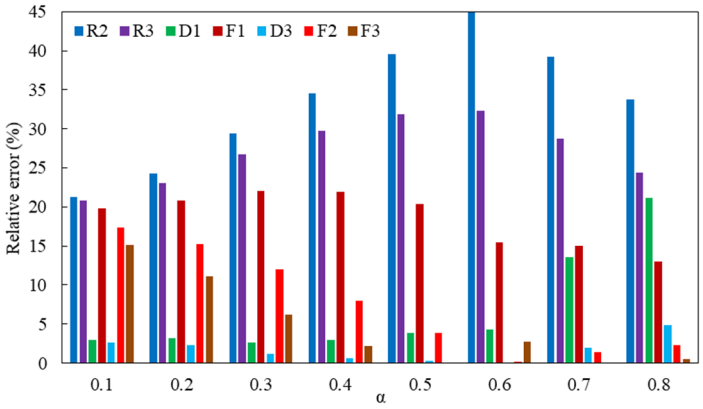

Fig. 2.5. Relative error of the top seven reaction mechanisms (F1, F2, F3, D1, D3, R2, and R3) for Artemisia pyrolysis [69].

2.2.4. Prediction of the conversion rate

In reverse, Eq. (2.10a) can be rewritten by substituting $d\alpha/dT$ into Eq. (2.10b),

$$\frac{d\alpha}{dT} = \frac{d\alpha}{d\theta}\frac{E_a}{RT^2} \tag{2.10b}$$

which forms a new expression for the conversion rate in terms of the temperature [70]. Compared with the typical Arrhenius-type model, Eq. (1.1), the new expression is recognised as a simplified kinetic model, primarily because it only contains one kinetic parameter E_a, free from the pre-exponential factor A and the heating rate β.

2.2.4.1 Theoretical validation

The simplified kinetic model was verified by comparing with the typical Arrhenius-type equation for various reaction mechanisms of solid fuel pyrolysis, as displayed in Fig. 2.6 [71]. The prediction results from the two models are highly consistent for the order reaction and diffusion reaction mechanisms, which validates the applicability of the simplified kinetic model to these reaction mechanisms. The considerable differences between the two predictions for the nucleation reaction mechanisms are probably because the approximation equation of $p(u)$ is not ideal for these reaction mechanisms.

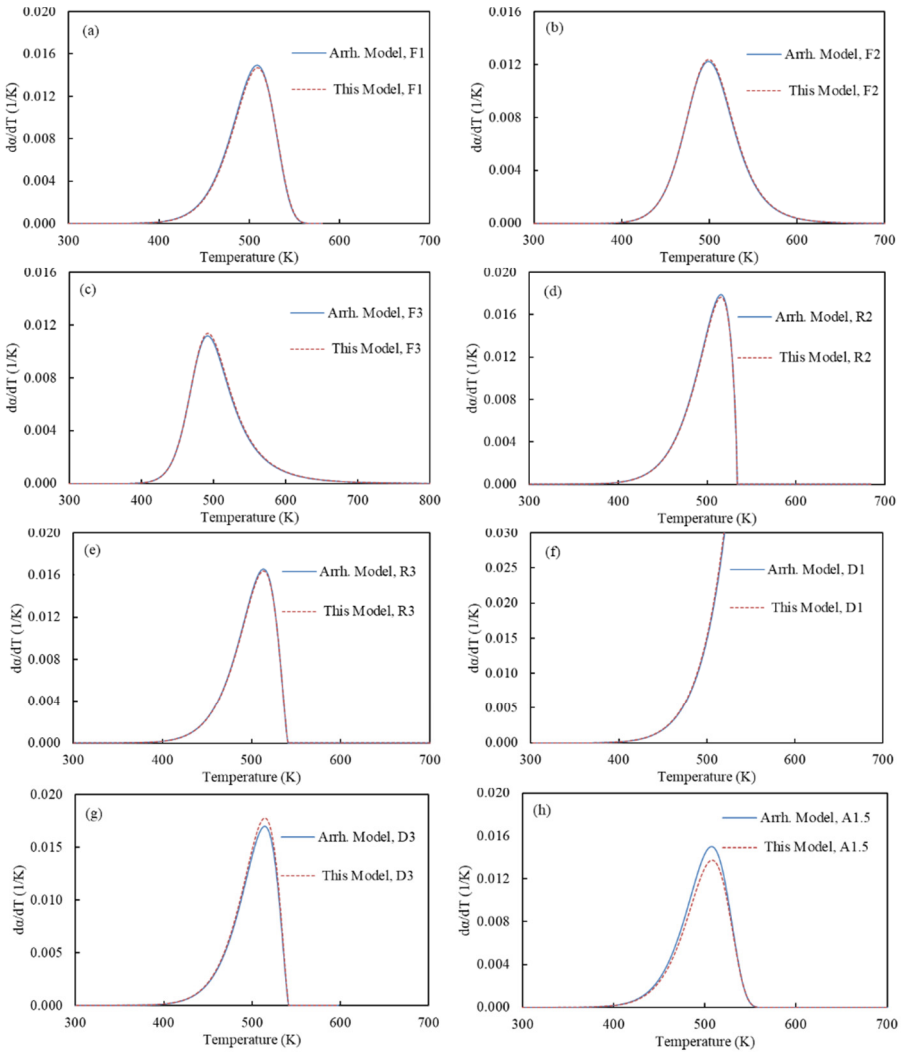

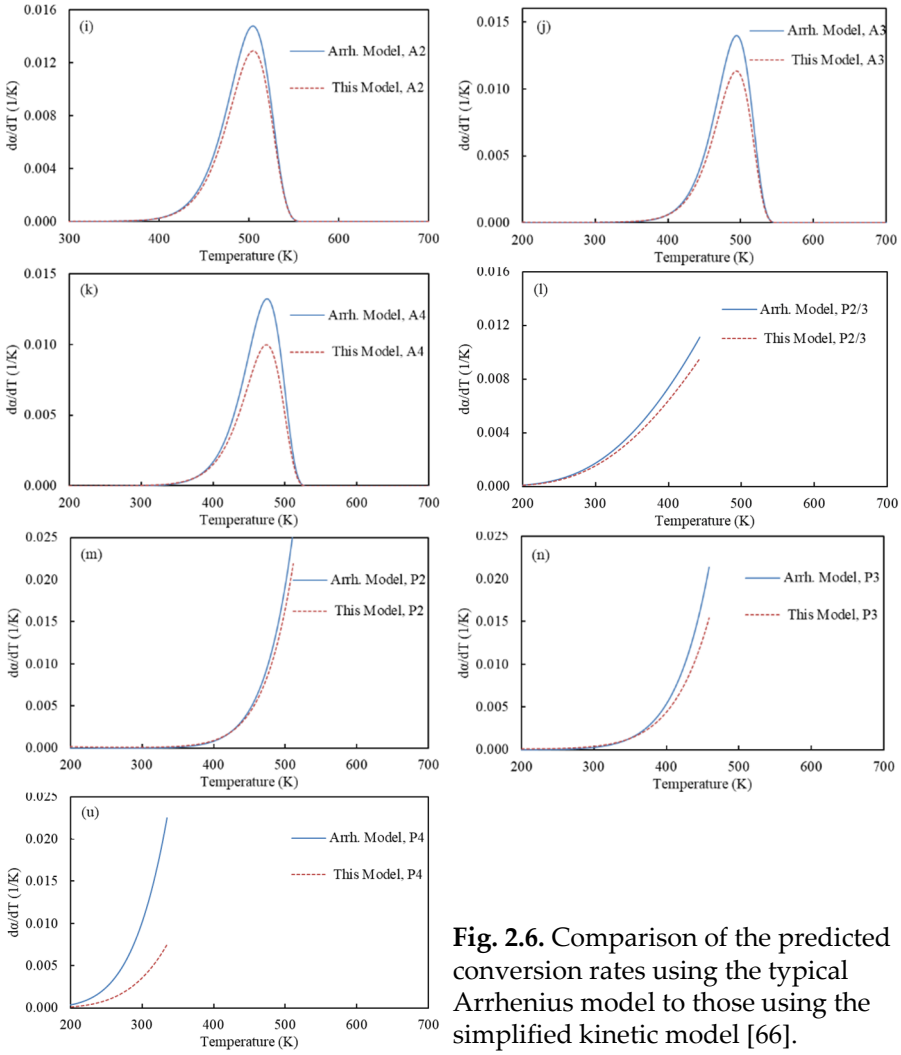

Fig. 2.6. Comparison of the predicted conversion rates using the typical Arrhenius model to those using the simplified kinetic model [66].

2.2.4.2 Experimental validation

The experimental validation results for the simplified kinetic model are presented in Fig. 2.7. The kinetics used in both models were calculated using the Coats-Redfern method, as described in Paper A. In short, the new model can predict the conversion rate with an acceptable error relative to the experimental data. It outperformed the conventional Arrhenius kinetic model when low-quality kinetics were used. A detailed comparison of the simplified

kinetic model and the conventional Arrhenius model is summarized in Table 2.2. More elaborations refer to Paper A.

Table 2.2 Comparison of the simplified kinetic model to the conventional Arrhenius-type kinetic model [66].

Kinetic models	Simplified kinetic model	Conventional Arrhenius model
Expression	$\frac{d\alpha}{dT} = \frac{d\alpha}{d\theta}\frac{E_a}{RT^2}$	$\frac{d\alpha}{dT} = \frac{A}{\beta}exp(-\frac{E_a}{RT})f(\alpha)$
Number of parameters	One, E_a	Two, A and E_a
Approximation equation	$p(u) = e^{-u}/u^2$	None
Conversion estimation for start up	All the common reaction models	P2/3, P2, P3, P4, A1.5, A2, A3, A4, D1
Applicability	•Very close to the conventional Arrhenius model with reliable kinetics. •Closer to the experimental data with low R^2 kinetics. •Remarkable differences at the initial and the ending stages using global kinetics. •Easier used in CFD models.	• Well accepted. • Larger difference to the experimental data with low R^2 kinetics. • Remarkable differences at the initial and the ending stages using global kinetics. • Easily used in CFD models.

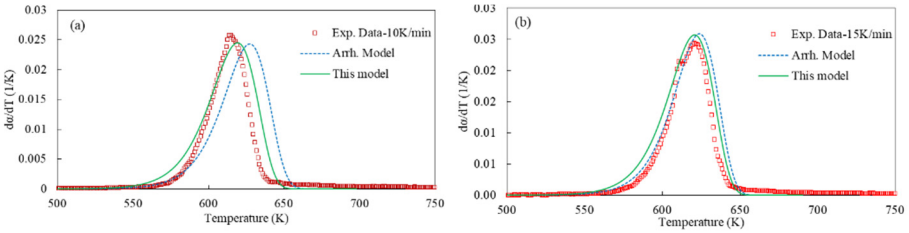

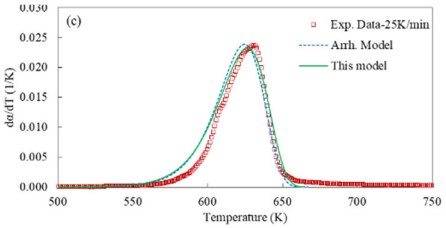

Fig. 2.7. Comparison of the typical Arrhenius model with the simplified kinetic model for predicting the conversion rate of cellulose pyrolysis [66].

2.2.5. Evaluation of kinetics

By separating the activation energy E_a from Eq. (2.10a), the expression of Eq. (2.10c) can be used to evaluate E_a, once the reaction mechanism and DTG data are available.

$$E_a = \frac{d\alpha}{dT}\frac{d\theta}{d\alpha}RT^2 \tag{2.10c}$$

The corresponding pre-exponential factor A can then be obtained using Eq. (2.12) to predict the conversion rate using Eq. (1.1) [66].

$$\ln A = \theta + \frac{E_a}{RT} + 2\ln\frac{E_a}{RT} + \ln\frac{\beta R}{E_a} \tag{2.12}$$

Compared to conventional model-free methods, this approach is simple and stable, as demonstrated by evaluating the kinetics of poplar wood pyrolysis. Table 2.3 presents the kinetics evaluated using this method and those from the Friedman method. The activation energies obtained using these two methods are shown in Fig. 2.8. Comparing the two methods, several consequences are summarized.

1) The activation energies obtained from this model were smaller and smoother than those obtained using the Friedman method with large fluctuations. The activation energies can be calculated directly using Eq. (2.10c). In contrast, linear data fitting is required in the Friedman method, which may lead to a computational error when the data are not linearly correlated.
2) The new method is more reliable because it does not result in negative values of E_a, as it is physically unrealistic. Moreover, the quality of obtained E_a using the Friedman method was over-reliant on the TGA data.
3) The new method demonstrated that E_a is influenced by the pyrolysis heating rate. The results prove that the activation energies vary

significantly with the conversion and differ slightly owing to the heating rate.

Table 2.3 Kinetics evaluation of poplar wood pyrolysis by this model and the Friedman method [66].

α	Friedman			This model						
				10K/min		15K/min		25K/min		
	E_a	A	R^2	E_a	A	E_a	A	E_a	A	$\overline{E_a}$
(-)	kJ/mol	1/s	(-)	kJ/mol	1/s	kJ/mol	1/s	kJ/mol	1/s	kJ/mol
0.01	-10.88	1.87E-08	0.9701	28.90	1.61E+00	4.90E-04	4.90E-04	11.42	1.57E-03	17.72
0.05	189.47	1.32E+15	0.8613	45.67	6.11E+00	1.00E+04	1.00E+04	78.60	2.97E+04	66.80
0.10	201.71	9.11E+15	0.9304	74.01	6.12E+03	1.94E+04	1.94E+04	85.66	1.45E+05	79.36
0.15	217.41	1.33E+17	0.9704	64.26	6.78E+02	6.34E+03	6.34E+03	81.33	5.38E+04	72.97
0.20	219.80	1.18E+17	0.9469	59.55	2.42E+02	7.42E+02	7.42E+02	73.97	1.06E+04	65.72
0.25	243.28	8.14E+18	0.9631	55.74	1.03E+02	2.62E+02	2.62E+02	67.32	2.46E+03	60.64
0.30	230.71	3.65E+17	0.9762	53.93	7.06E+01	1.44E+02	1.44E+02	64.33	1.27E+03	58.09
0.35	245.76	5.06E+18	0.9883	56.66	1.30E+02	2.09E+02	2.09E+02	64.13	1.24E+03	59.46
0.40	244.95	3.14E+18	0.9958	62.66	4.85E+02	1.12E+03	1.12E+03	69.08	3.52E+03	65.71
0.45	232.17	2.12E+17	0.9986	68.81	1.87E+03	3.84E+03	3.84E+03	76.49	1.65E+04	72.11
0.50	228.93	9.87E+16	0.9985	77.33	1.15E+04	1.95E+04	1.95E+04	83.46	6.98E+04	79.85
0.55	265.99	1.24E+20	0.9811	85.20	6.04E+04	5.37E+04	5.37E+04	105.15	5.71E+06	91.29
0.60	276.06	7.55E+20	0.9747	91.16	2.09E+05	1.88E+05	1.88E+05	106.69	8.03E+06	95.81
0.65	218.47	9.97E+15	0.996	96.03	5.68E+05	3.99E+05	3.99E+05	89.65	2.68E+05	92.97
0.70	226.71	4.51E+16	0.9961	96.52	6.53E+05	5.09E+05	5.09E+05	98.57	1.60E+06	96.44
0.75	228.72	5.39E+16	0.9947	91.25	2.29E+05	1.56E+05	1.56E+05	92.82	5.22E+05	90.77
0.80	269.22	6.73E+19	0.9869	67.52	1.89E+03	1.97E+03	1.97E+03	78.93	3.39E+04	70.94
0.85	831.70	5.26E+63	0.6459	12.03	9.97E-03	1.64E-02	1.64E-02	30.71	1.87E+00	18.41
0.90	-399.05	4.33E-33	0.4498	8.88	2.03E-03	6.93E-03	6.93E-03	10.79	1.60E-02	9.80
0.95	-181.98	2.86E-15	0.8758	6.55	5.62E-04	3.24E-03	3.24E-03	8.65	7.42E-03	7.70
0.99	-169.37	1.68E-13	0.9633	16.64	1.77E-03	1.64E-03	1.64E-03	17.25	2.80E-02	13.61

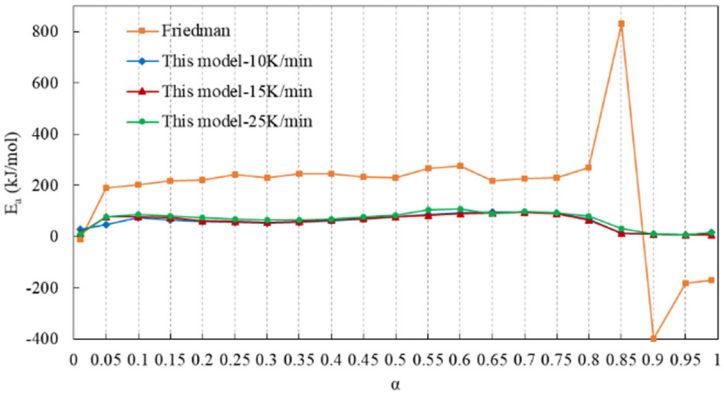

Fig. 2.8. Plots of the activation energies in Table 2.3 along with conversion and heating rate [66].

To validate the reliability of the kinetics, the conversion rate was calculated using Eq. (1.1) and the kinetics in Table 2.3, which was then compared with the experimental data, as illustrated in Fig. 2.9. From the comparison, it can be concluded that the kinetics of the two methods are reliable for predicting the conversion rate of poplar wood pyrolysis. Nevertheless, the kinetics evaluated using this method were more accurate in predicting the conversion rate near peak positions. For a better view, Table 2.4 summarizes and compares the two methods of evaluating kinetics, and a deeper discussion is given in Paper A.

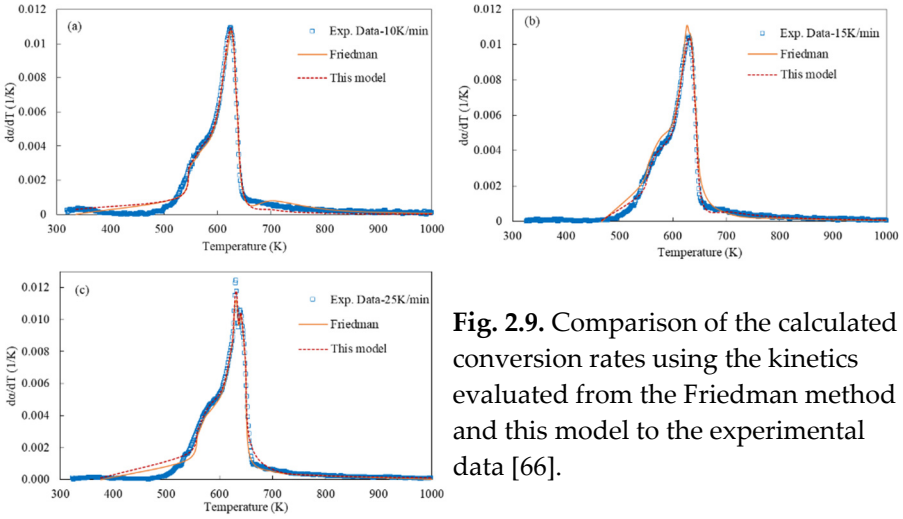

Fig. 2.9. Comparison of the calculated conversion rates using the kinetics evaluated from the Friedman method and this model to the experimental data [66].

Table 2.4 Summary of the new method and the Friedman method for evaluating kinetics [66].

Kinetics evaluation	Friedman method	This model
Data needed	TG and DTG data at least under three different heating rates.	TG and DTG data under a heating rate.
Assumptions	The kinetic rate constant is independent of the conversion. The reaction model is independent of the temperature. Kinetics are independent of heating rates.	The kinetic rate constant is independent of the conversion. The reaction model is independent of the temperature. Kinetics are dependent of heating rates.
Approximation equation	None.	$p(u) = e^{-u}/u^2$
Evaluation process	Plotting $\ln\left(\beta \frac{d\alpha}{dT}\right)$ versus $\frac{1}{T}$, E_a can be estimated by the slope of the linear trend line; A can be obtained from its intercept.	By Eq. (2.10c) and Eq. (2.12).
Error from[a]	Linear data fitting	Approximation equation
Application conversion range	0.05-0.95 are acceptable (depending). 0.1-0.8 are good. No more than 0.05 conversion step is recommended.	0-1, higher accuracy with smaller conversion steps.
Singular values	May be produced at the initial and ending stages.	Never.
Accurate[b]	Well accepted.	Performs better than the Friedman method.
Usage	Not very complicated.	Easy to use.

[a] The systematic error of the method itself.
[b] The consistency of the predicted conversion rate with the experimental data.

2.3. Summary

In Chapter 2, a universal description of solid fuel pyrolysis for all common reaction models is derived. The expressions of the universal model can be recognized as statistical distributions, based on their exclusive characteristics. This can be used to gain a better understanding and characterize solid fuel pyrolysis from a statistical perspective.

Subsequently, several applications based on the universal description are demonstrated to analyze the woody biomass pyrolysis process, that is, conversion peak identification, reaction mechanism determination, conversion rate prediction, and kinetics evaluation. A simplified kinetic model is derived based on this third application. Compared with the conventional model-free model, the simplified kinetic model stands out for its reliability, simplicity, and robustness in analyzing biomass pyrolysis. Finally, the activation energies of poplar wood pyrolysis are revealed, proving that the kinetics greatly depend on the conversion degree and are slightly influenced by the heating rate. The universal description and proposed applications are promising for solid fuel pyrolysis kinetic studies.

Paper A

A Simplified Kinetic Model Based on a Universal Description for Solid Fuels Pyrolysis: Theoretical Derivation, Experimental Validation, and Application Demonstration

Tianbao Gu, Zhufu Fu, Torsten, Berning, Xuantian Li and Chungen Yin

This paper has been published in the

Energy, Vol. 225, pp. 120133, 2021.

Energy 225 (2021) 120133

Contents lists available at ScienceDirect

Energy

journal homepage: www.elsevier.com/locate/energy

A simplified kinetic model based on a universal description for solid fuels pyrolysis: Theoretical derivation, experimental validation, and application demonstration

Tianbao Gu [a], Zhufu Fu [b], Torsten Berning [a], Xuantian Li [c], Chungen Yin [a, *]

[a] Department of Energy Technology, Aalborg University, DK-9220 Aalborg East, Denmark
[b] School of Environmental Science and Engineering, Tianjin University, Tianjin, 300072, China
[c] NJTECH Environmental Technologies, Ltd., Suite B-2020, 5 New Model Road, Nanjing, China

ARTICLE INFO

Article history:
Received 17 November 2020
Received in revised form
8 February 2021
Accepted 14 February 2021
Available online 2 March 2021

Keywords:
Biomass pyrolysis
Kinetic modeling
Universal description
Simplified kinetic model

ABSTRACT

A kinetic model for the prediction of the conversion rate is crucial for research and development of biomass pyrolysis. The complexity of the existing kinetic studies and the diversity in pyrolysis kinetic data largely compromise the application of kinetic models. For the purpose of developing a generalized kinetic model, in this paper, we derive a universal description for all the common reaction mechanisms of solid fuels pyrolysis, among which the first-order reactions can be described as standardized general extreme value distribution. Based on the universal description, a simplified kinetic model with only one kinetic parameter is proposed. Then, we perform an experimental study of cellulose and poplar wood pyrolysis in order to validate the new model and to demonstrate its usefulness. The prediction results of the new model are very consistent with those from the conventional Arrhenius model and also agree well with the experimental data. Afterwards, the new model is applied to evaluate the kinetics for poplar wood pyrolysis, and comparisons between our model results and the commonly used Friedman method in terms of accuracy and applicability are shown. The new model also illustrates that the activation energies vary remarkably with the conversion degree and heating rate.

1. Introduction

In the past decades, thermochemical conversion of biomass for renewable energy and chemicals production has drawn increasing attention worldwide [1,2]. Pyrolysis, not only a key inseparable stage of gasification and combustion but also an independent thermochemical technology, is very promising for bioenergy production [3]. However, the lack of reliable modeling tools suitable for biomass pyrolysis processes including reaction mechanisms, kinetic models, and species evolution has largely hindered the progress in its industrial applications [4,5]. Among these challenges, kinetic modeling that connects the scientific theories to engineering applications is one of the key bottlenecks for research and development of biomass pyrolysis [6]. It is of great significance to develop a reliable biomass pyrolysis kinetic model of great applicability.

In the previous kinetic models, the Arrhenius theory is commonly used, in which the conversion rate can be calculated by the kinetic rate constant (governed by the kinetic parameters i.e., activation energy, pre-exponential factor, and temperature order) multiplied with the reaction model function [7]. In previous kinetic studies, numerous researchers focused on the evaluation of the kinetic parameters such as the model-fitting method and the model-free (iso-conversional) method [8]. The model-fitting methods assume the reaction model in advance, and thus the kinetics can be evaluated by fitting the thermogravimetric analysis (TGA) data [9]. However, linear fitting of the TGA data can only be applied in a very limited conversion range. Hence, it is difficult to achieve reliable kinetics which can describe the entire pyrolysis process globally [10]. In addition, the kinetics achieved via the model-fitting methods are over-reliant on the assumption of the reaction model, consequently the kinetics are not generally suitable for further applications [11]. The iso-conversional methods, on the other hand, do not need to assume a reaction model [12], from which the activation energies are obtained by the slope of the linear fitting of a series of TGA data along the heating rates for at least

* Corresponding author.
E-mail address: chy@et.aau.dk (C. Yin).

https://doi.org/10.1016/j.energy.2021.120133
0360-5442/

Nomenclature

Symbols

A	pre-exponent factor (s^{-1})
E_a	activation energy (J· mol^{-1})
$k(T)$	kinetic rate constant (s^{-1})
m	Solid mass at time t (g)
m_0	Initial solid mass (g)
m_∞	Final solid mass (g)
$p(u)$	Temperature integral $p(u) = \int_u^\infty \frac{e^{-u}}{u^2} du$
R	Ideal gas constant (J K^{-1} mol^{-1})
t	Reaction time (s)
T	Temperature (K)
u	Dimensionless varaible $u = E_a/(RT)$
α	Conversion degree (−)
α_p	Peak conversion degree (−)
β	Heating rate (K min^{-1})
θ	Reaction progress factor (−)
θ_p	Peak reaction progress factor (−)

Abbreviations

CDF	Cumulative distribution function
CFD	Computational fluid dynamics
DAEM	Distributed activation energy model
DTG	Differential Thermogravimetry
FWO	Flynn-Wall-Ozawa
GEV	generalized extreme value
KAS	Kissinger-Akahira-Sunose
MSW	Municipal solid wastes
PDF	Probability density function
TGA	Thermogravimetric Analysis

three cases [13,14]. Besides the typical Arrhenius models, some other kinetic models based on statistical distributions have been recently developed, such as distributed activation energy method (DAEM) [15] and Weibull mixture model [16]. The DAEM assumes that the decomposition process is made by an infinite series of independent parallel reactions with various activation energies, which are governed by a statistical distribution [17]. The prediction results are considered as more precise, while the application is complicated with costly computational time [18]. Different from DAEM, the Weibull mixture model describes the decomposition rates via the probability density function (PDF) of the Weibull distribution instead of the typical Arrhenius equation. These two models show the strength of statistical distributions for the description of solid fuels decomposition, and provide another view for the development of kinetic models.

Apart from the above kinetic parameters' studies, a few works which try to model the solid pyrolysis universally have been made such as 'master plot' proposed by Criado [19] and the generalized kinetic model developed by Li et al. [20]. Criado's studies proposed a comprehensive equation named 'master plot' that can be plotted as a universal curve with respect to the conversion for a certain reaction model. The method of 'master plot' has been successfully used for the determination of feasible reaction mechanisms for solid fuels decomposition [21], but not for the kinetics evaluation. On the contrary, the generalized model for first-order reactions developed by Li et al. has been applied in the evaluation of kinetic parameters for biomass pyrolysis [20]. In the study of Li et al., the pyrolysis process can be modeled as a unified generalized extreme value (GEV) distribution [22], which is independent of activation energy, pre-exponential factor, or heating rate [23]. The conversion rate in terms of temperature can be obtained by transformation of the generalized model. It is a big step to model the pyrolysis in a generalized way, but the efforts are limited to the first-order reactions; the expressions of the generalized model for other reaction mechanisms still need to be refined.

To achieve a universal description that can be widely used for solid fuels decomposition, further mathematical development of the model of Li et al. other than for a first order reaction has been explored. The final form of the universal description has been derived in this paper. The detailed derivation process for first order reactions is shown, and the formulations of the generalized model for other commonly used reaction mechanisms of solid fuels decompositions are summarized. The universal description is rigorously consistent with the standardized GEV distribution for first order reactions, which explained why the Weibull distribution or other GEV distributions are capable of describing biomass pyrolysis. Subsequently, a simplified kinetic model with only one kinetic parameter has been developed based on the universal description. The prediction results of the conversion rate from the simplified model are highly consistent with those from the typical Arrhenius model by using the same kinetic parameters. In addition, the predicted conversion rates for cellulose pyrolysis via this model show better agreements with the experimental data compared to those via the typical Arrhenius model. Furthermore, the simplified model has been applied for evaluation of the kinetics for real biomass pyrolysis, from which the kinetic parameters perform better than those from the model-free methods in terms of accuracy and applicability. The activation energies during the pyrolysis process are proven instantaneous which are mainly dependent on conversion, and influenced by the heating rate.

2. Description of the simplified kinetic model

For the solid fuels pyrolysis, the conversion rate of solid decomposition can be written in the generalized form of Eq. (1) [20]:

$$\frac{d\alpha}{dt} = k(T) f(\alpha) \tag{1}$$

in which α is the conversion degree defined as the ratio of the mass loss at time t to the final mass loss [24], $f(\alpha)$ is the reaction model, and $k(T)$ is the kinetic rate constant, which is commonly expressed by the Arrhenius equation [25].

$$\alpha = \frac{m_0 - m}{m_0 - m_\infty} \tag{2}$$

$$k(T) = A\, exp\left(-\frac{E_a}{RT}\right) \tag{3}$$

In the above equations, m_0, m and m_∞ denote the initial mass, mass at time t, and the final mass, respectively. A, E_a, R and T represent the pre-exponential factor, activation energy, ideal gas constant, and the reaction temperature, respectively. For a constant heating rate $\beta \equiv dT/dt$ in the non-isothermal pyrolysis process, the conversion rate in Eq. (1) can be re-written in terms of temperature [26].

$$\frac{d\alpha}{dT}=\frac{A}{\beta}exp\left(-\frac{E_a}{RT}\right)f(\alpha) \tag{4}$$

2.1. The universal description of solid fuel pyrolysis for first order reaction mechanism

The kinetic rate constant $k(T)$ is assumed independent of the conversion degree α, and the reaction model $f(\alpha)$ is assumed independent of the temperature T [27]. With this, Eq. (1) can be rewritten by separating variables α and t, and then be integrated, which results in a new form of Eq. (1).

$$g(\alpha)\equiv\int_0^{\alpha}\frac{d\alpha}{f(\alpha)}=\int_0^{t}k(T)dt \tag{5}$$

Here, $g(\alpha)$ is a dimensionless variable that can be considered as an indication of the reaction progress. Taking the logarithm of Eq. (5) for both sides, and setting $\theta\equiv\ln g(\alpha)$, one obtains the expression for the alternative indicator of the reaction progress, θ:

$$\theta\equiv\ln g(\alpha)=\ln\int_0^{t}k(T)dt\ ,\ \text{and}\quad d\theta=\frac{k(T)dt}{\int_0^{t}k(T)dt}=\frac{k(T)}{g(\alpha)}dt \tag{6}$$

Then an expression for the conversion rate α with respect to θ, $d\alpha/d\theta$, can be obtained from Eqs. (1) and (6),

$$\frac{d\alpha}{d\theta}=\frac{d\alpha}{dt}\cdot\frac{dt}{d\theta}=k(T)f(\alpha)\cdot\frac{g(\alpha)}{k(T)}=f(\alpha)\cdot g(\alpha)=f(\alpha)\cdot\int_0^{\alpha}\frac{d\alpha}{f(\alpha)} \tag{7}$$

Eq. (7) shows that the reaction rate expressed in terms of $d\alpha/d\theta$ only depends on the reaction model $f(\alpha)$, whilst it is independent of the kinetic parameters (e.g., E_a and A) of $k(T)$ or heating rate.

For first-order reactions, the reaction model $f(\alpha)=1-\alpha$ [28], the reaction progress indicator θ and the reaction rate with respect to θ can be expressed as,

$$\theta\equiv\ln g(\alpha)=\ln\int_0^{\alpha}\frac{d\alpha}{f(\alpha)}=\ln\int_0^{\alpha}\frac{d\alpha}{1-\alpha}=\ln(-\ln(1-\alpha)) \tag{8}$$

$$\frac{d\alpha}{d\theta}=f(\alpha)\cdot\int_0^{\alpha}\frac{d\alpha}{f(\alpha)}=(1-\alpha)\cdot\int_0^{\alpha}\frac{d\alpha}{(1-\alpha)}=-(1-\alpha)\ln(1-\alpha) \tag{9}$$

From Eq. (8), one can express the conversion degree α in terms of the reaction progress indicator θ, and then express the conversion rate in terms of θ accordingly.

$$\alpha=1-\exp(-\exp(\theta))\ \text{ or }\ 1-\alpha=\exp(-\exp(\theta)) \tag{10}$$

$$\frac{d\alpha}{d\theta}=\exp(\theta)\cdot\exp(-\exp(\theta)) \tag{11}$$

As presented in Eq. (11), $\frac{d\alpha}{d\theta}\sim(-\theta)$ is precisely the same as the PDF of the standardized generalized extreme value (GEV) distribution ($\xi=0$) [22]. Fig. 1 shows the comparison of the generalized model for first order reaction to the standardized GEV distribution in terms of PDF and cumulative distribution function (CDF). Namely, the conversion rate for any first-order reaction, $\frac{d\alpha}{d\theta}$, with respect to θ, can be described by a generalized, standardized GEV distribution. This is why the Weibull distribution or other GEV distributions can be used for the description of biomass pyrolysis with the assumption of first-order reaction model [29].

In the universal description, the peak of the conversion rate is related to the maximum reaction rate of the pyrolysis process [20]. From $\frac{d^2\alpha}{d\theta^2}=0$, the peak position can be determined at $\theta_p\equiv0$. Therefore, for all first-order reactions, the peak conversion degree is $\alpha_p\equiv1-1/e\approx0.63$ and the peak conversion rate is $(d\alpha/d\theta)_p\equiv1/e\approx0.37$.

2.2. The universal description of solid fuel pyrolysis for other reaction mechanisms

For biomass pyrolysis, many reaction mechanisms have been proposed. Gai et al. have summarized the most common reaction mechanisms as four types: reaction order, nucleation, contracting geometry, and diffusion [13]. The derivation of the θ-based model for the other common reaction mechanisms is precisely the same as that for the first-order reaction, the only difference being $f(\alpha)$. The reaction model $f(\alpha)$ and the derived generalized model for the other common reaction mechanisms are summarized in Table 1. As plotted in Fig. 2, the reaction order and nucleation mechanisms can be considered as one group, obeying the GEV distribution with $\theta_p=0$ at the peak conversion rate; the Mample Power law, contracting geometry and diffusion reaction models can be viewed as another group with the range from $(-\infty)$ to zero of the reaction progress indicator θ. The conversion rates governed by the Mample Power law and three-dimensional diffusion (Jander, D3) show a monotonic increase along θ. Since the complexity of the expression of $f(\alpha)$ for the two-dimensional diffusion (D2) mechanism and the three-dimensional diffusion (Ginstling−Brounshtein, D4) mechanism, the conversion degree α can not be explicitly expressed by θ. Thus, the generalized model for the D2 and D4 reaction mechanisms cannot be expressed in terms of θ, the expressions respect of α are represented in Table 1.

The conventional Arrhenius theory is an analytical physics method, in which the conversion rate constant $k(T)$ is governed by the kinetic parameters (i.e., activation energy, pre-exponential factor and temperature order). The reactions during pyrolysis only occur if the energy absorbed from the environment of the reactants overcomes the activation energy [30]. On the other hand, the universal description describes the pyrolysis process in a statistical physics way, the conversion degree and the corresponding conversion rate can be expressed by the cumulative density function (CDF) and probability density function (PDF) of a statistical distribution, respectively. Since the solids pyrolysis can also be considered as a 'mass failure' progress, the mass fraction loss from one to zero is assumed to be governed by a specific statistical distribution function. Several models based on the statistical distributions i.e., Weibull distribution, Gaussian distribution, for description of the pyrolysis process are developed in this perspective [16,31]. Both the conventional Arrhenius model and the new statistical model are capable of describing biomass pyrolysis, but in different views, which offer different perspectives for research and development of solid fuels pyrolysis.

2.3. Derivation of the simplified kinetic model based on the universal description

For a constant heating rate of non-isothermal pyrolysis process,

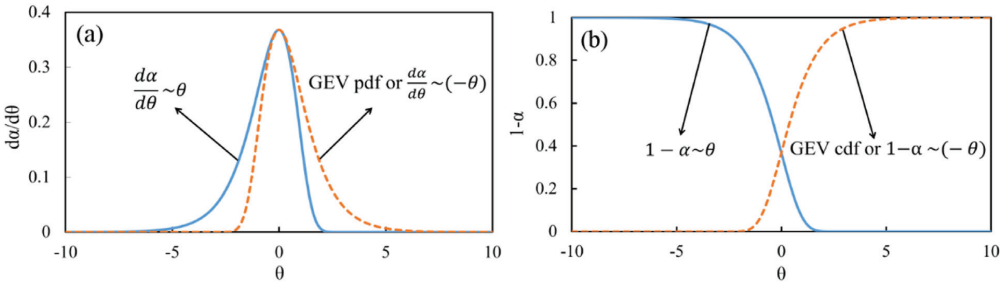

Fig. 1. Comparison of the reaction progress indicator θ-based conversion rate function to the standardized GEV distribution, (a) probability density function (pdf), (b) cumulative distribution function (cdf).

Table 1
The expressions of the universal description for the most common reaction mechanisms of solid fuels pyrolysis.

Mechanisms	$f(\alpha)$	$g(\alpha)\equiv e^{\theta}$	$\alpha \sim \theta$	$\frac{d\alpha}{d\theta}$	θ_p	α_p	$\left(\frac{d\alpha}{d\theta}\right)_p$
Reaction order: First-order (F1), Second-order (F2), Third-order (F3), nth-order (Fn)							
F1	$1-\alpha$	$-\ln(1-\alpha)$	$1-e^{(-e^{\theta})}$	$e^{\theta}\cdot e^{(-e^{\theta})}$	0	$1-1/e$	$1/e$
F2	$(1-\alpha)^2$	$\frac{\alpha}{1-\alpha}$	$1-\frac{1}{e^{\theta}+1}$	$\frac{e^{\theta}}{(e^{\theta}+1)^2}$	0	0.5	0.25
F3	$(1-\alpha)^3$	$[(1-\alpha)^{-2}-1]/2$	$1-\frac{1}{(2e^{\theta}+1)^{1/2}}$	$\frac{e^{\theta}}{(2e^{\theta}+1)^{3/2}}$	0	$1-\frac{\sqrt{3}}{3}$	$\frac{\sqrt{3}}{9}$
Fn	$(1-\alpha)^n$	$[(1-\alpha)^{-(n-1)}-1]/(n-1)$	$1-\frac{1}{[(n-1)e^{\theta}+1]^{1/(n-1)}}$	$\frac{e^{\theta}}{[(n-1)e^{\theta}+1]^{n/(n-1)}}$	0	$1-\left(\frac{1}{n}\right)\frac{1}{n-1}$	$\left(\frac{1}{n}\right)\frac{n}{n-1}$
Mampel Power Law							
P(2/3)	$2/3\alpha^{-1/2}$	$\alpha^{3/2}$	$e^{2/3\theta}$	$2/3e^{2/3\theta}$	0	1	2/3
P2	$2\alpha^{1/2}$	$\alpha^{1/2}$	$e^{2\theta}$	$2e^{2\theta}$	0	1	2
P3	$3\alpha^{2/3}$	$\alpha^{1/3}$	$e^{3\theta}$	$3e^{3\theta}$	0	1	3
P4	$4\alpha^{3/4}$	$\alpha^{1/4}$	$e^{4\theta}$	$4e^{4\theta}$	0	1	4
Nucleation							
A1.5	$1.5(1-\alpha)[-\ln(1-\alpha)]^{1/3}$	$[-\ln(1-\alpha)]^{2/3}$	$1-e^{(-e^{(3/2)\theta})}$	$3/2e^{(3/2)\theta}\cdot e^{(-e^{(3/2)\theta})}$	0	$1-1/e$	3/(2e)
A2	$2(1-\alpha)[-\ln(1-\alpha)]^{1/2}$	$[-\ln(1-\alpha)]^{1/2}$	$1-e^{(-e^{2\theta})}$	$2e^{2\theta}\cdot e^{(-e^{2\theta})}$	0	$1-1/e$	$2/e$
A3	$3(1-\alpha)[-\ln(1-\alpha)]^{2/3}$	$[-\ln(1-\alpha)]^{1/3}$	$1-e^{(-e^{3\theta})}$	$3e^{3\theta}\cdot e^{(-e^{3\theta})}$	0	$1-1/e$	$3/e$
A4	$4(1-\alpha)[-\ln(1-\alpha)]^{3/4}$	$[-\ln(1-\alpha)]^{1/4}$	$1-e^{(-e^{4\theta})}$	$4e^{4\theta}\cdot e^{(-e^{4\theta})}$	0	$1-1/e$	$4/e$
Contracting geometry: Contracting cylinder (R2), Contracting sphere (R3)							
R2	$2(1-\alpha)^{1/2}$	$1-(1-\alpha)^{1/2}$	$e^{\theta}\cdot(2-e^{\theta})$	$2e^{\theta}\cdot(1-e^{\theta})$	$\ln\frac{1}{2}$	$\frac{3}{4}$	0.5
R3	$3(1-\alpha)^{2/3}$	$1-(1-\alpha)^{1/3}$	$1-(1-e^{\theta})^3$	$3e^{\theta}\cdot(1-e^{\theta})^2$	$\ln\frac{1}{3}$	$1-\left(\frac{2}{3}\right)^3$	$\left(1-\frac{1}{3}\right)^2$
Diffusion: One-dimensional diffusion (D1), Three-dimensional diffusion (Jander, D3)							
D1	$1/(2\alpha)$	α^2	$e^{\theta/2}$	$1/2e^{\theta/2}$	0	1	0.5
D2	$[-\ln(1-\alpha)]^{-1}$	$(1-\alpha)\ln(1-\alpha)+\alpha$	–	$\alpha-\alpha/\ln(1-\alpha)-1$	–	–	–
D3	$3/2(1-\alpha)^{2/3}1-\alpha)(1-\alpha)(1-\alpha)^{1/3}]^{-1}$	$1-\alpha)(1-\alpha)(1-\alpha)^{1/3}]^2$	$1-(1-e^{\theta/2})^3$	$3/2e^{\theta/2}\cdot(1-e^{\theta/2})^2$	$2\ln\frac{1}{3}$	$1-\left(\frac{2}{3}\right)^3$	$\left(1-\frac{1}{3}\right)^2/2$
D4	$3/21-\alpha)(1-\alpha)(1-\alpha)^{1/3}]^{-1}$	$1-(2/3)\alpha-(1-\alpha)^{2/3}$	–	$\frac{3[1-(1-\alpha)^{2/3}]-\alpha}{2[1-(1-\alpha)^{1/3}]}$	–	–	–

if we let $u\equiv E_a/(RT)$, then $p(u)\equiv\int_u^{\infty}\frac{e^{-u}}{u^2}du$, Eq. (5) and Eq. (6) can be converted into Eq. (12) and Eq. (13), respectively.

$$g(\alpha)=\int_0^t k(T)dt=\frac{A}{\beta}\int_{T_0}^{T}\exp\left(-\frac{E_a}{RT}\right)dT=\frac{AE_a}{\beta R}\int_u^{\infty}\frac{e^{-u}}{u^2}du=\frac{AE_a}{\beta R}p(u) \tag{12}$$

$$\theta\equiv\ln(\alpha)=\ln\frac{AE_a}{\beta R}+\ln p(u) \tag{13}$$

On the other hand, inserting Eqs. (4) and (12) into Eq. (7) to replace $f(\alpha)$ and $g(\alpha)$, the relationship between θ-based conversion rate $d\alpha/d\theta$ and T-based conversion rate $d\alpha/dT$ can be obtained.

$$\frac{d\alpha}{d\theta}=\frac{\frac{d\alpha}{dt}}{A}e^{u}\cdot\frac{AE_a}{\beta R}p(u)=\frac{d\alpha}{dT}\frac{E_a}{R}e^{u}p(u) \tag{14}$$

Since there is no analytical solution of the temperature integral $p(u)$, it is always approximated numerically. In this study, we integrate the approximation equation $p(u)=e^{-u}/u^2$, which is used in KAS method [32], into Eq. (14), a much more simplified kinetic model with only one kinetic parameter (activation energy E_a) for

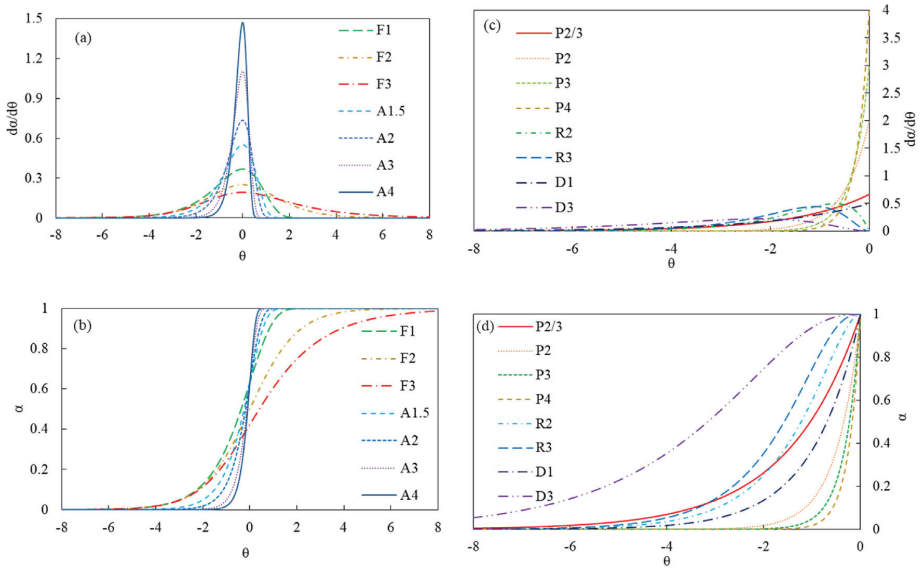

Fig. 2. The reaction progress indicator θ-based conversion rate $d\alpha/d\theta$ and θ-based conversion α for reaction order and nucleation mechanisms (a) and (b), and for contracting geometry and diffusion mechanisms (c) and (d).

the prediction of the conversion rate can be achieved as shown in Eq. (15a),

$$\frac{d\alpha}{dT} = \frac{d\alpha}{d\theta}\frac{E_a}{RT^2} \tag{15a}$$

where the universal description $d\alpha/d\theta$ can be obtained from Table 1 once the reaction model is determined. Then, the conversion rate can be evaluated with the only one kinetic parameter E_a for the solid fuel pyrolysis process. The solid decomposition rate dm/dt (kg/s) for usage in engineering applications can be calculated by the conversion rate times the solid initial decomposable mass and the heating rate.

$$\frac{dm}{dt} = (m_0 - m_\infty)\frac{d\alpha}{dt} = (m_0 - m_\infty)\beta\frac{d\alpha}{d\theta}\frac{E_a}{RT^2} \tag{16}$$

3. Validation and application of the simplified kinetic model

3.1. Theoretical validation of the simplified kinetic model

Fig. 3 presents the conversion rates predicted by the simplified kinetic model (Eq. (15a)) and the typical Arrhenius model (Eq. (4)) for the most commonly used reaction mechanisms of solid fuels pyrolysis. The prediction results from the simplified model and the typical Arrhenius model use the same kinetics which are from Ref. [33]. From the comparison results, the two prediction results reflect high consistency, particularly for order reaction models, contracting geometry reaction models, and diffusion reaction models (F1, F2, F3, R2, R3, D1, D3). For other reaction models, the predicted conversion rates from the two models also show the same trends with an acceptable range of error. The relatively large differences, i.e. nearby the peak positions for the nucleation reaction models, are probably due to the approximation equation used in the simplified model, which may not be precise enough for the complicated reaction mechanisms. Therefore, we conclude that the simplified model is theoretically validated. It can be used to predict the conversion rate, at least for the order reaction models, contracting geometry reaction models and diffusion reaction models dominated pyrolysis process. Moreover, the simplified kinetic model requires only one kinetic parameter (E_a) and is therefore regarded as more convenient for usage, the simplified equation can be conveniently implemented into computational fluid dynamics (CFD) models for description of solid fuels conversion process [34]. Furthermore, it avoids the error from evaluation of the pre-exponential factor A in applications.

For more convincing validation of the new model, another comparison of the predicted conversion rate from the simplified model and the conventional Arrhenius model using the kinetics in the Ref. [35] has been carried out. The comparison results are very consistent to Fig. 3, which are not discussed any more. The detailed results are given in Appendix, as seen in Table A.1 and Figs. A.1-A.3.

3.2. Experimental validation and application of the simplified kinetic model

3.2.1. Experiments description

To validate the simplified kinetic model and demonstrate its usefulness, we performed a series of thermogravimetric analysis (TGA) studies. Cellulose as one of the major components of biomass with simple structures is chosen as the experimental material for validation of the simplified kinetic model [30]. Diversely, poplar wood, one of the representative lignocellulosic biomass, is selected to test the usefulness of the simplified kinetic model for the description of real biomass pyrolysis [28]. The completely dried samples (10 mg) with an average diameter of less than 0.5 mm were analyzed through the Netzsch STA409PC thermal analyzer under the pure nitrogen atmosphere (20 ml/min flow rate, 99.999% purity). Each sample was heated from 25 to 1000 °C under the heating

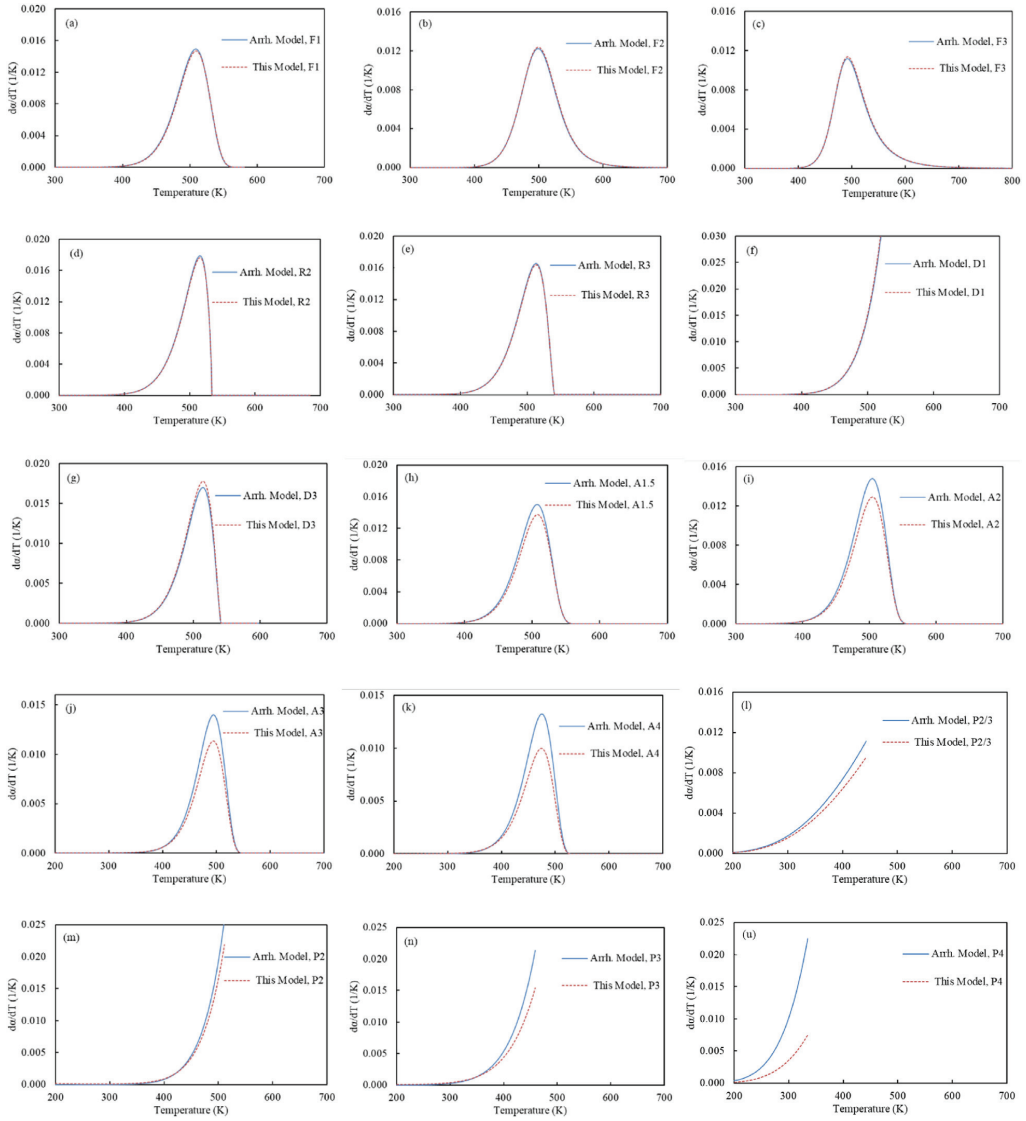

Fig. 3. Comparison of the predicted conversion rates by the simplified kinetic model and the Arrhenius model using the same kinetic parameters from the Ref. [33].

rates of 10, 15, and 25 K/min, respectively. For each run, after reaching the final temperature, the sample stays in the furnace for an extra 15 min until the mass of the sample does not change to avoid the experiments error.

3.2.2. Experimental validation of the simplified kinetic model

In order to verify the simplified model practically, the prediction results of the conversion rate are compared with cellulose DTG data. Before this, the global kinetic parameters (conversion range of 0.05–0.9) for the description of cellulose decomposition were evaluated by the Coats-Redfern method [36]. Fig. 4 illustrates the process for the evaluation of kinetics. The high R^2 of the linear data fitting indicates that the evaluated global kinetic parameters are reliable to be used for the description of cellulose pyrolysis process. The evaluated kinetics E_a and A are 212.46 kJ/mol and 7.63E+15 s^{-1}, 224.21 kJ/mol and 9.83E+16 s^{-1}, and 206.21 kJ/mol and 2.71E+15 $s^{-1}$for the TGA data under the heating rates of 10 K/min, 15 K/min, and 25 K/min, respectively. Afterwards, the evaluated global kinetics were integrated into the simplified model and the typical Arrhenius model to predict the conversion rate, respectively.

The first-order reaction model is selected as the reaction mechanism of cellulose pyrolysis [30] to predict the conversion rate of the two models. Since the universal description $d\alpha/d\theta$ for first-order reactions is zero if setting $\alpha = 0$ for initialization, which

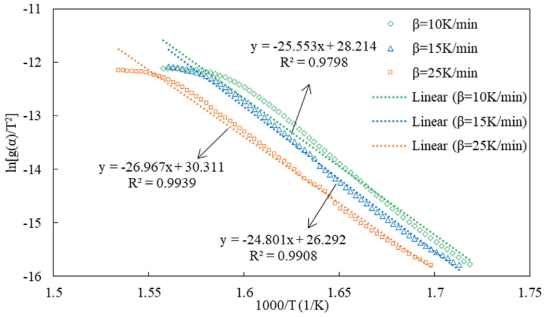

Fig. 4. Linear trend lines for obtaining the global kinetics for cellulose pyrolysis.

would lead the conversion rate from the simplified model always to be zero. To start up the simplified model, a tiny conversion value needs to be estimated for the initialization. Due to the fact that the Microsoft Excel stores 15 digits of precision, we choose 1×10^{-15} as the initial conversion to initialize the simplified model. The prediction results and the experimental DTG data are compared in Fig. 5. The following conclusions are drawn from the comparison. First, the predicted conversion rate via the simplified model are closer to the experimental data for all the heating rates compared to those from the typical Arrhenius model. Second, the simplified model is outstanding for predicting the conversion rate using the kinetics with low R^2, i.e., the case of 10 K/min heating rate as shown in Fig. (5a). This is due to that only one kinetic parameter E_a is used in the simplified model, whereas two kinetic parameters E_a and A are needed in the conventional Arrhenius model. The calculation of the pre-exponential factor A from the intercept is likely to introduce extra uncertainties. Third, there are remarkable differences between the experimental data and the predictions at the initial and the ending stages of the pyrolysis. This is attributed to the global kinetics not being sufficient to predict the conversion rate at the initial and ending stages. As researched in many other studies, the global kinetics are not able to describe the entire pyrolysis process precisely, distributed kinetic parameters are recommended to achieve more accurate prediction results [37].

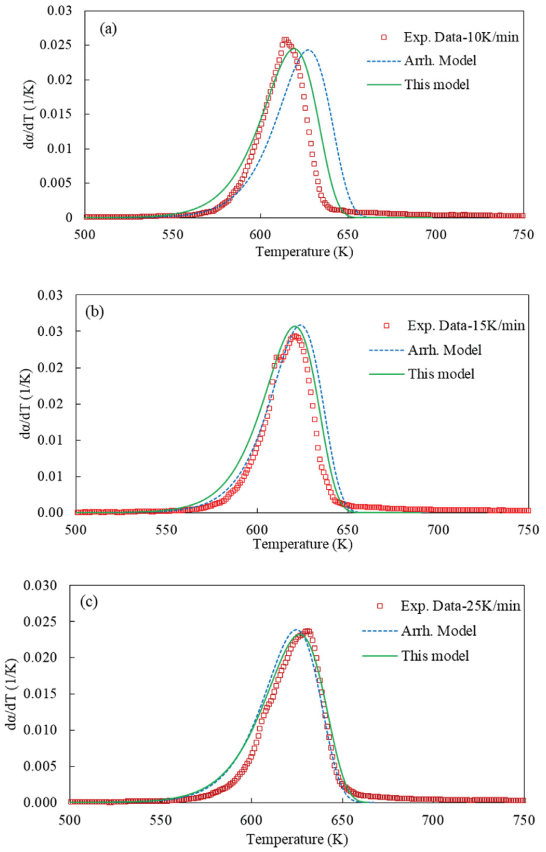

Fig. 5. Comparison of the predicted conversion rates by the simplified kinetic model with the experimental data for cellulose pyrolysis under (a) 10 K/min, (b) 15 K/min, and (c) 25 K/min heating rates.

Above all, the simplified kinetic model was validated experimentally and compared with the typical Arrhenius model. The two models show the similarity for prediction of the conversion rate, while the simplified kinetic model yields more reliable results than the typical Arrhenius model if lower R^2 kinetics are used. The simplified kinetic model is a further derivation of the conventional Arrhenius model, in which the universal description and a temperature integral approximation equation are used. Based on the above theoretical and experimental validation and analysis, the in-depth comparison of the simplified kinetic model and the conventional Arrhenius model was summarized in Table 2.

3.2.3. Application of the simplified kinetic model and comparison with model-free method

The above results confirmed that the simplified kinetic model is sufficient to predict the conversion rate with the given E_a. Alternatively, it can also be applied for the evaluation of kinetic parameters. Separating E_a from Eq. (15a), a new equation for evaluation of the activation energy is formed,

$$E_a = \frac{d\alpha}{dT}\frac{d\theta}{d\alpha}RT^2 \tag{15b}$$

where the data of $d\alpha/dT$ and T can be grabbed from the experimental DTG analysis, and $d\theta/d\alpha$ can be determined from Table 1 based on the chosen reaction mechanism. Similarly, integrating the temperature integral approximation equation $p(u) = e^{-u}/u^2$ to Eq. (13), the pre-exponential factor A then can be carried out by

$$\ln A = \theta + \frac{E_a}{RT} + 2\ln\frac{E_a}{RT} + \ln\frac{\beta R}{E_a} \tag{17}$$

Eq. (15b) and Eq. (17) present an easy way to determine the kinetic parameters directly, which does not need to make any data fitting as done in model-fitting or model-free methods. The two equations also theoretically prove that the kinetic parameters are dynamic during the pyrolysis process. In order to understand the kinetics evaluation via this model more clearly, it has been compared to the Friedman method, which is a widely used model-free method, as summarized in Table 3.

The evaluation results of the kinetic parameters by the Friedman method and this model are listed in Table A1. Each pair of kinetics are estimated at a certain conversion, which from 0.01 to 0.99 with a fixed conversion step of 0.05. The distributions of the activation energies along the conversion are plotted in Fig. 6. From the results, first, the obtained E_a from the Friedman method are larger than

Table 2
Comparison of the simplified kinetic model and the conventional Arrhenius model.

Kinetic models	The simplified model	The conventional Arrhenius model
Expression	$\frac{d\alpha}{dT} = \frac{d\alpha}{d\theta}\frac{E_a}{RT^2}$	$\frac{d\alpha}{dT} = \frac{A}{\beta}exp\left(-\frac{E_a}{RT}\right)f(\alpha)$
Number of parameters	One, E_a	Two, A and E_a
Approximation equation	$p(u) = e^{-u}/u^2$	None
Conversion estimation for start up	All the common reaction models	P2/3, P2, P3, P4, A1.5, A2, A3, A4, D1
Applicability	Very close to the conventional Arrhenius model with reliable kinetics; Closer to the experimental data with low R^2 kinetics; Remarkable differences at the initial and the ending stages using global kinetics; Easier used in CFD models with a simplified equation.	Well accepted; Larger difference to the experimental data with low R^2 kinetics; Remarkable differences at the initial and the ending stages using global kinetics; Easy used in CFD models.

Table 3
Comparison of the kinetics evaluation by the Friedman method and the simplified kinetic model.

Kinetics evaluation	Friedman method	This model
Data needed	TG and DTG data at least under three different heating rates [38].	TG and DTG data under a heating rate.
Assumptions	The kinetic rate constant is independent of the conversion; The reaction model is independent of the temperature; Kinetics are independent of heating rates.	The kinetic rate constant is independent of the conversion; The reaction model is independent of the temperature; Kinetics are dependent of heating rates.
Approximation equation	None.	$p(u) = e^{-u}/u^2$
Evaluation process	Plotting $\ln\left(\beta\frac{d\alpha}{dT}\right)$ versus $\frac{1}{T}$, Ea can be estimated by the slope of the linear trend line; A can be obtained from its intercept [27].	By the equations: $E_a = \frac{d\alpha}{dT}\frac{d\theta}{d\alpha}RT^2$ $\ln A = \theta + \frac{E_a}{RT} + 2\ln\frac{E_a}{RT} + \ln\frac{\beta R}{E_a}$
Error from[a]	Linear data fitting	Approximation equation
Application conversion range	0.05–0.95 are acceptable (depending); 0.1–0.8 are good; No more than 0.05 conversion step are recommended [39].	0-1, higher accurate with smaller conversion steps.
Singular values	May be produced at the initial and ending stages.	Never.
Accurate[b]	Well accepted [37].	Performs better than Friedman method
Usage	Not very complicated.	Easy to use.

[a] The systematic error of the method itself.
[b] The consistency of the predicted conversion rate with the experimental data.

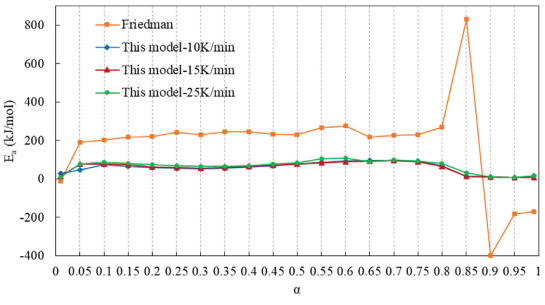

Fig. 6. Distributions of the activation energies evaluated by the Friedman method and the simplified kinetic model along the conversion.

those from this model and fluctuate dramatically. The values of evaluated E_a from Friedman method differ from −400 kJ/mol to 830 kJ/mol during the entire pyrolysis process, while those from this model are in the range of 6–107 kJ/mol. For the stable conversion stage (conversion range of 0.05–0.8), the average value of E_a evaluated from the Friedman method is 233 kJ/mol. Whereas, the average values of E_a evaluated from this model are 71.6, 74.6, and 82.3 kJ/mol for the pyrolysis process under the heating rate of 10 K/min, 15 K/min, and 25 K/min, respectively. The significant differences of the activation energies evaluated by the two methods are probably due to the very different evaluation processes used in the two methods. For the simplified model, there is only one kinetic parameter E_a, which is calculated by Eq. (15b) directly. Whereas for the Friedman method, there are two kinetic parameters, A and E_a, in which E_a is estimated from the slope of the linear trend of the $\ln\left(\beta\frac{d\alpha}{dT}\right)$ vs. $\frac{1}{T}$ plot and A is obtained from the intercept of the plot. The pairs of (A and E_a) estimated from the Friedman method are equivalent in effect to the one kinetic parameter E_a estimated from the simplified model. Second, there are some negative values of E_a produced by the Friedman method, owing to the inappropriate linear data fitting used here. It is noted that the negative E_a is not physically realistic even though the prediction results are close to the experimental data. The E_a that physically presents the energy needed to be overcome for the reaction, should be positive. The model-free methods assume the kinetic parameters are independent of the heating rates, from which the E_a are estimated by the slope of the linear trend lines of the data along the different heating rates. However, the kinetic parameters are actually relevant to the heating rates. If linear data fitting is used to the data where the E_a vary greatly due to the different heating rates, i.e., at the initial and ending stages, singular values will be then generated. On the contrary, the simplified model admits the relevance between the

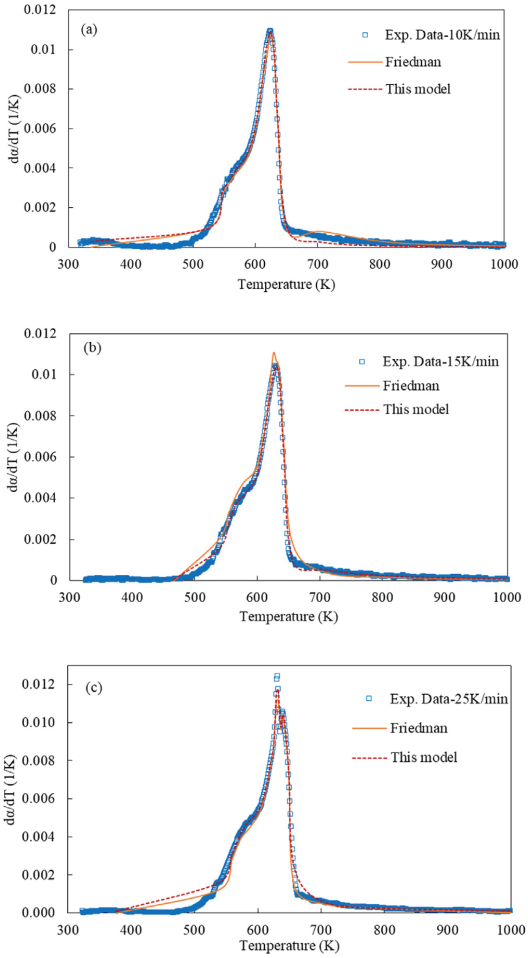

Fig. 7. Comparison of the experimental data of poplar wood pyrolysis with the predicted conversion rates using the dynamic kinetics evaluated from the simplified kinetic model and the Friedman method.

kinetics and the heating rates, the kinetics under each heating rate are estimated separately by Eq. (15b). The three terms, $d\alpha/$ dT, $d\theta/d\alpha$, and RT^2 in Eq. (15b), are positive. Therefore, the E_a estimated from this model will be always positive. At last, the values of E_a from this model differ largely along the conversion, and vary gently with the heating rates. However, at the initial and ending stages, the influences due to heating rates are significant. Theoretically from Eq. (15b), $d\theta/d\alpha$ is a function of conversion, and T depends on the heating rate, hence the E_a is relevant both to the conversion and the heating rate.

Fig. 7 displays the prediction results calculated by Eq. (4) using the dynamic kinetics evaluated from the Friedman method and this model in Table A1. First-order reaction model is selected as the reaction mechanism for modeling poplar wood pyrolysis [20]. It can be seen that both the two prediction results show good agreement with the experimental data. The predicted conversion rates by using the distributed kinetics show better accuracy than those using the global kinetics. Nevertheless, the prediction results using the kinetics evaluated from this model perform better at the complicated conversion stages, i.e., nearby the first and second peak positions. This can be explained by that the approximation equation used in this model is not sensible to the experimental data, whereas linear data fitting used in the Friedman method leads to large errors for the complicated conversion stages. At the initial and ending stages, the larger differences between the experimental data and the prediction results from the both methods are mainly due to the uncertainties of the experimental data at these stages. A smaller conversion step is recommended to evaluate the activation energies to predict the conversion rate more precisely at the beginning and ending pyrolysis process. In addition, the evaluation of the kinetics by this model is simpler than the Friedman and other model-free methods. The instantaneous kinetics can be easily obtained at any conversion degree, which shows the advantages in the application.

To show the ability of the new model for description of various solid fuels pyrolysis, the predicted conversion rates from this model and the experimental data of hemicellulose, lignin, PVC and MSW in the Ref. [29] have been compared. The validation for high heating rates pyrolysis process was achieved as well by comparing the calculation results to the cellulose pyrolysis experimental data under the heating rates of 60 K/min and 100 K/min in the Ref. [40]. To shorten the length of the paper, the results are plotted in Fig. A2 and Fig. A3, respectively. The comparison results prove that the new model can be used in various solid fuels and in higher heating rate conditions.

In short, the kinetic parameters for poplar wood pyrolysis were evaluated by the simplified model and the Friedman method. The prediction results using the kinetics from this model slightly outperform those using the kinetics from the Friedman method at the complicated conversion stages compared to the experimental data. More comparisons with different experimental data need to be obtained to confirm this preliminary conclusion. The simplified model also stands out by its stability and simplicity in application, which covers various solid fuels and different pyrolysis conditions. While, the simplified kinetic model has not been tested for extreme pyrolysis conditions, e.g., drop tube furnaces, flame assistant reactors and laser-heated apparatus, which provide much higher heating rates. Further works need to be obtained for validation and engineering application of the kinetic models to the solid fuels pyrolysis under extreme conditions.

4. Conclusions

In the present work, we propose a universal description for all the common reaction mechanisms of solid fuels pyrolysis, in which the description for the first-order reactions obeys the standardized general extreme value distribution. Based on the universal description, a new simplified kinetic model with only one kinetic parameter has been developed and validated. Compared to the conventional Arrhenius model, the new model more reliably and readily predicts the conversion rate of solid fuels pyrolysis. The new model is also applied to evaluate the kinetic parameters of biomass pyrolysis, which outperform the kinetics evaluated by the Friedman method when used in the conventional kinetic model for predicting biomass conversion rate. The kinetics are proven instantaneous during the pyrolysis process, which principally depend on the conversion degree, while gently influenced by the heating rate.

Credit author statement

Tianbao Gu: Methodology, Modeling, Writing – original draft preparation. Zhufu Fu: Experiments, Manuscript editing. Torsten

Berning: Supervision, Manuscript editing. Xuantian Li: Methodology, Manuscript editing. Chungen Yin: Supervision, Writing - Reviewing and Editing.

Declaration of competing interest

The authors declare that they have no known competing financial interests or personal relationships that could have appeared to influence the work reported in this paper.

Acknowledgements

This work was supported by the China Scholarship Council [201806250021]; Tianbao Gu acknowledges China Scholarship Council for the financial support of his study in Aalborg University. The authors are grateful for the valuable comments from all the reviewers that help a lot in improving the quality of the manuscript.

Appendix

Table A.1
Kinetic parameters evaluated by the Friedman method and the simplified model for poplar wood pyrolysis

Conversion	Friedman			This model						
				10K/min		15K/min		25K/min		$\overline{E_a}$
	E_a	A	R^2	E_a	A	E_a	A	E_a	A	
(−)	kJ/mol	1/s	(−)	kJ/mol	1/s	kJ/mol	1/s	kJ/mol	1/s	kJ/mol
0.01	−10.88	1.87E-08	0.9701	28.90	1.61E+00	4.90E-04	4.90E-04	11.42	1.57E-03	17.72
0.05	189.47	1.32E+15	0.8613	45.67	6.11E+00	1.00E+04	1.00E+04	78.60	2.97E+04	66.80
0.10	201.71	9.11E+15	0.9304	74.01	6.12E+03	1.94E+04	1.94E+04	85.66	1.45E+05	79.36
0.15	217.41	1.33E+17	0.9704	64.26	6.78E+02	6.34E+03	6.34E+03	81.33	5.38E+04	72.97
0.20	219.80	1.18E+17	0.9469	59.55	2.42E+02	7.42E+02	7.42E+02	73.97	1.06E+04	65.72
0.25	243.28	8.14E+18	0.9631	55.74	1.03E+02	2.62E+02	2.62E+02	67.32	2.46E+03	60.64
0.30	230.71	3.65E+17	0.9762	53.93	7.06E+01	1.44E+02	1.44E+02	64.33	1.27E+03	58.09
0.35	245.76	5.06E+18	0.9883	56.66	1.30E+02	2.09E+02	2.09E+02	64.13	1.24E+03	59.46
0.40	244.95	3.14E+18	0.9958	62.66	4.85E+02	1.12E+03	1.12E+03	69.08	3.52E+03	65.71
0.45	232.17	2.12E+17	0.9986	68.81	1.87E+03	3.84E+03	3.84E+03	76.49	1.65E+04	72.11
0.50	228.93	9.87E+16	0.9985	77.33	1.15E+04	1.95E+04	1.95E+04	83.46	6.98E+04	79.85
0.55	265.99	1.24E+20	0.9811	85.20	6.04E+04	5.37E+04	5.37E+04	105.15	5.71E+06	91.29
0.60	276.06	7.55E+20	0.9747	91.16	2.09E+05	1.88E+05	1.88E+05	106.69	8.03E+06	95.81
0.65	218.47	9.97E+15	0.996	96.03	5.68E+05	3.99E+05	3.99E+05	89.65	2.68E+05	92.97
0.70	226.71	4.51E+16	0.9961	96.52	6.53E+05	5.09E+05	5.09E+05	98.57	1.60E+06	96.44
0.75	228.72	5.39E+16	0.9947	91.25	2.29E+05	1.56E+05	1.56E+05	92.82	5.22E+05	90.77
0.80	269.22	6.73E+19	0.9869	67.52	1.89E+03	1.97E+03	1.97E+03	78.93	3.39E+04	70.94
0.85	831.70	5.26E+63	0.6459	12.03	9.97E-03	1.64E-02	1.64E-02	30.71	1.87E+00	18.41
0.90	−399.05	4.33E-33	0.4498	8.88	2.03E-03	6.93E-03	6.93E-03	10.79	1.60E-02	9.80
0.95	−181.98	2.86E-15	0.8758	6.55	5.62E-04	3.24E-03	3.24E-03	8.65	7.42E-03	7.70
0.99	−169.37	1.68E-13	0.9633	16.64	1.77E-03	1.64E-03	1.64E-03	17.25	2.80E-02	13.61

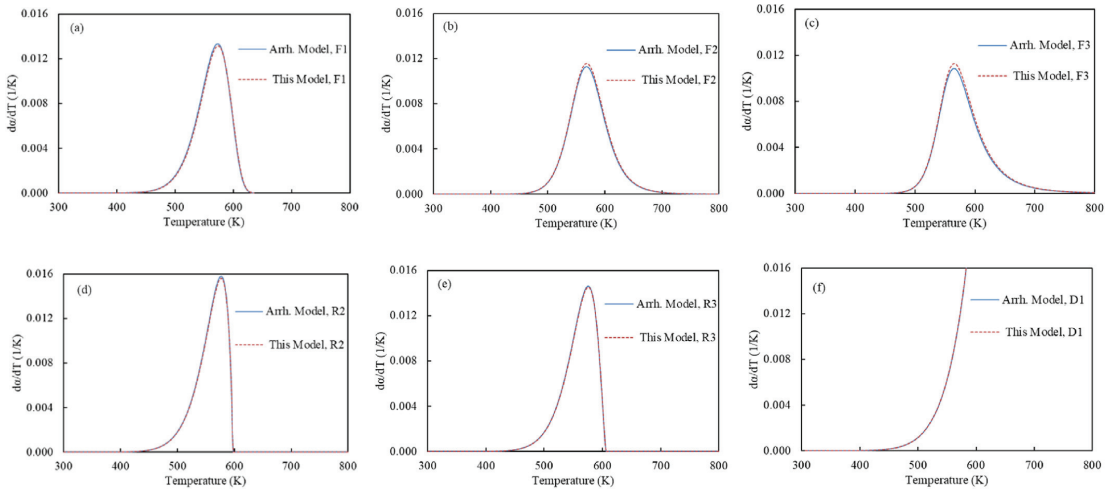

Fig. A.1. Comparison of the predicted conversion rates by the simplified kinetic model and the Arrhenius model using the same kinetic parameters from the Ref. [35].

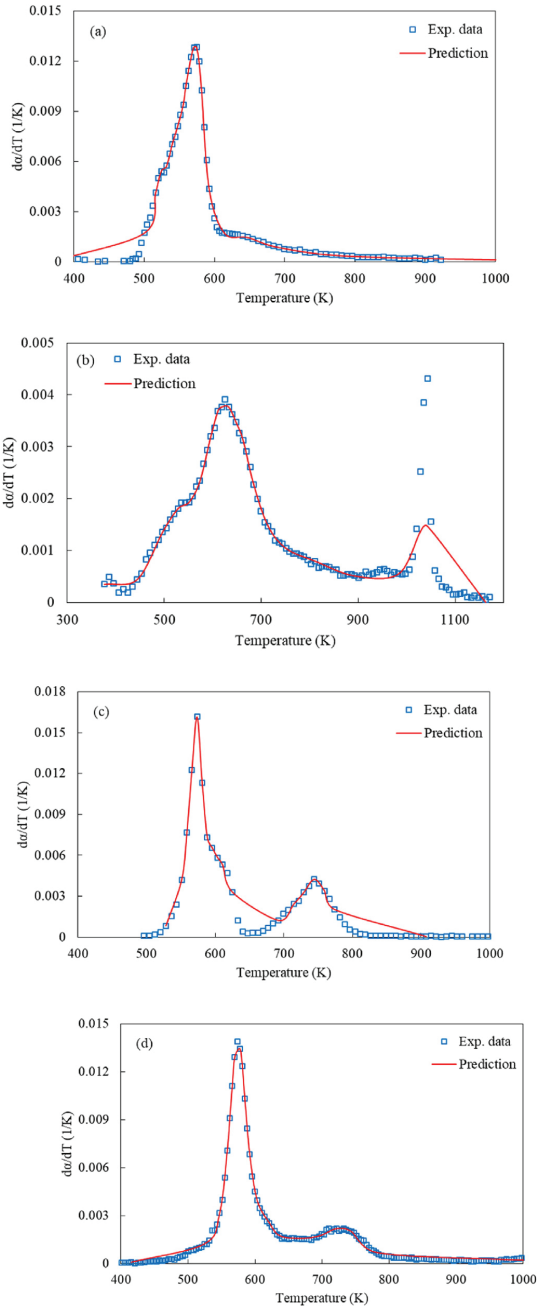

Fig. A.2. Comparison of the predicted conversion rate using the kinetics from this model and the experimental data of (a) hemicellulose, (b) lignin, (c) PVC and (d) MSW.

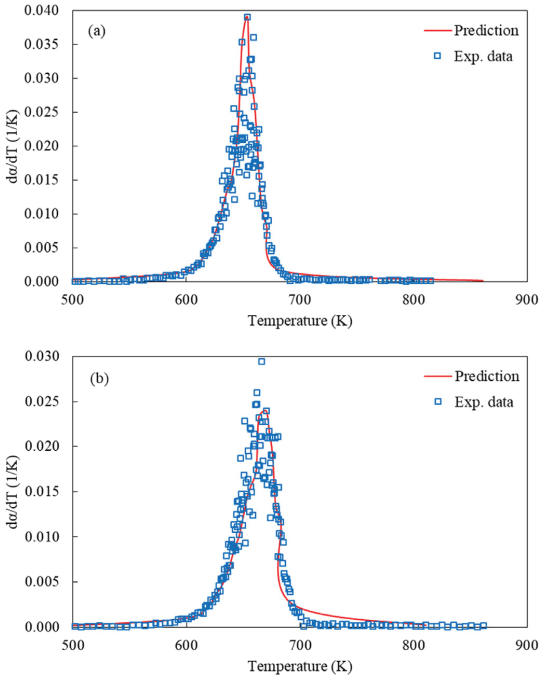

Fig. A.3. Comparison of the predicted conversion rate using the kinetics from this model and the experimental data of cellulose under the heating rate (a) 60 K/min and (b) 100 K/min.

References

[1] Sharma A, Pareek V, Zhang D. Biomass pyrolysis—a review of modelling, process parameters and catalytic studies. Renew Sustain Energy Rev 2015;50:1081–96. https://doi.org/10.1016/j.rser.2015.04.193.

[2] Heidari M, Salaudeen S, Arku P, Acharya B, Tasnim S, Dutta A. Development of a mathematical model for hydrothermal carbonization of biomass: comparison of experimental measurements with model predictions. Energy 2021;214:119020. https://doi.org/10.1016/j.energy.2020.119020.

[3] Nzihou A, Stanmore B, Lyczko N, Minh DP. The catalytic effect of inherent and adsorbed metals on the fast/flash pyrolysis of biomass: a review. Energy 2019;170:326–37. https://doi.org/10.1016/j.energy.2018.12.174.

[4] Chen X, Che Q, Li S, Liu Z, Yang H, Chen Y, et al. Recent developments in lignocellulosic biomass catalytic fast pyrolysis: strategies for the optimization of bio-oil quality and yield. Fuel Process Technol 2019;196:106180. https://doi.org/10.1016/j.fuproc.2019.106180.

[5] Zhang H, Wang Y, Shao S, Xiao R. An experimental and kinetic modeling study including coke formation for catalytic pyrolysis of furfural. Combust Flame 2016;173:258–65. https://doi.org/10.1016/j.combustflame.2016.08.019.

[6] Burra KRG, Gupta AK. Modeling of biomass pyrolysis kinetics using sequential multi-step reaction model. Fuel 2019;237:1057–67. https://doi.org/10.1016/j.fuel.2018.09.097.

[7] Richter F, Atreya A, Kotsovinos P, Rein G. The effect of chemical composition on the charring of wood across scales. Proc Combust Inst 2019;37:4053–61. https://doi.org/10.1016/j.proci.2018.06.080.

[8] Li M, Jiang L, He J, Sun J. Kinetic triplet determination and modified mechanism function construction for thermo-oxidative degradation of waste polyurethane foam using conventional methods and distributed activation energy model method. Energy 2019;175:1–13. https://doi.org/10.1016/j.energy.2019.03.032.

[9] Rony AH, Kong L, Lu W, Dejam M, Adidharma H, Gasem KAM, et al. Kinetics, thermodynamics, and physical characterization of corn stover (Zea mays) for solar biomass pyrolysis potential analysis. Bioresour Technol 2019;284:466–73. https://doi.org/10.1016/j.biortech.2019.03.049.

[10] Fisher T, Hajaligol M, Waymack B, Kellogg D. Pyrolysis behavior and kinetics of biomass derived materials. J Anal Appl Pyrol 2002;62:331–49. https://doi.org/10.1016/S0165-2370(01)00129-2.

[11] Conesa JA, Caballero J, Marcilla A, Font R. Analysis of different kinetic models in the dynamic pyrolysis of cellulose. Thermochim Acta 1995;254:175–92.

https://doi.org/10.1016/0040-6031(94)02102-T.
[12] Liu H, Wang C, Chen B, Zhang Z. A further study of pyrolysis of carbon fibre-epoxy composite from hydrogen tank: search optimization for kinetic parameters via a Shuffled Complex Evolution. J Hazard Mater 2019;374:20–5. https://doi.org/10.1016/j.jhazmat.2019.03.100.
[13] Gai C, Zhang Y, Chen W, Zhang P, Dong Y. Thermogravimetric and kinetic analysis of thermal decomposition characteristics of low-lipid microalgae. Bioresour Technol 2013;150:139–48. https://doi.org/10.1016/j.biortech.2013.09.137.
[14] Meng F, Zhou Y, Liu J, Wu J, Wang G, Li R, et al. Thermal decomposition behaviors and kinetics of carrageenan-poly vinyl alcohol bio-composite film. Carbohydr Polym 2018;201:96–104. https://doi.org/10.1016/j.carbpol.2018.07.095.
[15] Mirua K, Maki T. A simple method for estimating f(E) and k0(E) in the distributed activation energy model. Energy Fuels 1998;12:864–9. https://doi.org/10.1021/ef970212q.
[16] Janković B. The kinetic modeling of the non-isothermal pyrolysis of Brazilian oil shale: application of the Weibull probability mixture model. J Petrol Sci Eng 2013;111:25–36. https://doi.org/10.1016/j.petrol.2013.10.001.
[17] Fang S, Yu Z, Ma X, Lin Y, Chen L, Liao Y. Analysis of catalytic pyrolysis of municipal solid waste and paper sludge using TG-FTIR, Py-GC/MS and DAEM (distributed activation energy model). Energy 2018;143:517–32. https://doi.org/10.1016/j.energy.2017.11.038.
[18] Soria-Verdugo A, Garcia-Hernando N, Garcia-Gutierrez LM, Ruiz-Rivas U. Analysis of biomass and sewage sludge devolatilization using the distributed activation energy model. Energy Convers Manag 2013;65:239–44. https://doi.org/10.1016/j.enconman.2012.08.017.
[19] Criado JM. Kinetic analysis of DTG data from master curves. Thermochim Acta 1978;24:186–9. https://doi.org/10.1016/0040-6031(78)85151-X.
[20] Li X, Grace JR, Bi X, Campbell JS. A new pyrolysis model based on generalized extreme value (GEV) distributions and its application to lignocellulosic biomass. Fuel 2016;184:211–21. https://doi.org/10.1016/j.fuel.2016.07.012.
[21] Criado JM, Málek J, Ortega A. Applicability of the master plots in kinetic analysis of non-isothermal data. Thermochim Acta 1989;147:377–85. https://doi.org/10.1016/0040-6031(89)85192-5.
[22] Wang QJ. Estimation of the GEV distribution from censored samples by method of partial probability weighted moments. J Hydrol 1990;120:103–14. https://doi.org/10.1016/0022-1694(90)90144-M.
[23] Mallick D, Mahanta P, Moholkar VS. Co-gasification of coal and biomass blends: chemistry and engineering. Fuel 2017;204:106–28. https://doi.org/10.1016/j.fuel.2017.05.006.
[24] López-González D, Avalos-Ramirez A, Giroir-Fendler A, Godbout S, Fernandez-Lopez M, Sanchez-Silva L, et al. Combustion kinetic study of woody and herbaceous crops by thermal analysis coupled to mass spectrometry. Energy 2015;90:1626–35. https://doi.org/10.1016/j.energy.2015.06.134.
[25] Siddiqi H, Kumari U, Biswas S, Mishra A, Meikap BC. A synergistic study of reaction kinetics and heat transfer with multi-component modelling approach for the pyrolysis of biomass waste. Energy 2020;204:117933. https://doi.org/10.1016/j.energy.2020.117933.
[26] Ali I, Naqvi SR, Bahadar A. Kinetic analysis of Botryococcus braunii pyrolysis using model-free and model fitting methods. Fuel 2018;214:369–80. https://doi.org/10.1016/j.fuel.2017.11.046.
[27] Chong CT, Mong GR, Ng J, Chong WWF, Ani FN, Lam SS, et al. Pyrolysis characteristics and kinetic studies of horse manure using thermogravimetric analysis. Energy Convers Manag 2019;180:1260–7. https://doi.org/10.1016/j.enconman.2018.11.071.
[28] Slopiecka K, Bartocci P, Fantozzi F. Thermogravimetric analysis and kinetic study of poplar wood pyrolysis. Appl Energy 2012;97:491–7. https://doi.org/10.1016/j.apenergy.2011.12.056.
[29] Han Z, Li J, Gu T, Yan B, Chen G. The synergistic effects of polyvinyl chloride and biomass during combustible solid waste pyrolysis: experimental investigation and modeling. Energy Convers Manag 2020;222:113237. https://doi.org/10.1016/j.enconman.2020.113237.
[30] Wang S, Dai G, Ru B, Zhao Y, Wang X, Xiao G, et al. Influence of torrefaction on the characteristics and pyrolysis behavior of cellulose. Energy 2017;120:864–71. https://doi.org/10.1016/j.energy.2016.11.135.
[31] Janković B, Manić N, Stojiljković D, Jovanović V. TSA-MS characterization and kinetic study of the pyrolysis process of various types of biomass based on the Gaussian multi-peak fitting and peak-to-peak approaches. Fuel 2018;234:447–63. https://doi.org/10.1016/j.fuel.2018.07.051.
[32] Vo TK, Ly HV, Lee OK, Lee EY, Kim CH, Seo J, et al. Pyrolysis characteristics and kinetics of microalgal Aurantiochytrium sp. KRS101. Energy 2017;118:369–76. https://doi.org/10.1016/j.energy.2016.12.040.
[33] Almazrouei M, Janajreh I. Model-fitting approach to kinetic analysis of non-isothermal pyrolysis of pure and crude glycerol. Renew Energy 2020;145:1693–708. https://doi.org/10.1016/j.renene.2019.07.095.
[34] Gu T, Yin C, Ma W, Chen G. Municipal solid waste incineration in a packed bed: a comprehensive modeling study with experimental validation. Appl Energy 2019;247:127–39. https://doi.org/10.1016/j.apenergy.2019.04.014.
[35] Liu H, Wang C, Zhao W, Yang S, Hou X. Pyrolysis characteristics and kinetic modeling of Artemisia apiacea by thermogravimetric analysis. J Therm Anal Calorim 2018;131:1783–92. https://doi.org/10.1007/s10973-017-6599-3.
[36] Wu Z, Ma C, Jiang Z, Luo Z. Structure evolution and gasification characteristic analysis on co-pyrolysis char from lignocellulosic biomass and two ranks of coal: effect of wheat straw. Fuel 2019;239:180–90. https://doi.org/10.1016/j.fuel.2018.11.015.
[37] Wang S, Dai G, Yang H, Luo Z. Lignocellulosic biomass pyrolysis mechanism: a state-of-the-art review. Prog Energy Combust Sci 2017;62:33–86. https://doi.org/10.1016/j.pecs.2017.05.004.
[38] Mishra RK, Mohanty K, Wang X. Pyrolysis kinetic behavior and Py-GC–MS analysis of waste dahlia flowers into renewable fuel and value-added chemicals. Fuel 2020;260:116338. https://doi.org/10.1016/j.fuel.2019.116338.
[39] Vyazovkin S, Burnham AK, Criado JM, Pérez-Maqueda LA, Popescu C, Sbirrazzuoli N. ICTAC Kinetics Committee recommendations for performing kinetic computations on thermal analysis data. Thermochim Acta 2011;520:1–19. https://doi.org/10.1016/j.tca.2011.03.034.
[40] Yang X, Zhao Y, Li R, Wu Y, Yang M. A modified kinetic analysis method of cellulose pyrolysis based on TG–FTIR technique. Thermochim Acta 2018;665:20–7. https://doi.org/10.1016/j.tca.2018.05.008.

Paper B

Application of a New Statistical Model for the Description of Solid Fuel Decomposition in the Analysis of Artemisia apiacea Pyrolysis

Tianbao Gu, Torsten, Berning, and Chungen Yin

This paper has been published in the

Energies, Vol. 14(18), pp. 5789, 2021.

energies

MDPI

Article

Application of a New Statistical Model for the Description of Solid Fuel Decomposition in the Analysis of *Artemisia apiacea* Pyrolysis

Tianbao Gu, Torsten Berning and Chungen Yin *

AAU Energy, Aalborg University, DK-9220 Aalborg, Denmark; tig@et.aau.dk (T.G.); tbe@et.aau.dk (T.B.)
* Correspondence: chy@et.aau.dk

Abstract: Pyrolysis, one of the key thermochemical conversion technologies, is very promising to obtain char, oil and combustible gases from solid fuels. Kinetic modeling is a crucial method for the prediction of the solid conversion rate and analysis of the pyrolysis process. We recently developed a new statistical model for the universal description of solid fuel decomposition, which shows great potential in studying solid fuel pyrolysis. This paper demonstrates three essential applications of this new model in the analysis of *Artemisia apiacea* pyrolysis, i.e., identification of the conversion rate peak position, determination of the reaction mechanism, and evaluation of the kinetics. The results of the first application show a very good agreement with the experimental data. From the second application, the 3D diffusion-Jander reaction model is considered as the most suitable reaction mechanism for the description of Artemisia stem pyrolysis. The third application evaluates the kinetics of Artemisia stem pyrolysis. The evaluated kinetics vary with the conversion degree and heating rates, in which the activation energies and pre-exponential factors (i.e., lnA *vs.* E_a) show a linear relationship, regardless of the conversion and heating rates. Moreover, the prediction of the conversion rate using the obtained kinetics shows an excellent fit with the experimental data.

Keywords: pyrolysis; kinetic model; peak temperature; reaction mechanism; activation energy

Citation: Gu, T.; Berning, T.; Yin, C. Application of a New Statistical Model for the Description of Solid Fuel Decomposition in the Analysis of *Artemisia apiacea* Pyrolysis. *Energies* **2021**, *14*, 5789. https://doi.org/10.3390/en14185789

Academic Editors: Marek Sciazko and Wojciech Nowak

Received: 27 July 2021
Accepted: 10 September 2021
Published: 14 September 2021

1. Introduction

Biomass as the fourth largest primary energy resource shows great potential in sourcing the energy needs from renewables [1]. As reported by the International Energy Agency (IEA), bioenergy has the potential to provide 10% of the primary energy supply to the world by 2035, and biofuel will be capable to covering 27% of transportation fuel consumption by 2050 [2]. Thermochemical conversion technologies, as the key method to convert bioresources to energy and renewable products, have drawn more and more attention over the past decades [3,4]. Among thermochemical conversion technologies (i.e., pyrolysis, gasification, combustion, etc.), pyrolysis, which is not only a significant stage of combustion and gasification but also an independent key thermal conversion technology, presents great potential to produce high-quality renewable fuels [5,6].

The solid fuel pyrolysis process is the decomposition of the organics inside solids in the absence of oxygen. The solid conversion rate and products are of most interest for research studies and industry applications [7]. Kinetic modeling is regarded as a useful tool for the prediction of the solid conversion rate and even the species evolution [8]. In previous studies, typical kinetic models are always based on the Arrhenius theory, in which the conversion rate can be calculated by the kinetic constant, times the reaction model function [9]. To predict the solid conversion rate, evaluation of the kinetic parameters i.e., the pre-exponential factor, temperature order and activation energy, has been the focus in the previous studies, such as the model-fitting method and the model-free (isoconversional) method [10]. The model-fitting method, e.g., Coats–Redfern (CR) method, needs to assume the reaction model in advance, then the global kinetic parameters can be estimated by

fitting the thermogravimetric analysis (TGA) experimental data [11,12]. While the global kinetics from the model-fitting method are simple and convenient, it normally cannot output accurate predictions for more complex materials. In addition, the kinetics are over-reliant on the reaction model assumption, which limits its application. On the contrary, the model-free methods, e.g., Kissinger–Akahria–Sunose (KAS), Flynn–Wall–Ozawa (FWO), and the Friedman method, do not need to assume the reaction model, and the kinetics can be evaluated for a given conversion degree [13]. It requires a series of TGA data obtained under at least three different heating rates [14]. The activation energies evaluated from this method, regardless of the reaction model, are considered more reliable [15]. While the calculation of the pre-exponential factor is dependent on the selected reaction model.

Besides the typical kinetic models for the evaluation of kinetics, some studies have aimed at investigating reaction models. Gai et al. summarized commonly used reaction models for the description of the pyrolysis of solids [16]. Five groups of reaction models are classified, i.e., reaction order, Mampel power law, nucleation, contracting geometry and diffusion. In addition, Criado proposed an analytical way named the 'master plot' for the determination of the reaction mechanism from commonly used reaction models for solid pyrolysis [17]. Identification of the proper reaction model, other than from experience, is a big step, while the strength of the universal description with the kinetics needs to be further investigated. In this regard, a new model based on the generalized extreme value (GEV) distribution for first-order reactions has been reported by Li et al. [18]; it found that first-order pyrolysis processes could be modeled universally. It also illustrated the strength of the universal model for the solid conversion rate, which points to a new perspective for investigation of the kinetic model. Inspired by the work of Li et al., a universal model for the description of solid fuel pyrolysis for all the feasible reaction models was proposed in our previous study [19]. Experimental validations and comparisons to the typical kinetic model have followed. The properties of the universal model show great potential in understanding and analyzing the solid fuel pyrolysis process. Further applications and development of the universal model need to be carried out to enrich this new aspect.

In this study, the new statistical model that we recently developed to describe the pyrolysis of solids in a universal way is manifested briefly for the readability of this paper. Then three essential applications based on the model are applied in Artemisia stem pyrolysis, i.e., identification of the conversion rate peak position, determination of the reaction model and evaluation of the kinetics. The prediction results show a good agreement with the experimental data, the proposed methods also stand out by their simplicity and applicability. At last, the kinetic analysis of Artemisia stem pyrolysis was investigated for studying the characteristics of this vital wormwood biomass in Asia. The kinetic compensation effect (KCE) was analyzed as well. It shows that the activation energy of the Artemisia stem varies a lot along the conversion, and it is influenced by the heating rate as well.

2. Methods and Materials

To facilitate the understanding of this paper, both the new model for the description of solid fuel pyrolysis and the related TGA experiments of the Artemisia stem are briefly presented in this section. The experimental data obtained will be used for validation and applications of the presented model. More details can be found in the relevant references, e.g., the detailed derivation of the new model in our previous study [19].

2.1. The Model Description

For solid fuel pyrolysis, the Arrhenius theory is commonly used for the conversion process. The typical conversion rate of solid decomposition can be described as Equation (1) [20].

$$\frac{d\alpha}{dt} = k(T)f(\alpha) \tag{1}$$

where $k(T)$ is the kinetic constant, which is a function of the reaction temperature T; $f(\alpha)$ denotes the reaction model.

For nonisothermal experiments of a constant heating rate $\beta \equiv dT/dt$, the conversion rate can be expressed with respect to the temperature T as shown in Equation (2) [21].

$$\frac{d\alpha}{dT} = \frac{A}{\beta} exp\left(-\frac{E_a}{RT}\right) f(\alpha) \tag{2}$$

where A and E_a are the pre-exponential factor and activation energy, respectively. The conversion α is determined as the current mass loss over the final mass loss

$$\alpha = \frac{m_0 - m}{m_0 - m_\infty} \tag{3}$$

where m_0, m and m_∞ denote the initial solid mass (at $t = 0$), solid mass (at $t = t$) and the final solid mass (at $t = t_\infty$).

By integrating Equation (1) and setting $u \equiv E_a/(RT)$, the integration form of the conversion rate can be expressed as below [22].

$$g(\alpha) \equiv \int_0^\alpha \frac{d\alpha}{f(\alpha)} = \int_0^t k(T)dt = \frac{A}{\beta}\int_{T_0}^T \exp\left(-\frac{E_a}{RT}\right)dT = \frac{AE_a}{\beta R}p(u) \tag{4}$$

where $g(\alpha)$ is a dimensionless variable. The temperature integral $p(u) \equiv \int_u^\infty \frac{e^{-u}}{u^2}du$ does not have an analytical solution. Differentiating Equation (4), the new formulation can be obtained.

$$\frac{dg(\alpha)}{d\alpha} = \frac{1}{f(\alpha)} \tag{5}$$

For the reactions in which $g(\alpha) \neq 0$, we can derive Equation (6) from Equation (5).

$$\frac{dg(\alpha)}{d\alpha}\frac{1}{g(\alpha)} = \frac{d\ln g(\alpha)}{d\alpha} = \frac{1}{f(\alpha)}\frac{1}{g(\alpha)} \tag{6}$$

If we set a new variable named the reaction progress indicator $\theta \equiv \ln g(\alpha)$, then we can have [23].

$$\frac{d\alpha}{d\theta} = f(\alpha)\cdot g(\alpha) = f(\alpha)\cdot\int_0^\alpha \frac{d\alpha}{f(\alpha)} \tag{7}$$

For first-order reactions $f(\alpha) = 1 - \alpha$, the θ based conversion rate can be written fully explicitly with respect to θ.

$$\frac{d\alpha}{d\theta} = \exp(\theta)\cdot\exp(-\exp(\theta)) \tag{8}$$

Equation (8) is the universal expression we recently developed for the solid fuel pyrolysis of the first-order reaction model [19]. It is precisely consistent with the standardized generalized extreme value (GEV) distribution. More details about the $\theta-$based statistical kinetic model can be found in [19], e.g., the detailed derivation and plots. The expression of the new model is certain for a given reaction mechanism regardless of the kinetics and materials.

2.2. Experiments and Materials

The experimental data come from [24], in which the Artemisia stem samples with an average diameter less than 0.2 mm were analyzed through a Netzsch STA449F3 thermal analyzer under a pure nitrogen atmosphere. The samples for each TGA test were dried at 353 K for about 24 h in advance, and heated from 300 to 1000 K under the heating rates of 10, 20, 30, 40 and 50 K/min, respectively. The sample powder was held in an alumina cup during the test run.

3. Applications of the Developed Model to Artemisia Stem Pyrolysis

In this section, three applications of the new model, namely, identification of the conversion peak position, determination of the reaction mechanism, and evaluation of the kinetics, are demonstrated for Artemisia stem pyrolysis. The kinetic analysis of Artemisia pyrolysis is also carried out. The detailed description and results for each application are presented below.

3.1. Identification of the Conversion Rate Peak Position

As illustrated in Section 2, for a given reaction mechanism $f(\alpha)$, the peak of the conversion rate always occurs at a fixed reaction progress indicator θ_p. All the details of the most common pyrolysis mechanisms can be seen in Table 1 in our previous work [19]. Based on this characteristic, the peak position of the solid conversion rate can be easily obtained if the reaction mechanism is certain. Reference [24] concludes that the F1, F2, F3 and D3 reaction mechanisms are suitable for the description of Artemisia stem pyrolysis, in which $\theta_p \equiv 0$ for F1, F2, F3 and $\theta_p \equiv -2\ln 3$ for D3. The four reaction mechanisms are used for prediction of the conversion rate peak position by its characteristics.

Table 1. The model-predicted vs. experimentally determined temperature (in units of K) at the peak conversion rate during pyrolysis of Artemisia stem under different heat rates.

Heating Rate (K/min)	10	20	30	40	50
Exp.	581.8	589.5	596.2	609.3	609.9
F1 Pred.	582.9	591.6	597.6	606.8	610.5
F2 Pred.	573.0	581.1	587.2	596.6	599.7
F3 Pred.	565.9	573.5	579.6	590.1	595.3
D3 Pred.	588.0	597.2	603.5	613.2	615.7

Figure 1 plots the conversion progress indicator θ against the temperature of Artemisia stem pyrolysis under different heating rates. The identification of the conversion rate peak position with the assumption of F1, F2 and F3 reaction models is shown in Figure 1a, and the counterpart, using D3 as the reaction model, is shown in Figure 1b. The peak temperature of the conversion rate for each experiment can be estimated by the intersection of the curve and $\theta \equiv 0$ in Figure 1a or $\theta \equiv -2\ln 3$ in Figure 1b. The predicted results of the temperature at the peak conversion rate are listed in Table 1. Among the different reaction mechanisms, the predicted peak temperatures using the D3 reaction model are higher than those using the reaction order models. Compared to the experimental data, the predicted results based on the F1 reaction model show the best agreement with the experimental data. This conclusion illustrates that the F1 reaction mechanism is more suitable for the kinetic description around the conversion rate peak position than the others, whereas one cannot broadly conclude that it is more suitable during the overall pyrolysis process. Further work for the determination of the reaction mode for the whole pyrolysis process needs to be carried out.

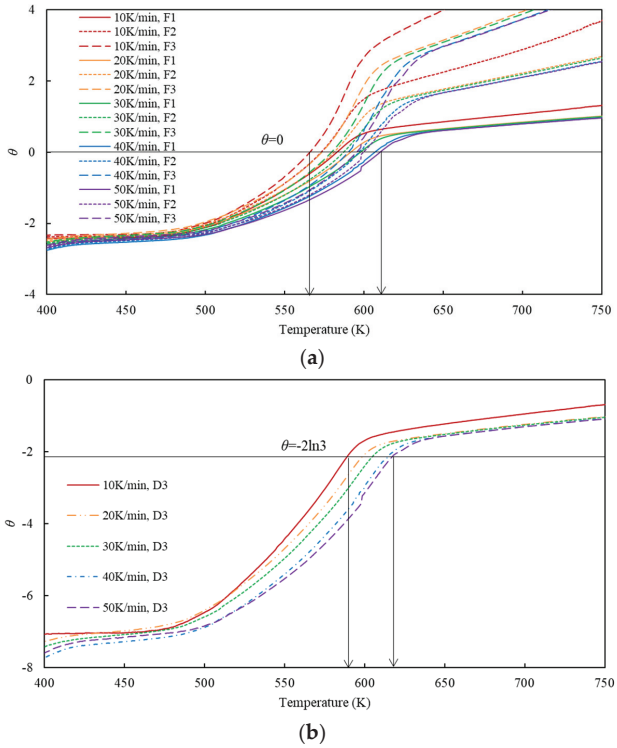

Figure 1. Identification of the conversion rate peak position based on the proposed method for the F1, F2 and F3 reaction model (**a**) and the D3 reaction model (**b**).

3.2. Determination of the Reaction Mechanism

The $\theta-$based conversion rate, on the other hand, can be expressed in Equation (9) [25],

$$\frac{d\alpha}{d\theta} = \frac{\frac{d\alpha}{dt}}{A} e^{u} \cdot \frac{AE_a}{\beta R} p(u) = \frac{d\alpha}{dT} \frac{E_a}{R} e^{u} p(u) \tag{9}$$

which shows the relation of the $\theta-$based conversion rate $d\alpha/d\theta$ with the temperature-based rate $d\alpha/dT$. To simplify Equation (9), the approximation equation of the temperature integral $p(u) = e^{-u}/u^2$ (where $u \equiv E_a/RT$), which was used in the KAS method [26], was applied in Equation (9). Another expression of the new model was formed in Equation (10) [19].

$$\frac{d\alpha}{d\theta} = \frac{d\alpha}{dT} \frac{RT^2}{E_a} \tag{10}$$

On the right-hand side of Equation (10), $d\alpha/dT$ can be obtained from the TGA data for each experiment with a fixed heating rate β, and E_a can be evaluated from model-free methods without the assumption of a reaction model.

The values of $d\alpha/d\theta$ can be determined from experimental data using Equation (10). The $d\alpha/d\theta$ can also be calculated by the universal expressions of the most common mechanisms of solid fuel pyrolysis, as derived and summarized in Table 1 in [19]. By comparing them as shown in Equation (11), the reaction model or mechanism best suited for the description of Artemisia stem pyrolysis may be determined.

$$Error^2 = \left[\left(\frac{d\alpha}{d\theta}\right)_{Uni} - \frac{d\alpha}{dT}\frac{RT^2}{E_a}\right]^2 \quad (11)$$

The smaller the $Error^2$ is, the closer the reaction model will be to the certain standard generalized model. This step is similar to the determination of reaction mechanisms by the 'master plot' [27]. However, using the approximation equation makes the expression simpler and more applicable than the 'master plot'.

Figure 2 shows the results of the difference in $d\alpha/d\theta$ calculated by the two methods as presented in Equation (11) for the conversion range of 0.1–0.8. Here it needs to be mentioned that the activation energies used in the calculation are from [24], evaluated by the KAS method based on the experimental data, since there is no assumption of the reaction model for the evaluation of the activation energies. Figure 2a plots the differences for all the common reaction mechanisms. The zoom-in of the seven plots at the bottom (F1, F2, F3, D1, D3, R2, R3), are considered better suited to describe Artemisia stem pyrolysis, as shown in Figure 2b.

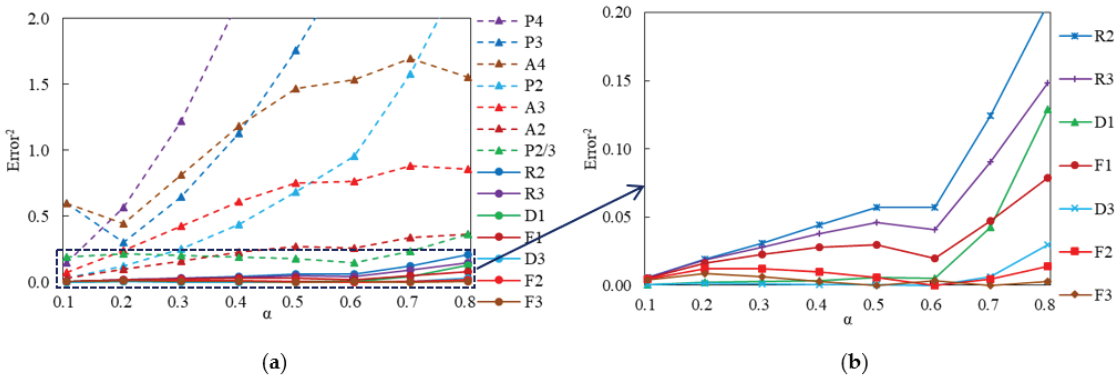

Figure 2. Difference in the $d\alpha/d\theta$ between the calculation of different potential reaction models (cf. Table 1 in [19] for details) and the experimental results, as calculated by Equation (11): (**a**) the plots for all the common reaction models (**b**) the zoom-in of the seven plots at the bottom.

To figure out the order of agreement of the seven reaction models with the experimental results, the relative error (RE) for the i^{th} reaction model (i = F1, F2, F3, D1, D3, R2, R3) at each conversion is defined as Equation (12).

$$RE_i = \left(Error^2\right)_i / \sum\left(Error^2\right)_i \times 100\% \quad (12)$$

From the comparison in Figure 3, we conclude that among all the reaction mechanisms, D3 and F3 are the two best reaction models to describe the Artemisia stem pyrolysis process with a total RE of 13.9 and 38.0, respectively, followed by D1, F2, F1, R3, and R2. This application shows that the new model can reliably and easily determine the feasible reaction mechanism in a relatively theoretical way for the pyrolysis of solids.

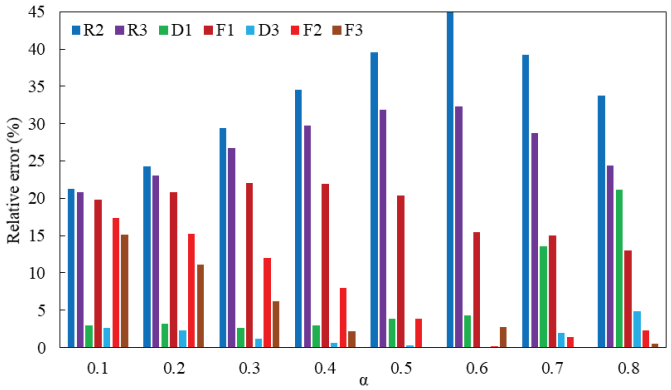

Figure 3. The relative error of the seven reaction models (F1, F2, F3, D1, D3, R2, R3).

3.3. Evaluation of the Kinetics

If the reaction mechanism is known for a pyrolysis process, one can reform Equation (10) to separate the activation energy, then the kinetics can be obtained via Equation (13). This shows another aspect of the model application. It is worth mentioning, Equations (10) and (13) are the same expression but in a different form. The former is used only if E_a is evaluated in advance by other methods, e.g., KAS, while the latter is used only if the reaction mechanism is determined in advance.

$$E_a = \frac{d\alpha}{dT}\frac{d\theta}{d\alpha}RT^2 \tag{13}$$

Using the approximation equation $p(u) = e^{-u}/u^2$ (where $u \equiv E_a/RT$), the pre-exponential factor can be calculated by reformulating $\theta \equiv \ln g(\alpha) = \ln \frac{AE_a}{\beta R} + \ln p(u)$ into Equation (14).

$$\ln A = \theta + \frac{E_a}{RT} + 2\ln\frac{E_a}{RT} + \ln\frac{\beta R}{E_a} \tag{14}$$

This method for evaluation of the kinetics was validated in our previous work [19].

The reaction model D3 was selected for the evaluation of the kinetic data, since it is the best reaction model for Artemisia stem pyrolysis as described in Section 3.2. The activation energies (E_a) and the pre-exponential factor (A) were evaluated by the new model with 0.05 as the conversion step. Figure 4 shows the evaluated activation energy distributions along the conversion for Artemisia stem pyrolysis under different heating rates, while Figure 5 plots the relationship of A and E_a. The evaluated kinetics vary with conversion degree and heating rates, because we assume the kinetics are dependent on conversion and heating rates in this method. From the results, a number of observations can be made. First, the activation energies vary a lot during the conversion: the minimum is 4 kJ/mol and the maximum is 295 kJ/mol. The values of the activation energies increase first and then decrease along the conversion degree. The peak value of the activation energy occurs around the conversion of 0.65. Second, the activation energies are different for the pyrolysis under different heating rates even at the same conversion. The difference is about 30 kJ/mol for the experiments with a heating value from 10 K/min to 50 K/min. This result is different from the typical isoconversional methods, which assume the activation energy is independent of the heating rate. Comparatively, the heating rate does not affect the activation energies as much as the conversion does. Third, in Figure 5, the lnA and E_a show a linear relationship, as the kinetic compensation effect (KCE) is expressed as $lnA = aE_a + b$ for the mutual dependence of the Arrhenius parameters caused by the properties of the general kinetic equation, i.e., the reaction temperature interval, conversion, reaction model and the isokinetic hypothesis [28]. The KCE plot shows the strength of the kinetic parameters regardless of the heating rate, which can be used to improve the

accuracy and stability of the kinetic analysis for solid fuel pyrolysis [29]. According to the fitting result, in this study the coefficient a = 0.2113, b = −7.8937 with the R^2 = 0.9928. The high R^2 value indicates the isokinetic hypothesis used in the evaluation of the kinetics for the D3 model is considered acceptable.

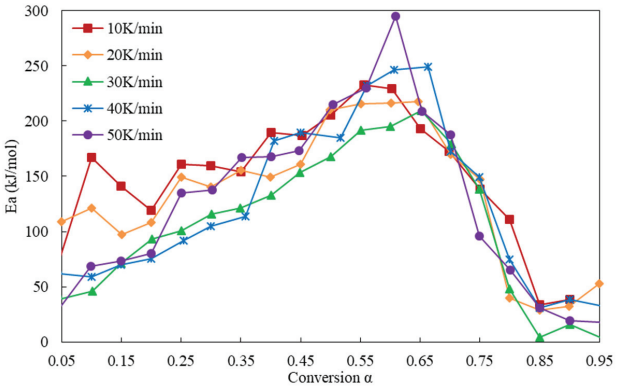

Figure 4. The activation energies E_a evaluated by the new model during Artemisia stem pyrolysis conversion α.

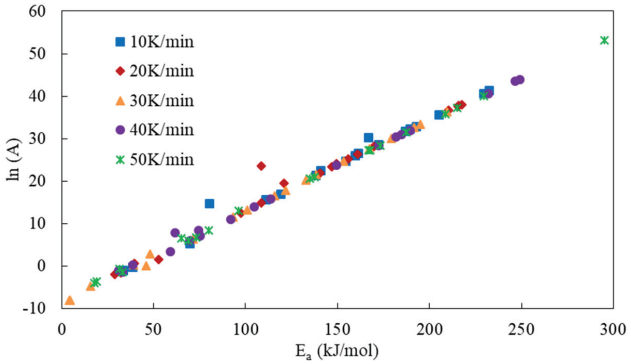

Figure 5. The relationship of the evaluated E_a and A.

To demonstrate the reliability of the evaluated kinetics from this model, Figure 6 compares the experimental data of Artemisia stem pyrolysis under different heating rates and the calculated conversion rates using the evaluated kinetics in Figures 4 and 5. D3 was chosen as the reaction model for the calculation of the solid conversion rate by Equation (2). The following conclusions are drawn from the comparison. First, the prediction results show good agreement with the experimental data. That illustrates the reliability and applicability of the evaluated kinetics from the model. Second, the calculated conversion rates fit the experimental data of 30 K/min best. That is probably due to the less noisy experimental data compared to the experiments under other heating rates. The accuracy of the kinetic model is sensitive to the quality of the experimental data. Third, the prediction error at the initial and ending stages are larger than those at the stable conversion stage. The greatest error may come from (1) the largest experimental error; (2) the complexity of the reaction model at the initial and ending stages. A smaller conversion step and multiple reaction models are recommended for calculation of the conversion rate at the beginning and ending stages of the pyrolysis.

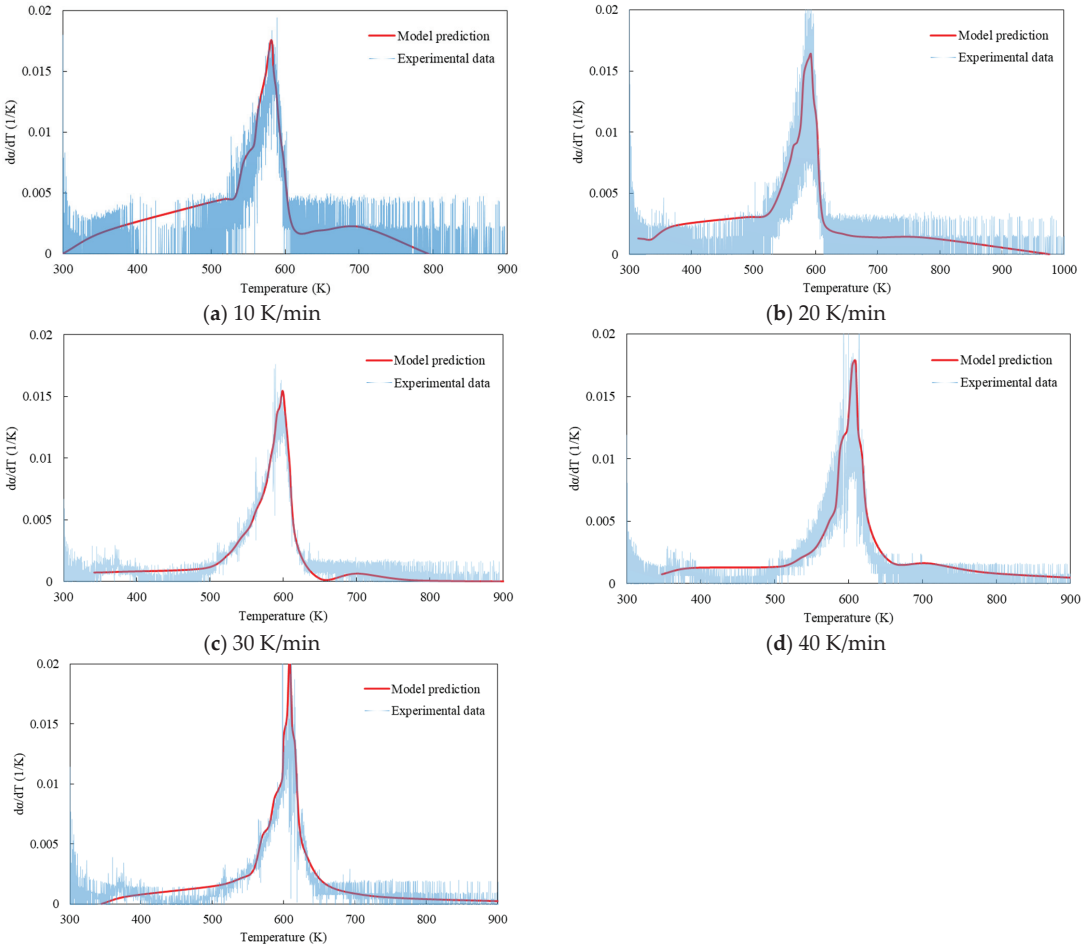

Figure 6. Comparison of the predicted conversion rate using the evaluated kinetics by the new model and the experimental data of Artemisia stem pyrolysis under different heating rates (**a**) 10 K/min, (**b**) 20 K/min, (**c**) 30 K/min, (**d**) 40 K/min and (**e**) 50 K/min.

To sum up, the activation energies of Artemisia stem pyrolysis vary a lot along the conversion and are lightly influenced by the heating rate. The evaluated kinetics are consistent with KCE expression. The kinetics evaluated by this model are reliable for predicting the solid conversion rate during the pyrolysis process. A smaller conversion step and a reasonable reaction mechanism are recommended for the kinetic analysis at the initial and ending stages of solid fuel pyrolysis.

4. Conclusions

In this paper, extended works based on a new statistical model for the description of solid fuel pyrolysis have been successfully carried out for the kinetic analysis of Artemisia stem pyrolysis. Three applications based on the new model are demonstrated: identification of the conversion rate position, determination of the reaction mechanism, and evaluation of the activation energies. Based on the assumed first-order reaction model, the identified conversion peak temperature showed a negligible difference compared to the

experimental data. The results of the determination of the reaction mechanism show the 3D diffusion-Jander reaction model fits Artemisia stem pyrolysis best. At last, the kinetics of Artemisia stem pyrolysis are proven to change with the conversion and heating rates. The kinetic compensation effect is shown in the evaluated kinetics as well. The evaluated kinetics are reliable to apply in the prediction of the solid conversion rate compared to experimental data.

Author Contributions: Conceptualization, T.G. and C.Y.; modeling, T.G.; writing—original draft preparation, T.G.; writing—review and editing, C.Y. and T.B.; supervision, C.Y. and T.B. All authors have read and agreed to the published version of the manuscript.

Funding: This research is partly supported by external funding from Innovation Fund Denmark (0143-00015B) and internal funding from AAU Energy.

Institutional Review Board Statement: Not applicable.

Informed Consent Statement: Not applicable.

Data Availability Statement: Not applicable.

Acknowledgments: Tianbao Gu would like to acknowledge the China Scholarship Council and AAU Energy for supporting his PhD study in Aalborg University. The authors are grateful to Changjian Wang with the School of Civil Engineering, Hefei University of Technology, Hefei, China, for sharing the original experimental data.

Conflicts of Interest: The authors declare no conflict of interest.

References

1. Demirbas, M.F.; Balat, M.; Balat, H. Potential Contribution of Biomass to the Sustainable Snergy Development. *Energy Conv. Manag.* **2009**, *50*, 1746–1760. [CrossRef]
2. Wang, S.; Dai, G.; Yang, H.; Luo, Z. Lignocellulosic Biomass Pyrolysis Mechanism: A State-of-the-Art Review. *Prog. Energy Combust. Sci.* **2017**, *62*, 33–86. [CrossRef]
3. Bridgwater, A.V. Renewable Fuels and Chemicals by Thermal Processing of Biomass. *Chem. Eng. J.* **2003**, *91*, 87–102. [CrossRef]
4. Chen, T.; Ku, X.; Lin, J.; Ström, H. CFD-DEM Simulation of Biomass Pyrolysis in Fluidized-Bed Reactor with a Multistep Kinetic Scheme. *Energies* **2020**, *13*, 5358. [CrossRef]
5. Nzihou, A.; Stanmore, B.; Lyczko, N.; Minh, D.P. The Catalytic Effect of Inherent and Adsorbed Metals on the Fast/Flash Pyrolysis of Biomass: A Review. *Energy* **2019**, *170*, 326–337. [CrossRef]
6. Khiari, B.; Jeguirim, M. Pyrolysis of Grape Marc from Tunisian Wine Industry: Feedstock Characterization, Thermal Degradation and Kinetic Analysis. *Energies* **2018**, *11*, 730. [CrossRef]
7. Zhang, H.; Wang, Y.; Shao, S.; Xiao, R. An Experimental and Kinetic Modeling Study Including Coke Formation For Catalytic Pyrolysis of Furfural. *Combust. Flame* **2016**, *173*, 258–265. [CrossRef]
8. Burra, K.R.G.; Gupta, A.K. Modeling of Biomass Pyrolysis Kinetics Using Sequential Multi-Step Reaction Model. *Fuel* **2019**, *237*, 1057–1067. [CrossRef]
9. Richter, F.; Atreya, A.; Kotsovinos, P.; Rein, G. The Effect of Chemical Composition on the Charring of Wood Across Scales. *Proc. Combust. Inst.* **2019**, *37*, 4053–4061. [CrossRef]
10. Li, M.; Jiang, L.; He, J.; Sun, J. Kinetic Triplet Determination and Modified Mechanism Function Construction for Thermo-Oxidative Degradation of Waste Polyurethane Foam Using Conventional Methods and Distributed Activation Energy Model Method. *Energy* **2019**, *175*, 1–13. [CrossRef]
11. Wu, Z.; Ma, C.; Jiang, Z.; Luo, Z. Structure Evolution and Gasification Characteristic Analysis on Co-pyrolysis Char from Lignocellulosic Biomass and Two Ranks of Coal: Effect Of Wheat Straw. *Fuel* **2019**, *239*, 180–190. [CrossRef]
12. Han, Z.; Li, J.; Gu, T.; Yan, B.; Chen, G. The Synergistic Effects of Polyvinyl Chloride and Biomass During Combustible Solid Waste Pyrolysis: Experimental Investigation and Modeling. *Energy. Conv. Manag.* **2020**, *222*, 113237. [CrossRef]
13. Noszczyk, T.; Dyjakon, A.; Koziel, J.A. Kinetic Parameters of Nut Shells Pyrolysis. *Energies* **2021**, *14*, 682. [CrossRef]
14. Meng, F.; Zhou, Y.; Liu, J.; Wu, J.; Wang, G.; Li, R.; Zhang, Y. Thermal Decomposition Behaviors and Kinetics of Carrageenan-Poly Vinyl Alcohol Bio-Composite Film. *Carbohydr. Polym.* **2018**, *201*, 96–104. [CrossRef]
15. Vyazovkin, S.; Burnham, A.K.; Criado, J.M.; Pérez-Maqueda, L.A.; Popescu, C.; Sbirrazzuoli, N. ICTAC Kinetics Committee Recommendations for Performing Kinetic Computations on Thermal Analysis Data. *Thermochim. Acta* **2011**, *520*, 1–19. [CrossRef]
16. Gai, C.; Zhang, Y.; Chen, W.; Zhang, P.; Dong, Y. Thermogravimetric and Kinetic Analysis of Thermal Decomposition Characteristics of Low-Lipid Microalgae. *Bioresour. Technol.* **2013**, *150*, 139–148. [CrossRef]
17. Criado, J.M. Kinetic Analysis of DTG Data from Master Curves. *Thermochim. Acta* **1978**, *24*, 186–189. [CrossRef]

18. Li, X.; Grace, J.R.; Bi, X.; Campbell, J.S. A New Pyrolysis Model Based on Generalized Extreme Value (GEV) Distributions and its Application to Lignocellulosic Biomass. *Fuel* **2016**, *184*, 211–221. [CrossRef]
19. Gu, T.; Fu, Z.; Berning, T.; Li, X.; Yin, C. A simplified kinetic model based on a universal description for solid fuels pyrolysis: Theoretical Derivation, Experimental Validation, and Application Demonstration. *Energy* **2021**, *225*, 120133. [CrossRef]
20. Kim, G.; Lee, D.; Jeon, C. Fundamental Characteristics and Kinetic Analysis of Lignocellulosic Woody and Herbaceous Biomass Fuels. *Energies* **2019**, *12*, 1008. [CrossRef]
21. Ali, I.; Naqvi, S.R.; Bahadar, A. Kinetic Analysis of Botryococcus Braunii Pyrolysis Using Model-Free and Model Fitting methods. *Fuel* **2018**, *214*, 369–380. [CrossRef]
22. Chong, C.T.; Mong, G.R.; Ng, J.; Chong, W.W.F.; Ani, F.N.; Lam, S.S.; Ong, H.C. Pyrolysis characteristics and kinetic studies of Horse Manure Using Thermogravimetric Analysis. *Energy. Conv. Manag.* **2019**, *180*, 1260–1267. [CrossRef]
23. Málek, J. The Kinetic Analysis of Non-Isothermal Data. *Thermochim. Acta* **1992**, *200*, 257–269. [CrossRef]
24. Liu, H.; Wang, C.; Zhao, W.; Yang, S.; Hou, X. Pyrolysis Characteristics and Kinetic Modeling of Artemisia Apiacea by Thermogravimetric Analysis. *J. Anal. Calorim.* **2018**, *131*, 1783–1792. [CrossRef]
25. Mianowski, A.; Baraniec, I. Three-Parametric Equation in Evaluation of Thermal Dissociation of Reference Compound. *J. Therm. Anal. Calorim.* **2009**, *96*, 179–187. [CrossRef]
26. Vo, T.K.; Ly, H.V.; Lee, O.K.; Lee, E.Y.; Kim, C.H.; Seo, J.; Kim, J.; Kim, S. Pyrolysis Characteristics and Kinetics of Microalgal Aurantiochytrium Sp. KRS101. *Energy* **2017**, *118*, 369–376. [CrossRef]
27. Criado, J.M.; Málek, J.; Ortega, A. Applicability of the Master Plots in Kinetic Analysis of Non-Isothermal Data. *Thermochim. Acta* **1989**, *147*, 377–385. [CrossRef]
28. Koga, N. A Review of the Mutual Dependence of Arrhenius Parameters Evaluated by the Thermoanalytical Study of Solid-State Reactions: The Kinetic Compensation Effect. *Thermochim. Acta* **1994**, *244*, 1–20. [CrossRef]
29. Zhu, H.; Liu, N. Kinetic analysis based on the kinetic compensation effect and optimization calculation. *Thermochim. Acta* **2020**, *690*, 178686. [CrossRef]

Chapter 3. Advanced Simulation of MSW Combustion

Chapter 3 elaborates on the methodology for the advanced simulation of a moving grate boiler combusting 750 tons of MSW per day. The modeling strategy, bed model description, freeboard simulation, and reliability tests are illustrated. Subsequently, two numerical investigations on the targeted boiler are carried out to accommodate feedstock diversity, resulting in two papers, Papers C and D. In Paper C, the impacts of incinerating the new MSW due to waste classification are revealed, and corresponding actions in terms of air supply and thermal input are proposed and conducted. In Paper D, co-firing MSW with sewage sludge and industrial solid waste under different operation conditions are performed and compared, producing guidelines for the stable and clean co-combustion. The primary findings and conclusions of the two numerical investigations are presented in this chapter. More detailed results and discussions are provided in Papers C and D.

3.1. Simulation strategy

In grate-firing boilers, solid fuel is first fed into the boiler and accumulates in a porous fuel bed, where the solids undergo thermal conversion processes, that is, moisture evaporation, devolatilization, char combustion, and gasification. Consequently, the syngas released from the fuel bed flows into the freeboard, where the combustibles are burned out with a secondary air (SA) supply [72]. In this scenario, the freeboard offers radiative flux to heat the fuel bed for solid conversion; the fuel bed converts the solid fuel to combustible gases entering the freeboard, as shown in Fig. 3.1(a). Accordingly, the coupled strategy is typically used to model such a grate boiler, namely, model the fuel bed and freeboard independently, and then couple them together by the heat and mass transfer at the interaction surface, as shown in Fig. 3.1(b). In this Ph.D. thesis, a stand-alone fuel bed model for the description of the solid fuel conversion on the moving grate is developed, and a CFD simulation of the turbulent reacting flow in the freeboard is performed using ANSYS Fluent. The freeboard simulation compiles a user-defined function (UDF) containing the results from the bed model, that is, profiles of temperature, gas species, and velocity at the bed top as the inlet

[73]. The heat flux onto the fuel bed is exported from the freeboard simulation and integrated into the bed model for the next coupling iteration.

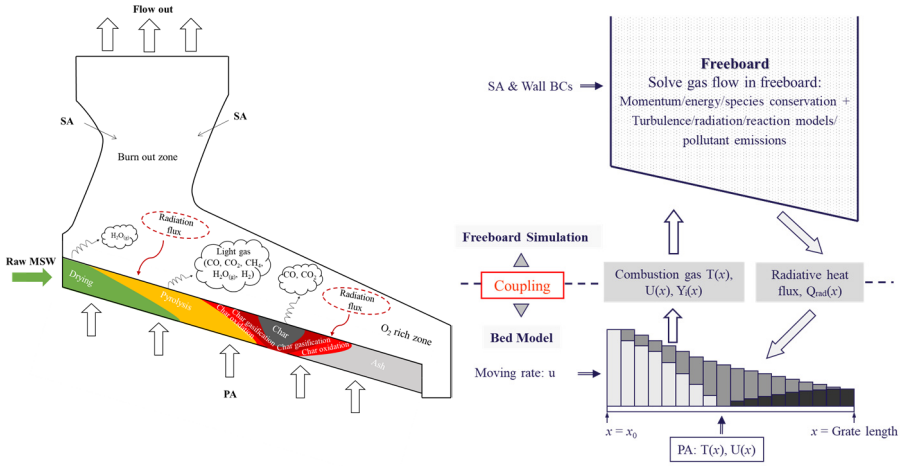

Fig. 3.1. Sketch of grate-firing MSW (a) and modeling strategy (b) [74].

3.2. Modeling of the fuel bed

The modeling of fuel bed on moving grate is based on an in-house bed model, namely BASIC (Bulk Accumulated Solids Incineration Code), which is established on a fixed-bed combustor, as presented in [58]. The detailed model description, discretisation, and validation of the original fixed-bed model are given in [58]. In this study, the transformation of the model from a fixed bed to a moving grate bed was accomplished. In addition, several significant updates and extensions have been made to better describe solid fuel combustion on moving grates. The framework of the fixed-bed model, transformation process, key updates and extensions, and a summary of the latest bed model are presented in this section.

3.2.1. Framework of the fixed bed model

The in-house fixed-bed model is a one-dimensional (1D) transient model, in which the fuel bed is treated as a porous zone with initially uniform porosity, as shown in Fig. 3.2(a). The in-house bed model describes the solid-to-gas conversion processes, that is, drying, devolatilization, and char oxidation, under the framework of heat and mass transfer in the dense fuel bed. The primary concerns in bed modeling are the phase-to-phase conversion, heat

production and transfer, elemental balance, and superficial fluid flow. The transport equations for both the solid and gas phases are developed based on the Euler-Euler approach, that is, the two phases are treated as continuous. The major assumptions of the bed model are as follows.

1) The packed fuel bed is assumed to be a porous zone with an initially uniform porosity [75].
2) The solid particles are assumed to be thermally thin owing to their small Biot number in average [47].
3) The solid and gas phases were assumed to be in thermal equilibrium, and only one comprehensive energy equation was solved [76, 77].
4) The solid moving velocity caused by particle shrinking was neglected to simplify the solid transport equation [78].
5) The gases released from devolatilization consist of five species: CO, CO_2, H_2, CH_4 and $H_2O_{(g)}$, the coefficients of which are calculated based on the elements and energy balances of the solid fuel [79].
6) The properties of the gases included in the model, namely N_2, O_2, CO, CO_2, H_2, CH_4, $H_2O_{(g)}$, NH_3, NO, H_2S, and SO_2, follow the ideal gas law.

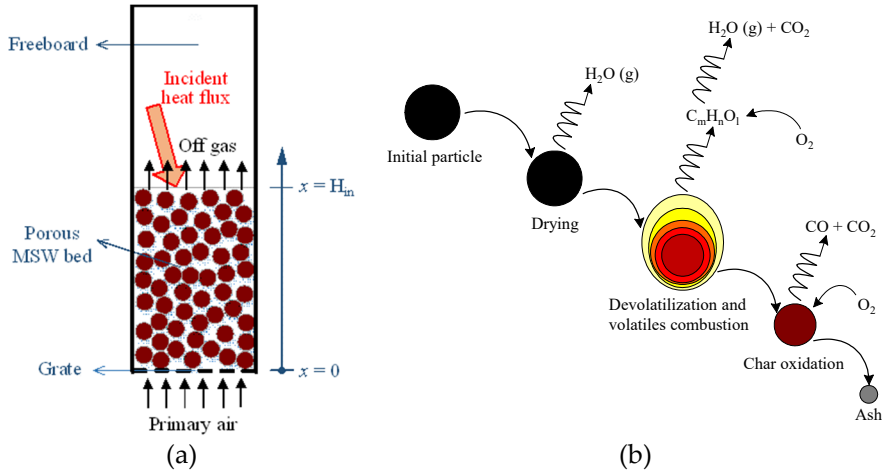

Fig. 3.2. Schematic of the fixed fuel bed (a) and undergo processes of solids combustion in the bed (b) [58].

3.2.2. Transformation of the model from fixed bed to moving-grate bed

For dense fuel bed combustion, including fixed bed and moving-grate bed, the combustion mechanisms are the same. As presented in Fig. 3.3, the combustion metrics of the fuel bed slice at x-meter of the moving grate are

consistent with those of fixed bed at combustion time t ($x = x_0 + ut$). The combustion characteristics on the moving grate along the length from $x = x_0$ to $x = L$ one-to-one correspond to those on the fixed bed from $t = t_0$ to $t = t_{end}$ [80]. Accordingly, the two-dimensional (2D) steady moving-grate bed model can be mapped from the 1D transient fixed-bed model. For the boiler under study, the residence time of the fuel on the grate is 5400 s. Hence, the fuel bed on the moving grate is divided into 540 slices along the grate length, and the calculation results from the transient bed model are recorded every 10 s to map each set of results to the corresponding fuel bed slice on the moving grate.

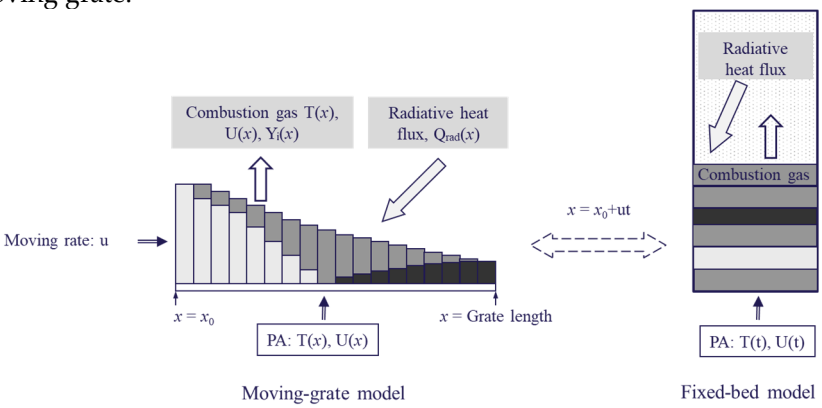

Fig. 3.3. The model transformation from fixed bed to moving-grate bed [74].

3.2.3. Key updates and extensions of the bed model

3.2.3.1 NO_x formation modeling in the fuel bed

It is necessary to investigate NO_x pollutant emissions for high-nitrogen content solid fuels, such as sewage sludge; therefore, in this study, the bed model is extended to include NO_x formation [81]. Owing to the relatively low temperature during solid fuel bed combustion, thermal NO_x is not considered, only fuel NO_x formation is included in the bed model [82]. Since NO accounts for 95% of the total NO_x pollutants, it is assumed to be the only species of NO_x to represent NO_x pollutants [83].

In solid fuel combustion, fuel-N is typically divided into volatile-N and char-N, with an approximate ratio of 80/20 to 30/70 in biomass. A ratio of 75/25 is used in this study [84]. Volatile-N, which is released as almost 90% NH_3 and 10% HCN, is assumed to be 100% converted into NH_3 in the bed model [85]. Meanwhile, char-N is considered to be completely oxidised to NO during char

burning, and char also acts as a reducing agent to reduce NO [86]. The formation scheme of fuel NO_x in the bed model is shown in Fig. 3.4. The corresponding chemical kinetics are listed in Table 3.3.

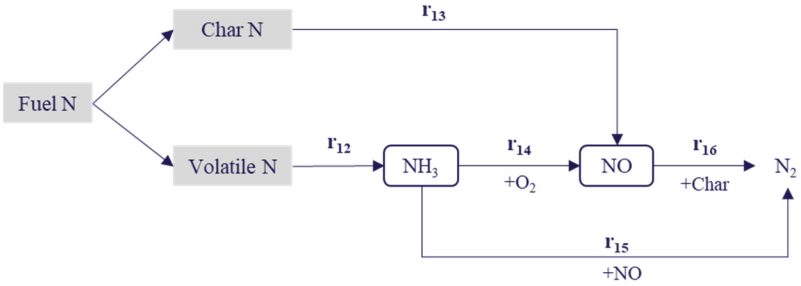

Fig. 3.4. Fuel NO_x formation scheme used in the bed model [87].

3.2.3.2 Other key updates of the bed model

To better describe solid conversion on the moving grate, several key updates were achieved in this study. For instance, a diffusion term for the description of solid mixing is added, char gasification is integrated and the air supply mode is changed from a fixed flowrate to a segmented flowrate. The key updates are presented in Table 3.1.

Table 3.1 Summary of the key updates of the bed model [74].

Term	In my previous work [58]	This study
Solid continuity equation	Update bulk solid density	Update porosity
Solid mixing	Not considered	Add a diffusion term in solid species transport equations [88]
Char reaction	$C + \alpha O_2 = 2(\alpha - 1)CO + (2\alpha - 1)CO_2$	$C + \alpha O_2 = 2(\alpha - 1)CO + (2\alpha - 1)CO_2$ $C + CO_2 = 2CO$ $C + H_2O = CO + H_2$ [89]
CO combustion rate	$r_{co} = R_1$	$r_{co} = \begin{cases} R_1, H_2O > 0 \\ R_2, H_2O = 0 \end{cases}$
Radiation flux	Fixed value	Profile reported from Fluent
Air supply	Fixed flowrate	Segmented flowrate along the grate
Inlet diffusion of species	Enabled	Disabled to keep mass balance accurately

[a] $R_1 = 2.239 \times 10^{12} \exp\left(-\frac{1.702 \times 10^5}{RT}\right) CO \cdot O_2^{0.25} \cdot H_2O^{0.5}$

[b] $R_2 = 7.05 \times 10^6 \exp\left(-\frac{9.68 \times 10^4}{RT}\right) CO$ [90]

3.2.4. Summary of the new bed model

The updates and extensions resulted in a new bed model for moving-grate fuel beds. The transport equations and boundary conditions of the gas and solid phases in the porous bed are summarized in Tables 3.2 [91].

Table 3.2 Transport equations and boundary conditions of the latest bed model [74, 87].

Gas continuity	$\frac{\partial(\phi\rho_g)}{\partial t} + \nabla\cdot(\rho_g\mathbf{u}) = S_g$
Gas species	$\frac{\partial(\phi\rho_g Y_{ig})}{\partial t} + \nabla\cdot(\rho_g\mathbf{u}Y_{ig}) = \nabla\cdot(D_{ig}\nabla(\phi\rho_g Y_{ig})) + S_{ig}$
Gas momentum	$\frac{\partial(\phi\rho_g u)}{\partial t} + \nabla\cdot(\rho_g\mathbf{u}u) = -\nabla P - \frac{\mu u}{K} - \beta\rho_g u^2$
Solid continuity/Porosity model	$\frac{\partial((1-\phi)\rho_s)}{\partial t} = -S_g$
Solid species	$\frac{\partial((1-\phi)\rho_s Y_{is})}{\partial t} = \nabla\cdot(D_s\nabla((1-\phi)\rho_s Y_{is})) + r_{is}$
Energy equation	$\frac{\partial(\phi\rho_g C_{pg}T + (1-\phi)\rho_s C_{ps}T)}{\partial t} + \nabla\cdot(\rho_g\mathbf{u}C_{pg}T) = \nabla\cdot(k_{eff}\nabla T) + S_T$
Boundary conditions at bed bottom surface	$\rho u = \rho_{in}u_{in};\ \frac{\partial P}{\partial x} = 0$ $Y_{ig} = Y_{ig,in};\ Y_{is} = Y_{is,in}$ $T = T_{in}$
Boundary conditions at bed top surface	$\frac{\partial u}{\partial x} = 0;\ P \equiv P_{atm}$ $AD_{ig}\frac{\partial Y_{ig}}{\partial x} = Ah_M(Y_{ig,\infty} - Y_{ig});\ \frac{\partial Y_{is}}{\partial x} = 0$ $k_{eff}A\frac{\partial T}{\partial x} = Ah_T(T_\infty - T_s) + A\varepsilon\sigma(T_{rad}^4 - T_s^4)$

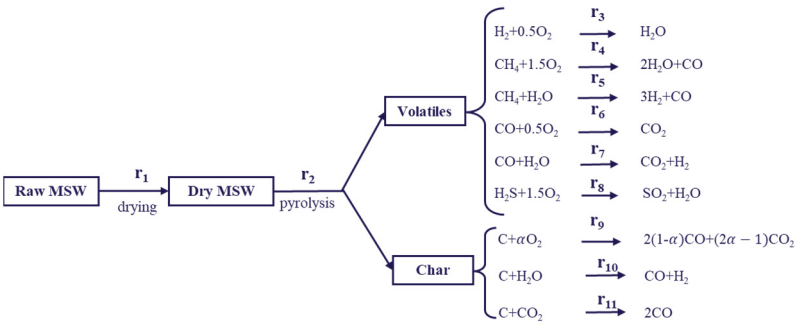

Fig. 3.5. Major reaction scheme of the latest bed model [58, 74].

Except fuel NO_x formation, the reaction scheme of major components is illustrated in Fig. 3.5. The corresponding kinetics for calculating the chemical reaction rates are listed in Table 3.3. The symbols used are listed under the nomenclature.

Table 3.3 Kinetics for the reactions used in the latest bed model [58, 74, 87].

No.	Rate expression	A (s^{-1})	b	E (J/kmol)
1	$r_1 = \begin{cases} A_s h_s\left(C_{w,s} - C_{w,g}\right) & T < 373K \\ \dfrac{A_s\left[h_T\left(T - T_{evp}\right) + \varepsilon\sigma\left(T^4 - T_{evp}^4\right)\right]}{H_{evp}} & T \geq 373K \end{cases}$	–	–	–
2	$r_2 = -\dfrac{\partial \rho_v}{\partial t} = k_2 \rho_v$	3.40×10^{4}	0	6.90×10^{7}
3	$r_3 = \dfrac{\partial C_{H_2}}{\partial t} = k_3 C_{H_2}^{0.25} C_{O_2}^{1.5}$	6.80×10^{15}	-1	1.67×10^{8}
4	$r_4 = \dfrac{\partial C_{CH_4}}{\partial t} = k_4 C_{CH_4}^{0.7} C_{O_2}^{0.8}$	5.01×10^{11}	0	2.00×10^{8}
5	$r_5 = \dfrac{\partial C_{CH_4}}{\partial t} = k_5 C_{CH_4} C_{H_2O}$	3.00×10^{8}	0	1.26×10^{8}
6	$r_6 = \dfrac{\partial C_{CO}}{\partial t} = k_6 C_{CO} C_{O_2}^{0.25} C_{H_2O}^{0.5}$	2.24×10^{12}	0	1.70×10^{8}
7	$r_7 = \dfrac{\partial C_{CO}}{\partial t} = k_7 C_{CO} C_{H_2O}$	2.75×10^{9}	0	8.40×10^{7}
8	$r_8 = \dfrac{\partial C_{H_2S}}{\partial t} = k_8 C_{H_2S} C_{O_2}$	6.50×10^{8}	0	8.97×10^{7}
9	$r_9 = -\dfrac{\partial \rho_c}{\partial t} = k_9 \rho_c$	0.658	1	7.48×10^{7}
10	$r_{10} = -\dfrac{\partial \rho_c}{\partial t} = k_{10} \rho_c$	3.42	1	1.30×10^{8}
11	$r_{11} = -\dfrac{\partial \rho_c}{\partial t} = k_{11} \rho_c$	3.42	1	1.30×10^{8}
12	$r_{12} = \dfrac{\partial C_{NH_3}}{\partial t} = r_2 Y_{N,vol} M_{w,NH_3} / M_{w,N}$	–	–	–
13	$r_{13} = \dfrac{\partial C_{NO}}{\partial t} = r_3 Y_{N,char} M_{w,NO} / M_{w,N}$	–	–	–
14	$r_{14} = \dfrac{\partial C_{NH_3}}{\partial t} = k_{14} X_{NH_3} X_{O_2}^{a}$ $a = \begin{cases} 1.0, & X_{O_2} \leq 4.1\times10^{-3} \\ -3.95 - 0.9\ln X_{O_2}, & 4.1\times10^{-3} < X_{O_2} \leq 1.11\times10^{-2} \\ -0.35 - 0.1\ln X_{O_2}, & 1.11\times10^{-2} < X_{O_2} \leq 0.03 \\ 0, & X_{O_2} > 0.03 \end{cases}$	4.00×10^{6}	0	1.34×10^{8}
15	$r_{15} = \dfrac{\partial C_{NH_3}}{\partial t} = k_{15} X_{NH_3} X_{NO}$	1.80×10^{8}	0	1.13×10^{8}
16	$r_{16} = \dfrac{\partial C_{NO}}{\partial t} = k_{16} \bar{p}_{NO} \cdot \rho_s A_s M_{w,NO}$ $\bar{p}_{NO}$ is the mean NO partial pressure, which calculated using Dalton's law: $\bar{p}_{NO} = \bar{p} X_{NO}$ (atm).	230 mol/(m²·s·atm)	0	1.43×10^{8}

The in-house bed model was programmed in MATLAB implementing the SIMPLE algorithm for the inner loop (at each time step). The central differencing scheme and fully implicit scheme are employed to discretize the convection and transient terms, respectively [92]. The coding flowchart is illustrated in Fig. 3.6.

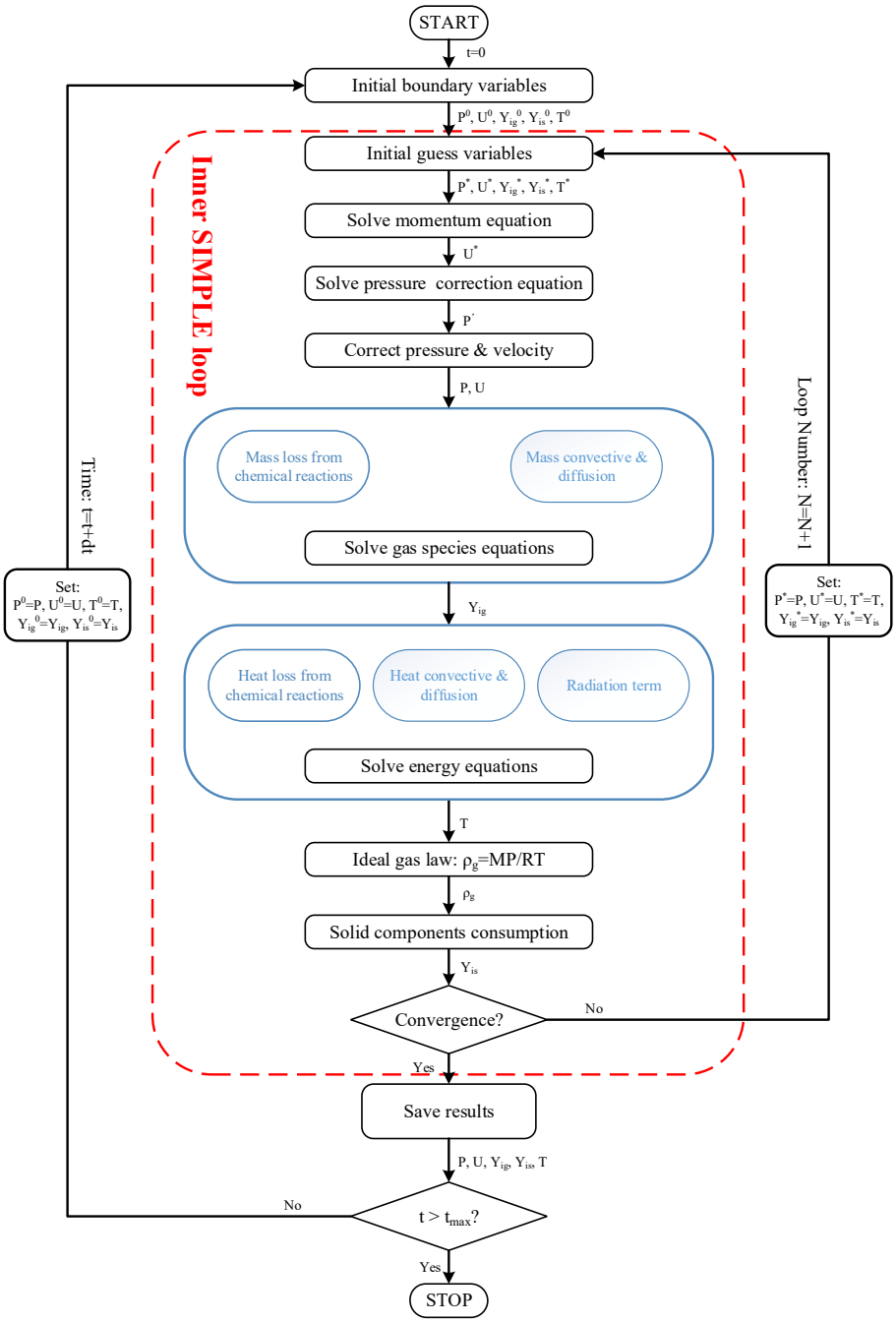

Fig. 3.6. Solving flowchart for programming the bed model [58].

3.3. Modeling of the freeboard

In this section, the modeling process of the boiler freeboard is elaborated, including the boiler description, CAD model of the geometry, meshing, and settings of the CFD solver.

3.3.1. Boiler description

The moving-grate boiler studied is an operating boiler from a WtE plant in China, with a designed thermal capacity of 65.42 MW_{th} for incinerating 750 tons of MSW per day. Fig. 3.7 shows the 2D design diagram of the major-featured boiler with three measurement points. The grate, with alternating forward and backward movements, consists of five individual sub-grates that have an independent air supply system at the bottom. The lengths of the first four sub-grates are equal, that is, 2.0625 m, whereas the last sub-grate is 2.75 m long. The width is 11 m for all the five sub-grates. In addition to the secondary air (PA) supply, 40 SA nozzles with diameters of 50 and 80 mm (20 of each) were distributed on the front and rear walls in the vertical chamber. The cold-water pipes are attached to the walls after the SA nozzles to recycle heat. Subsequently, the flue gas passes through several heat exchangers for further cooling and finally flows out from the boiler outlet.

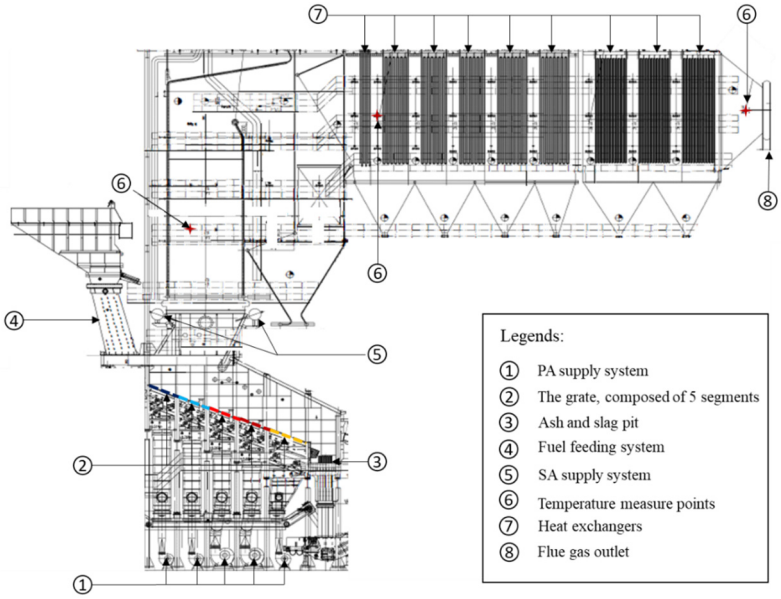

Fig. 3.7. Diagram of the moving-grate boiler under study [74].

3.3.2. Modeling process

Modeling of the freeboard is performed in ANSYS using a self-defined workflow on Workbench, namely, CAD modeling for the geometry by SpaceClaim, meshing by ICEM, and CFD simulation by Fluent [59, 93, 94]. The modeling process for each part is as follows.

3.3.2.1 Geometry and mesh

The 2D diagram of the boiler is imported into SpaceClaim and extruded in the width dimension, resulting in the 3D geometry depicted in Fig. 3.8. The boiler can be divided into the furnace part and the heat exchanger part, in which the former is marked in orange and the latter is marked in blue and yellow. The furnace is also separated into a combustion zone and a vertical chamber. The combustion zone is rounded by adiabatic material, and the vertical chamber attaches cold-water pipes to the walls. The SA nozzles are placed at the intersection of the two sections, at a horizontal angle of 20 °. The parts named in Fig. 3.8 will be mentioned in the subsequent sections for discussion.

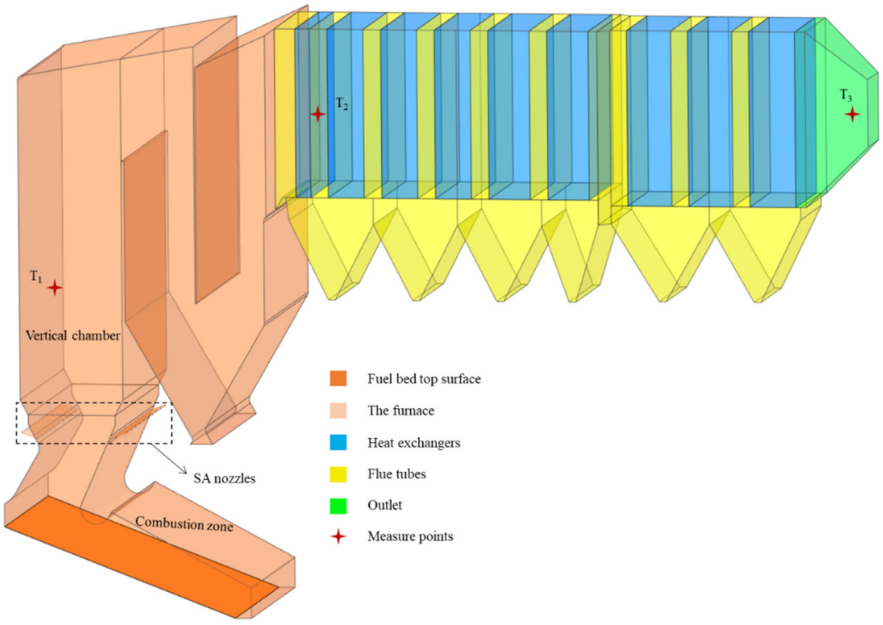

Fig. 3.8. The CAD model of the boiler under study [74].

Table 3.4 Mesh qualities in various criteria [74].

Total cells	16,221,691
Equiangle skewness (0-0.3 very high quality, 0.3-0.5 high, 0.5-0.8 acceptable)	>0.69: 0% 0.5-0.69: 0.73% 0.3-0.5: 5.33% 0-0.3: 93.94%
Angle (0-90°, the closer to 90° the better quality, should be greater than 18°)	>30° 30°-45°: 0.67% 45°-63°: 5.27% 63°-90°: 94.06%
Jacobian Matrix (0-1, should be greater than 0.2)	>0.342
Aspect ratio	1.42-9.41 5-9.41: 1.84% <5: 98.16%

The meshes of the computational domain are all created as structured hexahedral meshes using ICEM, with a total cell number of 16, 221, 691. The meshes are recognized as sufficiently dense to achieve mesh-independent solutions in practice, not only because of the mesh number crushes typically used in similar simulations [95, 96], but also for the quality assessment in various aspects, as listed in Table 3.4. The shell meshes of the outer walls and the magnified view near the SA nozzles are shown in Fig. 3.9.

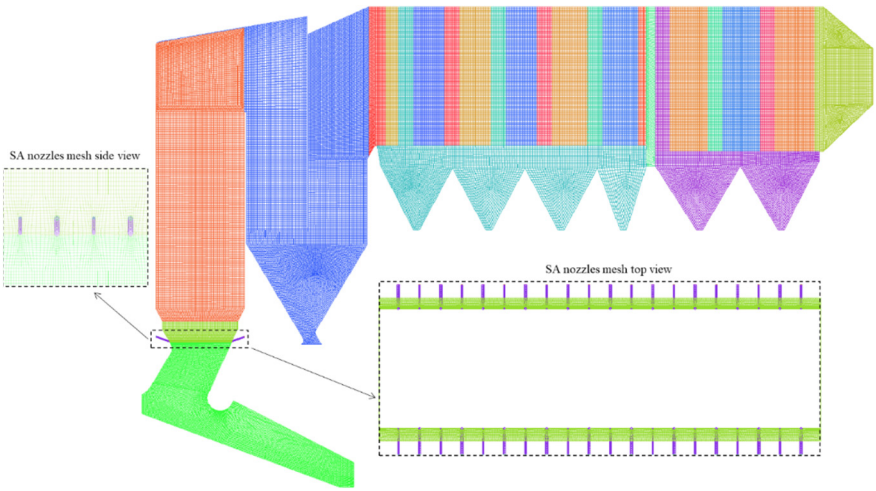

Fig. 3.9. Shell meshes of the boiler outer walls and the zoom-in view of the meshed nearby SA nozzles [74].

3.3.2.2 CFD simulation

The CFD simulation of the freeboard is performed using ANSYS Fluent, in which an inlet profile UDF carrying the calculation results from the bed model is compiled. The global combustion reactions, consisting of a 2-step WD mechanism for light hydrocarbons and a 1-step combustion mechanism for H_2 are included, as shown in Table 3.5 [97]. Fuel NO_x and thermal NO_x formation are modeled in the freeboard simulation [98] using the equilibrium approach to calculate the O-atom concentration [59]. In addition, a refined weighted sum of grey gases model (WSGGM) is employed by another UDF file for a more suitable description of the radiation properties of the flue gas [99]. The turbulence, radiation, and heat exchangers are also appropriately modeled, in the freeboard simulation, as summarized in Table 3.6.

Table 3.5 Chemical reactions and its kinetics for freeboard simulation, where $k = AT^b \exp\left(-\frac{E_a}{RT}\right)$, units in m, s, kmol, J, K [74, 100].

Reactions	*A*	*b*	*E*	Rate expressions
$CO + 0.5O_2 = CO_2$	2.239×10^{12}	0	1.7×10^{8}	$r = \frac{\partial[CO]}{\partial t} = k[CO][O_2]^{0.25}[H_2O]^{0.5}$
$H_2 + 0.5O_2 = H_2O$	6.8×10^{15}	-1	1.67×10^{8}	$r = \frac{\partial[H_2]}{\partial t} = k[H_2]^{0.25}[O_2]^{1.5}$
$CH_4 + 1.5O_2 = CO + 2H_2O$	5.012×10^{11}	0	2×10^{8}	$r = \frac{\partial[CH_4]}{\partial t} = k[CH_4]^{0.7}[O_2]^{0.8}$

Table 3.6 Key models used in the freeboard simulation [74].

Fuel bed inlet	Compiling a UDF of inlet profile
Turbulence model	Realizable $k-\varepsilon$ model with standard wall function, $I = 0.16{Re_{D_H}}^{-1/8}$ for calculation of the turbulence intensity for the inlet boundary condition [47, 56].
Gaseous combustion	2-step Westbrook and Dryer mechanism for light hydrocarbons, one-step global combustion mechanism for H_2 [53],finite rate/eddy-dissipation model for turbulence-chemistry interaction [63].
Radiation model	P-1 model, a refined WSGGM for evaluation gases radiation properties [61].
NO_x formation	Fuel and thermal NO_x formation using equilibrium approach.
Heat exchangers	Porous zone with pressure and heat drops.
Boundary conditions	Velocity inlet, pressure outlet, temperature thermal condition for walls.
Numerical methods	SIMPLE algorithm; 2nd order upwind scheme for all transport equations [92].

3.4. Reliability tests of the simulation

In this section, the reliability of the simulation is verified in several aspects, i.e., mas balance of the major elements, mesh and time-step independence, coupling convergence of the bed model and freeboard simulation, and experimental validation.

3.4.1. Element balance test of the bed model

The in-house bed model is not a well-used CFD solver, such as Fluent or OpenFOAM, which has proven to be trustworthy. It is necessary to check the mass balance of major elements (C, H and O). In Fig. 3. 10, a comparison of the overall mass balance and element balance for C-atom, H-atom, and O-atom is presented, that is, the mass profiles at the inlet and outlet of the bed model are compared. The high consistency of the mass profiles at the inlet and outlet verified the reliability of the bed model in terms of element balance.

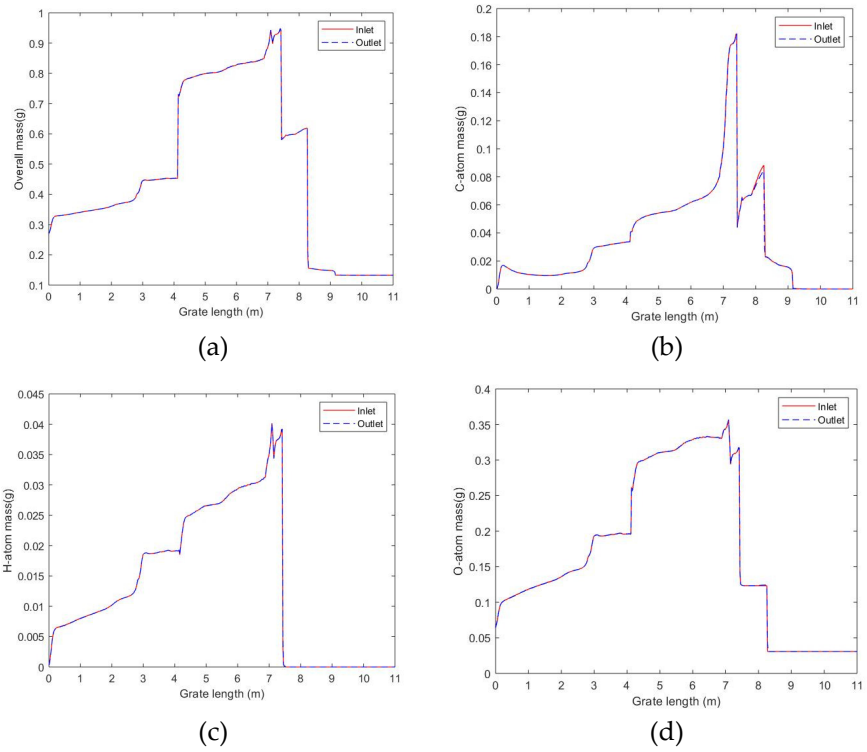

Fig. 3.10. Mass and elements balance tests of the bed model.

3.4.2. Mesh and time-step independence tests

To achieve reliable simulation results, mesh and time-step independence tests of the bed model are performed in advance [101]. The key features of the bed modeling results, that is, the solid mass along the grate and temperature profile of the top surface, using different mesh numbers and time-step sizes, are compared in Fig. 3.11. From the comparison of Fig. 3.11(a) and (b), using mesh numbers 400, 500, and 600 does not affect the results significantly. However, the time step size remarkably influenced the results of the bed model. Minor differences were observed between using a time step of 0.005s and 0.01 s, and major differences were observed when using 0.02 s as the time-step in Fig. 3.11(c) and (d). Considering the accuracy and time-cost of the computation, mesh number 500 and time-step 0.01 s are used in the bed model for all the cases. For the 3D steady simulation of the freeboard, more than 1,600,000 structured hexahedral meshes used in this study are considered sufficiently dense to obtain mesh-independent results.

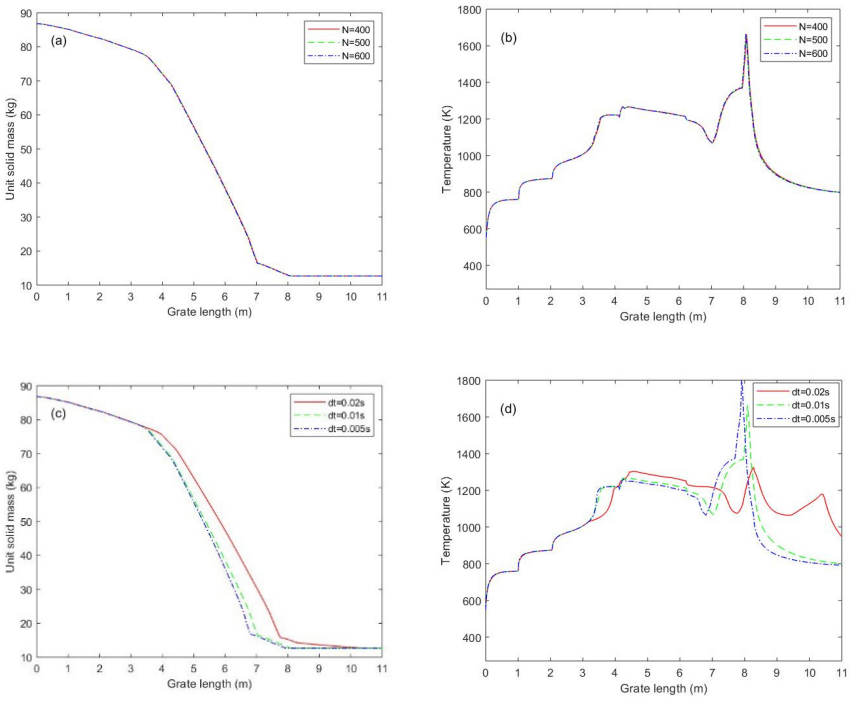

Fig. 3.11. Mesh and time-step independence tests of the bed model [74].

3.4.3. Coupling convergence

The bed model is developed as a stand-alone model (programmed in MATLAB), thus manual coupling between the bed model and freeboard simulation is used, following the below steps [87].

Step 1: Execute the bed model code with an initial guessed radiation temperature and over-bed temperature employed in the thermal boundary condition at the top surface.
Step 2: Run Fluent with a UDF carrying the bed model results, and then export the radiation temperature profile along the grate.
Step 3: Execute the bed model again with the new radiation temperature profile, and check the radiation heat transfer rate at the top surface.
Step 4: Rerun Fluent with a UDF carrying the new results from the bed model, and then check the radiation heat transfer rate to the bed top surface and export the radiation temperature profile.
Step 5: Compare the absolute value of the two heat transfer rates (negative in Fluent). If there is no significant difference, the coupling convergence is achieved; otherwise, return to Step 3 and repeat the procedure.

Fig. 3.12(a) demonstrates the two radiation heat transfer rates at the bed top along the coupling times for one simulation case. It can be observed that the difference in the radiation heat transfer rate in the bed model and Fluent simulation is negligible after three coupling times. The profiles of the radiation temperature exported from Fluent in Coupling II and Coupling III are also not significantly different from each other, as depicted in Fig. 3.12(b). Hence, we conclude that the coupling between the bed model and freeboard simulation converges. All the simulation results presented in this study are achieved after three to four times of coupling.

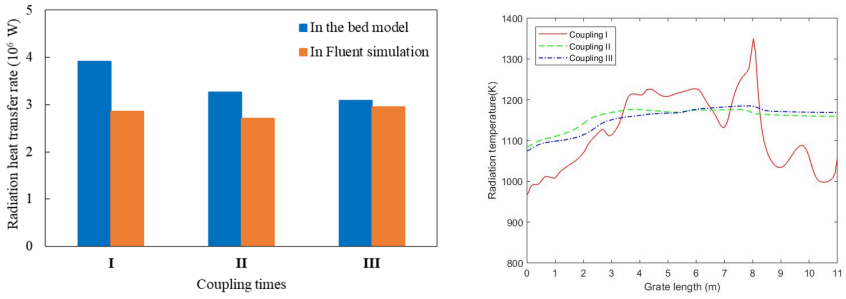

(a) (b)

Fig. 3.12. Coupling of the bed model and the freeboard simulation [87].

3.4.4. Model validation

The bed model has been independently validated in a previous study [58] by comparing the experimental data of MSW combustion in a fixed-bed incinerator. In this study, the results of the freeboard simulation coupled with the bed model are validated by the operation data for incinerating the current feedstock (Case 1 in [74]), as shown in Fig. 3.13. The comparison indicates that the simulation results agree well with the operation data at different measurement points, satisfying the engineering requirements for such an industrial-scale boiler. Hence, it can be concluded that the model is valid and reliable for simulating solid waste combustion in the boiler.

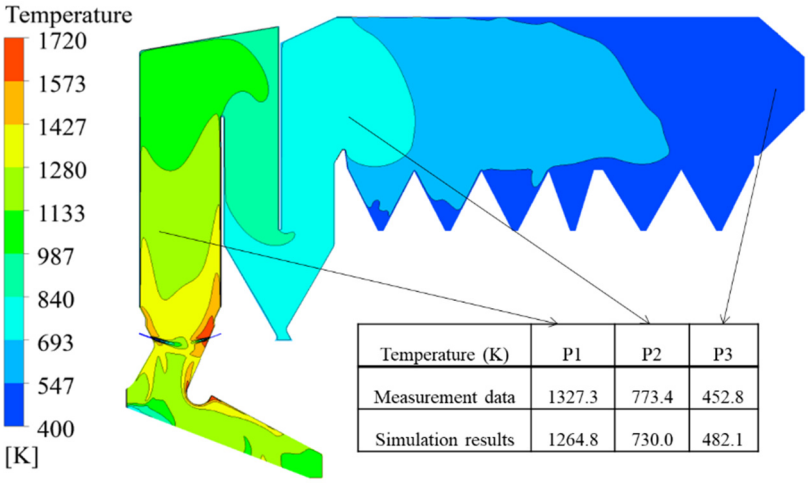

Temperature (K)	P1	P2	P3
Measurement data	1327.3	773.4	452.8
Simulation results	1264.8	730.0	482.1

Fig. 3.13. Comparison of the simulated temperature to the operation data at different positions [74, 87].

3.5. Simulation-based investigation: Impacts of feedstock change

This investigation targets to the recently implemented waste classification in China, which significantly influences the properties of MSW for incineration. The incineration of new MSW under the current operating conditions is explored based on the simulation, and several impacts are marked. Subsequently, adjustments of air supply solutions and thermal input are proposed and conducted, which effectively eliminate the potential issues. This investigation focuses on the major combustion features, NO_x formation and emissions are not included. The significant results and conclusions are presented. More details refer to Paper C.

3.5.1. Simulation cases

Four simulation cases, namely, Case 1, Case 2a, Case 2b, and Case 2c, are conducted for burning two feedstocks, i.e., Feedstock 1 and Feedstock 2. The fuel properties of the two feedstocks are presented in Table 3.7, where Feedstock 1 represents the current incinerating feedstock used in Case 1 for model validation. Feedstock 2 represents the potential feedstock due to the recent waste classification used in Cases 2a, 2b and 2c, to investigate the impacts and the solutions due to the feedstock change.

Table 3.7 Properties of the feedstocks used in this study [74].

MSW	Proximate analysis, wt% ar[a]				Ultimate analysis, wt% daf[b]						LHV, kJ/kg ar[a]
	Moisture	Volatile	Fixed carbon	Ash	C	H	O	N	S	Cl	
Feedstock 1	45.40	31.90	8.10	14.60	52.63	7.45	36.91	1.19	1.12	0.70	7536
Feedstock 2	39.23	41.25	10.48	9.04	52.63	7.45	36.91	1.19	1.12	0.70	10223

[a] As received basis (ar)
[b] Dry ash free basis (daf)

Table 3.8 Operation conditions of the simulated cases [74].

Operation conditions		Unit	Case 1	Case 2a	Case 2b	Case 2c
Thermal capacity		MW_{th}	65.42	65.42	65.42	71.96
Feedstock	Feeding rate	t/h	31.25	23.04	23.04	25.34
	Bed height	m	1	1	1	1
	Resident time	h	1.5	1.5	1.5	1.5
Grate dimensions	Length	m	11	11	11	11
	Width	m	12.5	12.5	12.5	12.5
Overall air supply	Excess air ratio	(-)	1.2	1.2	1.2	1.216
	PA: SA	(-)	6:4	6:4	5:5	5:5
Primary air	Flow rate	kg/h	64543	61535	51533	56686
	Temperature	℃	220	220	220	220
	Distribution	%	15:15:30:30:10	15:15:30:30:10	14:16:34:28:8	14:16:34:28:8
Secondary air	Flow rate	kg/h	43561	41531	51533	56686
	Temperature	℃	40	40	40	40
	Nozzle diameter	mm	50/80	50/80	50/80	50/80
	Horizontal angle	°	20	20	20	20

The adjustments of the air supply used in Cases 2b and 2c are based on the simulation analysis of Case 2a, targeting elimination of the potential issues, as explained in [74]. Table 3.8 summarizes the operation conditions of the four cases, including the feeding rate, thermal input, excess air ratio, and PA distribution. In terms of the operating conditions, Case 2a is precisely consistent with Case 1, Case 2b is consistent with Case 2a except for the excess air ratio and PA distribution, and Case 2c is consistent with Case 2b except for the expansion of the thermal input to 110%. The purpose of conducting Case 2c is to test the feasibility of maintaining the disposal ability of the boiler to the most extent, of incinerating the new MSW under the proposed air supply solution.

3.5.2. Comparison and analysis of the cases incinerating new MSW

The comparison of the Cases 2a and 2b incinerating new MSW under different operation conditions is presented in this section. The visible results and corresponding discussions for Cases 1 and 2c refer to Paper C and will not be presented in this section. Fig. 3.14 illustrates the bed model results from the two cases: mass of the solid fuel and its components along the grate (a), and profiles of velocity (b), temperature (c), mass fraction of O_2 (d), H_2O (e), CO (f), and CO_2 (h) at ¼ height, ½ height, ¾ height, and top surface. Moreover, the velocity profile at the bottom surface also reflects the adjustment of the PA distribution under different sub-grates. As depicted in Fig. 3.14(a), the combustion process can be generally divided into four stages for the both two cases. Some significant differences owing to air supply adjustments are also observed, as discussed in Paper C. The highlights from the comparison of the bed model results are summarized below.

1) The bed ignition is slightly ahead after reducing the PA supply under the first sub-grate, because the relatively lower PA flow promotes the heating up of the bed in the initial stage.
2) Stage III, i.e., the char reaction stage, is expanded remarkably for Case 2b, most likely because of the decreased PA supply under the fourth sub-grate. The maximum bed temperature is reduced from 1596 K to 1523 K, which improves the service life of the grate.
3) Following MSW burnout, the bed top surface temperature of Case 2b is slightly higher than Case 2a (988.6 K vs. 946.7 K), primarily due to the PA reduction from 10% to 8% under the last sub-grate.

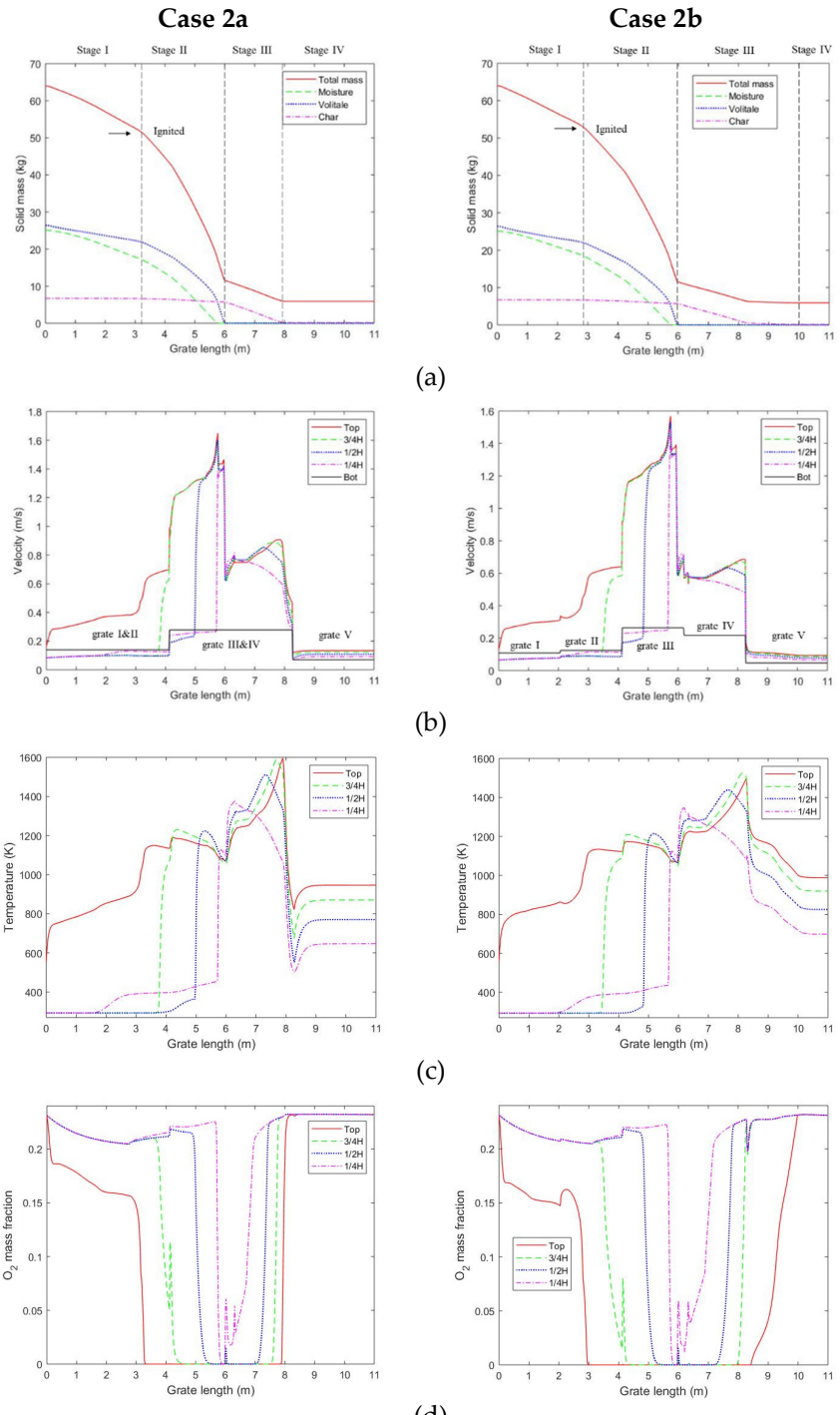
Case 2a
Case 2b
Stage I
Stage II
Stage III
Stage IV
Total mass
Moisture
Volitale
Char
Ignited
Solid mass (kg)
Grate length (m)
(a)
Top
3/4H
1/2H
1/4H
Bot
Velocity (m/s)
grate I&II
grate III&IV
grate V
grate I
grate II
grate III
grate IV
(b)
Temperature (K)
(c)
O2 mass fraction
(d)

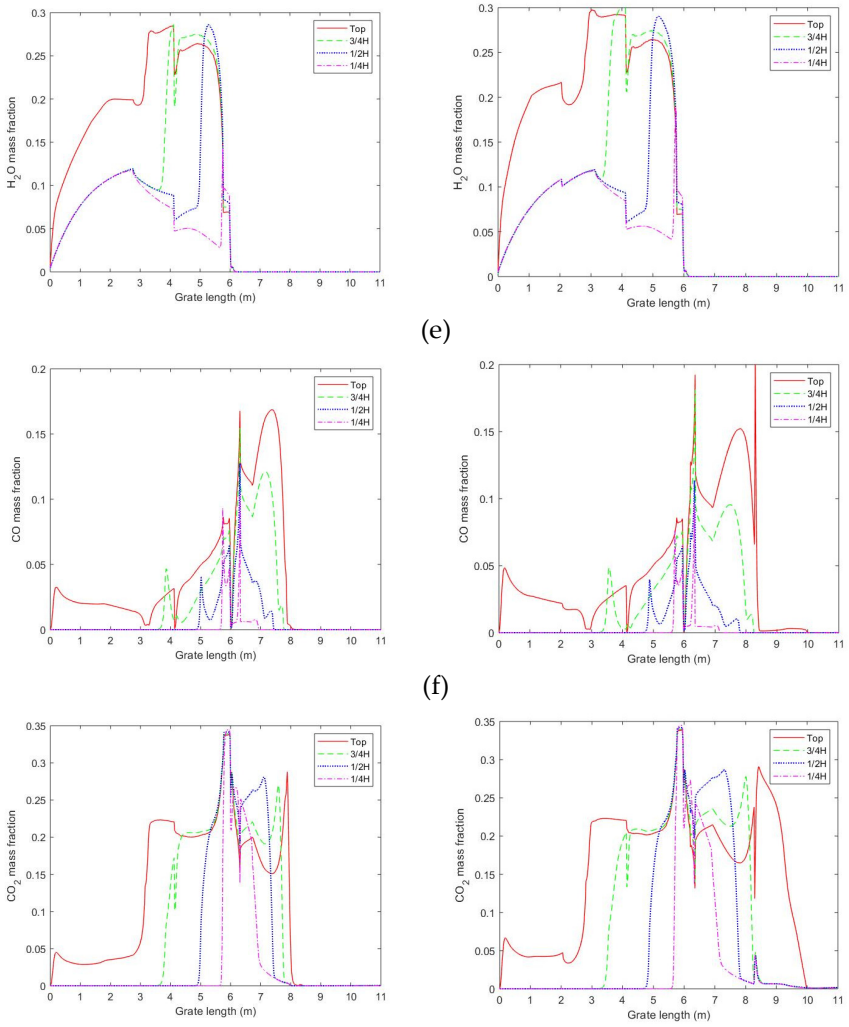

Fig. 3.14. Bed model results: Profiles of solid mass (a), velocity (b), temperature (c), mass fractions of O_2 (d), H_2O (e), CO (f) and CO_2 (h) at different bed height for Case 2a (left) and Case 2b (right) [74].

Fig. 3.15 presents the freeboard simulation results of Case 2a and Case 2b, i.e., contours of temperature (a), mass fractions of O_2 (b), CO (c), CO_2 (d), and H_2O (e) of the flue gas at the freeboard middle plane. The comparison and discussion have been elaborated in Paper C, several highlights are summarized below.

1) Generally, the furnace temperature in Case 2b is higher than that in Case 2a. This attributes to more combustibles entering the freeboard after reducing the PA: SA ratio from 6:4 to 5:5.
2) The O_2-rich zone above the last sub-grate in Case 2b is smaller than that in Case 2a, as shown in Fig. 3.15(b). This is considered to ensure the uniformity of temperature in the combustion zone.
3) The mixing in the furnace is enhanced owing to the increase of SA supply, which intensifies the combustion reactions near the SA nozzles.

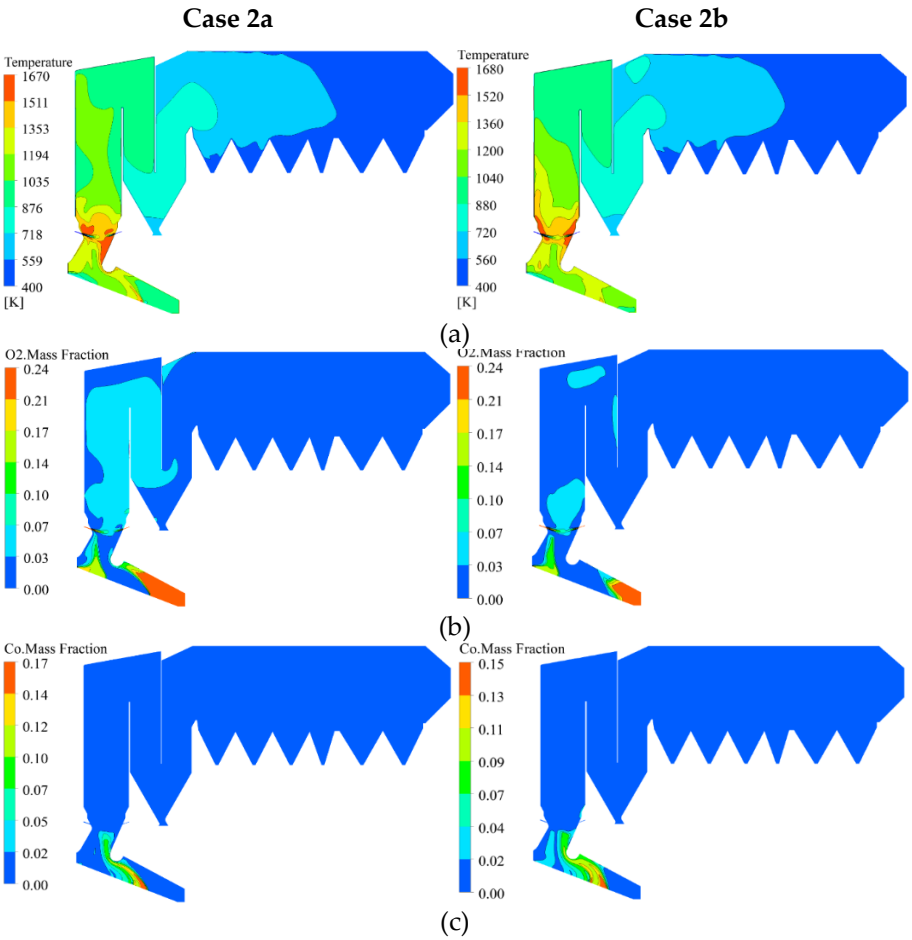

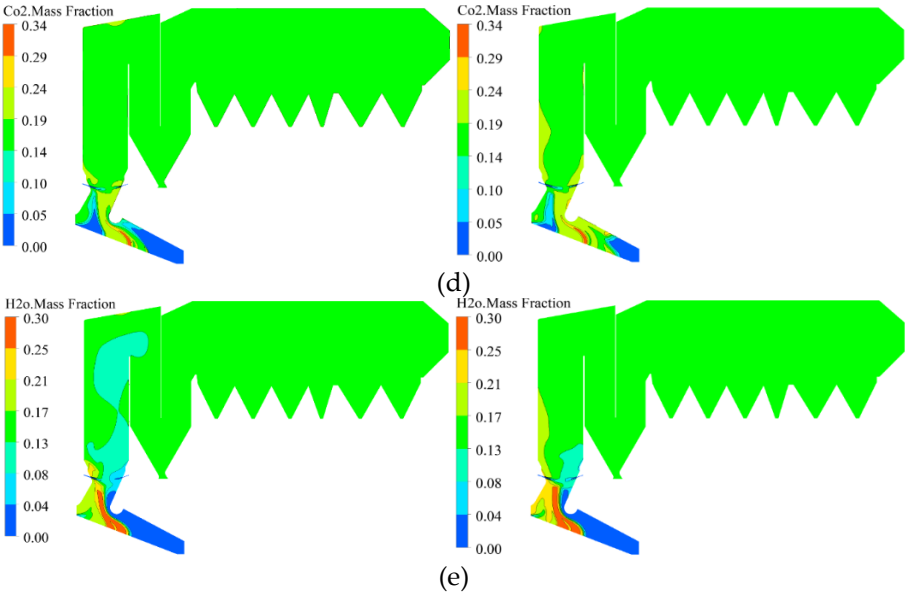

Fig. 3.15. Freeboard simulation results: Contours of temperature (a), mass fractions of O_2 (b), CO (c), CO_2 (d), and H_2O (e) at the middle plane of the freeboard for Case 2a (left) and Case 2b (right) [74].

In short, compared to the case of the new MSW incineration while maintaining current operating conditions, the adjustments to air supply support the new MSW combustion in several aspects, as summarized below.

1) Reducing the maximum temperature of the fuel bed is profitable for a long lifetime.
2) Narrowing the O_2-rich area in the combustion zone avoids O_2 waste and maintains the temperature uniformity.
3) Improving the mixing in the furnace to enhance the combustion reactions.

3.5.3. Quantitative analysis of the fluid flow

To better analyze the gas flow in the freeboard, the uniformity index for velocity (UIV) and mixing index represented by the turbulent kinetic energy (TKE) are defined by Eq. (3.1) and Eq. (3.2), respectively [61].

$$\mathrm{UIV} = 1 - 0.5 \sum_{j=1}^{n} \left| \left(\frac{u_j}{u_{avg}} - 1 \right) \right| \cdot \frac{V_j}{V_{tot}} \tag{3.1}$$

$$\mathrm{TKE} = \frac{1}{2}\overline{u_i' u_i'} = \frac{1}{2}\left(\overline{u_x'^2} + \overline{u_y'^2} + \overline{u_z'^2}\right) = \frac{3}{2}\overline{u_i'^2}, \tag{3.2}$$

where n, u_j and V_j denote the number of cells, velocity magnitude, and volume of each cell in the zone of interest, respectively. V_{tot} and u_{avg} represent the total volume of the zone and the volume-averaged velocity, respectively. $\overline{u_i'}$ indicates the average velocity fluctuation in i direction ($i = x, y, z$) of the cell.

According to the definition of the UIV and TKE, the closer the UIV is to 1, the more uniform the flow; the larger the TKE, the more intense the mixing. Fig. 3.16(a) presents the calculated values of UIV and the volume-averaged TKE in the combustion zone for the cases incinerating the new MSW, namely, Cases 2a, 2b, and 2c. The results reveal that the UIV is slightly reduced, while the TKE is greatly increased by adjusting the air supply and thermal input [102]. To obtain a better view, the normalized UIV and TKE of Cases 2b and 2c are compared, with Case 2a as the benchmark case, as shown in Fig. 3.16(b). Compared to the benchmark case, the UIV is reduced by 7.23% and 8.91%, while the TKE is increased by 51.39% and 81.04%, respectively, for Cases 2b and 2c.

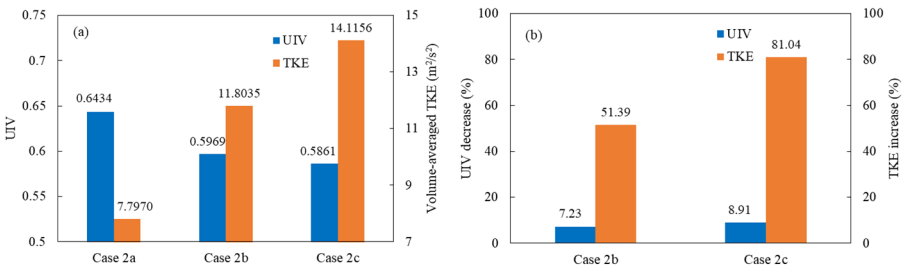

Fig. 3.16. Comparison of the UIV and TKE in the combustion zone for Case 2a, 2b and 2c [74].

3.5.4. Conclusions of the investigation on impacts of feedstock change

In this study, the incineration of new MSW in the same boiler was virtually tested based on the simulation, and several potential issues influencing the combustion stability and efficiency are observed. Subsequently, corresponding adjustments in terms of air supply and thermal input are proposed and executed in the simulation to cost-efficiently address these issues. The main conclusions of this study are as follows.

1) Incineration of new MSW while maintaining the current operating conditions may lead to ineffective utilization of oxygen, non-uniform distribution of temperature, and low mixing.
2) The proposed adjustments effectively address the potential problems and improve the boiler's stability.
3) It is feasible to operate the boiler with 110% of the designed thermal input to incinerate the new feedstock, recycle more energy, and retain its disposal capacity to the greatest extent.

3.6. Simulation-based investigation: Co-combustion of MSW and sludge

This investigation aimed to test the feasibility of stable and clean co-combustion of MSW and sewage sludge in an existing boiler. To promote MSW co-firing with raw sewage sludge, industrial solid waste of high heating value is blended for co-combustion, as the supporting fuel. Combustion stability and NO_x emissions are the primary concerns in this study because of the high moisture and nitrogen content in the blend feedstock. First, the combustion features and NO_x emissions for incinerating four different blends were probed and compared. Subsequently, a new PA supply solution was proposed and verified to be useful for NO_x reduction. Finally, the recommended co-combustion case is picked out, followed by an in-depth analysis. The main results and conclusions are presented; more details are elaborated in Paper D.

3.6.1. Co-combustion cases

The proximate and ultimate analyses of the three types of solid wastes used for co-combustion are listed in Table 3.9. The purpose of choosing the industrial solid waste as a fuel is to improve the heating value of the blended feedstock to assist in co-combustion.

Considering the co-combustion stability in an MSW boiler, the current MSW is blended as the dominant component in the feedstock. Blend ratios from 50 wt% to 80 wt% with a 10 wt% gradient of MSW are used to investigate the impacts of the co-combustion feedstocks, resulting in four kinds of blends. The corresponding ratios of sewage sludge to industrial waste are computed based on the consistent heating value principle with MSW, to maintain the disposal ability and thermal input of the boiler. The blends used and cases simulated in this co-combustion study are listed in Table 3.10. The co-

combustion blends: Blends 1, 2, 3, and 4, correspond to the simulated cases: Case 1(a,b), Case 2(a,b), Case 3(a,b), and Case 4(a,b), respectively. To simplify the simulation process, the kinetics of devolatilization and char burning for the three solid wastes are assumed consistent.

Table 3.9 Fuel properties of the used solid wastes in co-combustion [87].

Solid wastes	Proximate analysis, wt% ar[a]				Ultimate analysis, wt% daf[b]						LHV, kJ/kg ar[a]
	Moisture	Volatile	Fixed carbon	Ash	C	H	O	N	S	Cl	
MSW	45.40	31.90	8.10	14.60	52.63	7.45	36.91	1.19	1.12	0.70	7536
Sludge	80.00	10.51	1.20	8.29	51.90	7.44	6.38	28.9	4.57	0.82	1172
Industrial waste	7.56	72.20	8.75	11.49	57.86	6.88	31.41	1.58	1.85	0.41	18840

[a] As received basis (ar)
[b] Dry ash free basis (daf)

For NO_x reduction, a new PA supply solution is proposed and verified by the model, in addition to the currently used PA for incinerating MSW. The objectives and corresponding actions in terms of PA adjustment are explained in [87]. The new PA distribution, which is used in Cases (1,2,3,4)b, is presented in Table 3.10.

Table 3.10 Simulation cases for the co-combustion study [87].

Case	Feedstock blend			PA distribution along the grate (wt%)
	MSW / Sludge / Industrial waste (wt%)	LHV (kJ/kg, ar[a])	Fuel-N (wt %, daf[b])	
Case 1a	50.0 / 32.0 / 18.0	7534	4.24	15 / 15 / 30 / 30 / 10 (Currently used PA distribution)
Case 2a	60.0 / 25.6 / 14.4	7535	3.61	
Case 3a	70.0 / 19.2 / 10.8	7535	3.00	
Case 4a	80.0 / 12.8 / 7.2	7535	2.39	
Case 1b	50.0 / 32.0 / 18.0	7534	4.24	14 / 16 / 28 / 32 / 10 (Adjusted PA distribution)
Case 2b	60.0 / 25.6 / 14.4	7535	3.61	
Case 3b	70.0 / 19.2 / 10.8	7535	3.00	
Case 4b	80.0 / 12.8 / 7.2	7535	2.39	

3.6.2. Comparison of NO_x emissions for the simulated cases

The profiles of the temperature, NH_3, and NO mass fractions at the bed top of the eight cases, which influences NO_x formation, are compared in Fig. 3.17. The observations are discussed in detail in Paper D and have several consequences, as illustrated below.

1) The adjustment of PA under the first two sub-grates promotes slightly more NH_3 entering the freeboard, which is conducive to the NO reduction in the boiler.
2) Following the adjustment of PA under the third sub-grate, additional NO is reduced by the released NH_3 at the third stage, where the temperature remained at approximately 1200 K.
3) The increase in PA supply under the fourth sub-grate promotes NO reduction by the heterogeneous reaction with char.

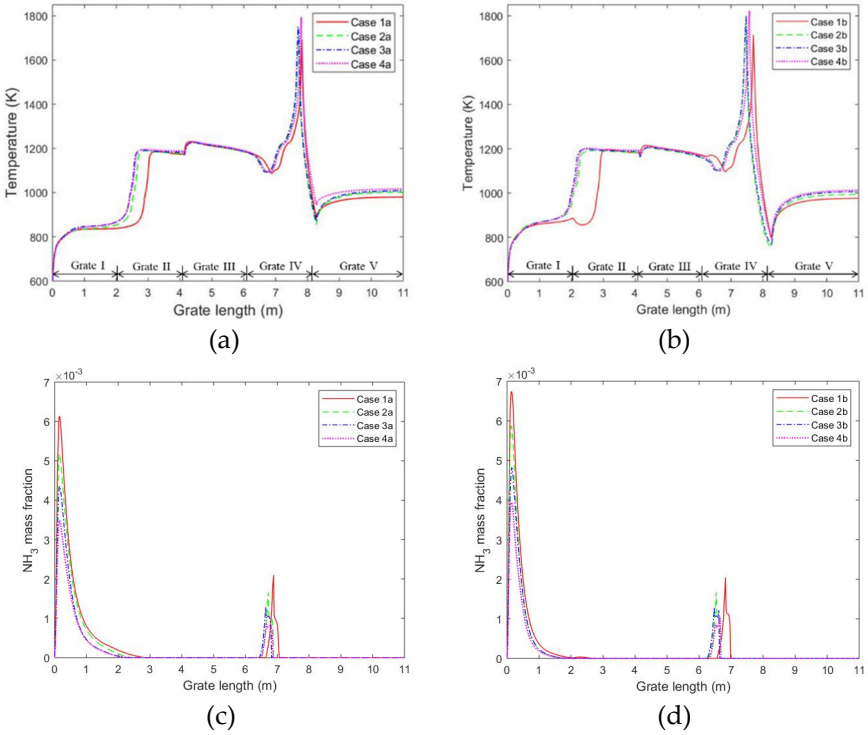

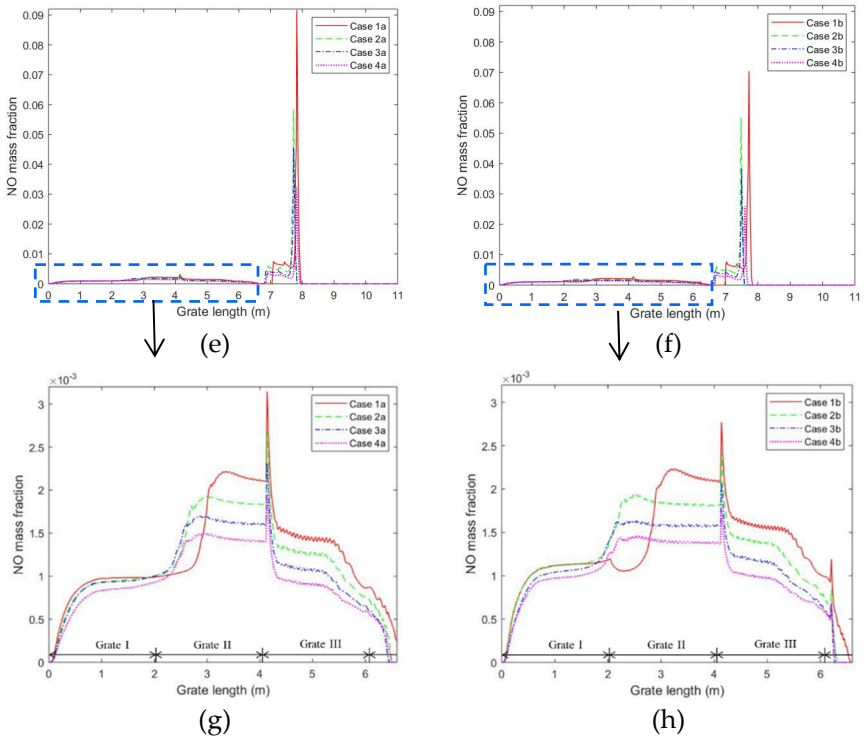

Fig. 3.17. Comparison of the profiles of temperature, NH_3 and NO at the bed top for the eight cases [87].

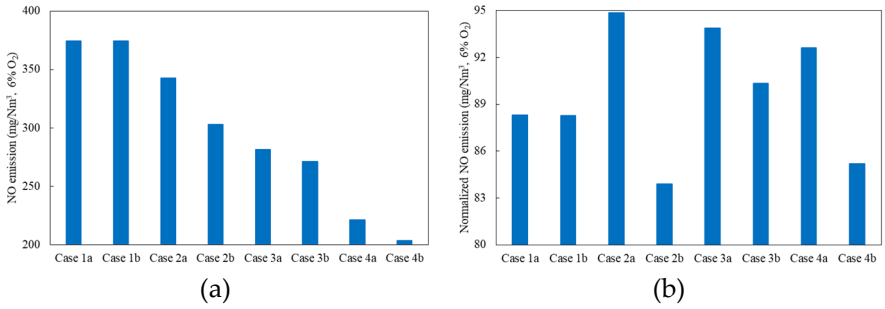

Fig. 3.18. NO emissions of the eight cases under study at boiler outlet [87].

To characterize the NO emissions of the eight cases at the boiler outlet, the absolute NO emissions with a standardised unit mg/Nm^3 under the 6% O_2 reference condition, are compared in Fig. 3.18(a). The normalized NO emissions, which are calculated using Eq. (3.3), is further compared in Fig.

3.18(b) to eliminate the impact of the fuel-N content in the blends. The comparison results indicated that Case 2b was the best case for NO emissions.

$$Normalized\ NO\ emission = \frac{NO\ emission\ (mg/Nm^3)}{Fuel - N(wt\%)} \quad (3.3)$$

To quantitatively analyze the reduction of NO by the PA adjustment, the percentage of NO reduction for incinerating the four blends is calculated using Eq. (3.4) and presented in Fig. 3.19. The results show that using the new PA solution reduces NO emissions to some extent compared with the currently used PA for incinerating all four blends. The new solution benefits most from the combustion of Blend 2, reducing NO emissions by 11.54 %. The PA adjustment is verified to be effective for NO reduction, and Case 2b is selected as the recommended co-combustion case to be implemented in the boiler.

$$NO\ reduction\ \% = \frac{(NO\ emission\ of\ Case\ a - NO\ emission\ of\ Case\ b)}{NO\ emission\ of\ Case\ a} \times 100 \quad (3.4)$$

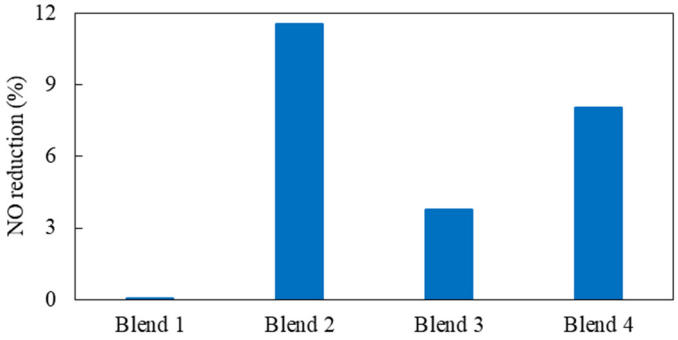

Fig. 3.19. NO reduction by PA adjustment for burning the four blends [87].

3.6.3. Feasibility of the recommended co-combustion case

An in-depth analysis of the recommended co-combustion case, namely Case 2b, is presented in Paper D to address its feasibility. Figs. 3.20 and 3.21 illustrate the key results, including NO_x in the fuel bed and the interest zone of the freeboard (combustion zone and vertical chamber marked in Fig. 3.8). In short, the results prove that the blended feedstock can be stably converted, via four stages along the grate. The syngas released from the fuel bed is burned out on the freeboard, with reasonable distributions of gas species. The area-weighted average mass fractions of O_2, CO_2, and CO are 3.19%, 17.95%, and 21.66 ppm at the boiler outlet, respectively. The final NO_x emissions of

the boiler, under removal-free conditions, is 302.88 mg/Nm^3 (6% O_2 reference condition). Case 2b is proven to be feasible for MSW co-firing with sewage sludge and industrial solid waste. Additional supported results and discussion refer to Paper D.

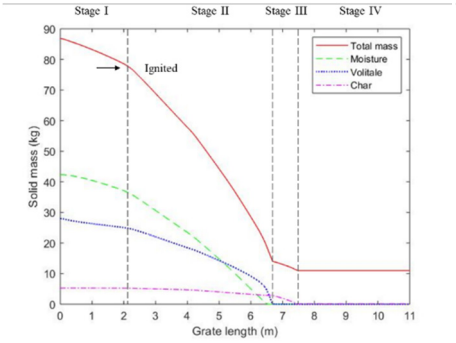

(a)

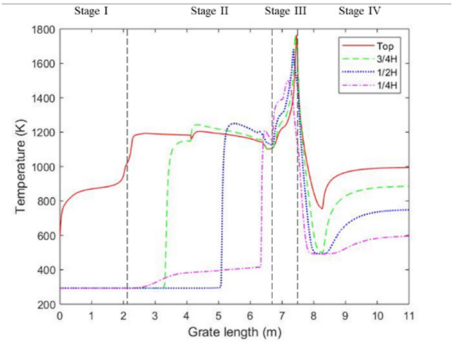

(b)

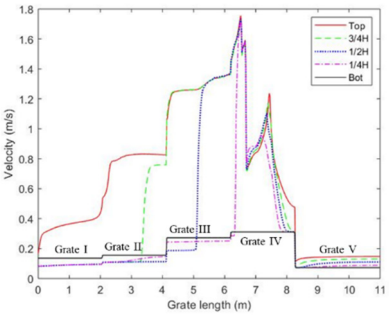

(c)

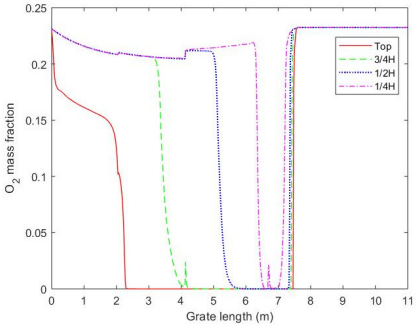

(d)

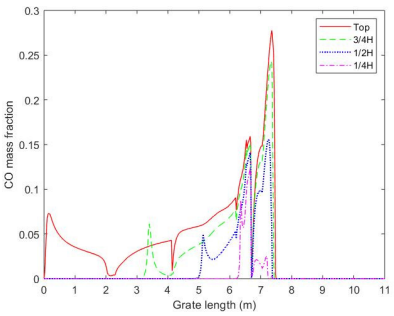

(e)

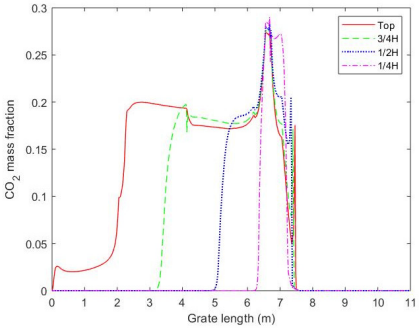

(f)

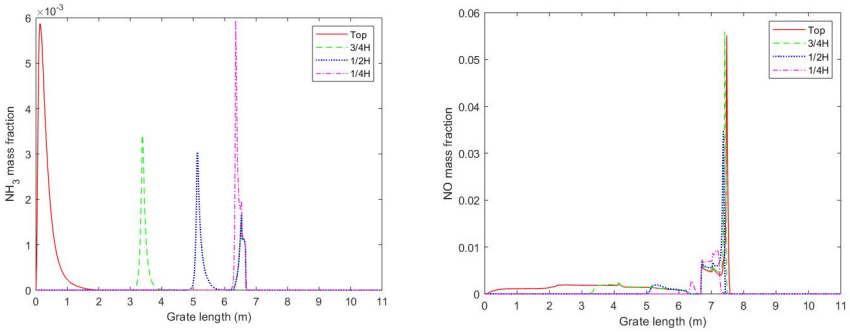

(g) (h)

Fig. 3.20. Case 2b bed model results: Profiles of solid mass, temperature, velocity, O_2, CO, CO_2, NH_3 and NO [87].

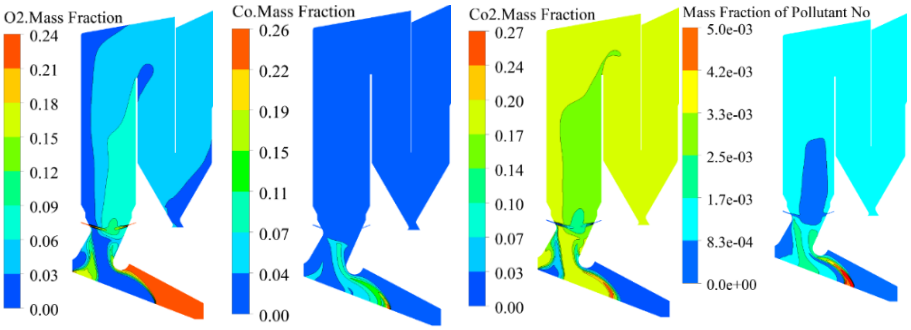

(a) (b) (c) (d)

Fig. 3.21. Case 2b freeboard simulation results: Contours of O_2, CO,CO_2 and NO at the middle plane [87].

3.6.4. Conclusions of the co-combustion study

In this study, the co-combustion of MSW, sewage sludge, and industrial solid waste, in which industrial solid waste acts as the supporting fuel, was investigated. Eight simulation cases for incinerating different blends under two types of air supply distributions are conducted and compared in terms of NO_x emissions. The significant findings of this study are as follows.

1) The blended feedstock of 60.0 wt% MSW, 25.6 wt% sludge and 14.4 wt% industrial waste is recommended for co-combustion.
2) The new solution of air supply is effective in the reduction of NO_x, up to 11.54% for incineration of the recommended blend.

3) The co-combustion of MSW and sewage sludge in the existing boiler is feasible by blending industrial solid waste of high heating value.

3.7. Summary

In Chapter 3, an in-house fixed-bed model is extended to a moving-grate bed model with some key updates and extensions to better describe solid fuel conversion in large-scale MSW boilers. The mesh and time-step independence of the bed model as well as the element balance are verified. The bed model was then coupled with the CFD simulation of freeboard, resulting in an advanced simulation of a 750 t/d MSW grate boiler. A comparison between the simulation results and boiler operation data validates the reliability and applicability of the advanced simulation.

Subsequently, the advanced simulation is deployed to investigate the impacts of incinerating potential feedstocks in the existing MSW boiler and virtually test the proposed solutions. Two numerical studies, that is, the impacts of feedstock change and co-combustion of MSW and sewage sludge, were carried out. The former study reveals the characteristics of incinerating new MSW based on waste classification and proposes effective adjustments to the air supply and thermal input. This offers valuable references for boiler adjustments to satisfy the implementation of waste classification. The latter study probes the feasibility of the stable and clean co-combustion of MSW, sewage sludge, and industrial solid waste in an current boiler, which provides useful guidelines for the co-combustion of MSW, sewage sludge, and industrial waste with low NO_x emissions. The advanced simulation is recognized as powerful and efficient for analyzing the characteristics of solid fuel incineration and optimizing, retrofitting and adjusting similar types of boilers.

Paper C

Advanced Simulation of a 750 t/d Municipal Solid Waste Grate Boiler to Better Accommodate Feedstock Changes due to Waste Classification

Tianbao Gu, Wenchao Ma, Torsten, Berning, Zhenning Guo, Ronnie Andersson and Chungen Yin

This paper has been published in the

Energy, Vol. 254, pp. 124338, 2022.

Energy 254 (2022) 124338

Contents lists available at ScienceDirect

Energy

journal homepage: www.elsevier.com/locate/energy

Advanced simulation of a 750 t/d municipal solid waste grate boiler to better accommodate feedstock changes due to waste classification

Tianbao Gu [a], Wenchao Ma [b], Torsten Berning [a], Zhenning Guo [c], Ronnie Andersson [d], Chungen Yin [a, *]

[a] AAU Energy, Aalborg University, Aalborg, Denmark
[b] School of Environmental Science and Engineering, Tianjin University, Tianjin, China
[c] Institute of Technology, Everbright Envirotech (China) Ltd., Nanjing, China
[d] Department of Chemistry and Chemical Engineering, Chalmers University of Technology, Gothenburg, Sweden

ARTICLE INFO

Article history:
Received 9 December 2021
Received in revised form
25 April 2022
Accepted 18 May 2022
Available online 25 May 2022

Keywords:
MSW incineration
Grate boiler
Bed model
CFD simulation
Air supply
Waste classification

ABSTRACT

To better accommodate changes in municipal solid waste (MSW) properties due to waste classification, advanced computational fluid dynamics (CFD) simulations are carried out for a 750 t/d MSW moving-grate boiler. A moving-grate bed model is developed and iteratively coupled to the freeboard simulation which is performed in Ansys Fluent. The model is first validated by the measurement data for the daily operation case incinerating current feedstock. Then, the model is deployed to investigate the impacts of feedstock change and adjust boiler operation for better accommodating the new MSW. The results indicate incineration of the new MSW leads to irrational utilization of oxygen, non-uniform temperature distribution and low mixing, while maintaining current operation conditions. Subsequently, adjustments of air supply and thermal input are proposed and conducted by the model, which address the potential issues and benefit boiler operation and energy recycling. Finally, the uniformity of velocity and turbulent kinetic energy which indicates mixing, are compared for different cases. The latter is increased by 51.39% and 81.04% after the adjustments of air supply and thermal input. The investigation provides solid references for incinerating new MSW in the current boiler.

1. Introduction

Municipal solid waste (MSW) incineration, which can efficiently reduce the mass and volume and recycle energy, is recognized as promising in MSW disposal [1]. Grate-firing technology, one of the key combustion technologies, has been widely used in MSW incineration due to its stability and flexibility. A great number of waste-to-energy (WtE) plants using grate-firing technology have been built to dispose the MSW, especially for the high-moisture or low-heating-value MSW [2]. By 2018, there have been 331 incinerators (which are dominated by grate-firing incinerators) with a total capacity of 133.08 million tons per year in China, and at least 80 WtE units are under construction [3]. Most of the WtE plants are designed and operated based on the low heating value (around 7530 kJ/kg) MSW. However, the MSW properties will change dramatically, as a result of the mandatory implementation of waste classification as per July 2019 [4]. According to the rules of the waste classification, domestic waste is mandatorily sorted into four categoriesdry waste, wet waste, recyclable waste and hazardous waste, among which the first one is used as the feedstock in incineration plants. Shanghai has been the first city to implement waste classification standards, followed by 46 other major cities in China by the end of 2020 [4]. As reported in Ref. [5], the moisture content of MSW for incineration will drop by 13.6%, while the heating value will increase by 16.2%, due to the implementation of the new waste classification. This will significantly impact the operation status of the existing MSW incinerators, such as combustion instability and inefficiency [6]. The current incinerators designed and operated based on the previous MSW properties, need to be adjusted or retrofitted urgently

Computational fluid dynamics (CFD) simulation, which can predict the heat and mass transfer, reactions, and distribution of products, has been widely applied in MSW incineration for design and optimization [7]. Both commercial and open-source software are developed for better application of CFD simulation in multiple

* Corresponding author.
E-mail addresses: tig@energy.aau.dk, chy@energy.aau.dk (T. Gu), chy@et.aau.dk (C. Yin).

https://doi.org/10.1016/j.energy.2022.124338
0360-5442/

Nomenclature

Symbols

A	pre-exponent factor (s^{-1})
b	temperature order
C_{pg}	gas specific heat capacity (J/(kg K))
C_{ps}	solid specific heat capacity (J/(kg K))
D_g	effective gas diffusivity (m^2/s)
d_p	solid particle diameter (m)
E	activation energy (J/kmol)
h_f	standard enthalpy of formation (J/mol)
h_M	
h_T	heat transfer coefficient (W/(m^2 K))
K	bed permeability
k_{eff}	effective thermal conductivity (W/(m K))
k_g	gas thermal conductivity (W/(m K))
k_s	solid thermal conductivity (W/(m K))
P	gas pressure (Pa)
R	universal gases constant (J/(mol K))
r	reaction rate (kg/(m^3 s))
S_g	conversion rate from solid to gas (kg/(m^3 s))
S_T	
t	time (s)
T	temperature (K)
T_{in}	initial temperature (K)
T_{rad}	radiation temperature (K)
T_∞	the freeboard temperature (K)
u	superficial gas velocity in bed model (m/s)
u_{avg}	volume-averaged velocity magnitude (m/s)
u_j	velocity magnitude of cell j (m/s)
u_i'	fluctuating velocity components (m/s)
V_j	volume of cell j in the zone (m^3)
V_{tot}	total volume of the zone (m^3)
Y_{ig}	mass fractions of gas species
$Y_{ig,in}$	initial mass fractions of gas species
$Y_{ig,s}$	gas mass fractions
Y_{is}	solid mass fraction
$Y_{ig,\infty}$	mass fraction of air
	mass transfer coefficient (m/s) *Greek letters*
β	drag force coefficient
ε	system emissivity
μ	mixture gas dynamic viscosity (Pa s)
σ	Boltzmann radiation constant (W/(m^2 K^4))
τ_{ij}	viscous stress in j dimension (Pa)
ρ_g	gas density (kg/m^3)
ρ_s	solid bulk density (kg/m^3)
ρ_{is}	bulk density of i solids composition (kg/m^3)
φ	bed void fraction
	source term of energy equation (J/(m^3 s)) *Abbreviations*
BASIC	Bulk Accumulated Solids Incineration Code
CFD	Computational fluid dynamics
MSW	Municipal solid wastes
TKE	Turbulent kinetic energy (J/kg)
UIV	Uniformity index for velocity
UDF	User-defined function
WtE	Waste to energy

scientific areas [8]. Furthermore, CFD simulation appears to be particularly important, due to the high cost of experimental investigations and the complexity of large-scale incinerators [9]. As a result, numerous CFD simulation studies on grate-firing MSW incineration have been conducted [10], in which the coupled modeling strategy is mostly employed [11]. Here the bed model provides the inlet boundary conditions, i.e., temperature, velocity and species profiles for the freeboard simulation. In return, the freeboard simulation quantifies the radiation heat flux to the fuel bed [12]. For example, Rajh et al. simulate a waste wood grate-firing incinerator using the coupled strategy [13]. A 1-D empirical bed model has been developed for describing the fuel bed conversion, and the freeboard simulation has been carried out using Ansys Fluent [14]. The in-depth analysis of the freeboard, e.g., the distributions of temperature, velocity and species are well performed, while the 1-D empirical bed model is not able to yield the details of the fuel bed during combustion

In order to better understand the solid fuel conversion process, Yang et al. developed a comprehensive bed model named FLIC (Fluid Dynamic Incineration Code) and coupled it with the freeboard simulation [15]. Comprehensive modeling of the solid conversion on the grate is a significant step forward, and it further increases the accuracy and validity of the freeboard simulation [16]. Subsequently, various simulation studies using the 'FLIC + Fluent' mode have been attempted, such as Lin's study of MSW and sludge co-combustion [17], and Yan's study of the impacts of pre-heating primary air [12]. However, the simulation study on MSW feedstock diversities due to waste classification has not been investigated. The adjustment for meeting feedstock diversity needs to be explored. Furthermore, the previous bed model can be improved from the modeling perspective, such as bed porosity variation, multiple reactions, etc. [18]. Our previous study, which produces an advanced in-house bed model BASIC (Bulk Accumulated Solids Incineration Code), has reviewed the shortcomings of existing bed models and further works for improvement [19]. Afterward, CFD simulation of MSW boiler coupled with the advanced bed model is needed, to complete the advanced modeling work of MSW grate-firing.

To sum up, the simulation study targeting waste classification in China is crucial and urgent. Advanced modeling work for grate boiler simulation should also be conducted. Bearing this in mind, this paper simulates a 750 t/d MSW moving grate boiler in 4 cases by CFD coupled with the in-house bed model. The objectives of this study are

1) to develop and validate the advanced model for moving-grate boilers (Case 1)
2) to investigate the impacts of feedstock change (Case 2a)
3) to adjust air supply to better accommodate the new feedstock (Case 2 b)
4) to expand thermal input for benefiting the boiler operation (Case 2c)

The findings are of great significance in guiding the boiler operation for incinerating the new MSW, in order to address the potential consequences due to the waste classification.

2. Modeling and simulation description

In grate-firing incinerators, the solid fuel is converted to gases on the grate via drying, pyrolysis, char oxidation and gasification processes [20]. The drying and devolatilization fronts typically migrate downward from the top of the bed, but char burning moves upward from the bottom due to insufficient oxygen supply in the

primary air [17]. The produced gases with combustibles flow into freeboard and burn out with the secondary air (SA) supply, as shown in Fig. 1(a). Therefore, the coupled strategy, i.e., modeling the fuel bed and freeboard separately and then coupling them together, is usually used in modeling grate-firing boilers and also in this work, as presented in Fig. 1(b). The 2D steady moving-grate bed model is mapped from an in-house 1D transient fixed-bed model, since the combustion mechanisms are the same in the two beds [16]. The combustion metrics at the x-meter point of the grate are the same as those at time $t\,(x = x_0 + u_{grate}t)$ of the fixed bed, where x_0 denotes the initial position of the grate, and u_{grate} is the grate moving rate [21]. The transformation diagram of the bed model is presented in Fig. 1(b). In this study, the residence time of MSW is 5400 s, therefore the 2D fuel bed is divided into 540 slices along the grate length. The unit fuel bed (in one slice) is modeled by the fixed-bed model with the results recorded every 10 s, for mapping them to each fuel bed slice on the moving grate.

2.1. Framework of the bed model

The 1D transient in-house bed model, which describes the solids conversion process and heat and mass transfer in a dense fuel bed, has been first developed and presented in detail in our previous work [19]. Here, the model is briefly summarized, in which the differences between the literature work and our previous work are highlighted. It is assumed that the volatiles are converted to carbon monoxide (CO), carbon dioxide (CO_2), methane (CH_4), hydrogen (H_2) and water vapor (H_2O) during the devolatilization process [22]. The conversion coefficients of CO, CO_2, CH_4, H_2 and H_2O are calculated by the elements and heat balance. The gases released from the bed consist of oxygen (O_2), H_2O, CO, CO_2, CH_4, H_2 and nitrogen (N_2). Compared to the previous bed models, our new bed model refines the boundary conditions, from zero-gradient to heat and mass transfer between the bed and the freeboard. Additionally, the lumped volatile is replaced by a mixture of gas species to adapt the diversity of MSW [23]. More homogeneous reactions with H_2O are considered as well, for a better description of the high-moisture MSW combustion. Besides, several key updates of the bed model are implemented in this study, to more reasonably describe the combustion process on moving grates, as summarized in Table 1.

The governing equations and boundary conditions of the latest bed model are summarized in Table 2 and Table 3, respectively. All the corresponding variables are explained in the Nomenclature table.

2.2. Three-dimensional CFD modeling of the boiler freeboard

The three-dimensional CFD simulation of the freeboard is performed using ANSYS, i.e., the geometry is abstracted in ANSYS SpaceClaim, the mesh is created in ANSYS ICEM, and ANSYS Fluent is applied as the CFD solver. The targeted boiler, the methods used and major achievements in each section are elaborated below.

2.2.1. Boiler description

The 750 t/d moving-grate MSW boiler with a designed thermal capacity of 65.42 MW_{th} is targeted in this study, as shown in Fig. 2. The grate comprises five sub-grates each with its independent air supply, where the length of each first four sub-grate is 2.0625 m, the length of the last one is 2.75 m. The initial bed height is approximate 1 m, and MSW stays roughly 1.5 h until the end of the grate, where the ash leaves into the ash pit. The SA nozzles of φ 50 mm and φ 80 mm (20 of each) are distributed on the front and rear walls with a horizontal angle of 20°. The cold-water pipes are attached to the boiler walls in the vertical chamber. Several heat exchangers further cool down the flue gas in the last section of the boiler.

The properties of the two different feedstocks are summarized in Table 4. Feedstock 1 is currently combusted in the boiler, Feedstock 2 refers to the new MSW composition due to the waste classification, which will be incinerated in the same boiler in the upcoming future. The fuel properties of Feedstock 2 are derived based on the identical volatile with Feedstock 1, and the changes in moisture and heating value reported in Ref. [5]. The volatile with 18,780 kJ/kg heating value for the two feedstocks is converted into

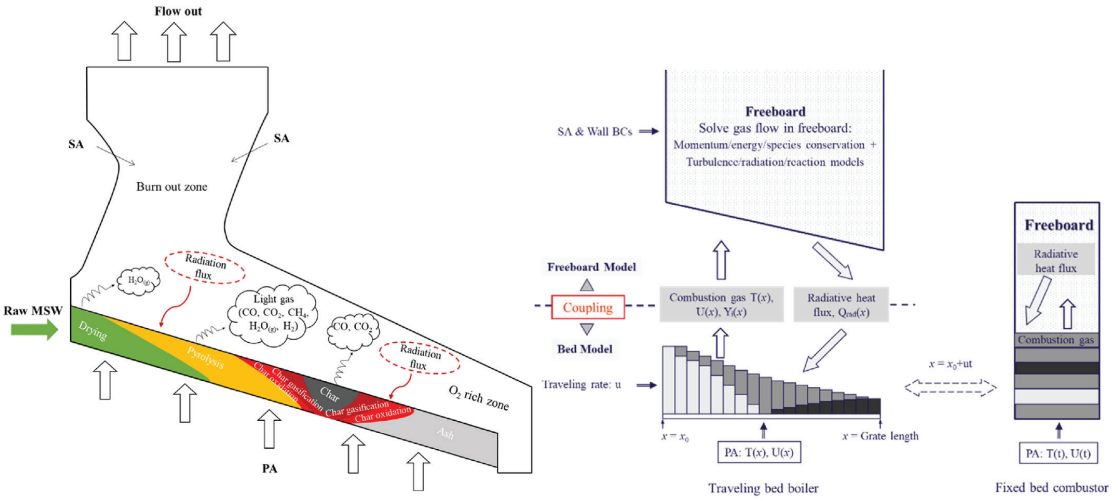

Fig. 1. Sketch of the MSW grate-firing incinerator and the modeling strategy.

Table 1
Summary of the major updates of the in-house bed model over our previous work.

Term	Our previous work [19]	This study
Solid continuity equation	Update bulk solid density	Update porosity
Solid mixing	Not considered	Add a diffusion term in solid species transport equations [16]
Char reaction	$C+\alpha O_2 = 2(\alpha-1)CO+(2\alpha-1)CO_2$	$C+\alpha O_2 = 2(\alpha-1)CO+(2\alpha-1)CO_2$ $C+CO_2 = 2CO$ $C+H_2O = CO+H_2$ [24]
CO combustion chemical rate	$r_{co} = R_1$	$r_{co} = \begin{cases} R_1, & H_2O>0 \\ R_2, & H_2O=0 \end{cases}$
Radiation from the freeboard	Fixed value	Profile exported from Fluent
Air supply	Fixed flowrate	Segmented flowrate along the grate
Inlet diffusion of species	Yes	Removed to keep mass balance accurately

a $R_1 = 2.239\times10^{12}\exp\left(-\frac{1.702\times10^5}{RT}\right)CO\cdot O_2^{0.25}\cdot H_2O^{0.5}$

b $R_2 = 7.05\times10^6\exp\left(-\frac{9.68\times10^4}{RT}\right)CO$ [25]

Table 2
Summary of the governing equations of the bed model.

Gas continuity	$\frac{\partial(\varphi\rho_g)}{\partial t}+\nabla\cdot(\rho_g\mathbf{u}) = S_g$
Gas species	$\frac{\partial(\varphi\rho_g Y_{ig})}{\partial t}+\nabla\cdot(\rho_g\mathbf{u}Y_{ig}) = \nabla\cdot(D_g\nabla(\varphi\rho_g Y_{ig}))+S_{ig}$
Gas momentum	$\frac{\partial(\varphi\rho_g u)}{\partial t}+\nabla\cdot(\rho_g\mathbf{u}u) = -\nabla P-\frac{\mu u}{K}-\beta\rho_g u^2$
Solid continuity/Porosity model	$\frac{\partial((1-\varphi)\rho_s)}{\partial t} = -S_g$
Solid species	$\frac{\partial((1-\varphi)\rho_s Y_{is})}{\partial t} = \nabla\cdot(D_s\nabla((1-\varphi)\rho_s Y_{is}))+r_{is}$
Energy equation	$\frac{\partial(\varphi\rho_g C_{pg}T+(1-\varphi)\rho_s C_{ps}T)}{\partial t}+\nabla\cdot(\rho_g\mathbf{u}C_{pg}T) = \nabla\cdot(k_{eff}\nabla T)+S_T$

Table 3
Boundary conditions of the bed model.

Boundary conditions at bed bottom	$\rho u = \rho_{in}u_{in};\ \frac{\partial P}{\partial x}=0$ $Y_{ig} = Y_{ig,in};\ Y_{is} = Y_{is,in}$ $T = T_{in}$
Boundary conditions at bed top	$\frac{\partial u}{\partial x}=0;\ P\equiv P_{atm}$ $A\frac{\partial Y_{ig}}{\partial x} = Ah_M(Y_{ig,\infty}-Y_{ig});\ \frac{\partial Y_{is}}{\partial x}=0$ $k_{eff}A\frac{\partial T}{\partial x} = Ah_T(T_\infty-T_s)+Ae\sigma(T_{rad}^4-T_s^4)$

light gases according to Eq. (1).

$$\text{Volatile (CH2·731O0.8522)} \equiv 0.251CO + 0.220CO_2 + 0.136H_2 + 0.530CH_4 + 0.150H_2O \quad (1)$$

The operation conditions for the four cases are listed in Table 5, in which Case 1 is the current operation condition incinerating Feedstock 1. The characteristics and adjustments of the new MSW, i.e., Feedstock 2, incineration are investigated in Case 2a, 2 b and 2c.

2.2.2. Freeboard modeling methods

Fig. 3 presents the computational domain of the CFD simulation for the boiler. The furnace (orange color) can be divided into two parts: combustion zone, which is under the SA supply, and vertical chamber, which attaches water pipes on the walls. To perform reliable CFD simulation, a high-quality mesh is achieved in advance as shown in Fig. 4. The mesh, with 16,221,691 cells in total, is created as structured hexahedral mesh using ANSYS ICEM. The mesh qualities for various criteria are presented in Table 6. Compared to the usually used millions of cells in the similar scale boiler simulation, the meshes used in this work are considered dense enough to obtain the practically mesh-independent solutions [26].

The 3-D steady simulation of the freeboard is carried out using Ansys Fluent 19.1. A User-defined function (UDF) has been compiled to input the bed model results, i.e., temperature profile, velocity profile, and gas species fractions. The radiation properties of the mixture gas are modeled by a refined weighted sum of gray gases model (WSGGM) via the other UDF file, which is more reliable than the default one in Fluent [27]. The gas reactions and their corresponding chemical kinetics are presented in Table 7. The key models and numerical methods used in this study are summarized in Table 8.

3. Results and discussion

The simulation results for the four cases and the relevant discussion are illustrated in this section, as well as the mesh and time-step independence tests and the model validation. In order to more deeply analyze the fluid flow in the freeboard, quantitative analysis in terms of mixing and uniformity is also carried out in this section.

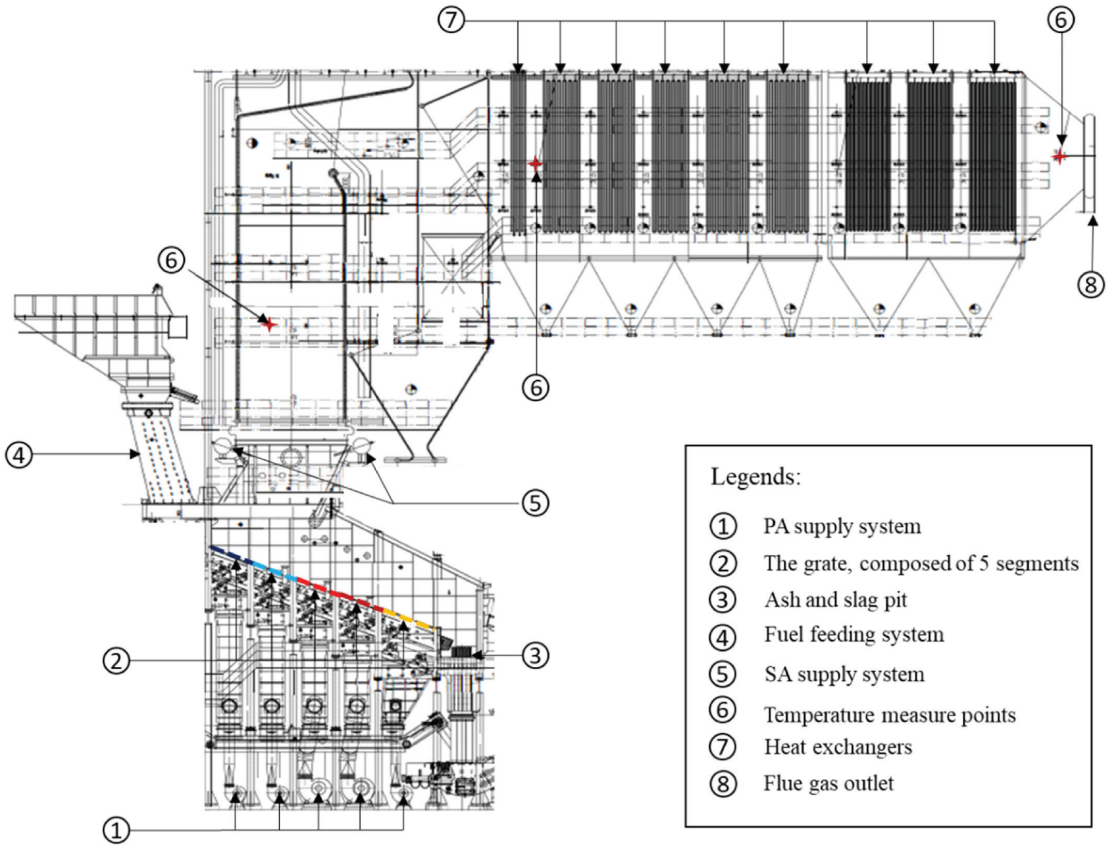

Fig. 2. Design diagram of the 750 t/d MSW grate boiler.

Table 4
Proximate and ultimate analysis of the feedstocks.

MSW	Proximate analysis, wt% ar[a]				Ultimate analysis, wt% daf[b]						LHV, kJ/kg ar[a]
	Moisture	Volatile	Fixed carbon	Ash	C	H	O	N	S	Cl	
Feedstock 1	45.40	31.90	8.10	14.60	52.63	7.45	36.91	1.19	1.12	0.70	7536
Feedstock 2	39.23	41.25	10.48	9.04	52.63	7.45	36.91	1.19	1.12	0.70	10,223

[a] As received basis (ar).
[b] Dry ash free basis (daf).

3.1. Mesh and time-step independence tests

In order to evaluate the mesh independence, the bed model results are compared with mesh numbers 400, 500 and 600, respectively. Fig. 5(a and b) compares the two key profiles, i.e., the solid mass and the top surface temperature, which shows no significant difference. On the other hand, Fig. 5(c and d) compares the bed model results using different time steps i.e., 0.02 s, 0.01 s and 0.005 s. The comparison shows that the bed model results with time-step 0.02 s are very different from those with a smaller time-step, while the results with time-step 0.01 s and 0.005 s show only minor differences. Considering computational efficiency, the mesh number 500 and time-step 0.01 s are used in the bed model for all the cases under study.

3.2. Case 1 – simulation and validation of real incineration of the current feedstock

3.2.1. Bed model results

After four times of coupling, the heat transfer rate at the bed top surface between the fuel bed and freeboard is consistent with each other. Fig. 6 illustrates the final modeling results from the bed model for Case 1. The 220 °C preheated primary air is segmentally supplied with the velocity of 0.146 m/s, 0.292 m/s and 0.073 m/ from the grate length of 0–4.2 m (the first two sub-gates), 4.2–8.3 m (the third and fourth sub-grates) and 8.3–11 m (the

Table 5
Summary of the operation conditions for different simulation cases.

Operation conditions		Unit	Case 1	Case 2a	Case 2 b	Case 2c
Thermal capacity		MW_{th}	65.42	65.42	65.42	71.96
Feedstock	Feeding rate	t/h	31.25	23.04	23.04	25.34
	Initial bed height	m	1	1	1	1
	Fuel resident time	h	1.5	1.5	1.5	1.5
Grate dimensions	Length	m	11	11	11	11
	Width	m	12.5	12.5	12.5	12.5
Overall air supply	Excess air ratio	(−)	1.2	1.2	1.2	1.216
	PA: SA	(−)	6:4	6:4	5:5	5:5
Primary air	Flow rate	kg/h	64,543	61,535	51,533	56,686
	Temperature	°C	220	220	220	220
	Distribution	%	15:15:30:30:10	15:15:30:30:10	14:16:34:28:8	14:16:34:28:8
Secondary air	Flow rate	kg/h	43,561	41,531	51,533	56,686
	Temperature	°C	40	40	40	40
	Nozzle diameter	mm	50/80	50/80	50/80	50/80
	Horizontal angle	°	20	20	20	20

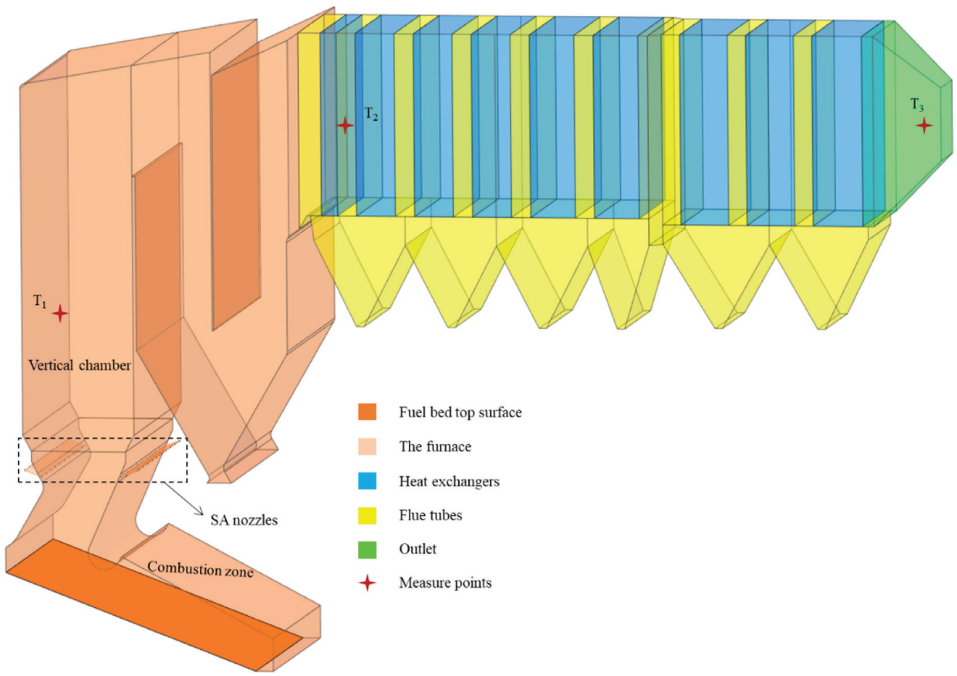

Fig. 3. The 3D CAD model of the MSW grate-firing boiler.

last sub-grate), respectively. Fig. 6(a) presents the mass of MSW and its components (moisture, volatile and char) on the grate. Fig. 6(b–h) presents the profiles of temperature, velocity, mass fractions of H_2O, O_2, CO, CO_2 and CH_4 at the bed top surface, ¾ height, ½ height, and ¼ height along the grate, respectively. Fig. 6(c) also shows the velocity profile at the bottom surface, i.e., the segmented PA supply. From the results, one can see the MSW incineration can be roughly divided into four stages. Stage I lies on the 0–2.88 m length of the grate, where the evaporation process is dominating. The devolatilization is progressing gradually and the fuel bed is heated up smoothly. Moisture vapor is released heavily, while the combustible gases, e.g., CO, CH_4, are liberated slowly, and volatile combustion is only limited to the fuel bed top and its vicinity as shown in Fig. 6(a,b,d,f,h).

Stage II, i.e., 2.88–7.44 m length of the grate, the drying, devolatilization and char reaction processes are progressing rapidly, as shown in Fig. 6(a). A large amount of volatiles are released and combusted from the top to bottom. The bed temperature increases dramatically after the homogeneous combustion fronts arrive, and remains stable, meanwhile the O_2 decreases to zero as a result of the rapid consumption. The volatile combustion dominates the temperature increase and O_2 consumption in Stage II. Due to the rise of PA supply from sub-grate II to sub-grate III at 4.125 m of the grate, the temperature increase and sharp peaks of gas mass fractions at that point, are captured in the profiles. Evaporation of the fuel bed is fully completed at 7.07 m of the grate, which is earlier

Table 6
The key qualities of the mesh under different criteria.

Total cells	16,221,691
Equiangle skewness (0–0.3 very high quality, 0.3–0.5 high, 0.5–0.8 acceptable)	>0.69: 0% 0.5–0.69: 0.73% 0.3–0.5: 5.33% 0–0.3: 93.94%
Angle (0–90°, the closer to 90° the better quality, should be greater than 18°)	>30° 30°–45°: 0.67% 45°–63°: 5.27% 63°–90°: 94.06%
Jacobian Matrix (0–1, should be greater than 0.2)	>0.342
Aspect ratio	1.42–9.41 5–9.41: 1.84% <5: 98.16%

Table 7
Kinetics of reactions in freeboard simulation (Units in m, s, kmol, J, K) [28].

Reactions	*A*	*b*	*E*	Rate orders
$CO + 0.5O_2 = CO_2$	2.239×10^{12}	0	1.7×10^{8}	$r = \frac{\partial[CO]}{\partial t} = k[CO][O_2]^{0.25}[H_2O]^{0.5}$
$H_2 + 0.5O_2 = H_2O$	6.8×10^{15}	−1	1.67×10^{8}	$r = \frac{\partial[H_2]}{\partial t} = k[H_2]^{0.25}[O_2]^{1.5}$
$CH_4 + 1.5O_2 = CO + 2H_2O$	5.012×10^{11}	0	2×10^{8}	$r = \frac{\partial[CH_4]}{\partial t} = k[CH_4]^{0.7}[O_2]^{0.8}$

[a]. $k = AT^b e^{-E/(RT)}$

Table 8
Summary of the essential models and numerical methods used in this study.

Overall modeling strategy	Bed model coupled with freeboard simulation.
Fuel bed modeling	In-house bed model [19].
Freeboard simulation	ANSYS Fluent 19.1.
Turbulence model	Realizable $k-\varepsilon$ model with standard wall function, $I = 0.16Re_{D_H}{}^{-1/8}$ for calculation of the turbulence intensity for the inlet boundary condition [12].
Gaseous combustion	2-step Westbrook and Dryer (WD) mechanism for light hydrocarbons, one-step global combustion mechanism for H_2, finite rate/eddy-dissipation model for turbulence-chemistry interaction [29].
Radiation model	P-1 model, a refined WSGGM for evaluation gases radiation properties [30].
Flow through heat exchangers	Porous zone with pressure and heat drops.
Boundary conditions	Velocity inlet, pressure outlet, temperature thermal condition for walls.
Numerical methods	SIMPLE algorithm; 2nd order upwind scheme for all transport equations.

than the completion of devolatilization i.e., 7.50 m of the grate. The accomplishment of devolatilization indicates the ending of Stage II and the beginning of Stage III.

Stage III, i.e., only char reaction stage, lies on 7.44–9.20 m length of the grate. Due to the reduction of the PA supply at 8.3 m length of the grate, Stage III can be divided into two parts, i.e., 7.44–8.3 m length and 8.3–9.2 m length of the grate. Unlike volatile combustion, the char reactions, i.e., oxidation and gasification, propagate upwards. The temperature at ¼ height of the bed increases first, and the top surface temperature increases last. In the first half Stage III, because of the large amount of O_2 supply, the temperature goes up rapidly and reaches a peak with a maximum value of 1535 K at 8.3 m shown in Fig. 6(b). O_2 is consumed and close to zero, which attributes to the dynamic balance of the reactions. Meanwhile, the high temperature accelerates the gasification reaction a lot, leading to the remarkable increase of CO and decrease of CO_2 in the first half Stage III as shown in Fig. 6(f and g). In the second half Stage III, O_2 supply is reduced, and the char consumption rate slows down. The temperature begins to decline, consequently, the gasification reaction rate decreases and the oxidation rate rises up relatively. As a result, the mass fraction of CO decreases and CO_2 increases in the second half Stage III as shown in Fig. 6(f and g). The temperature at ½ height, ¾ height and the top surface rise to a second peak, since the increase of the oxidation reactions. Whereas the temperature at ¼ height goes down continually because the char is already completely consumed. The O_2 mass fraction returns to air level after the local char burns out as shown in Fig. 6(e), CO and CO_2 mass fractions in the bed turn to zero after the full consumption of the remaining char as shown in Fig. 6(f and g).

Stage IV, i.e., 9.20–11 m grate length, is the last stage, where all the reactions are accomplished. Temperature goes down by the PA flow and finally remains stable, O_2 at the top surface increases to air level after the char totally burned out, only ash and very few char residuals are left on the grate.

3.2.2. Model validation and the freeboard simulation results

After calculation of the bed model, the obtained results are integrated into the freeboard simulation. The model is validated by comparing the final simulation results, i.e., after the coupling convergence, with the operation data inside the boiler as listed in Table 9. The simulation shows a good agreement with the operation data, the accuracy fills the requirements of engineering application.

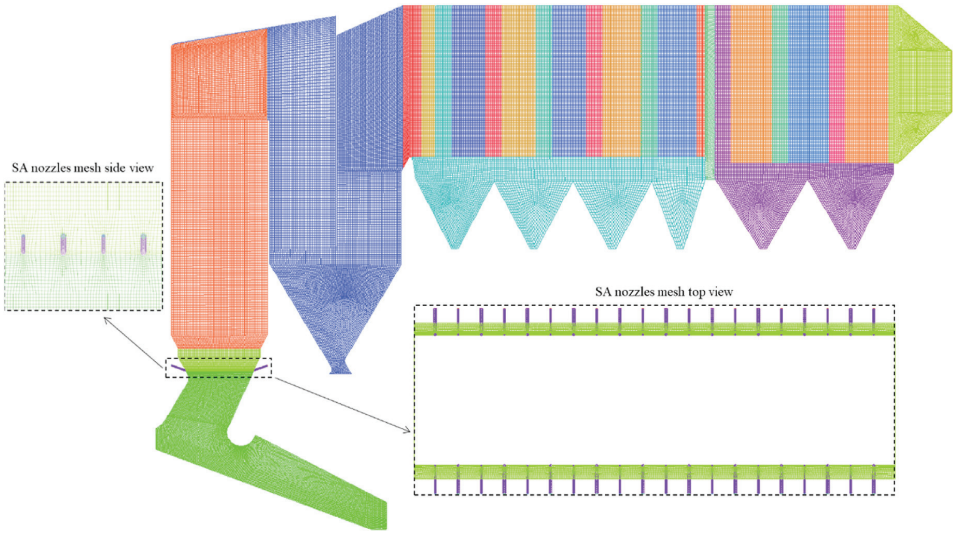

Fig. 4. The shell meshes of the outer walls and the mesh elements nearby the SA nozzles.

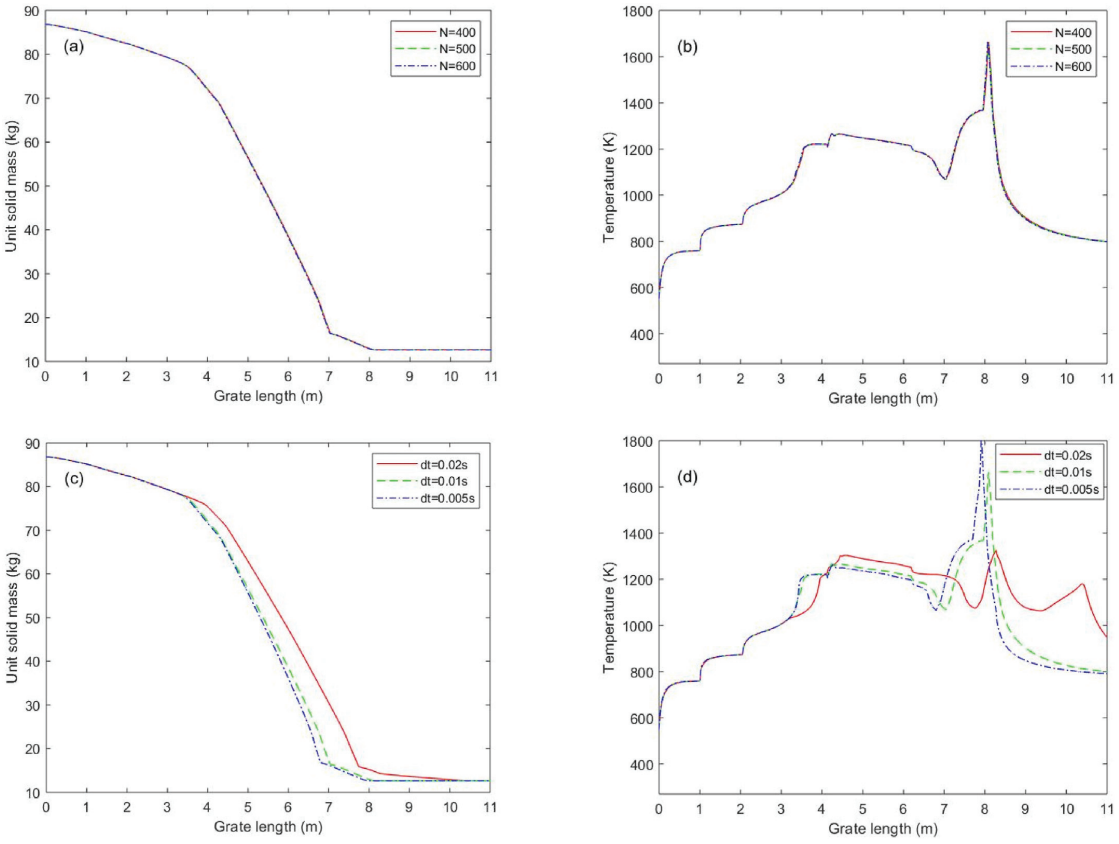

Fig. 5. Mesh and time-step independent tests of the bed model.

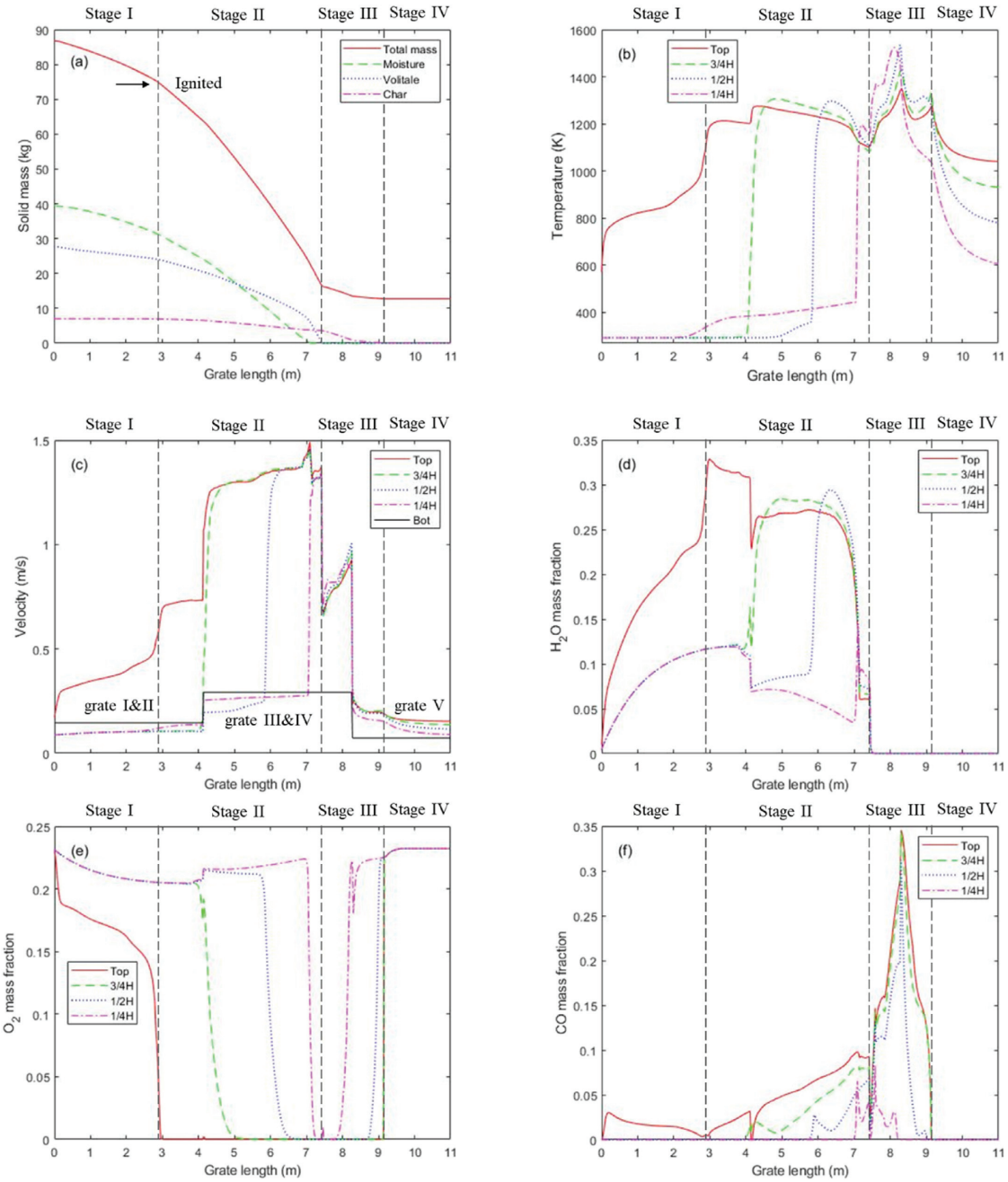

Fig. 6. Case 1 – The bed model results of solid mass (a), temperature profile (b), velocity profile (c), H_2O (d), O_2 (e), CO (f), CO_2 (g) and CH_4 (h) mass fractions at different bed heights along the grate.

Thus, we conclude that the model is validated, and it can be used for investigation of the boiler.

Fig. 7 presents the contours of temperature, O_2, CO, CO_2, H_2O and CH_4 mass fractions of the flue gas at the middle plane of the freeboard for Case 1. The following conclusions are revealed. First, the incineration of the combustibles causes the high temperature of flue gas in the furnace. The peak temperature is 1720 K, occurring nearby the SA nozzles due to O_2 supply and mixing. Then the flue gas flows into the vertical chamber, where it is cooled down by the water pipes, resulting in an average temperature of 670 K before entering the heat exchanger zone. Second, distributions of gas species in the combustion zone are consistent with the species profiles released from the bed, i.e., the water vapor is liberated first, followed by CH_4, CO and CO_2. An O_2-rich area is formed above the sub-grate V in the combustion zone. The combustibles are mainly consumed in the combustion zone, a small amount of CO is burned out in the vertical chamber. Here CO_2 and H_2O become the dominant species in the flue gas besides N_2. At last, the flue gas finally flows out from the boiler outlet surface after interacting with several heat exchangers. The final area-weighted average mass fractions of O_2, CO_2 and H_2O at the boiler outlet are 3.04%, 18.46% and 16.92%, respectively.

3.3. Case 2a and 2 b — impacts of feedstock change and suggested adjustment of air supply

The simulation of Case 2a for the new MSW (Feedstock 2) is performed under the same operation conditions as Case 1, i.e., thermal capacity, the excess air ratio, and PA distribution rate along the grate, etc. Due to the higher quality of the new MSW, the feeding rate and the total combustion air are reduced from 31.25 t/h to 23.04 t/h and from ca. 108.1 t/h to 103.1 t/h, respectively. Based on the simulation results, the main impacts or problems are summarized in Table 10. To accommodate the new feedstock better, some actions made accordingly in Case 2 b are also shown in Table 10. The detailed operation conditions of Case 2a and Case 2 b are presented in Table 5, and the simulation results are demonstrated and compared below.

3.3.1. Bed model results of the new feedstock incineration

The results from the bed model, i.e., solid mass, velocity profile, temperature profile, mass fraction profiles of gas species, for Case 2a (left) and Case 2 b (right) are presented in Fig. 8. The PA supply adjustment can be observed by comparing the velocity profile at the bottom surface as shown in Fig. 8(b). By comparing the simulation results from the two scenarios, various conclusions are drawn. First, numerous volatiles are ignited at 3.15 m and 2.86 m of the grate for Case 2a and 2 b, respectively. The slight reduction of the PA under the first sub-grate benefits for heating the bed. As shown in Fig. 8(e), the water vapor profiles of the two cases are similar, while the larger value of Case 2 b in Stage II is probably due to the downturn of the PA compare to Case 2a. Second, the completion point of evaporation and devolatilization are almost the same for the two cases, i.e., around 5.7 m and 6 m, respectively as shown in Fig. 8(a). In Stage III, CO and CO_2 mass fractions have no big difference between the two cases, due to the sufficient air supply for both cases as shown in Fig. 8(f and g).

Third, the char reaction stage of Case 2a is finished at 7.98 m of the grate resulting in a peak temperature of 1596 K. While the char reaction stage of Case 2 b is expanded a lot, accomplishing at 9.98 m. Meanwhile, the maximum temperature in this stage is decreased to 1523 K as shown in Fig. 8(a,c), which benefits the grate service life. In addition, the remarkable reduction of PA supply from sub-grate V slows down the remaining char reaction rate of Case 2 b, leading to the temperature decrease at 8.3—9.98 m of the grate as shown in Fig. 8(c). Consequently, the gasification rate is reduced, resulting in less CO and more CO_2 production as shown in Fig. 8(f and g). At last, after the combustion is fully accomplished, the mass fractions of the species produced by MSW down to zero, and the bed is cooled down by the PA supply. The final temperature at the top surface is 946.7 K for Case 2a and 988.6 K for Case 2 b, the O_2 mass fraction returns to the air level at 8.15 m and 10.04 m for Case 2a and 2 b, respectively.

Table 9
Comparison of the simulation with the operation data.

Temperature (K)	P1	P2	P3
Measurement data	1327.3	773.4	452.8
Simulation results	1264.8	730.0	482.1

3.3.2. Freeboard simulation results of the new feedstock incineration

Fig. 9 presents the freeboard simulation results of Case 2a (left) and 2 b (right), i.e., temperature contour and the major gas species

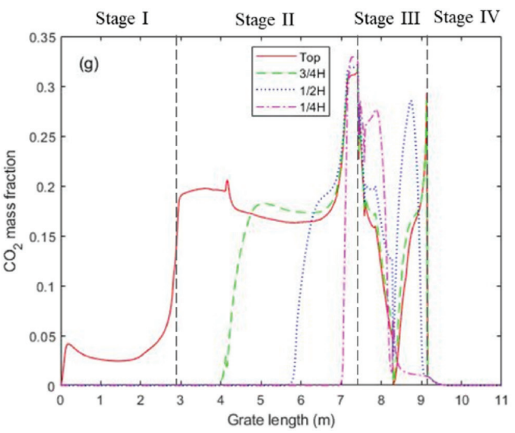

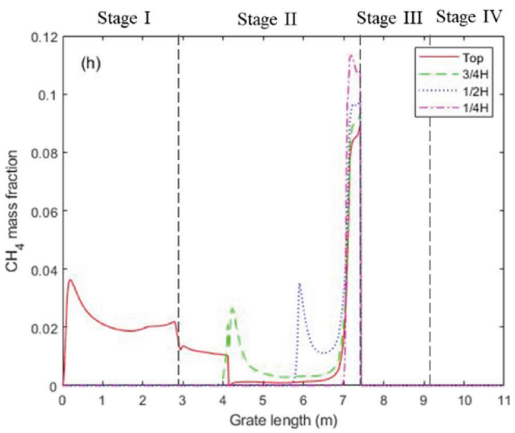

Fig. 6. (*continued*).

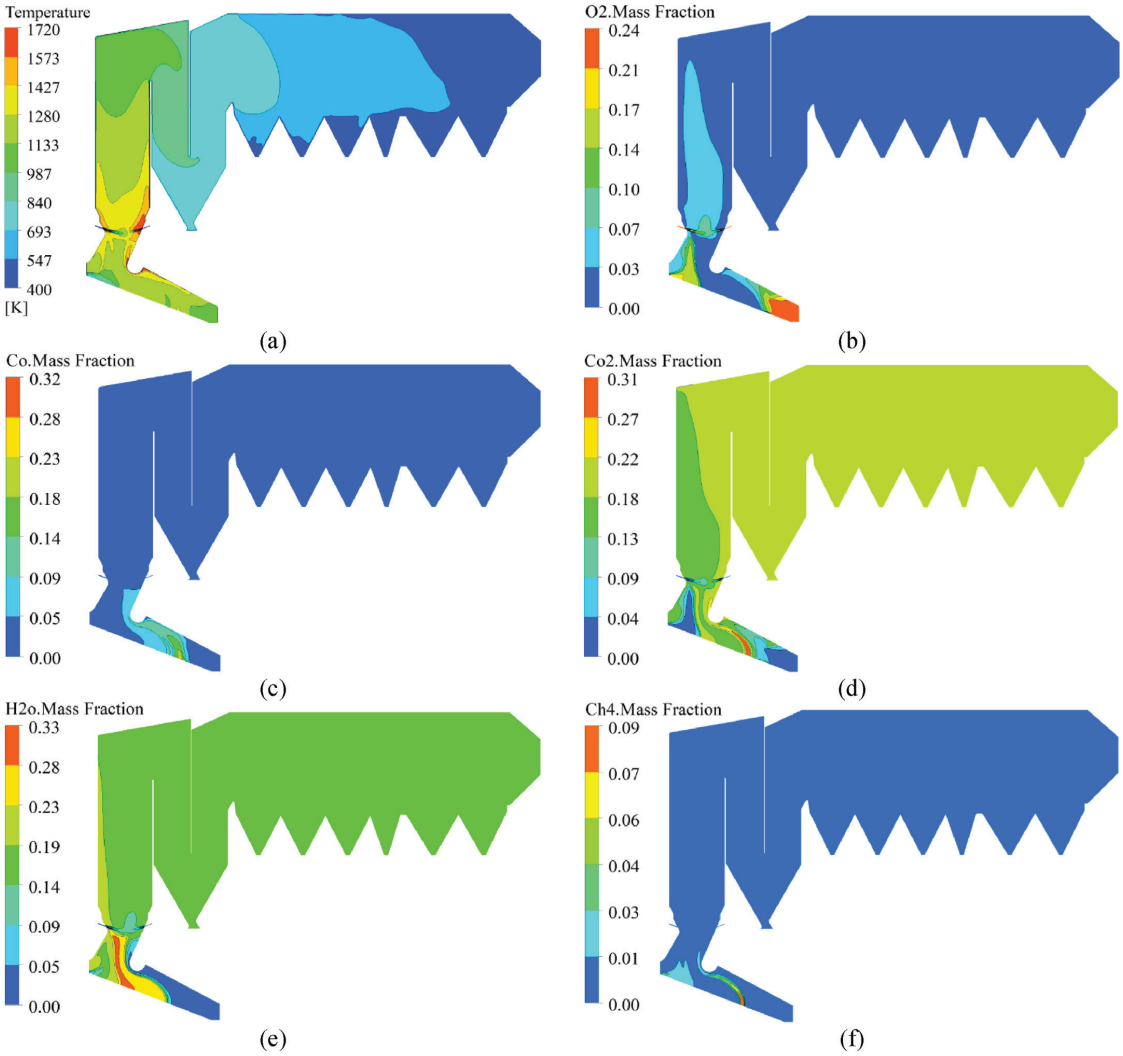

Fig. 7. Case 1 – Contours of temperature (a), mass fraction of O_2 (b), CO (c), CO_2 (d), H_2O (e) and CH_4 (f) of the flue gas at the middle plane of the freeboard.

Table 10
The impacts of switching to the new feedstock while retaining the current operation conditions vs. the corresponding actions to accommodate the new feedstock better.

Case 2a: Impacts or problems when switching to the new feedstock while retaining current operation conditions	Case 2 b: Adjustments of air supply to better accommodate the new feedstock
Reduced mixing due to reduced feedstock feeding rate and thus reduced SA supply	Change the overall PA/SA split ratio from the original 6:4 to 5:5
Evaporation finishes earlier due to lower feedstock moisture and pyrolysis/char reactions start earlier at the 2nd sub-grate	Reduce PA rate under the first sub-grate from 15% to 14%; increase PA under the second sub-grate from 15% to 16%
Too abundant PA supply in the last char burning stage	Increase PA rate at the third sub-grate from 30% to 34%; reduce PA at the fourth sub-grate from 30% to 28%
Earlier completion of the overall combustion in fuel bed, leading to a large O_2-rich area in the combustion zone	Reduce the overall PA supply and reduce PA rate of the last grate from 10% to 8%

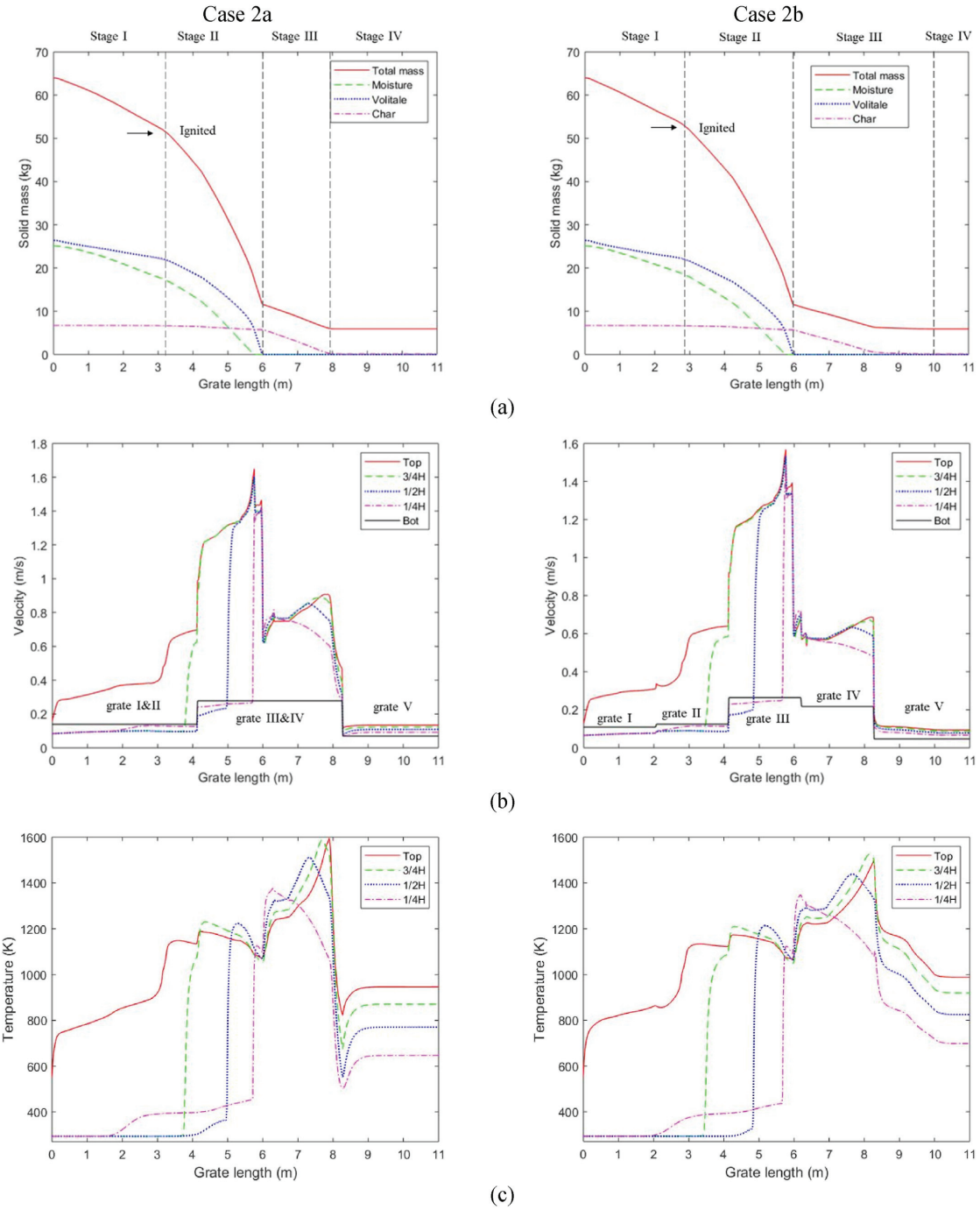

Fig. 8. Case 2a (left) vs. Case 2 b (right) – The bed model results of the solid mass (a), velocity profile (b), temperature profile (c), mass fraction of O_2 (d), H_2O (e), CO (f) and CO_2 (h) at different bed heights along the grate.

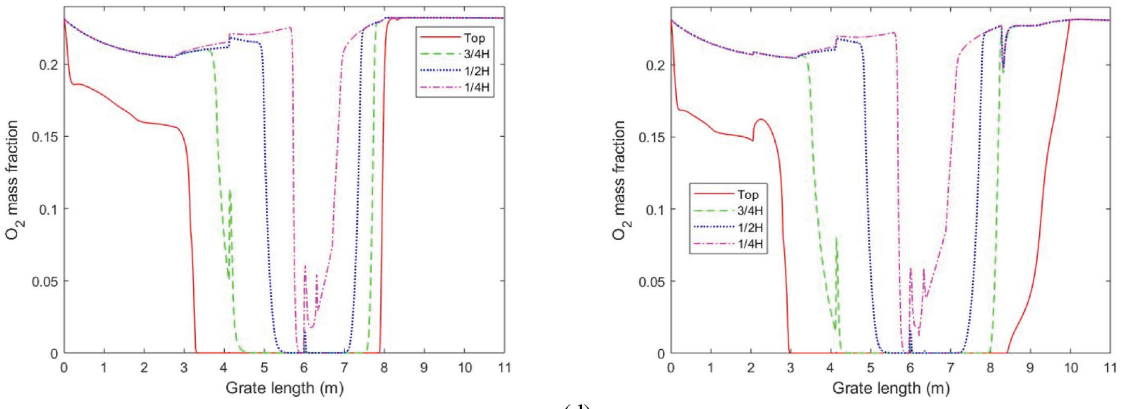

(d)

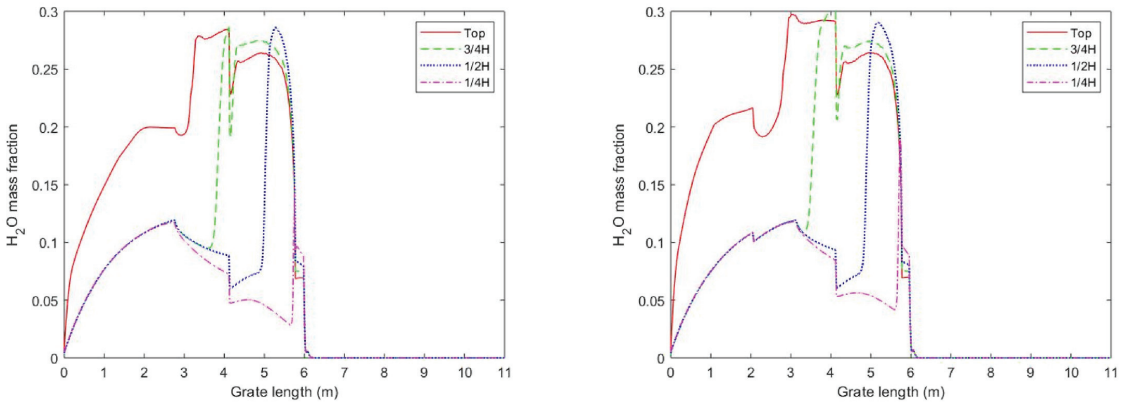

(e)

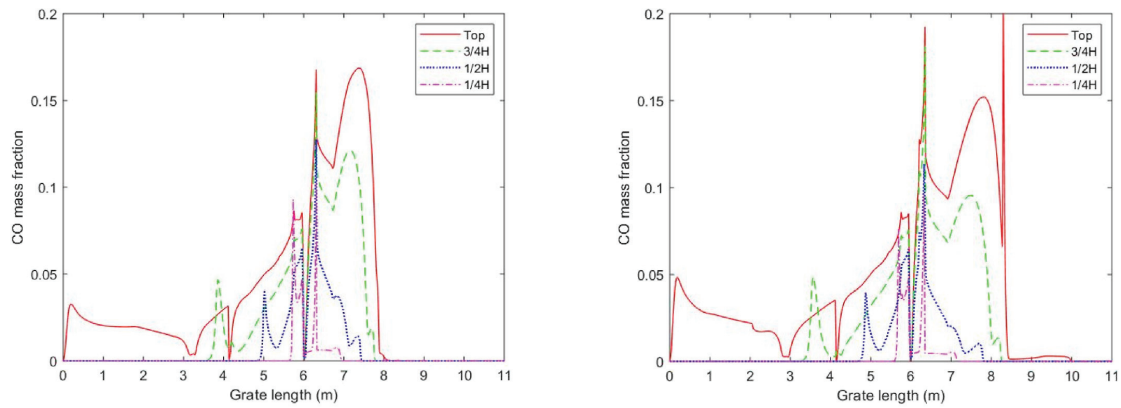

(f)

Fig. 8. (*continued*).

contours at the middle plane. Comparing the simulation results of the two cases, several conclusions are drawn. First, the temperature distribution in the freeboard is qualitatively similar, while the temperature value of Case 2 b is, in general, slightly higher than those in Case 2a as shown in Fig. 9(a). This can be attributed to the more combustible gases (mainly by CO) entering into the freeboard and the more O_2 supplement from SA of Case 2 b as shown in Fig. 9(c). Second, the O_2-rich area in Case 2a is apparently larger than those in Case 2 b, it leads to a larger low-temperature area in the combustion zone as illustrated in Fig. 9(a and b). The adjustment of the PA supply benefits the uniformity of the temperature distribution in the combustion zone. Third, the gas mixing is improved due to the enhancement of SA supply in Case 2 b. The majority of combustibles are burned out nearby the SA nozzles, where the O_2 was mainly consumed. In contrast, due to the lower mixing, O_2 has not been consumed sufficiently nearby the SA supply in Case 2a as shown in Fig. 9(b). At last, after the secondary combustion, the combustible gases are consumed and close to zero. Here O_2 mass fraction is reduced to around 3.3%, H_2O and CO_2 become the dominant species with the mass fraction of 13.8% and 19.5%, respectively. The area-averaged temperature at the outlet surface for the two cases are almost the same, i.e., 474.8 K for Case 2a, 474.4 K for Case 2 b.

In short, by comparing the simulation results of Case 2a and 2 b, it becomes clear that the air supply adjustments benifit the new MSW combustion in the following aspects:

1) The maximum temperature in the fuel bed is reduced, which is beneficial for the service life of the grate.
2) The mixing is improved, which ensures the secondary combustion in the furnace.
3) More combustibles enter into the freeboard, benefiting energy recycling.
4) The O_2-rich area is decreased, which is profitable for the uniformity of temperature distribution of the combustion zone.

3.4. Case 2c — investigation of expanding thermal capacity for the new feedstock incineration

The three scenarios above are all based on the boiler's designed thermal capacity, while the MSW mass consumption for the new feedstock incineration decreased by 26.3% compared to incinerating the current feedstock. On the other hand, the boiler is capable be operated at 110% of thermal capacity according to its specifications. In order to maintain the boiler's disposal ability and recycle more energy, characteristics of the boiler operation with 110% designed thermal capacity need to be investigated. In other words, the MSW disposal ability is increased by 10% without exceeding the maximum thermal capacity of the boiler for burning the new feedstock. The relevant simulation results of Case 2c are presented and discussed below.

3.4.1. Bed model results of the expanded thermal capacity case

Above all, the solids conversion and the profiles of temperature and the main species are very similar to those of Case 2 b, as presented in Fig. 10. The completion of the solid combustion process on the grate is almost the same as Case 2 b, i.e., around 10 m of the grate. That can be explained by the same fuel and air supply ratio and PA distribution. The homogeneous ignition of the fuel bed for Case 2c, i.e., 2.77 m, occurs a little bit ahead compared to that in Case 2 b, i.e., 2.86 m. This is probably because of the expanded thermal capacity in Case 2c, radiating more heat flux to the fuel bed. In addition, the maximum temperature of the bed reaches 1552 K, which is slightly higher than that in Case 2 b (1523 K), while it is still lower than that in Case 2a (1596 K). These results prove that the expanded thermal input operation will not lead to the extreme conditions of the fuel bed.

3.4.2. Freeboard simulation results of the expanded thermal capacity case

For the expanded thermal capacity operation Case 2c, the

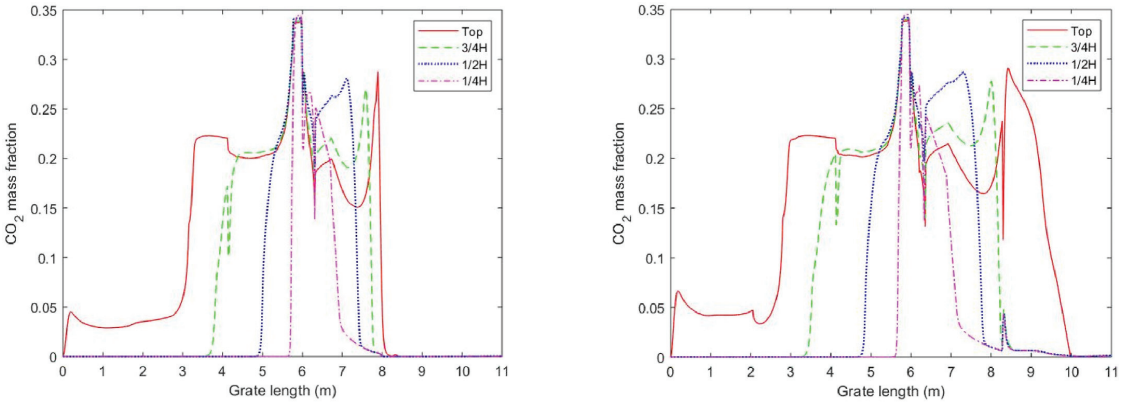

Fig. 8. (*continued*).

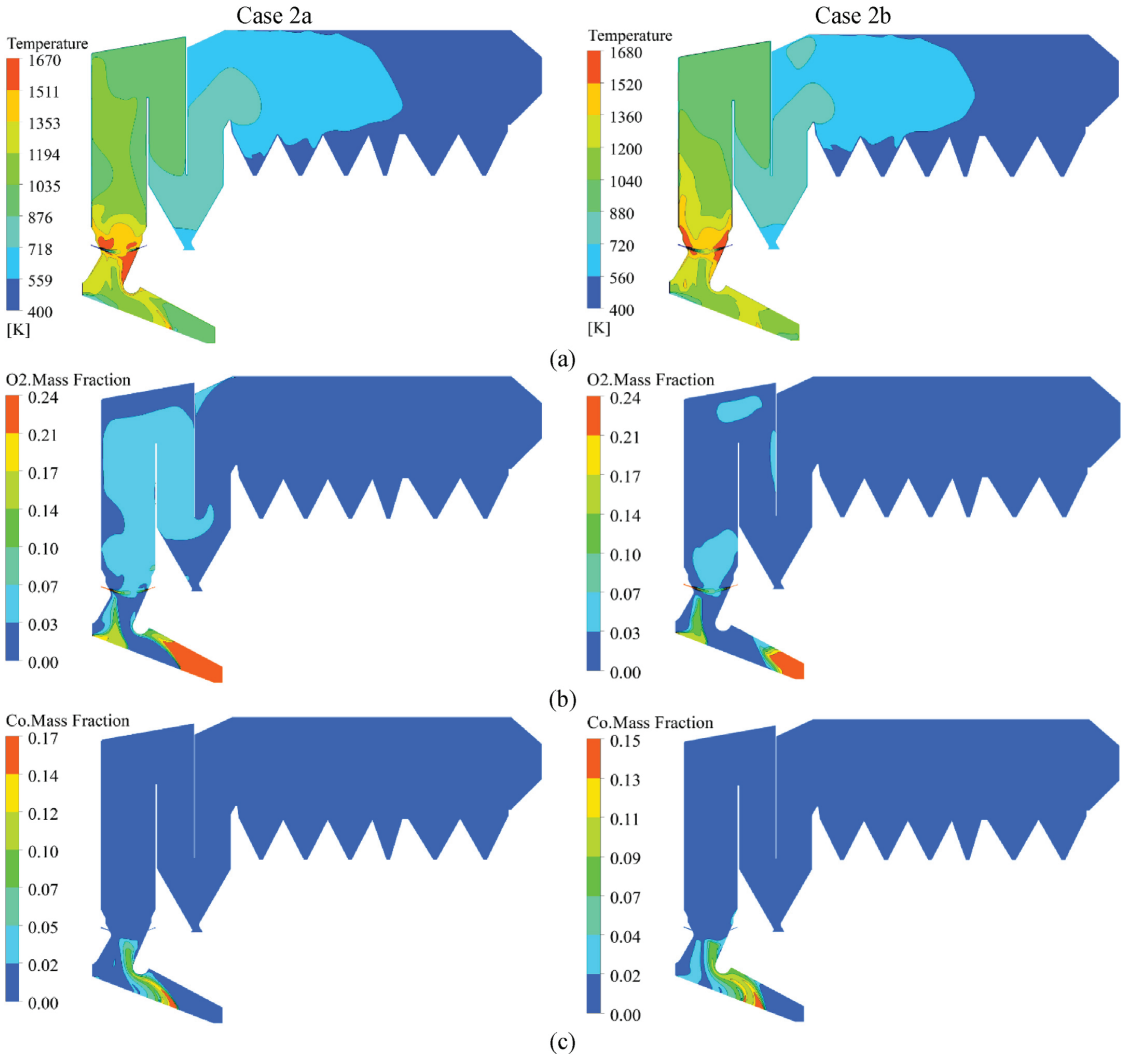

Fig. 9. Case 2a (left) vs. Case 2 b (right) – Contours of temperature (a), mass fraction of O_2 (b), CO (c), CO_2 (d) and H_2O (e) of the flue gas at the middle plane of the freeboard.

contours of temperature, O_2, CO and CO_2 mass fractions at the middle plane in the freeboard are presented in Fig. 11. The contours show similarity with those in Case 2 b. While the O_2 mass fraction in the vertical chamber of Case 2c is in general higher than those in Case 2 b as shown in Fig. 11(b). That is probably caused by more combustibles flowing into the freeboard by the expansion of the thermal input in Case 2c, and the combustibles are not completely consumed in the vertical chamber. The small contribution of combustion of the combustibles in the vertical chamber leads to a higher temperature than Case 2 b. At last, the area-averaged temperature at the outlet surface is 482.8 K, which is higher than that in Case 2a and 2 b. Guidelines for adjustments of the steam system can be consequently considered.

In short, expanding thermal capacity of the boiler for the new MSW incineration is feasible. The combustion process undergoes well maintaining the operation conditions used in Case 2 b, only

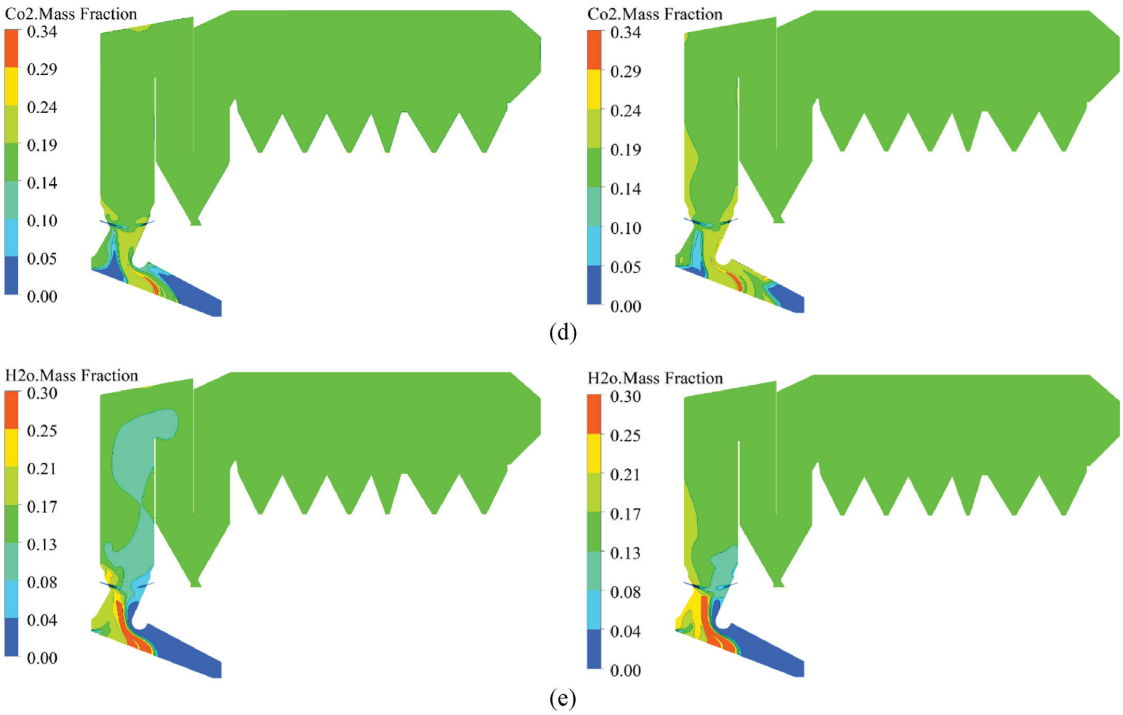

Fig. 9. (*continued*).

with more energy generation. The adjustment of the thermal input is effective for retaining the MSW disposal ability and power generation of the boiler for incinerating the new feedstock.

3.5. Comparison of the fluid flow of the cases incinerating the new MSW

To particularly analyze the fluid flow in freeboard of the new MSW incineration, the uniformity index for velocity (UIV) and mixing index, are defined and compared. The UIV is defined to characterize the global uniformity of the fluid flow as expressed in Eq. (2) [30].

$$\mathrm{UIV} = 1 - 0.5\sum_{j=1}^{n}\left|\left(\frac{u_j}{u_{avg}} - 1\right)\right| \cdot \frac{V_j}{V_{tot}} \tag{2}$$

Here n denotes the number of cells in the zone of interest, u_j and V_j represent the velocity magnitude and the volume of each cell j, u_{avg} and V_{tot} indicate volume-averaged velocity magnitude and total volume of the zone.

The turbulent kinetic energy (TKE) is used as a mixing index as defined in Eq. (3) [31].

$$\mathrm{k} = \frac{1}{2}\overline{u_i' u_i'} = \frac{1}{2}\left(\overline{u_x'^2} + \overline{u_y'^2} + \overline{u_z'^2}\right) = \frac{3}{2}\overline{u_i'^2} \tag{3}$$

where $\overline{u_i'}$ is average fluctuating velocity components ($i = 1, 2, 3$). The volume-averaged TKE of the zone is used to characterize the global mixing. According to the definition, the value of UIV is between 0 and 1, when the UIV equals 1, the fluid flow is completely uniform. On the other hand, the higher the TKE is, the stronger the mixing is. However, the higher TKE may lead to a lower UIV of the fluid flow, therefore a reasonable balance point between UIV and TKE is needed [30].

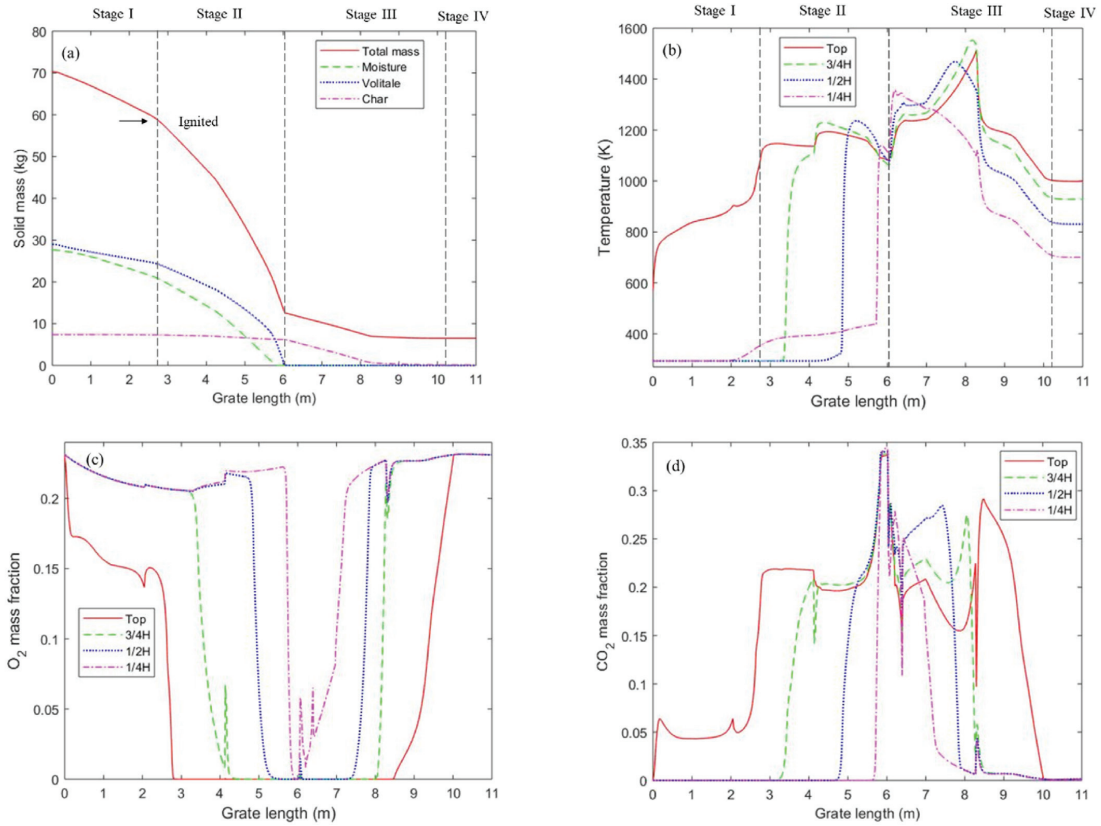

Fig. 10. Case 2c – The bed model results of the solid mass (a), temperature profile (b), O_2 (c) and CO_2 (d) mass fractions at different bed heights along the grate.

Fig. 12 compares the UIV and the volume-averaged TKE in the combustion zone (shown in Fig. 3) of Case 2a, 2 b and 2c. The UIV is slightly decreased, whereas the volume-averaged TKE increases remarkably due to the adjustments of air supply and fuel feeding rate. Using Case 2a as the normalized case, the UIV is reduced by 7.23% and 8.91% for Case 2 b and 2c, respectively. Whereas, the TKE increased by 51.39% and 81.04% for Case 2 b and 2c as shown in Fig. 12(b). These results agree with our expectation, i.e., increased mixing with a tiny sacrifice of uniformity by the adjustments of the air and feedstock supply. In addition, the expanded thermal capacity case with more feedstock and air supply is expected to improve the fullness of the boiler, which is considered to benefit the boiler stability [32].

4. Conclusions

In this paper, advanced CFD simulations of MSW incineration in an industrial grate-firing boiler have been carried out by the in-house bed model coupled with ANSYS Fluent. The simulation results are validated by the operation data inside the boiler at different points. Then, the model is deployed to analyze the new MSW combustion targeting the recently implemented waste classification regulations in China. Several disadvantages, i.e., too abundant O_2 supply for fuel bed, non-uniform temperature distribution and low mixing in freeboard, are captured for the new MSW combustion under current operation conditions. Subsequently, adjustments in air supply and thermal input are proposed and verified by the advanced CFD simulation, to better accommodate the new MSW incineration. The results prove that the adjustments are not only effective in addressing the potential issues, but benifit the boiler operation and energy recycling. At last, quantitative analysis of velocity uniformity and mixing, in the combustion zone is explored for different simulation cases. The adjustments of air supply and thermal input increase the mixing by 51.39% and 81.04%, respectively. The results provide crucial references for the boiler adjustments to meet the waste classification implementation.

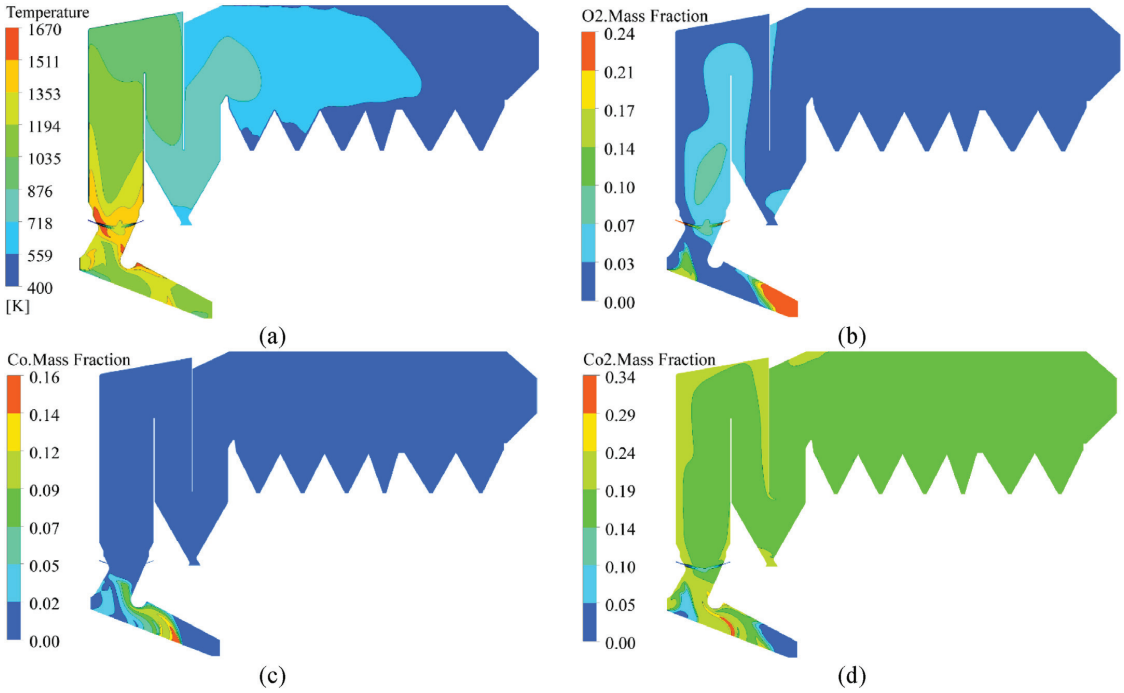

Fig. 11. Case 2c – Contours of temperature (a), O_2 (c), CO (c) and CO_2 (d) mass fractions of the flue gas at the middle plane of the freeboard.

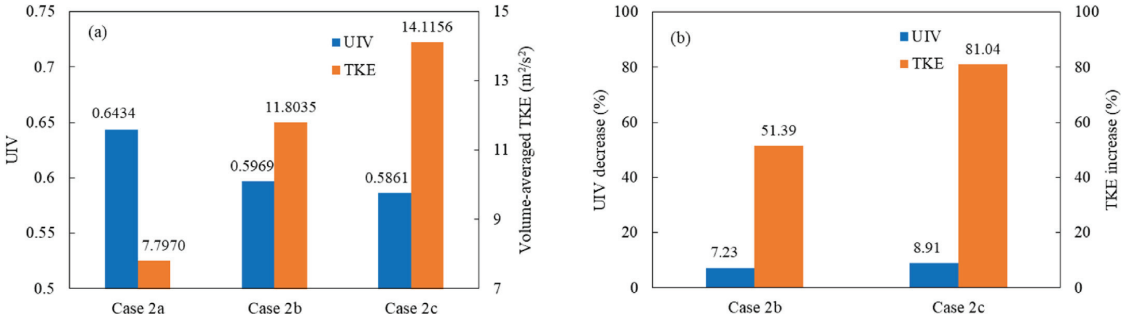

Fig. 12. Comparison of the absolute UIV and TKE of Case 2a, 2 b and 2c (a), and the variation of UIV and TKE of Case 2 b and 2c based on Case 2a (b).

Declaration of competing interest

The authors declare that they have no known competing financial interests or personal relationships that could have appeared to influence the work reported in this paper.

Acknowledgments

Tianbao Gu acknowledges China Scholarship Council (CSC) for the financial support of this PhD study at Aalborg University. This work was also partially supported by the National Key R&D Project of China [2020YFC1908604].

References

[1] Lu JW, Zhang SK, Hai J, Lei M. Status and perspectives of municipal solid waste incineration in China: a comparison with developed regions. Waste Manag 2017;69:170–86. https://doi.org/10.1016/j.wasman.2017.04.014.

[2] Yin C, Rosendahl LA, Kaer SK. Grate-firing of biomass for heat and power production. Prog Energ Combust 2008;34(6):725–54. https://doi.org/10.1016/j.pecs.2008.05.002.

[3] Cui CY, Liu Y, Xia B, Jiang XY, Skitmore M. Overview of public-private partnerships in the waste-to-energy incineration industry in China: status, opportunities, and challenges. Energy Strategy Rev 2020;32. https://doi.org/10.1016/j.esr.2020.100584.

[4] Tong YQ, Liu JF, Liu SZ. China is implementing "Garbage Classification" action. Environ Pollut 2020;259. https://doi.org/10.1016/j.envpol.2019.113707.

[5] Chen SS, Huang JL, Xiao TT, Gao J, Bai JF, Luo W, et al. Carbon emissions under different domestic waste treatment modes induced by garbage classification: case study in pilot communities in Shanghai, China. Sci Total Environ 2020;717. https://doi.org/10.1016/j.scitotenv.2020.137193.

[6] Zheng ZM, Yang WM, Wang H, Zhou AQ, Cai YT, Zeng G, et al. Development of a mechanistic fouling model for predicting deposit formation in a woodchip- fired grate boiler. Energy 2021;220. https://doi.org/10.1016/j.energy.2020.119699.

[7] Xia ZH, Long JS, Yan S, Bai L, Du HL, Chen CX. Two-fluid simulation of moving grate waste incinerator: comparison of 2D and 3D bed models. Energy 2021;216. https://doi.org/10.1016/j.energy.2020.119257.

[8] Ruckert FU, Lehser-Pfeffermann D, Theis D, Kim JP, Schargen A, Zorbach I, et al. A new simulation model for grate firing systems in OpenFOAM. Energy 2021;216. https://doi.org/10.1016/j.energy.2020.119226.

[9] Yin CG, Yan JY. Oxy-fuel combustion of pulverized fuels: combustion fundamentals and modeling. Appl Energy 2016;162:742–62. https://doi.org/10.1016/j.apenergy.2015.10.149.

[10] Costa M, Curcio C, Piazzullo D, Rocco V, Tuccillo R. RDF incineration modelling trough thermo-chemical conversion and gaseous combustion coupling. Energy 2018;161:974–87. https://doi.org/10.1016/j.energy.2018.07.142.

[11] Xu JC, Liao YF, Yu ZS, Cai ZL, Ma XQ, Dai MQ, et al. Co-combustion of paper sludge in a 750 t/d waste incinerator and effect of sludge moisture content: a simulation study. Fuel 2018;217:617–25. https://doi.org/10.1016/j.fuel.2017.12.118.

[12] Yan M, Antoni, Wang JY, Hantoko D, Kanchanatip E. Numerical investigation of MSW combustion influenced by air preheating in a full-scale moving grate incinerator. Fuel 2021;285. https://doi.org/10.1016/j.fuel.2020.119193.

[13] Rajh B, Yin C, Samec N, Hribersek M, Zadravec M. Advanced modelling and testing of a 13 MWth waste wood-fired grate boiler with recycled flue gas. Energy Convers Manag 2016;125:230–41. https://doi.org/10.1016/j.enconman.2016.02.036.

[14] ANSYS fluent theory guidevol. 15317. ANSYS Drive Canonsburg; 2021. Release 2021 R1 ed: ANSYS, Inc., 2600.

[15] Yang YB, Goh YR, Zakaria R, Nasserzadeh V, Swithenbank J. Mathematical modelling of MSW incineration on a travelling bed. Waste Manag 2002;22(4):369–80. https://doi.org/10.1016/S0956-053x(02)00019-3.

[16] Bin Yang Y, Swithenbank J. Mathematical modelling of particle mixing effect on the combustion of municipal solid wastes in a packed-bed furnace. Waste Manag 2008;28(8):1290–300. https://doi.org/10.1016/j.wasman.2007.04.012.

[17] Lin H, Ma XQ. Simulation of co-incineration of sewage sludge with municipal solid waste in a grate furnace incinerator. Waste Manag 2012;32(3):561–7. https://doi.org/10.1016/j.wasman.2011.10.032.

[18] Yang YB, Yamauchi H, Nasserzadeh V, Swithenbank J. Effects of fuel devolatilisation on the combustion of wood chips and incineration of simulated municipal solid wastes in a packed bed. Fuel 2003;82(18):2205–21. https://doi.org/10.1016/S0016-2361(03)00145-5.

[19] Gu TB, Yin CG, Ma WC, Chen GY. Municipal solid waste incineration in a packed bed: a comprehensive modeling study with experimental validation. Appl Energy 2019;247:127–39. https://doi.org/10.1016/j.apenergy.2019.04.014.

[20] Muthuraman M, Namioka T, Yoshikawa K. Characteristics of co-combustion and kinetic study on hydrothermally treated municipal solid waste with different rank coals: a thermogravimetric analysis. Appl Energy 2010;87(1):141–8. https://doi.org/10.1016/j.apenergy.2009.08.004.

[21] Sun R, Ismail TM, Ren XH, El-Salam MA. Numerical and experimental studies on effects of moisture content on combustion characteristics of simulated municipal solid wastes in a fixed bed. Waste Manag 2015;39:166–78. https://doi.org/10.1016/j.wasman.2015.02.018.

[22] Zhou H, Jensen AD, Glarborg P, Jensen PA, Kavaliauskas A. Numerical modeling of straw combustion in a fixed bed. Fuel 2005;84(4):389–403. https://doi.org/10.1016/j.fuel.2004.09.020.

[23] Zhou AQ, Xu HP, Yang WM, Tu YJ, Xu MC, Yu WB, et al. Numerical study of biomass grate boiler with coupled time dependent fuel bed model and computational fluid dynamics based freeboard model. Energy Fuel 2018;32(9):9493–505. https://doi.org/10.1021/acs.energyfuels.8b01823.

[24] Nugraha MG, Saptoadi H, Hidayat M, Andersson B, Andersson R. Particle modelling in biomass combustion using orthogonal collocation. Appl Energy 2019;255. https://doi.org/10.1016/j.apenergy.2019.113868.

[25] Babushok VI, Dakdancha AN. Global kinetic-parameters for high-temperature gas-phase reactions. Combust Explo Shock+. 1993;29(4):464–89. https://doi.org/10.1007/Bf00782974.

[26] Xia ZH, Shan P, Chen CX, Du HL, Huang J, Bai L. A two-fluid model simulation of an industrial moving grate waste incinerator. Waste Manag 2020;104:183–91. https://doi.org/10.1016/j.wasman.2020.01.016.

[27] Yin CG. Refined weighted sum of gray gases model for air-fuel combustion and its impacts. Energy Fuel 2013;27(10):6287–94. https://doi.org/10.1021/ef401503r.

[28] Zadravec T, Yin CG, Kokalj F, Samec N, Rajh B. The impacts of different profiles of the grate inlet conditions on freeboard CFD in a waste wood-fired grate boiler. Appl Energy 2020;268. https://doi.org/10.1016/j.apenergy.2020.115055.

[29] Hu ZF, Jiang EC, Ma XQ. Numerical simulation on NOx emissions in a municipal solid waste incinerator. J Clean Prod 2019;233:650–64. https://doi.org/10.1016/j.jclepro.2019.06.127.

[30] Rajh B, Yin C, Samec N, Hribersek M, Kokalj F, Zadravec M. Advanced CFD modelling of air and recycled flue gas staging in a waste wood-fired grate boiler for higher combustion efficiency and greater environmental benefits. J Environ Manag 2018;218:200–8. https://doi.org/10.1016/j.jenvman.2018.04.030.

[31] Versteeg HKMW. An introduction to computational fluid dynamics: the finite volume method. second ed. England: Pearson Education Limited; 2007.

[32] Li ZX, Qiao XQ, Miao ZQ. A novel burner arrangement scheme with annularly combined multiple air fl ows for wall-tangentially fi red pulverized coal boiler. Energy 2021;222. https://doi.org/10.1016/j.energy.2021.119912.

Paper D

Stable and Clean Co-combustion of Municipal Sewage Sludge with Solid Wastes in a Grate Boiler: A Modeling-based Feasibility Study

Tianbao Gu, Wenchao Ma, Zhenning Guo, Torsten, Berning and Chungen Yin

This paper has been submitted in the

Fuel, April 2022.

The layout has been revised.

Stable and clean co-combustion of municipal sewage sludge with solid wastes in a grate boiler: A modeling-based feasibility study

Tianbao Gu[a], Wenchao Ma[b*], Zhenning Guo[c], Torsten Berning[a], Chungen Yin[a*]

[a]*AAU Energy, Aalborg University, Aalborg, Denmark*
[b]*School of Environmental Science and Engineering, Tianjin University, Tianjin, China*
[c]*Institute of Technology, Everbright Envirotech (China) Ltd., Nanjing, China*

Corresponding authors: mawc916@tju.edu.cn, chy@energy.aau.dk

Abstract

Municipal sewage sludge not only has very high moisture content and low heating value but also carries lots of nitrogen, making it difficult to attain stable and clean co-combustion with municipal solid waste (MSW) in existing MSW incinerators. Blending other high-heating value solid waste as assistive fuel in co-firing sewage sludge and MSW is considered feasible to improve the combustion stability and maintain the disposal capacity of the incinerator. This paper numerically investigates MSW co-firing sewage sludge and industrial solid waste in a moving-grate MSW boiler with a capacity of 750 t/d. Since the co-combustion stability and nitrogen oxides (NO_x) emissions are among the main concerns, different blends of the three wastes and under-grate primary air (PA) distributions are probed and compared. First, a validated in-house bed model, comprehensively describing the solid fuel conversion process and heat and mass transfer phenomena on moving grates, is extended to include NO_x formation and emissions and employed to simulate the combustion of various blends on the grate. Then, the fuel bed model is iteratively coupled with the simulation of the freeboard in the boiler. For the various blends investigated in this study, co-combusting up to 25.6 wt% sewage sludge, with about 14.4 wt% industrial solid waste and 60 wt% MSW in the existing boiler, is feasible and recommended. By properly tuning the under-grate PA distribution, the stable, efficient and clean combustion of the feedstock blend has been achieved. Compared to the original PA distribution, up to 11.54% reduction of NO_x emission from the boiler is attained, because of the enhancement of nitric oxide (NO) reduction reactions with ammonia (NH_3) and char by adjusting the PA distribution. At last, an in-depth analysis of co-combusting the recommended blend using the modified PA distribution is addressed. This study provides a valuable reference and guideline for stable and clean co-combustion of sewage sludge in existing MSW incinerators.

Keywords: Co-combustion; Solid waste; Sewage sludge; NO_x emissions; Grate boiler

Nomenclature

Symbols			
a	oxygen reaction order (-)	S_T	energy source term (J/(m^3 s))
A	pre-exponent factor (s^{-1})	t	time (s)
A_{BET}	BET surface area (m^2/kg)	T	temperature (K)
C_{NH_3}	NH_3 concentration (kg/m^3)	T_{in}	initial temperature (K)
C_{NO}	NO concentration (kg/m^3)	T_{rad}	radiation temperature (K)
C_{pg}	gas specific heat capacity (J/(kg K))	T_∞	the freeboard temperature (K)
D_g	effective gas diffusivity (m^2/s)	u	grate movement rate (m/s)
D_s	solid species diffusivity (m^2/s)	$\boldsymbol{u}$	superficial velocity in fuel bed (m/s)
E	activation energy (J/mol)	X	molar fraction (-)
h_M	mass transfer coefficient (m/s)	Y	mass fraction (-)
h_T	heat transfer coefficient (W/(m^2 K))	α	O_2 coefficient of char burning (-)
K	bed permeability	ε	system emissivity (-)
k_{eff}	thermal conductivity (W/(m K))	σ	Boltzmann constant (W/(m^2 K^4))
M_w	molar weight (kg/kmol)	ρ_g	gas density (kg/m^3)
P	gas pressure (Pa)	ρ_s	solid bulk density (kg/m^3)
$\bar{p}$	mean NO pressure (atm)	ϕ	bed porosity (-)
$\bar{p}_{NO}$	mean NO partial pressure (atm)	*Abbreviations*	
r	reaction rate (kg/(m^3 s))	BASIC	Bulk Accumulated Solids Incineration Code
R	universal gases constant (J/(mol K))	CFD	Computational fluid dynamics
R_c	char burning rate (kg/(m^3 s))	MSW	Municipal solid wastes
r_{CO}	CO rection rate (kg/(m^3 s))	WSGGM	Weighted sum of gray gases model
R_c	char burning rate (kg/(m^3 s))	LHV	Low heating value
R_{vol}	devolatilization rate (kg/(m^3 s))	PA	Primary air
t	time (s)	SA	Secondary air
S_g	overall solid conversion rate (kg/(m^3 s))	UDF	User-defined function
S_{ig}	gas species reaction rate (kg/(m^3 s))	WtE	Waste to energy

1. Introduction

Grate-firing, which can largely reduce the mass and volume of solid waste and recycling energy, is recognized as a stable, efficient and clean technology for solid waste disposal [1, 2]. Due to its fuel flexibility and operation stability, grate-firing technology is favored in industrial applications of municipal solid waste (MSW) combustion [3]. Thousands of waste-to-energy (WtE) plants have been built to dispose solid waste and recycle energy using grate-firing boilers, where most of the boilers are designed and operated based on the local MSW properties [4]. However, with the dramatic increase in the production of the other solid waste, e.g., municipal sewage sludge and industrial solid waste, the current MSW boilers need to be adjusted or retrofitted to meet the demands of handling various solid wastes [5]. Co-combustion of solid wastes in existing incinerators is considered an efficient and feasible way to meet the requirement and reduce the difficulties of the boiler adjustments or retrofits to the most extent [6]. For example, Bhuiyan et al. have investigated the co-firing of biomass and coal in a small-scale furnace, presenting the impacts of co-firing ratio on the combustion metrics [7]. Afterwards, co-firing biomass with coal in a large-scale incinerator has been studied, revealing the co-combustion features under air and oxy-fuel conditions [8]. In [9], emission and distribution of polycyclic aromatic hydrocarbons (PAHs) during MSW co-firing with coal are investigated. The results indicate the MSW/coal co-combustion can reduce the yield and toxicity of PAHs.

Whereas, for co-firing MSW and sewage sludge, the high moisture content in raw sewage sludge makes it difficult to achieve stable combustion [10]. Zhou et al. have tested the organic pollutants emission from MSW co-firing a small amount of sewage sludge (5 wt%), which shows the possibility to dispose sludge safely by co-combustion with MSW [11]. In [6], a numerical study on MSW co-combustion with paper sludge is presented, proving the partially dried paper sludge is more proper than the wet raw paper sludge for the co-combustion in terms of corrosion mitigation. The drying pretreatment benefits the co-combustion of sludge and MSW, while it is not cost-efficient for the plant. The economic analysis of MSW co-firing with sewage sludge of 30-40% water content has been performed in [12]. The results show co-firing MSW with semi-dry sludge is feasible, while the boiler efficiency and power generation would be reduced. Besides the drying pretreatment, blending high heating value feedstock such as industrial solid waste is also an effective way to improve the co-combustion performance. To the best of the authors' knowledge, the investigation of co-firing MSW and sewage sludge with industrial solid waste in a large-scale MSW grate boiler has not been attempted. In order to find a feasible and cost-efficient way for co-firing MSW with sewage sludge, this paper investigates the co-combustion of MSW, sewage sludge and industrial solid waste, in which the industrial solid waste serves as a supporting fuel.

In practice, testing the co-combustion of new feedstock directly in MSW boilers is very risky and costly [13]. Computational fluid dynamics (CFD), which is able to predict the detailed reaction process and distributions of temperature, velocity,

pressure and species in reactors [14], is a powerful and cost-efficient tool to guide and optimize the operation of incinerators [15]. Several studies on CFD simulation of solid waste incinerators have been carried out, e.g., a numerical investigation on biomass combustion in a bubbling fluidized bed has been performed in [16], under the Euler-Euler framework. The characteristics of co-combusting corn straw and pinewood chips in a grate-firing biomass boiler are studied in [17]. The impacts on combustion efficiency and carbon conversion have been revealed based on the simulation results. A comprehensive CFD model has been developed and validated for describing biomass conversion process in large reciprocating grate boilers [18]. Moreover, Lin *et al*. have simulated a co-combustion case of MSW and sewage sludge via ANSYS Fluent, to investigate the impacts of the feedstock blending ratios on the grate boiler [5]. However, the combustion characteristics and pollutant emissions from MSW co-combustion with multiple wastes, i.e., sewage sludge and industrial solid waste, have not been explored. It is particularly crucial for the co-combustion with municipal sewage sludge, due to its very high nitrogen content [19]. In short, the numerical study for co-combustion of MSW with sewage sludge and industrial solid waste considering NO_x pollutants is strongly desired.

In this paper, the co-combustion of MSW, municipal sewage sludge and industrial solid waste in an existing 750 t/d MSW grate boiler is numerically investigated. The conversion process of the feedstock blend on the grate is modeled by an in-house bed model BASIC (Bulk Accumulated Incineration Code), which has been validated by the experimental data in our previous works [20]. The freeboard simulation is carried out by ANSYS Fluent and is iteratively coupled with the results from the bed model, which is also verified by the boiler operation data in [21]. In order to characterize the NO_x pollutant during combustion, the bed model is extended to accommodate NO_x formation and emissions, as well as the freeboard simulation. After that, simulations for co-firing four different blends under the original primary air (PA) distribution are conducted. And then, a new PA supply distribution targeting NO_x reduction is proposed and applied in each blend combustion. The objective of this study is to virtually test the feasibility of co-firing MSW with sewage sludge and industrial solid waste in an existing MSW boiler, considering low NO_x emission.

2. Simulation method and NO_x formation modeling

2.1 Boiler description and simulation strategy

The boiler under study is a moving-grate MSW boiler in operation with 65.42 MW_{th} thermal input and 750 t/d disposal capacity. The grate is 11 m long in total and is lengthwise divided into five individual sub-grates, each of which is equipped with an independent primary air (PA) supply. The first four sub-grates is 2.0625 m long each, and the fifth sub-grate is 2.75 m long. The current segmented proportion of PA supply under each sub-grate is 15:15:30:30:10. The initial bed height at the fuel inlet is approximate 1 m, and the solid waste stays roughly 1.5 h until the end of the grate. The boiler incinerating MSW alone has been simulated in our previous work, where

the CAD geometry of the boiler, mesh and the simulation details have been presented as well [21]. The simulation results agree well with the operation data inside the boiler. The 3D geometry of the calculation domain and the coupled modeling strategy are illustrated in Fig. 1. The fuel bed model used in this study is transformed from an in-house bed model BASIC, which was developed in our previous work [20]. The freeboard simulation is carried out by ANSYS Fluent [22], which implements the results of the fuel bed model into the CFD simulation via a User-Defined Function (UDF). The radiation heat flux to the fuel bed and the flue gas temperature above the bed top surface are exported from Fluent and iteratively integrated into the bed model.

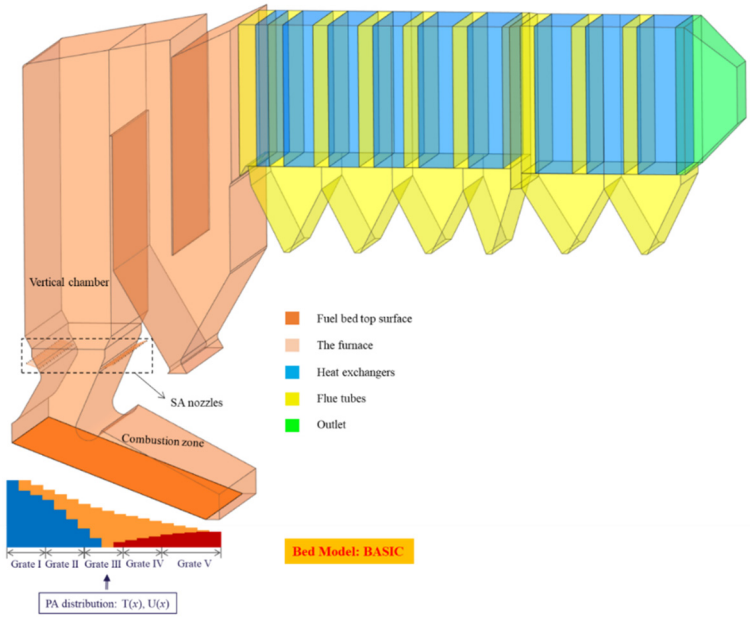

Figure 1 The 3D geometry of the grate-firing boiler and modeling strategy

2.2 Description of the fuel bed model for moving grate

2.2.1 Transformation of the model from fixed bed to moving grate

In this study, the 2D steady bed model describing solids conversion on a moving grate is transformed from a stand-alone 1D transient bed model developed to model MSW combustion in a fixed bed [20]. As shown in Fig. 2, the entire fuel bed on the moving grate can be divided into finite columns. Each of them can be recognized as a slice of fixed fuel bed. The combustion metrics of the column at x-meter are consistent with those of a fixed bed at combustion time $t(x = x_0 + ut)$, when other conditions are the same. In other words, the combustion metrics on the moving grate along the length from $x = 0$ to $x = L$ are mapped from those on the corresponding fixed bed from $t = 0$ to $t = t_{end}$, in which the time elapsed in the fixed bed model is mapped into the lengthwise distance along the moving-grate model. In this way, transformation from the 1D transient fixed bed model to the 2D steady moving grate model is achieved.

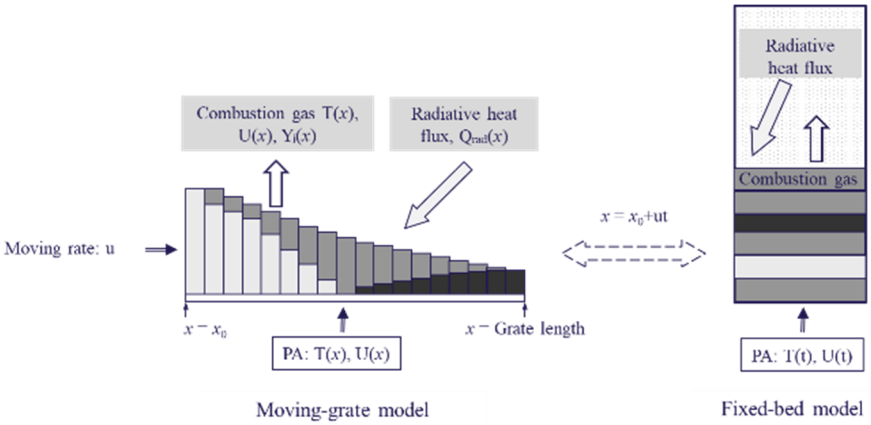

Figure 2 Model transformation from fixed bed to moving-grate bed

2.2.2 Incorporating NO_x formation in the bed model

Nitrogen oxides, collectively termed NO_x, are formed during combustion processes, primarily as nitric oxide (NO) [23]. In MSW grate boilers, NO_x pollutants are formed both in the fuel bed and the freeboard. The fuel NO_x formation dominates the former one, and the latter one mainly consists of thermal NO_x formation and fuel NO_x formation [24], since thermal NO_x is formed by the reaction of nitrogen (N_2)and oxygen (O_2), where high temperature is the essential prerequisite (usually occurs above 1673 K) [25]. In one of our previous studies, a detailed fuel NO_x formation model in a small-scale fixed bed was developed [26], which includes lots of intermediate reactions and species. Due to its complexity, it is not friendly in applications, especially for large-scale boilers. Therefore, in this study, we employ a simplified NO_x formation scheme consisting of five global reactions into the fuel bed model, to make it applicable in the simulation of large-scale boilers. The model assumes that nitric oxide (NO) is the only NO_x pollutant since it accounts for about 95% of the total NO_x pollutant during combustion [27].

Fuel nitrogen, which is always included in the organic compounds of solid fuels, contributes to the formation of fuel NO_x during incineration [28]. For solid fuel, fuel-N is contained in volatiles and char and released during the pyrolysis and char-burning processes, respectively. Based on the literature review, char-N accounts for approximately 20%-30% of the fuel-N in biomass, which can be oxidized to 75-100% NO [29]. In this study, we assume that the amount of char-N is 25% of the fuel-N, and it is completely oxidized to NO during char burning [24]. On the other hand, the volatile-N released consists of approximately 90% NH_3 and 10% HCN [30]. In this study, volatile-N is assumed to be 100% converted into NH3 to improve computational efficiency. The reaction pathway for fuel NO_x formation used in the bed model is described in Fig. 3. Three heterogeneous reactions and two homogeneous reactions related to NO_x formation are integrated into the bed model. The reaction rate and its corresponding kinetics for each reaction are listed in Table 1.

Table 1 Reaction expression and kinetics of fuel NO_x formation in the bed model [31]

No.	Rate expression	A	E (J/mol)
1	$r_1 = \frac{\partial C_{NH_3}}{\partial t} = R_{vol} Y_{N,vol} M_{w,NH_3} / M_{w,N}$	–	–
2	$r_2 = \frac{\partial C_{NO}}{\partial t} = R_c Y_{N,char} M_{w,NO} / M_{w,N}$	–	–
3	$r_3 = \frac{\partial C_{NH_3}}{\partial t} = A X_{NH_3} X_{O_2}^a e^{-E/RT}$ $a = \begin{cases} 1.0, & X_{O_2} \le 4.1 \times 10^{-3} \\ -3.95 - 0.9 \ln X_{O_2}, & 4.1 \times 10^{-3} < X_{O_2} \le 1.11 \times 10^{-2} \\ -0.35 - 0.1 \ln X_{O_2}, & 1.11 \times 10^{-2} < X_{O_2} \le 0.03 \\ 0, & X_{O_2} > 0.03 \end{cases}$	4.0×10^6 s^{-1}	133947.2
4	$r_4 = \frac{\partial C_{NH_3}}{\partial t} = A X_{NH_3} X_{NO} e^{-E/RT}$	1.8×10^8 s^{-1}	113017.95
5	$r_5 = \frac{\partial C_{NO}}{\partial t} = A e^{-E/RT} \bar{p}_{NO} \cdot \rho_s A_{BET} M_{w,NO}$ $\bar{p}_{NO}$ is the mean NO partial pressure, which calculated using Dalton's law: $\bar{p}_{NO} = \bar{p} X_{NO}$ (atm). A_{BET}=BET surface area (m^2/kg).	230 mol/(m^2·s·atm)	142737.485

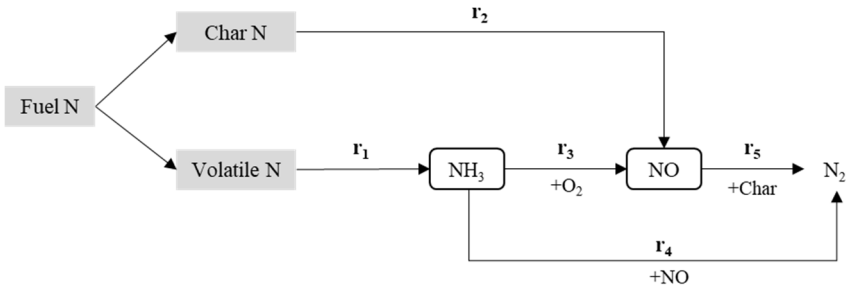

Figure 3 Fuel NO_x reaction scheme in the bed model

2.2.3 Summary of the moving-grate bed model

In order to better describe MSW conversion on the moving grate, several significant updates have been made in the bed model besides NO_x formation, as listed below.

- Using solid physical density and updating porosity when solving the continuity equation of solid phase, instead of updating the bulk solid density in the original model.
- Incorporating solid mixing by a diffusion term in the solid species equations, to model the impacts of the solid movements [32].
- Considering the char gasification reactions with water vapor and carbon dioxide.
- Revising the calculation of CO combustion rate, i.e., free from H_2O concentration in the char combustion stage.
- Coupling the radiation profile exported from the freeboard simulation in the bed model.
- Modifying the air supply from a fixed flowrate to a distribution along grate.

The summary of the key updates and comparison with the original bed model are presented in Table 2.

Table 2 Summary of the major updates of the in-house bed model in this study over our previous work

Term	Our previous work [20]	This study
Solid continuity equation	Update bulk solid density	Update porosity
Solid mixing	Not considered	Add a diffusion term in solid species transport equations
Char reaction	$C + \alpha O_2 = 2(\alpha - 1)CO + (2\alpha - 1)CO_2$	$C + \alpha O_2 = 2(\alpha - 1)CO + (2\alpha - 1)CO_2$ $C + CO_2 = 2CO$ $C + H_2O = CO + H_2$ [33]
CO combustion chemical rate	$r_{co} = R_1$	$r_{co} = \begin{cases} R_1, H_2O > 0 \\ R_2, H_2O = 0 \end{cases}$
Radiation from the freeboard	Fixed value	Profile exported from Fluent
Air supply	Fixed flowrate	Segmented flowrate along the grate
Inlet diffusion of species	Enabled	Disabled to keep mass balance accurately

[a] $R_1 = 2.239 \times 10^{12} \exp\left(-\frac{1.702 \times 10^5}{RT}\right) CO \cdot O_2^{0.25} \cdot H_2O^{0.5}$

[b] $R_2 = 7.05 \times 10^6 \exp\left(-\frac{9.68 \times 10^4}{RT}\right) CO$ [34]

Table 3 Transport equations and boundary conditions used in the bed model

Gas continuity	$\frac{\partial(\phi\rho_g)}{\partial t} + \nabla \cdot (\rho_g \mathbf{u}) = S_g$
Gas species	$\frac{\partial(\phi\rho_g Y_{ig})}{\partial t} + \nabla \cdot (\rho_g \mathbf{u} Y_{ig}) = \nabla \cdot (D_{ig} \nabla(\phi\rho_g Y_{ig})) + S_{ig}$
Gas momentum	$\frac{\partial(\phi\rho_g u)}{\partial t} + \nabla \cdot (\rho_g \mathbf{u} u) = -\nabla P - \frac{\mu u}{K} - \beta\rho_g u^2$
Solid continuity/Porosity model	$\frac{\partial((1-\phi)\rho_s)}{\partial t} = -S_g$
Solid species	$\frac{\partial((1-\phi)\rho_s Y_{is})}{\partial t} = \nabla \cdot (D_s \nabla((1-\phi)\rho_s Y_{is})) + r_{is}$
Energy equation	$\frac{\partial(\phi\rho_g C_{pg} T + (1-\phi)\rho_s C_{ps} T)}{\partial t} + \nabla \cdot (\rho_g \mathbf{u} C_{pg} T) = \nabla \cdot (k_{eff} \nabla T) + S_T$
Boundary conditions at bed bottom	$\rho u = \rho_{in} u_{in};\ \frac{\partial P}{\partial x} = 0$ $Y_{ig} = Y_{ig,in};\ Y_{is} = Y_{is,in}$ $T = T_{in}$
Boundary conditions at bed top	$\frac{\partial u}{\partial x} = 0;\ P \equiv P_{atm}$ $AD_{ig} \frac{\partial Y_{ig}}{\partial x} = Ah_M(Y_{ig,\infty} - Y_{ig});\ \frac{\partial Y_{is}}{\partial x} = 0$ $k_{eff} A \frac{\partial T}{\partial x} = Ah_T(T_\infty - T_s) + A\varepsilon\sigma(T_{rad}^4 - T_s^4)$

The governing equations and boundary conditions used in the bed model are summarized in Table 3. Explanations of the symbols refer to Nomenclature.

2.3 The freeboard 3D simulation with NO_x formation modeling

The 3D steady simulation of the freeboard is performed in ANSYS Fluent. The results from the bed model are integrated into the freeboard simulation by compiling a UDF, i.e., the results of the velocity, temperature and species profiles at the bed top surface

are defined using a DEFINE_PROFILE C source code and complied in ANSYS Fluent [22]. The realizable $k-\varepsilon$ model with standard wall function is used for modeling the turbulence of the flow [35]. The radiation in the furnace is modeled with the P-1 model, and the radiation properties of the gas species are calculated by a refined weighted sum of gray gases model (WSGGM) by the other UDF file, which shows more accuracy than the default one [36]. The finite rate / eddy-dissipation model has been used to compute the turbulence-chemistry rates of the reactions [15]. The NO_x formation, i.e., thermal NO_x and fuel NO_x, in the freeboard simulation is considered in this numerical study as well [37]. The equilibrium approach is used to calculate the O-atom concentration, which is contained in the expression of the thermal NO_x formation rate [31]. The NH_3 and NO profiles from the bed model are also integrated into the freeboard simulation as the initial condition of the fuel NO_x formation model. The NO_x model is solved together with the other variables simultaneously in the freeboard simulation. The key models and numerical methods used in the freeboard simulation are summarized in Table 4, more details refer to [21].

Table 4 Key models and numerical methods incorporated in the freeboard simulation

Coupling bed model	UDF of inlet profile
Turbulence model	Realizable $k-\varepsilon$ model with standard wall function, $I = 0.16{Re_{D_H}}^{-1/8}$ for calculation of the turbulence intensity for the inlet boundary condition [35].
Gaseous combustion	2-step Westbrook and Dryer (WD) mechanism for light hydrocarbons, one-step global combustion mechanism for H_2, finite rate/eddy-dissipation model for turbulence-chemistry interaction [37].
Radiation model	P-1 model, a refined WSGGM for evaluation gases radiation properties [38].
NO_x formation and emissions	Thermal and fuel NO_x, equilibrium approach used for calculation of O-atom.
Flow through heat exchangers	Porous zone with pressure and heat drops.
Boundary conditions	Velocity inlet, pressure outlet, temperature thermal condition for walls.
Numerical methods	SIMPLE algorithm; 2nd order upwind scheme for all transport equations.

2.4 Coupling of the bed model and the freeboard simulation

The bed model is developed as a stand-alone MATLAB code, which receives the incident radiation heat flux from the freeboard and provides the in-bed solid waste conversion products to the freeboard. The coupling between the in-bed combustion modelling and the freeboard simulation is achieved manually, in which the incident radiation heat transfer is used as the coupling convergence parameter. The coupling is elaborated in more detail below.

Step 1: Run the bed model with an initial guess of the radiation temperature and over-bed temperature profile, which are used as the boundary condition at

the fuel bed top. Among the detailed results of the in-bed combustion, the profiles of the velocity, species and temperature of the combustion products along the top surface of the fuel bed are used as the inlet boundary condition (via UDF) for the freeboard simulation.

Step 2: Compile the UDF for the grate inlet condition, run the freeboard simulation in Fluent, and then export the radiation and over-bed temperature profiles.

Step 3: Integrate the new temperature profiles from Fluent and run the bed model again, and then check the radiation heat transfer rate at the bed top surface.

Step 4: Rerun the freeboard simulation case with the new bed model results, and then export the temperature profiles and radiation heat transfer rate to the bed top surface.

Step 5: Compare the two radiation heat transfer rates (negative value in Fluent). If there is no significant difference, the coupling is converged and the results are saved for analysis and discussion. Otherwise, go back to Step 3 and repeat the procedure.

Fig. 4 shows the coupling process for simulation of the boiler incinerating current feedstock, where one can see, after three times of coupling the radiation heat transfer rate and the radiation profile are no longer changed significantly. All the simulation results presented in this study are achieved after three to four times of manual coupling.

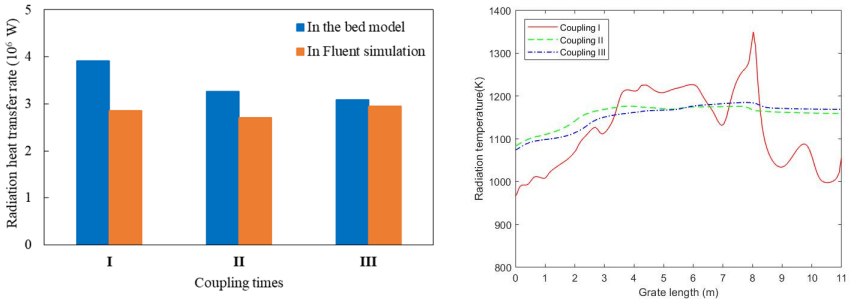

(a) (b)

Figure 4 Coupling process of the bed model and the freeboard simulation

2.5 Co-combustion cases under study

This study aims to investigate the MSW and municipal sewage sludge co-combustion. However, the heating values of the two kinds of solid wastes are both very low, especially for sewage sludge. In order to ease the ignition and incineration stability, industrial solid waste, which is one of the high heating-value wastes, is also employed as one of the fuels for co-combustion. The three kinds of solid wastes, i.e., MSW, sewage sludge and industrial solid waste, are blended accordingly for co-combustion in the existing MSW boiler. The properties of the three kinds of waste are listed in Table 5. To simplify the bed model, the kinetics of the devolatilization and char reactions for the sludge and industrial waste are assumed to be the same as the MSW. The feedstock blend for co-combustion is recognized as a new fuel with its own properties.

Table 5 Proximate and ultimate analysis of the different kinds of solid wastes under study

Solid wastes	Proximate analysis, wt% ar[a]				Ultimate analysis, wt% daf[b]						LHV,
	Moisture	Volatile	Fixed carbon	Ash	C	H	O	N	S	Cl	kJ/kg ar[c]
MSW	45.40	31.90	8.10	14.60	52.63	7.45	36.91	1.19	1.12	0.70	7536
Sludge	80.00	10.51	1.20	8.29	51.90	7.44	6.38	28.9	4.57	0.82	1172
Industrial waste	7.56	72.20	8.75	11.49	57.86	6.88	31.41	1.58	1.85	0.41	18840

[a] As received basis (ar)

[b] Dry ash free basis (daf)

To ensure the co-combustion operation stability in the MSW boiler, MSW should be the major fuel (≥50%) of the feedstock blend. Thus, four kinds of blends with the MSW blending ratios 50% (Blend 1), 60% (Blend 2), 70% (Blend 3) and 80% (Blend 4) are used for the simulation cases to investigate the impacts of the blending ratios. Compared to the MSW currently incinerated in the grate boiler, the heating value of the industrial waste is higher while the heating value of the sewage sludge is lower. To maintain the thermal input and disposal capacity of the boiler, all the blends have the same heating value as the MSW, by adjusting the blending ratios. The blending ratios of the four kinds of blends and their corresponding contents of fuel-N are listed in Table 6.

The solid conversion in the fuel bed usually can be divided into four stages along the grate: drying-dominated, devolatilization-dominated, char reaction-dominated and ash cooling. In the drying stage, the primary air from beneath the grate can be reduced. In the devolatilization stage, a careful consideration of the primary air needs to be made. On the one hand, primary air needs to be provided for partial oxidation of the released volatiles to assure sufficient heat can be generated locally to dry and heat up the feedstock towards the grate surface. On the other hand, too much primary air not only burns out the volatiles locally at the locations where they are released but also compromises the downward propagation of the drying and combustion fronts towards the grate surface. In the char reaction stage, sufficient primary air needs to be provided to minimize the unburnt char in the ash, preferably with CO as the main char oxidation product. To achieve the reduction of NO_x (thermal $DeNO_x$), the PA distribution under the five sub-grates is modified. According to the chemical reaction scheme of NO_x, the adjustments aim at reducing the NO formation reaction (r_3 in Fig. 3) and enhancing the NO reduction reactions (r_4 and r_5 in Fig. 3) in the combustion stages, meanwhile keeping more NH_3 released into the freeboard in the evaporation dominated stage. The objectives and the corresponding adjustments for PA supply are listed in Table 7. In this way, eight cases with four kinds of blends and two kinds of PA distributions for co-combustion are studied by the model, as shown in Table 6. The flowrates of primary air and secondary air (SA) supply and the fuel feeding rates for all the co-combustion cases are the same as those currently used in the boiler for incinerating MSW, in which the overall excess air ratio is 1.2 with the split ratio 60/40 of PA/SA [21].

Table 6 Eight cases with four different feedstock/blends and two different PA distributions

Case	Feedstock blend			PA distribution along the grate (wt%)
	MSW / Sludge / Industrial waste (wt%)	LHV (kJ/kg, ar[a])	Fuel-N (wt %, daf[b])	
Case 1a	50.0 / 32.0 / 18.0	7534	4.24	15 / 15 / 30 / 30 / 10 (Currently used PA distribution)
Case 2a	60.0 / 25.6 / 14.4	7535	3.61	
Case 3a	70.0 / 19.2 / 10.8	7535	3.00	
Case 4a	80.0 / 12.8 / 7.2	7535	2.39	
Case 1b	50.0 / 32.0 / 18.0	7534	4.24	14 / 16 / 28 / 32 / 10 (Adjusted PA distribution)
Case 2b	60.0 / 25.6 / 14.4	7535	3.61	
Case 3b	70.0 / 19.2 / 10.8	7535	3.00	
Case 4b	80.0 / 12.8 / 7.2	7535	2.39	

[a] As received basis (ar)

[b] Dry ash free basis (daf)

Table 7 Explanation of the PA distribution adjustments for Case b

Objectives	Adjustments
To avoid oxygen waste and slightly accelerate the conversion rate in evaporation dominated stage.	Change the PA distribution under the first two sub-grates from 15:15 to 14:16.
To reduce the reaction rate of NH_3 +O_2 and enhance the reaction of NH_3+NO in devolatilization dominated stage.	Reduce the air supply rate under the third sub-grate from 30% to 28%.
To enhance the NO reduction reaction with char at the char reaction stage.	Increase PA under the fourth sub-grate from 30 % to 32%.

3. Results and discussion

3.1 Simulation validation

The simulation, i.e., BASIC coupled with Fluent, has been validated by comparing the results with the measurement data at different positions inside the boiler for incinerating current MSW. As shown in Fig. 5, the predicted temperature and the measurement data show good agreements, meeting the requirements for engineering application. Hence, the simulation used in this study is recognized as reliable. For more details about the validation, refer to [21].

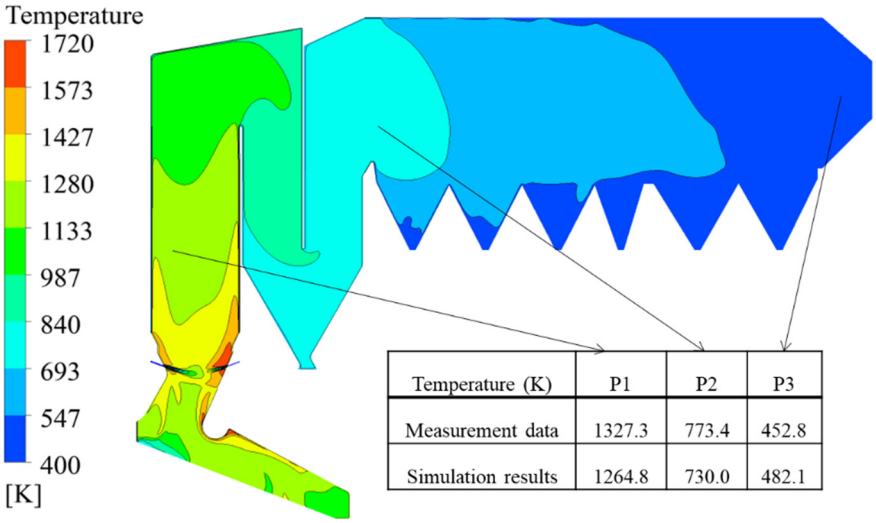

Temperature (K)	P1	P2	P3
Measurement data	1327.3	773.4	452.8
Simulation results	1264.8	730.0	482.1

Figure 5 Validation of the MSW grate boiler simulation

3.2 Comparison of the simulation results for different cases

The validated simulation is then deployed to investigate the co-combustion of MSW and sewage sludge with industrial solid waste in the same boiler. The variables temperature, NH_3 and NO mass fractions, which affect NO_x formation during combustion are compared and analyzed. The comparison of the eight cases is to study the impacts of the blending ratio of different feedstock. Case 1a-4a retains the current lengthwise PA distribution used in the MSW incinerator, and Case 1b-4b uses an adjusted lengthwise PA distribution.

Fig. 6 presents the profiles of temperature (a,b) and the mass fractions of NH_3 (c,d) and NO (e-h) at the top surface of the fuel bed for the eight cases. The profiles of these variables at different heights in the fuel bed for a representative case are elaborated in Section 3.3. First, the trend of the temperature profiles is the same, i.e., increasing at the initial stage (ca. 0-2.5 m), remaining steady at the stable combustion stage (ca. 2.5-6.4 m), reaching a sharp peak at the following char reaction stage (ca. 6.4-8.1 m), and falling down after char burn out. The temperature at the stable combustion stage remains around 1200 K, which is suitable for NO reduction by ammonia released from volatiles. The spiking temperature around 1775 K at the char burning stage also benefits the heterogeneous of NO and char. Moreover, the peak temperature at the char burning stage of the cases with the new PA supply (Case b) is slightly higher (around 20 K) than those maintaining the current PA supply (Case a), promoting the reduction of NO by char. It can be explained by a bit more air supply under the fourth sub-grate for Case b (32%) compared to Case a (30%), which is helpful for NO reduction. In addition, the heating up of the fuel bed is delayed for incinerating Blend 1 (Case 1a and 1b), which is probably due to the highest water content (49.7%) for co-combustion with 32 wt% sludge. The increase of the relatively cooler air supply

under the second sub-grate in Case 1b hinders the heat conduction, leading to the mutation in the temperature profile at 2.0625 m compared to Case 1a.
Second, for all the cases, NH_3 at the top surface reaches a peak at the initial stage and then decreases to zero by the reactions with O_2 and NO, as shown in Fig. 6c and 6d. Meanwhile, NO mass fraction is increased as shown in Fig. 6g and 6h, i.e., the zoom-in figure of NO mass fractions. At the end of the devolatilization process, NH_3 mass fraction goes to another peak and finally falls down to zero after accomplishing the devolatilization at around 7 m of the grate. It is due to the accomplishment of evaporation in the entire bed, the devolatilization rate is accelerated, resulting lots of volatile-N is released at ca. 6.5-7 m of the grate. The differences of the NH_3 profiles of Case 1-4 are mainly caused by the volatiles-N content in its feedstock. On the other hand, compared to Case a and its corresponding Case b, the NH_3 mass fractions of the syngas for the cases using the new PA distribution are higher than those maintaining the current PA supply. That is because of the reduction of PA supply under the first sub-grate for Case b. More NH_3 into the freeboard benefits NO reduction according to the NO_x formation mechanism.

Third, for the NO profiles, the mass fraction of NO remains at a low level before the accomplishment of devolatilization (around 0-7 m of grate length), as shown in Fig. 6e and 6f. It is attributed to a small amount of NO being released from char-N and the reduction by NH_3 released from volatile-N, which usually occurs ranging temperature from 1130 to 1400 K for fuel-rich conditions [39]. To better view the NO profiles at 0-6.6 m length of the grate, the zoom-in figure of NO mass fractions is presented in Fig. 6g (Case a) and 6h (Case b). The results show that NO mass fraction at 2-6.6 m of grate length from Case b is slightly smaller than those from the corresponding Case a. That proves the reduction of oxygen supply under the third sub-grate promotes the competing reaction of NH_3+NO. Afterwards, NO mass fraction reaches a sharp peak at the char burning stage, caused by the large amount of NO liberation from char-N and the absence of the reduction by NH_3. Nevertheless, the NO peaks of Case b are smaller than those from the corresponding Case a, which is probably due to the enhancement of the heterogeneous reaction of NO and char, after revising the relevant PA ratio from 30% to 32%.

In short, the bed model results reflect the following consequences of the co-combustion.

1) Slightly more NH_3 is released into the freeboard at the initial stage after the PA adjustment under the first two sub-grates.
2) More NO is reduced by NH_3 in the fuel bed during the devolatilization process after adjusting the PA supply under third sub-grate.
3) The slight increase of the PA rate under the fourth sub-grate enhances the NO reduction reaction with char.

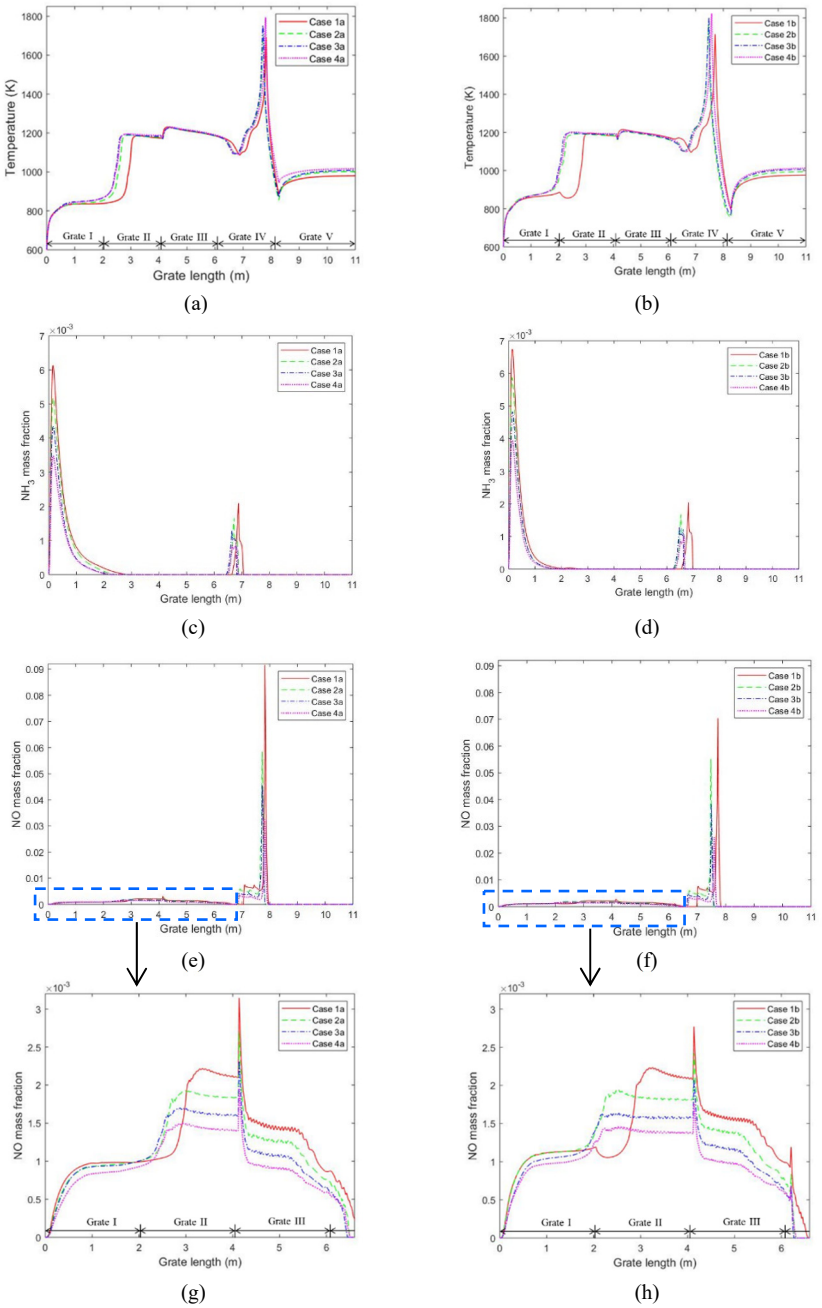

Figure 6 Comparison of temperature, NH_3 and NO profiles from the bed model for co-combustion with different feedstocks (Case 1, 2, 3 and 4) under different PA distributions (Case a and b)

Fig. 7 presents the temperature contours at the middle plane in the interest zone (combustion zone and vertical chamber) of the freeboard for the eight simulation cases. First, the temperature distributions for all the executed cases show the similarity in the freeboard, i.e., the high-temperature zone occurs nearby the SA supply and decreases gradually by the cold water pipes attached to the vertical chamber and the heat exchangers. The temperature in the combustion zone and the vertical chamber maintains a high value (above 1100 K) for all the cases, which is essential for decomposing the toxic organic matter [40]. Second, comparing Case b and the corresponding Case a, a gentle decrease in temperature has been observed in Case b. That may be explained by the fewer CO entering into the freeboard at the char burning stage after the PA adjustment. The decrease of the temperature is believed to be beneficial to the NO_x reduction in the freeboard, since thermal NO_x formation is very sensitive to temperature, according to the previous studies [41]. Third, the temperature peak in the freeboard increases when the mass fraction of MSW in the blend increases (in the order of Blend 1-4). It is probably due to the lower moisture content in the blend with more MSW.

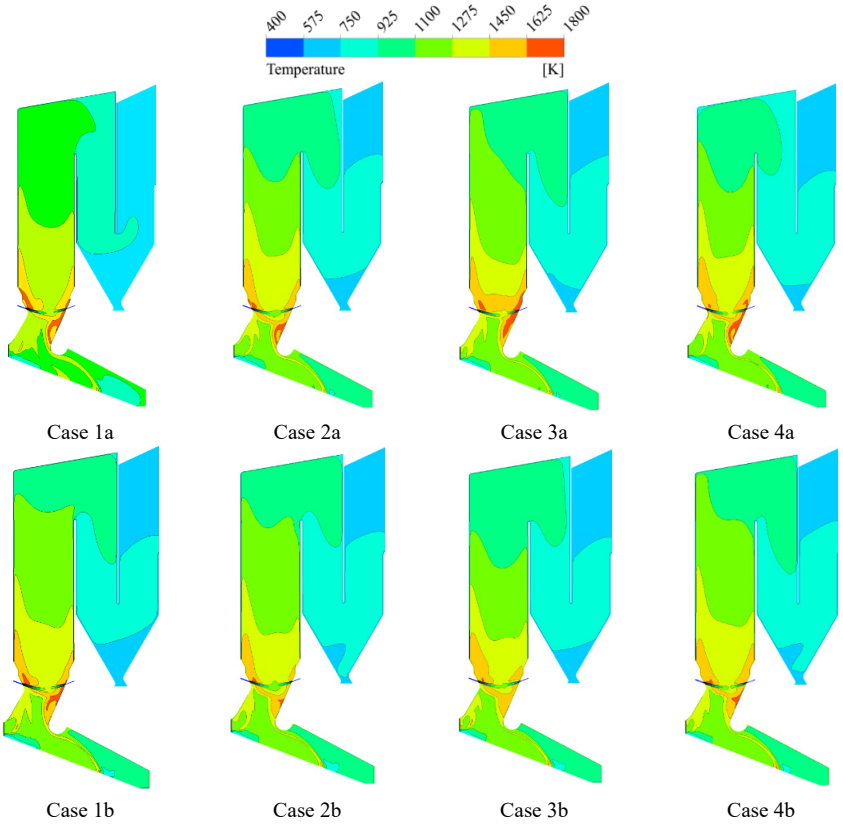

Figure 7 Comparison of the temperature contours of the flue gas at the middle plane of the freeboard for co-combustion with different feedstocks (Case 1, 2, 3 and 4) under different PA distributions (Case a and b)

Fig. 8a compares the absolute NO emission at the boiler outlet, which shows a decreasing trend from Case 1a to Case 4b. The magnitude, i.e., hundreds mg/Nm^3 (6% O_2 reference condition), meets the boiler operation experience [6]. It should be mentioned that the absolute values of NO emission for different cases may not be directly compared, since the fuel-N content differs a lot in the four blends as seen in Table 6. Therefore, the normalized NO emission calculated by Eq. (1) is presented in Fig. 8b.

$$Normalized\ NO\ emission = \frac{NO\ emission\ (mg/Nm^3)}{Fuel - N(wt\%)} \quad (1)$$

The result shows that Case 2b is the best case in terms of NO emission, followed by Case 4b and 1b. The PA adjustment is proven to be effective for NO elimination.

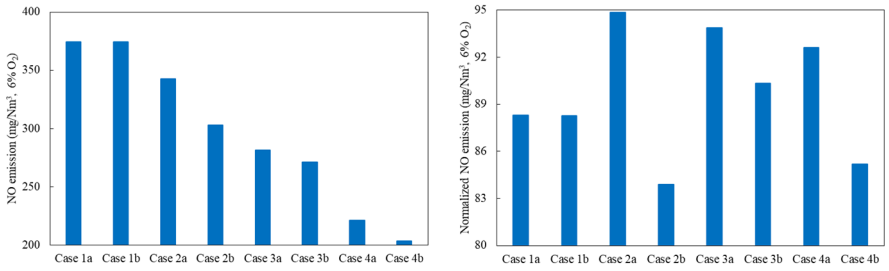

a b

Figure 8 Comparison of the NO emission at boiler outlet for all the cases

To better analyze the NO elimination, Fig. 9 quantitatively presents NO emission reduction by the PA adjustment for incinerating different blends. The NO emission reduction is characterized by Eq. (2) based on the data shown in Fig. 5a.

$$NO\ reduction\ \% = \frac{(NO\ emission\ of\ Case\ a - NO\ emission\ of\ Case\ b)}{NO\ emission\ of\ Case\ a} \times 100 \quad (2)$$

The results show that the PA adjustment benefits mostly the incineration of Blend 2, in which the NO emission is reduced by 11.54%. For combusting Blend 1, Blend 3 and Blend 4, the new PA distribution reduces NO emission by 0.02%, 3.76% and 8.03%, respectively. Thus, Case 2b is picked out as the best case, which is recommended to be implemented in the boiler.

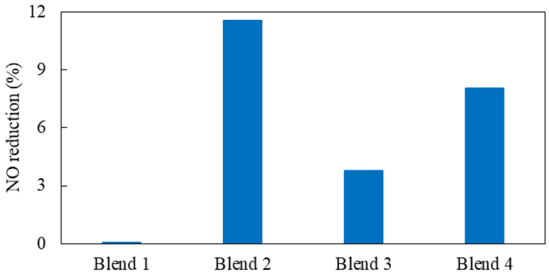

Figure 9 Reduction of the NO emission due to PA supply adjustment

3.3 In-depth analysis for the best case

The in-depth analysis of the best co-combustion cases, i.e., Case 2b, is illustrated in this section. Fig. 10 shows the bed model results, in which Fig. 10(a) presents the solid mass of the feedstock and its components (moisture, volatile and char) along the grate. The profiles along the grate of temperature, velocity, mass fractions of O_2, CO, CO_2 and NO_x pollutant profiles (NH_3 and NO) at the bed top surface, ¾ height, ½ height, and ¼ height are presented in Fig. 10(b-h), respectively. The high temperature propagates from top to bottom, resulting in the solid conversion layer by layer along the grate. The PA distribution is also presented in Fig. 10c as the velocity profile at the bed bottom surface. The results show that the solid waste conversion can be roughly divided into four stages, i.e., Stage I: 0-2.13 m length of the grate, Stage II: 2.13-6.74 m length of the grate, Stage III: 6.74-7.52 m length of the grate, and Stage IV: 7.52-11 m length of the grate, as divided in Fig. 10a and 10b.

In Stage I, the fuel bed is heated up by the heating flux from the freeboard, moisture is evaporated and a small number of gas species, e.g., CO and CO_2, are released from the volatiles. The mass fraction of NH_3 at the top surface reaches a peak, due to the low temperature preventing the relevant reactions that consume NH_3 from taking place [31]. After ignition of the fuel bed, the combustion process moves to Stage II, where the majority of the solid mass is reduced. The processes of moisture evaporation, devolatilization and char consumption enter into a steady status, and propagate from top to bottom. The temperature rises rapidly after the arrival of the combustion front. Meanwhile, O_2 is consumed to be zero as a result of reaching the dynamic balance between combustion reactions and air supply. NH_3 is released layer by layer from the volatile-N, contributing to several peaks in Fig. 10g along the grate. In Stage III, i.e., the char reaction stage, a large amount of heat is liberated due to char burning, resulting in the temperature peak as shown in Fig. 10b. The char-N is released as NO in large quantities during char burning. With the absence of NO reduction reaction by NH_3, NO mass fraction goes to a high peak at this stage as shown in Fig. 10h. Finally, the combustion process moves to Stage IV, i.e., the cool down stage, after the solid fuel is completely burned out. The mass fractions of CO, CO_2, NH_3, NO and all the other gas species converted from the solid waste turn to zero, and the mass fraction of O_2 returns to air level. The fuel bed is cooled down by the PA under the last sub-grate and remains stable.

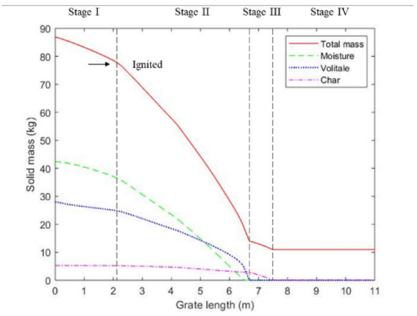

(a)

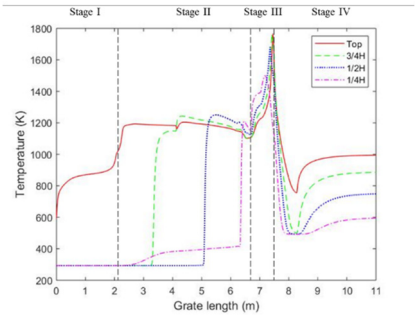

(b)

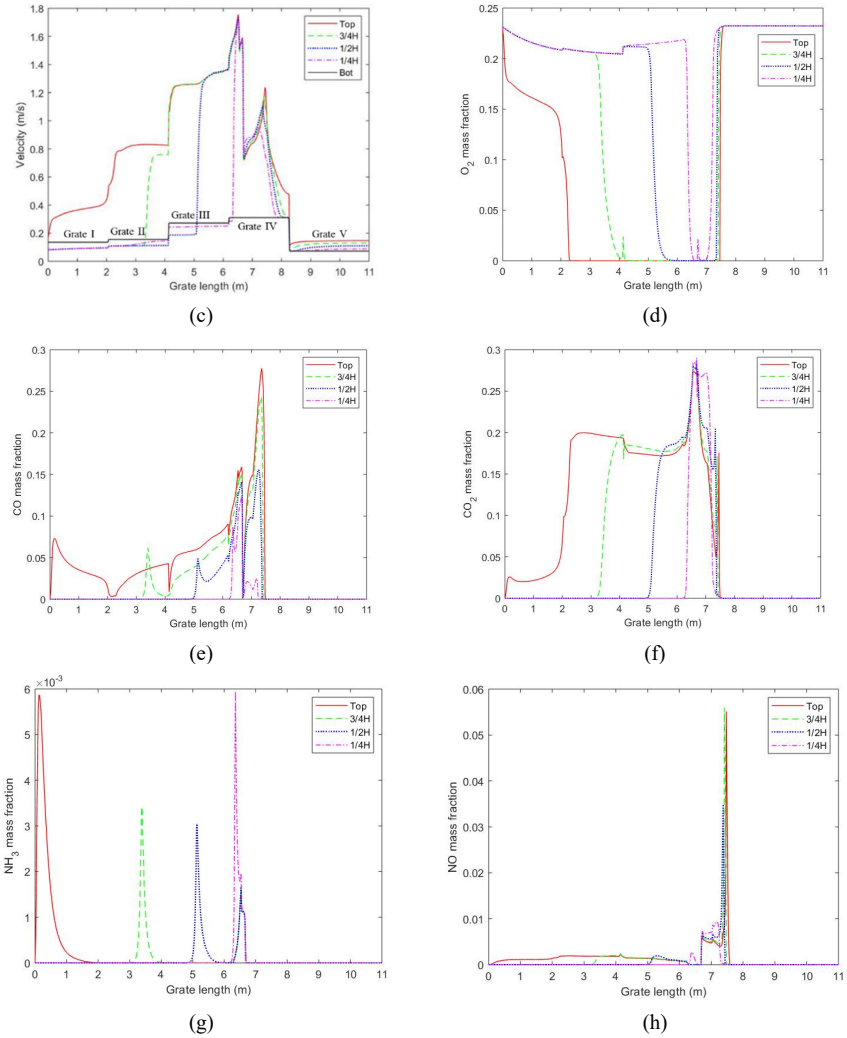

Figure 10 The bed model results of solid mass (a), temperature profile (b), velocity profile (c), O_2 (d), CO (e), CO_2 (f), NH_3 (g) and NO (h) mass fractions at different bed heights along the grate for Case 2b

Fig. 11 shows the contours of the major species of the flue gas, i.e., O_2, CO, CO_2, and NO pollutants at the middle plane in the interest zone (combustion zone and vertical chamber) of the freeboard for Case 2b. A big oxygen-rich area in the combustion zone above the fifth sub-grate is observed in Fig. 8a. Attention needs to be paid when operating the boiler under the same conditions as Case 2b to avoid oxygen waste in practice. As presented in Fig. 11b, the main combustible gas CO is burned out in the combustion zone and turns to close to zero near the SA supply region. And then CO_2 becomes one of the major species in the overall boiler domain, as shown in Fig. 11c.

The NO pollutant distribution becomes uniformly after the competition reactions of NO_x formation and elimination in the combustion zone and the vertical chamber, where the temperature is relatively high. The area-weighted average mass fractions of O_2, CO_2, and CO at the outlet surface of the boiler are 3.19%, 17.95% and 21.66 ppm, respectively. The NO emission without any additional removal measures is 302.88 mg/Nm^3 (6% O_2 reference condition) at the boiler outlet.

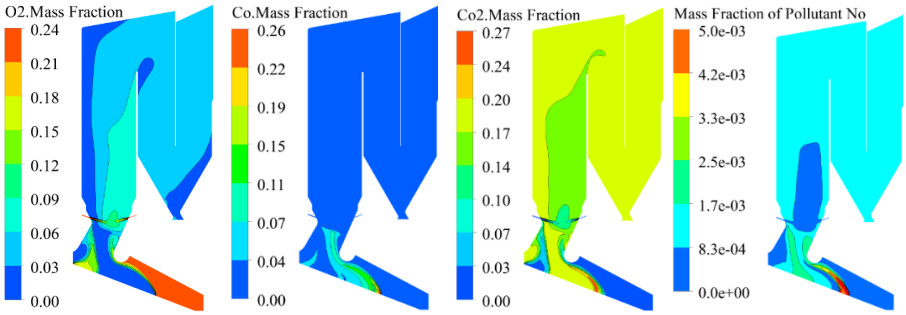

Figure 11 Contours of mass fractions for major gas species O_2 (a), CO (b), CO_2 (c) and NO pollutant (d) of the flue gas at the middle plane of the freeboard for Case 2b

4. Conclusions

In this paper, co-combustion of MSW and municipal sewage sludge with industrial solid waste in an existing MSW boiler has been simulated by an in-house bed model coupled with the freeboard simulation. NO_x formation from solid fuel has been integrated into the bed model, and both thermal NO_x and fuel NO_x are performed in the freeboard simulation which is carried out using ANSYS Fluent. Eight cases with four kinds of blends and two kinds of primary air distributions are conducted to reveal the stability and impacts on NO_x emissions. The best case with a new air supply is pick out, considering the low NO_x emissions. The combustion characteristics of temperature distribution and major species are analyzed, which yields significant references for co-firing MSW, sludge and industrial solid waste in the current boiler.

5. Outlook

Although the simulation described in this study has been validated and applied to study the co-combustion of various solid wastes, some hypotheses used in the modeling process may limit its accuracy and applicability. Several improvements and extensions worthy of attempting in the future are highlighted below.

1) Reliable kinetics for different solid waste decomposition can be implemented in the fuel bed modeling to more accurately simulate various feedstocks conversion, such as in co-combustion cases.
2) A comprehensive model for describing the solid fuel motions due to grate

movements and solids shrinking is desired to be integrated into the bed model, with the consideration of mass balance and volume change.

3) A more complex radiation model is worth to be incorporated into the bed model, instead of considering it in the effective thermal conductivity, which is currently used.
4) Simulation of the De-NO_x process in the boiler can be considered, to guide the operation of the NO_x removal system.

Acknowledgments

Tianbao Gu acknowledges China Scholarship Council (CSC) for the financial support of this PhD study at Aalborg University. This work is partially supported by the National Key R&D Project of China [2020YFC1908604].

References

[1] Yin C, Rosendahl LA, Kaer SK. Grate-firing of biomass for heat and power production. Prog Energ Combust 2008;34(6):725-54. https://doi.org/10.1016/j.pecs.2008.05.002

[2] Karim MR, Naser J. CFD modelling of combustion and associated emission of wet woody biomass in a 4 MW moving grate boiler. Fuel 2018;222:656-74. https://doi.org/10.1016/j.fuel.2018.02.195

[3]Yin CG, Li SS. Advancing grate-firing for greater environmental impacts and efficiency for decentralized biomass/wastes combustion. Enrgy Proced 2017;120:373-9. https://doi.org/10.1016/j.egypro.2017.07.220

[4] Cui CY, Liu Y, Xia B, Jiang XY, Skitmore M. Overview of public-private partnerships in the waste-to-energy incineration industry in China: Status, opportunities, and challenges. Energy Strateg Rev 2020;32. https://doi.org/10.1016/j.esr.2020.100584

[5] Lin H, Ma XQ. Simulation of co-incineration of sewage sludge with municipal solid waste in a grate furnace incinerator. Waste Manage 2012;32(3):561-7. https://doi.org/10.1016/j.wasman.2011.10.032

[6] Xu JC, Liao YF, Yu ZS, Cai ZL, Ma XQ, Dai MQ, et al. Co-combustion of paper sludge in a 750 t/d waste incinerator and effect of sludge moisture content: A simulation study. Fuel 2018;217:617-25. https://doi.org/10.1016/j.fuel.2017.12.118

[7] Bhuiyan AA, Naser J. Computational modelling of co-firing of biomass with coal under oxy-fuel condition in a small scale furnace. Fuel 2015;143:455-66. https://doi.org/10.1016/j.fuel.2014.11.089

[8] Bhuiyan AA, Naser J. CFD modelling of co-firing of biomass with coal under oxy-fuel combustion in a large scale power plant. Fuel 2015;159:150-68. https://doi.org/10.1016/j.fuel.2015.06.058

[9] Peng NN, Li Y, Liu ZG, Liu TT, Gai C. Emission, distribution and toxicity of polycyclic aromatic hydrocarbons (PAHs) during municipal solid waste (MSW) and coal co-combustion. Sci Total Environ 2016;565:1201-7. https://doi.org/10.1016/j.scitotenv.2016.05.188

[10]Hu SC, Ma XQ, Lin YS, Yu ZS, Fang SW. Thermogravimetric analysis of the co-combustion of paper mill sludge and municipal solid waste. Energ Convers Manage 2015;99:112-8. https://doi.org/10.1016/j.enconman.2015.04.026

[11]Zhong RG, Wang C, Zhang ZT, Liu QC, Cai ZW. PCDD/F levels and phase distributions in a full-scale municipal solid waste incinerator with co-incinerating sewage sludge. Waste Manage 2020;106:110-9. https://doi.org/10.1016/j.wasman.2020.03.020

[12]Chen LM, Liao YF, Ma XQ. Economic analysis on sewage sludge drying and its co-combustion in municipal solid waste power plant. Waste Manage 2021;121:11-22. https://doi.org/10.1016/j.wasman.2020.11.038

[13]Fu Z, Zhang SH, Li XP, Shao JG, Wang K, Chen HP. MSW oxy-enriched incineration technology applied in China: Combustion temperature, flue gas loss and economic considerations. Waste Manage 2015;38:149-56. https://doi.org/10.1016/j.wasman.2014.12.026

[14]Versteeg H K MW. An Introduction to Computational Fluid Dynamics: The Finite Volume Method. Second Edition ed. England: Pearson Education Limited; 2007.
[15]Haberle I, Skreiberg O, Lazar J, Haugen NEL. Numerical models for thermochemical degradation of thermally thick woody biomass, and their application in domestic wood heating appliances and grate furnaces. Prog Energ Combust 2017;63:204-52. https://doi.org/10.1016/j.pecs.2017.07.004
[16]Diba F, Karim MR, Naser J. Numerical modelling of a bubbling fluidized bed combustion: A simplified approach. Fuel 2020;277. https://doi.org/10.1016/j.fuel.2020.118170
[17]Zhou AQ, Xu HP, Meng XX, Yang WM, Sun R. Development of a numerical model for co-combustion of the blended solid waste fuel in the grate boiler. Chem Eng J 2021;405. https://doi.org/10.1016/j.cej.2020.126604
[18]Karim MR, Bhuiyan AA, Sarhan AR, Naser J. CFD simulation of biomass thermal conversion under air/oxy-fuel conditions in a reciprocating grate boiler. Renew Energ 2020;146:1416-28.
[19]Zhang SR, Jiang XG, Lv GJ, Liu BX, Jin YQ, Yan JH. SO2, NOx, HF, HCl and PCDD/Fs emissions during Co-combustion of bituminous coal and pickling sludge in a drop tube furnace. Fuel 2016;186:91-9. https://doi.org/10.1016/j.fuel.2016.08.061
[20]Gu TB, Yin CG, Ma WC, Chen GY. Municipal solid waste incineration in a packed bed: A comprehensive modeling study with experimental validation. Appl Energ 2019;247:127-39. https://doi.org/10.1016/j.apenergy.2019.04.014
[21]Gu T, Ma W, Berning T, Guo Z, Andersson B, Yin C. Advanced simulation of a 750 t/d municipal solid waste grate boiler to better accommodate feedstock changes due to waste classification. Energy 2022;In Press:124338. https://doi.org/10.1016/j.energy.2022.124338
[22]ANSYS Fluent Customization Manual. Release 2021 R1 ed.: ANSYS, Inc., 2600 ANSYS Drive Canonsburg, PA 15317; 2021.
[23]Glarborg P, Miller JA, Ruscic B, Klippenstein SJ. Modeling nitrogen chemistry in combustion. Prog Energ Combust 2018;67:31-68. https://doi.org/10.1016/j.pecs.2018.01.002
[24]Zhou H, Jensen AD, Glarborg P, Kavaliauskas A. Formation and reduction of nitric oxide in fixed-bed combustion of straw. Fuel 2006;85(5-6):705-16. https://doi.org/10.1016/j.fuel.2005.08.038
[25]Anca-Couce A, Sommersacher P, Evic N, Mehrabian R, Scharler R. Experiments and modelling of NOx precursors release (NH3 and HCN) in fixed-bed biomass combustion conditions. Fuel 2018;222:529-37. https://doi.org/10.1016/j.fuel.2018.03.003
[26]Ma WC, Ma C, Liu X, Gu TB, Thengane SK, Bourtsalas A, et al. Nox formation in fixed-bed biomass combustion: Chemistry and modeling. Fuel 2021;290. https://doi.org/10.1016/j.fuel.2020.119694
[27]Xiao KK, Yu ZC, Wang H, Yang JK, Liang S, Hu JP, et al. Investigation on emission control of NOx precursors and phosphorus reclamation during pyrolysis of ferric sludge. Sci Total Environ 2019;670:932-40. https://doi.org/10.1016/j.scitotenv.2019.03.223

[28]Deng L, Jin X, Zhang Y, Che DF. Release of nitrogen oxides during combustion of model coals. Fuel 2016;175:217-24. https://doi.org/10.1016/j.fuel.2016.02.047
[29]Hashemi H, Hansen S, Toftegaard MB, Pedersen KH, Jensen AD, Dam-Johansen K, et al. A Model for Nitrogen Chemistry in Oxy-Fuel Combustion of Pulverized Coal. Energ Fuel 2011;25(10):4280-9. https://doi.org/10.1021/ef200853t
[30]Liu H, Gibbs BM. Modelling of NO and N2O emissions from biomass-fired circulating fluidized bed combustors. Fuel 2002;81(3):271-80. https://doi.org/10.1016/S0016-2361(01)00170-3
[31]ANSYS Fluent Theory Guide. Release 2021 R1 ed.: ANSYS, Inc., 2600 ANSYS Drive Canonsburg, PA 15317; 2021.
[32]Bin Yang Y, Swithenbank J. Mathematical modelling of particle mixing effect on the combustion of municipal solid wastes in a packed-bed furnace. Waste Manage 2008;28(8):1290-300. https://doi.org/10.1016/j.wasman.2007.04.012
[33]Nugraha MG, Saptoadi H, Hidayat M, Andersson B, Andersson R. Particle modelling in biomass combustion using orthogonal collocation. Appl Energ 2019;255. https://doi.org/10.1016/j.apenergy.2019.113868
[34]Babushok VI, Dakdancha AN. Global Kinetic-Parameters for High-Temperature Gas-Phase Reactions. Combust Explo Shock+ 1993;29(4):464-89. https://doi.org/10.1007/BF00782974
[35]Yan M, Antoni, Wang JY, Hantoko D, Kanchanatip E. Numerical investigation of MSW combustion influenced by air preheating in a full-scale moving grate incinerator. Fuel 2021;285. https://doi.org/10.1016/j.fuel.2020.119193
[36]Yin CG. Refined Weighted Sum of Gray Gases Model for Air-Fuel Combustion and Its Impacts. Energ Fuel 2013;27(10):6287-94. https://doi.org/10.1021/ef401503r
[37]Hu ZF, Jiang EC, Ma XQ. Numerical simulation on NOx emissions in a municipal solid waste incinerator. J Clean Prod 2019;233:650-64. https://doi.org/10.1016/j.jclepro.2019.06.127
[38]Rajh B, Yin C, Samec N, Hribersek M, Kokalj F, Zadravec M. Advanced CFD modelling of air and recycled flue gas staging in a waste wood-fired grate boiler for higher combustion efficiency and greater environmental benefits. J Environ Manage 2018;218:200-8. https://doi.org/10.1016/j.jenvman.2018.04.030
[39]Mendiara T, Glarborg P. Ammonia chemistry in oxy-fuel combustion of methane. Combust Flame 2009;156(10):1937-49. https://doi.org/10.1016/j.combustflame.2009.07.006
[40]Xia ZH, Shan P, Chen CX, Du HL, Huang J, Bai L. A two-fluid model simulation of an industrial moving grate waste incinerator. Waste Manage 2020;104:183-91. https://doi.org/10.1016/j.wasman.2020.01.016
[41]Mousavi SM, Fatehi H, Bai XS. Numerical study of the combustion and application of SNCR for NOx reduction in a lab-scale biomass boiler. Fuel 2021;293. https://doi.org/10.1016/j.fuel.2021.120154

Chapter 4. Final Remarks

This Ph.D. project developed a novel kinetic model and an advanced CFD simulation, contributing to biomass pyrolysis and combustion, respectively. On the one hand, the developed models for kinetic analysis are validated and utilized in characterizing biomass pyrolysis, which demonstrates a new perspective for investigating solid fuel pyrolysis. On the other hand, the advanced CFD simulation containing an in-house bed model is validated and deployed to test and adjust a MSW boiler operation for incinerating new feedstocks. The two modelling works from this Ph.D. project are meaningful and potential for further utilization and expansion. The main scientific contributions and several future perspectives of this Ph.D. project are outlined below.

4.1. Main contributions

The main contributions of the study on kinetic modeling of biomass pyrolysis are as follows.

- A universal description for solid fuel pyrolysis is derived, of which several utilizations, such as identification of the conversion rate peak and determination of the reaction mechanism, are proposed.
- A simplified kinetic model that outperforms the conventional kinetic model in terms of accuracy and simplicity is developed and applied to characterize biomass pyrolysis.
- The kinetics of poplar wood pyrolysis are revealed, which vary with the conversion and heating rates to different extents.

The main contributions of the study on biomass combustion simulation are highlighted as follows.

- An in-house bed model is developed for describing solid fuel conversion on moving grates, including fuel NO_x formation.
- The simulation of the entire boiler is accomplished by the bed model coupled with the freeboard simulation performed in ANSYS Fluent and validated by operation data.

- A numerical study of incinerating new feedstock due to waste classification is performed, providing appropriate air supply and thermal input adjustments.
- The co-combustion of MSW, sewage sludge and industrial solid waste is investigated based on an advanced simulation, yielding feasible operation guidelines considering NO_x reduction.

4.2. Future perspectives

The modeling works carried out in this Ph.D. project are considered good starting points for pyrolysis modeling and combustion simulation of biomass. Further developments and applications based on the developed kinetic model and advanced CFD simulation are worth to be attempted. The assumptions and simplifications used in this project can be reconsidered to solve the drawbacks and enhance the accuracy and applicability of the developed models. Several encouraging perspectives for future work are as follows.

For kinetic modeling of biomass pyrolysis:

- The universal description and related applications should be extended to multistep reaction mechanisms to better analyse real biomass pyrolysis. In practice, the reaction mechanism for biomass pyrolysis is not global.
- The modeling work of species evolution during the pyrolysis process is encouraged by combining the proposed kinetic model and reliable reaction schemes. It would promote the application of biomass pyrolysis for modeling the solid decomposition rate and predicting the production.
- A set of distributed kinetics for biomass pyrolysis, along with the conversion and heating rates is worth to be evaluated, based on the developed model and corresponding experimental data. This would benefit engineering applications and CFD simulations of biomass thermal conversion.

For biomass combustion simulation:

- A complex sub-model describing particle motions driven by the grate movements, solid conversion and interaction, with acceptable computation cost, is demanded in the bed model. The solid density,

bed porosity, and bed volume change need to be comprehensively considered to ensure the precise mass balance.

- The lateral heat transfer and the thermal impacts of the grate should be considered in the fuel bed model. As a substitute, a real 2D steady bed model can be developed to describe the real steady status of moving-grate beds.
- Upgrading the bed model from 'thermally thin' to 'thermally thick' is meaningful, where a reasonable compromise is probably needed considering the non-uniformity of particles and computational cost.
- Distributed kinetics based on the universal description or evaluated by the new kinetic model for the decomposition of various feedstocks should be employed, to replace the currently used global kinetics in the bed model.
- Automatic coupling between the bed model (programmed by MATLAB) and freeboard simulation in ANSYS Fluent is worth to attempted, i.e., compiling the entire bed model into the CFD simulation of the boiler.

Bibliography

[1] Sansaniwal SK, Rosen MA, Tyagi SK. Global challenges in the sustainable development of biomass gasification: An overview. Renew Sust Energ Rev. 2017;80:23-43.
[2] Demirbas MF, Balat M, Balat H. Potential contribution of biomass to the sustainable energy development. Energ Convers Manage. 2009;50(7):1746-60.
[3] IRENA. World Energy Transitions Outlook: 1.5°C Pathway. Abu Dhabi: International Renewable Energy Agency, 2021.
[4] Wang SR, Dai GX, Yang HP, Luo ZY. Lignocellulosic biomass pyrolysis mechanism: A state-of-the-art review. Prog Energ Combust. 2017;62:33-86.
[5] Yin C, Rosendahl LA, Kaer SK. Grate-firing of biomass for heat and power production. Prog Energ Combust. 2008;34(6):725-54.
[6] Pang SS. Advances in thermochemical conversion of woody biomass to energy, fuels and chemicals. Biotechnol Adv. 2019;37(4):589-97.
[7] Huang X, Ren J, Ran JY, Qin CL, Yang ZQ, Cao JP. Recent advances in pyrolysis of cellulose to value-added chemicals. Fuel Process Technol. 2022;229.
[8] Babu BV. Biomass pyrolysis: a state-of-the-art review. Biofuel Bioprod Bior. 2008;2(5):393-414.
[9] Papari S, Hawboldt K. A review on the pyrolysis of woody biomass to bio-oil: Focus on kinetic models. Renew Sust Energ Rev. 2015;52:1580-95.
[10] Slopiecka K, Bartocci P, Fantozzi F. Thermogravimetric analysis and kinetic study of poplar wood pyrolysis. Appl Energ. 2012;97:491-7.
[11] Akhtar A, Krepl V, Ivanova T. A Combined Overview of Combustion, Pyrolysis, and Gasification of Biomass. Energ Fuel. 2018;32(7):7294-318.
[12] Waheed QMK, Nahil MA, Williams PT. Pyrolysis of waste biomass: investigation of fast pyrolysis and slow pyrolysis process conditions on product yield and gas composition. J Energy Inst. 2013;86(4):233-41.
[13] Sterner M, Specht M. Power-to-Gas and Power-to-X-The History and Results of Developing a New Storage Concept. Energies. 2021;14(20).
[14] Wang SR, Lin HZ, Ru B, Dai GX, Wang XL, Xiao G, et al. Kinetic modeling of biomass components pyrolysis using a sequential and coupling method. Fuel. 2016;185:763-71.
[15] Mladenovic M, Paprika M, Marinkovic A. Denitrification techniques for biomass combustion. Renew Sust Energ Rev. 2018;82:3350-64.
[16] Marangwanda GT, Madyira DM, Babarinde TO. Combustion models for biomass: A review. Energy Rep. 2020;6:664-72.
[17] Yin CG, Yan JY. Oxy-fuel combustion of pulverized fuels: Combustion

fundamentals and modeling. Appl Energ. 2016;162:742-62.
[18] Bugge M, Skreiberg O, Haugen NEL, Carlsson P, Houshfar E, Lovas T. Numerical simulations of staged biomass grate fired combustion with an emphasis on NOx emissions. Clean, Efficient and Affordable Energy for a Sustainable Future. 2015;75:156-61.
[19] Silva J, Teixeira J, Teixeira S, Preziati S, Cassiano J. CFD Modeling of Combustion in Biomass Furnace. Enrgy Proced. 2017;120:665-72.
[20] Hameed S, Sharma A, Pareek V, Wu HW, Yu Y. A review on biomass pyrolysis models: Kinetic, network and mechanistic models. Biomass Bioenerg. 2019;123:104-22.
[21] Mishra G, Bhaskar T. Non isothermal model free kinetics for pyrolysis of rice straw. Bioresource Technol. 2014;169:614-21.
[22] Siddiqi H, Kumari U, Biswas S, Mishra A, Meikap BC. A synergistic study of reaction kinetics and heat transfer with multi-component modelling approach for the pyrolysis of biomass waste. Energy. 2020;204.
[23] Ali I, Naqvi SR, Bahadar A. Kinetic analysis of Botryococcus braunii pyrolysis using model-free and model fitting methods. Fuel. 2018;214:369-80.
[24] Jomaa G, Goblet P, Coquelet C, Morlot V. Kinetic modeling of polyurethane pyrolysis using non-isothermal thermogravimetric analysis. Thermochim Acta. 2015;612:10-8.
[25] Wang SR, Ru B, Lin HZ, Dai GX, Wang YR, Luo ZY. Kinetic Study on Pyrolysis of Biomass Components: A Critical Review. Curr Org Chem. 2016;20(23):2489-513.
[26] Zhai M, Guo L, Zhang Y, Dong P, Qi GL, Huang YD. Kinetic Parameters of Biomass Pyrolysis by TGA. Bioresources. 2016;11(4):8548-57.
[27] El-Sayed SA, Mostafa ME. Pyrolysis characteristics and kinetic parameters determination of biomass fuel powders by differential thermal gravimetric analysis (TGA/DTG). Energ Convers Manage. 2014;85:165-72.
[28] Wu ZQ, Ma C, Jiang Z, Luo ZY. Structure evolution and gasification characteristic analysis on co-pyrolysis char from lignocellulosic biomass and two ranks of coal: Effect of wheat straw. Fuel. 2019;239:180-90.
[29] Coats AW, Redfern JP. Kinetic Parameters from Thermogravimetric Data. Nature. 1964;201(491):68-&.
[30] Liu HR, Wang CJ, Zhao WP, Yang SL, Hou XT. Pyrolysis characteristics and kinetic modeling of Artemisia apiacea by thermogravimetric analysis. J Therm Anal Calorim. 2018;131(2):1783-92.
[31] Sfakiotakis S, Vamvuka D. Development of a modified independent parallel reactions kinetic model and comparison with the distributed activation energy model for the pyrolysis of a wide variety of biomass fuels.

Bioresource Technol. 2015;197:434-42.
[32] Bach QV, Chen WH. Pyrolysis characteristics and kinetics of microalgae via thermogravimetric analysis (TGA): A state-of-the-art review. Bioresource Technol. 2017;246:88-100.
[33] Tian XJ, Dai LL, Wang YP, Zeng ZH, Zhang SM, Jiang L, et al. Influence of torrefaction pretreatment on corncobs: A study on fundamental characteristics, thermal behavior, and kinetic. Bioresource Technol. 2020;297.
[34] Ahmad MS, Mehmood MA, Liu CG, Tawab A, Bai FW, Sakdaronnarong C, et al. Bioenergy potential of Wolffia arrhiza appraised through pyrolysis, kinetics, thermodynamics parameters and TG-FTIR-MS study of the evolved gases. Bioresource Technol. 2018;253:297-303.
[35] Vo TK, Ly HV, Lee OK, Lee EY, Kim CH, Seo JW, et al. Pyrolysis. characteristics and kinetics of microalgal Aurantiochytrium sp KRS101. Energy. 2017;118:369-76.
[36] Chong CT, Mong GR, Ng JH, Chong WWF, Ani FN, Lam SS, et al. Pyrolysis characteristics and kinetic studies of horse manure using thermogravimetric analysis. Energ Convers Manage. 2019;180:1260-7.
[37] Cai JM, Wu WX, Liu RH. An overview of distributed activation energy model and its application in the pyrolysis of lignocellulosic biomass. Renew Sust Energ Rev. 2014;36:236-46.
[38] Gai C, Zhang YH, Chen WT, Zhang P, Dong YP. Thermogravimetric and kinetic analysis of thermal decomposition characteristics of low-lipid microalgae. Bioresource Technol. 2013;150:139-48.
[39] Criado JM. Kinetic-Analysis of Dtg Data from Master Curves. Thermochim Acta. 1978;24(1):186-9.
[40] Criado JM, Malek J, Ortega A. Applicability of the Master Plots in Kinetic-Analysis of Non-Isothermal Data. Thermochim Acta. 1989;147(2):377-85.
[41] Luo LP, Zhang ZY, Li C, Nishu, He F, Zhang XG, et al. Insight into master plots method for kinetic analysis of lignocellulosic biomass pyrolysis. Energy. 2021;233.
[42] Han ZX, Li J, Gu TB, Yan BB, Chen GY. The synergistic effects of polyvinyl chloride and biomass during combustible solid waste pyrolysis: Experimental investigation and modeling. Energ Convers Manage. 2020;222.
[43] Mallick D, Mahanta P, Moholkar VS. Co-gasification of coal and biomass blends: Chemistry and engineering. Fuel. 2017;204:106-28.
[44] Jankovic B. The kinetic modeling of the non-isothermal pyrolysis of Brazilian oil shale: Application of the Weibull probability mixture model. J Petrol Sci Eng. 2013;111:25-36.
[45] Li XT, Grace JR, Bi XT, Campbell JS. A new pyrolysis model based on

generalized extreme value (GEV) distributions and its application to lignocellulosic biomass. Fuel. 2016;184:211-21.
[46] Zhou AQ, Xu HP, Yang WM, Tu YJ, Xu MC, Yu WB, et al. Numerical Study of Biomass Grate Boiler with Coupled Time Dependent Fuel Bed Model and Computational Fluid Dynamics Based Freeboard Model. Energ Fuel. 2018;32(9):9493-505.
[47] Haberle I, Skreiberg O, Lazar J, Haugen NEL. Numerical models for thermochemical degradation of thermally thick woody biomass, and their application in domestic wood heating appliances and grate furnaces. Prog Energ Combust. 2017;63:204-52.
[48] Rajh B, Yin C, Samec N, Hribersek M, Zadravec M. Advanced modelling and testing of a 13 MWth waste wood-fired grate boiler with recycled flue gas. Energ Convers Manage. 2016;125:230-41.
[49] Yang YB, Goh YR, Zakaria R, Nasserzadeh V, Swithenbank J. Mathematical modelling of MSW incineration on a travelling bed. Waste Manage. 2002;22(4):369-80.
[50] Mahmoudi AH, Markovic M, Peters B, Brem G. An experimental and numerical study of wood combustion in a fixed bed using Euler-Lagrange approach (XDEM). Fuel. 2015;150:573-82.
[51] Ostermeier P, Fischer F, Fendt S, DeYoung S, Spliethoff H. Coarse-grained CFD-DEM simulation of biomass gasification in a fluidized bed reactor. Fuel. 2019;255.
[52] Wissing F, Wirtz S, Scherer V. Simulating municipal solid waste incineration with a DEM/CFD method - Influences of waste properties, grate and furnace design. Fuel. 2017;206:638-56.
[53] Haugen NEL, Bugge M, Mack A, Li T, Skreiberg Ø. Bed Model for Grate-Fired Furnaces: Computational Fluid Dynamics Modeling and Comparison to Experiments. Energ Fuel. 2022;36(11):5852-67.
[54] Xia ZH, Shan P, Chen CX, Du HL, Huang J, Bai L. A two-fluid model simulation of an industrial moving grate waste incinerator. Waste Manage. 2020;104:183-91.
[55] Yang YB, Yamauchi H, Nasserzadeh V, Swithenbank J. Effects of fuel devolatilisation on the combustion of wood chips and incineration of simulated municipal solid wastes in a packed bed. Fuel. 2003;82(18):2205-21.
[56] Yan M, Antoni, Wang JY, Hantoko D, Kanchanatip E. Numerical investigation of MSW combustion influenced by air preheating in a full-scale moving grate incinerator. Fuel. 2021;285.
[57] Ismail TM, Abd El-Salam M, El-Kady MA, El-Haggar SM. Three dimensional model of transport and chemical late phenomena on a MSW

incinerator. Int J Therm Sci. 2014;77:139-57.
[58] Gu TB, Yin CG, Ma WC, Chen GY. Municipal solid waste incineration in a packed bed: A comprehensive modeling study with experimental validation. Appl Energ. 2019;247:127-39.
[59] ANSYS Fluent Theory Guide. Release 2021 R1 ed: ANSYS, Inc., 2600 ANSYS Drive Canonsburg, PA 15317, 2021.
[60] Karim MR, Naser J. CFD modelling of combustion and associated emission of wet woody biomass in a 4 MW moving grate boiler. Fuel. 2018;222:656-74.
[61] Rajh B, Yin C, Samec N, Hribersek M, Kokalj F, Zadravec M. Advanced CFD modelling of air and recycled flue gas staging in a waste wood-fired grate boiler for higher combustion efficiency and greater environmental benefits. J Environ Manage. 2018;218:200-8.
[62] Yang YB, Ryu C, Goodfellow J, Sharifi VN, Swithenbank J. Modelling waste combustion in grate furnaces. Process Saf Environ. 2004;82(B3):208-22.
[63] Hu ZF, Jiang EC, Ma XQ. Numerical simulation on NOx emissions in a municipal solid waste incinerator. J Clean Prod. 2019;233:650-64.
[64] Lopez-Gonzalez D, Avalos-Ramirez A, Giroir-Fendler A, Godbout S, Fernandez-Lopez M, Sanchez-Silva L, et al. Combustion kinetic study of woody and herbaceous crops by thermal analysis coupled to mass spectrometry. Energy. 2015;90:1626-35.
[65] Lai C-D. Generalized Weibull Distributions. London: Springer, 2014.
[66] Gu TB, Fu ZF, Berning T, Li XT, Yin CG. A simplified kinetic model based on a universal description for solid fuels pyrolysis: Theoretical derivation, experimental validation, and application demonstration. Energy. 2021;225.
[67] Jankovic B, Manic N, Stojiljkovic D, Jovanovic V. TSA-MS characterization and kinetic study of the pyrolysis process of various types of biomass based on the Gaussian multi-peak fitting and peak-to-peak approaches. Fuel. 2018;234:447-63.
[68] Wang SR, Dai GX, Ru B, Zhao Y, Wang XL, Xiao G, et al. Influence of torrefaction on the characteristics and pyrolysis behavior of cellulose. Energy. 2017;120:864-71.
[69] Gu TB, Berning T, Yin CG. Application of a New Statistical Model for the Description of Solid Fuel Decomposition in the Analysis of Artemisia apiacea Pyrolysis. Energies. 2021;14(18).
[70] Mianowski A, Baraniec I. Three-parametric equation in evaluation of thermal dissociation of reference compound. J Therm Anal Calorim. 2009;96(1):179-87.
[71] Almazrouei M, Janajreh I. Model-fitting approach to kinetic analysis of

non-isothermal pyrolysis of pure and crude glycerol. Renew Energ. 2020;145:1693-708.
[72] Yin CG, Rosendahl L, Kaer SK, Sorensen H, Clausen S, Hille T, et al. Modeling and experiments of Biomass combustion in a large-scale grate boiler. Challenges of Power Engineering and Environment, Vols 1 and 2. 2007:1173-+.
[73] ANSYS Fluent Customization Manual. Release 2021 R1 ed: ANSYS, Inc., 2600 ANSYS Drive Canonsburg, PA 15317, 2021.
[74] Gu T, Ma W, Berning T, Guo Z, Andersson B, Yin C. Advanced simulation of a 750 t/d municipal solid waste grate boiler to better accommodate feedstock changes due to waste classification. Energy. 2022;254:124338.
[75] Goh YR, Yang YB, Zakaria R, Siddall RG, Nasserzadeh V, Swithenbank J. Development of an incinerator bed model for municipal solid waste incineration. Combust Sci Technol. 2001;162:37-58.
[76] Lu H, Robert W, Peirce G, Ripa B, Baxter LL. Comprehensive study of Biomass particle combustion. Energ Fuel. 2008;22(4):2826-39.
[77] Mehrabian R, Zahirovic S, Scharler R, Obernberger I, Kleditzsch S, Wirtz S, et al. A CFD model for thermal conversion of thermally thick biomass particles. Fuel Process Technol. 2012;95:96-108.
[78] van der Lans RP, Pedersen LT, Jensen A, Glarborg P, Dam-Johansen K. Modelling and experiments of straw combustion in a grate furnace. Biomass Bioenerg. 2000;19(3):199-208.
[79] Yin CE, Kaer SK, Rosendahl L, Hvid SL. Co-firing straw with coal in a swirl-stabilized dual-feed burner: Modelling and experimental validation. Bioresource Technol. 2010;101(11):4169-78.
[80] Sun R, Ismail TM, Ren XH, El-Salam MA. Numerical and experimental studies on effects of moisture content on combustion characteristics of simulated municipal solid wastes in a fixed bed. Waste Manage. 2015;39:166-78.
[81] Zhang SR, Jiang XG, Lv GJ, Liu BX, Jin YQ, Yan JH. SO2, NOx, HF, HCl and PCDD/Fs emissions during Co-combustion of bituminous coal and pickling sludge in a drop tube furnace. Fuel. 2016;186:91-9.
[82] Glarborg P, Miller JA, Ruscic B, Klippenstein SJ. Modeling nitrogen chemistry in combustion. Prog Energ Combust. 2018;67:31-68.
[83] Xiao KK, Yu ZC, Wang H, Yang JK, Liang S, Hu JP, et al. Investigation on emission control of NOx precursors and phosphorus reclamation during pyrolysis of ferric sludge. Sci Total Environ. 2019;670:932-40.
[84] Hashemi H, Hansen S, Toftegaard MB, Pedersen KH, Jensen AD, Dam-Johansen K, et al. A Model for Nitrogen Chemistry in Oxy-Fuel Combustion

of Pulverized Coal. Energ Fuel. 2011;25(10):4280-9.
[85] Liu H, Gibbs BM. Modelling of NO and N2O emissions from biomass-fired circulating fluidized bed combustors. Fuel. 2002;81(3):271-80.
[86] Zhou H, Jensen AD, Glarborg P, Kavaliauskas A. Formation and reduction of nitric oxide in fixed-bed combustion of straw. Fuel. 2006;85(5-6):705-16.
[87] Gu T, Ma W, Guo Z, Berning T, Yin C. Stable and clean co-combustion of municipal sewage sludge with solid wastes in a grate boiler: A modeling-based feasibility study. Fuel. 2022;JFUE-D-22-02434 (Under review).
[88] Bin Yang Y, Swithenbank J. Mathematical modelling of particle mixing effect on the combustion of municipal solid wastes in a packed-bed furnace. Waste Manage. 2008;28(8):1290-300.
[89] Nugraha MG, Saptoadi H, Hidayat M, Andersson B, Andersson R. Particle modelling in biomass combustion using orthogonal collocation. Appl Energ. 2019;255.
[90] Babushok VI, Dakdancha AN. Global Kinetic-Parameters for High-Temperature Gas-Phase Reactions. Combust Explo Shock+. 1993;29(4):464-89.
[91] Civan F. Porous Media Transport Phenomena: John Wiley & Sons, Inc., Hoboken, New Jersey, 2011.
[92] Versteeg H K MW. An Introduction to Computational Fluid Dynamics: The Finite Volume Method. Second Edition ed. England: Pearson Education Limited, 2007.
[93] ANSYS ICEM CFD User's Manual. Release 2021 R1 ed: ANSYS, Inc., 2600 ANSYS Drive Canonsburg, PA 15317, 2021.
[94] Discovery SpaceClaim. Release 2021 R1 ed: ANSYS, Inc., 2600 ANSYS Drive Canonsburg, PA 15317, 2021.
[95] Xu JC, Liao YF, Yu ZS, Cai ZL, Ma XQ, Dai MQ, et al. Co-combustion of paper sludge in a 750 t/d waste incinerator and effect of sludge moisture content: A simulation study. Fuel. 2018;217:617-25.
[96] Lin H, Ma XQ. Simulation of co-incineration of sewage sludge with municipal solid waste in a grate furnace incinerator. Waste Manage. 2012;32(3):561-7.
[97] Westbrook CK, Dryer FL. Simplified Reaction-Mechanisms for the Oxidation of Hydrocarbon Fuels in Flames. Combust Sci Technol. 1981;27(1-2):31-43.
[98] Mousavi SM, Fatehi H, Bai XS. Numerical study of the combustion and application of SNCR for NOx reduction in a lab-scale biomass boiler. Fuel. 2021;293.
[99] Yin CG. Refined Weighted Sum of Gray Gases Model for Air-Fuel

Combustion and Its Impacts. Energ Fuel. 2013;27(10):6287-94.
[100] Zadravec T, Yin CG, Kokalj F, Samec N, Rajh B. The impacts of different profiles of the grate inlet conditions on freeboard CFD in a waste wood-fired grate boiler. Appl Energ. 2020;268.
[101] Almohammadi KM, Ingham DB, Ma L, Pourkashan M. Computational fluid dynamics (CFD) mesh independency techniques for a straight blade vertical axis wind turbine. Energy. 2013;58:483-93.
[102] Li ZX, Qiao XQ, Miao ZQ. A novel burner arrangement scheme with annularly combined multiple air fl ows for wall-tangentially fi red pulverized coal boiler. Energy. 2021;222.

ISSN (online): 2446-1636
ISBN (online): 978-87-7573-884-7

AALBORG UNIVERSITY PRESS